

University of Warsaw
Faculty of Physics



Anna Jacyszyn-Dobrzeńska

Analysis of the three dimensional
structure of the Magellanic System
based on classical pulsators
from the OGLE project

Doctoral thesis in astrophysics

Thesis prepared under the supervision of
prof. dr hab. Igor Soszyński
and **dr Dorota Skowron**
Astronomical Observatory

Warszawa, July 2021

Abstract

The Large and Small Magellanic Cloud (LMC and SMC, respectively) are among our closest galaxies. Together with the surrounding structures, they constitute the Magellanic System. This system can be named our “local laboratory” in the context of interacting galaxies. One of the most important evidences of these interactions is the existence of a structure spanning the area between the Magellanic Clouds, namely the Magellanic Bridge. In this doctoral thesis I analyzed the three dimensional structure of the Magellanic Clouds and the Magellanic Bridge. I based my studies on classical pulsating stars from the OGLE Collection of Variable Stars.

In the first part of my doctoral thesis I presented an analysis of the three dimensional spatial distribution of classical Cepheids in the Magellanic System (Jacyszyn-Dobrzniecka et al., 2016, *Acta Astronomica*, 66, 149). In the LMC, Cepheids form substructures located in the plane of the disk, mainly in the bar and the northern arm. In the SMC, these stars are distributed more regularly and form a tri-axial ellipsoid, of which the longest axis is five times longer than the other two axes. The SMC is elongated almost along the line of sight.

The second part of the thesis presents an analysis of the three dimensional distribution of old pulsating stars – RR Lyrae variables (Jacyszyn-Dobrzniecka et al., 2017, *Acta Astronomica*, 67, 1). In both Magellanic Clouds these stars form regular structures that can be described by tri-axial ellipsoids. I also compared the distributions of classical Cepheids and RR Lyrae stars, showing that the old stellar population reveal far broader distributions and do not form any additional substructures in contrast to young stars.

In the next step I presented a detailed analysis of an updated sample of classical Cepheids located in the Magellanic Bridge (Jacyszyn-Dobrzniecka et al., 2020, *The Astrophysical Journal*, 889, 25). I showed that classical Cepheids form a connection between the Clouds in both two and three dimensions. Moreover, ages of most of the Cepheids support the hypothesis that these stars were formed in situ in the Bridge as an effect of the last encounter of the Clouds. Anomalous Cepheids that were also added to the Bridge sample are spread more evenly and do not form an evident connection between both galaxies.

The last part of my doctoral thesis concerns a detailed analysis of the distribution of RR Lyrae stars in the Magellanic Bridge (Jacyszyn-Dobrzniecka et al., 2020, *The Astrophysical Journal*, 889, 26). In this study I showed that these old pulsating stars are present in the Bridge area, however they do not form an evident connection between the Clouds and their distribution rather resembles two overlapping halos. Additionally, I presented a reconstruction of the analysis performed by Belokurov et al. (2017, *Monthly Notices of the Royal Astronomical Society*, 466, 4711) showing that it is not possible to obtain their bridge-like connection without many non-physical spurious sources in the final sample.

Streszczenie

Analiza trójwymiarowej struktury Systemu Magellana na podstawie klasycznych gwiazd pulsujących z projektu OGLE

Obłoki Magellana są jednymi z najbliższych nam galaktyk. Łącznie z otaczającymi strukturami tworzą System Magellana, który można nazwać naszym „lokalnym laboratorium” w kontekście oddziaływań międzygalaktycznych. Jednym z ich najważniejszych rezultatów jest istnienie struktury rozciągającej się pomiędzy Obłokami, zwanej Mostem Magellana. W ramach niniejszej rozprawy doktorskiej zbadałam trójwymiarową strukturę Obłoków Magellana oraz Mostu Magellana. Wykorzystałam w tym celu klasyczne gwiazdy pulsujące, będące zarazem świecami standardowymi, pochodzące z Kolekcji Gwiazd Zmiennych projektu OGLE.

Pierwsza część mojej pracy doktorskiej przedstawia analizę trójwymiarowego rozkładu cefeid klasycznych w Systemie Magellana (Jacyszyn-Dobrzeniecka i in., 2016, *Acta Astronomica*, 66, 149). W Wielkim Obłoku Magellana są one skupione w wyraźnych strukturach leżących w płaszczyźnie dysku – głównie w poprzeczce oraz ramieniu północnym. W Małym Obłoku Magellana cefeidy klasyczne rozłożone są bardziej równomiernie i tworzą strukturę o kształcie elipsoidy trójosiowej, której najdłuższa oś jest pięciokrotnie dłuższa niż krótkie osie. Mały Obłok Magellana jest rozciągnięty prawie wzdłuż linii widzenia.

Kolejny etap przedstawia analizę trójwymiarowego rozkładu gwiazd pulsujących typu RR Lutni, należących do starej populacji gwiazdowej (Jacyszyn-Dobrzeniecka i in., 2017, *Acta Astronomica*, 67, 1). W obydwu Obłokach Magellana gwiazdy te tworzą regularne struktury, które można opisać za pomocą trójosiowych elipsoid. Porównanie otrzymanych przeze mnie rozkładów dla gwiazd obydwu typów wskazuje na to, że gwiazdy stare rozłożone są na znacznie większym obszarze, a także nie tworzą wyraźnych podstruktur, w przeciwieństwie do gwiazd młodych.

W następnej części pracy przedstawiłam szczegółową analizę zaktualizowanej próbki cefeid klasycznych zaklasyfikowanych jako przynależące do Mostu Magellana (Jacyszyn-Dobrzeniecka i in., 2020, *The Astrophysical Journal*, 889, 25). Wykazałam, że cefeidy klasyczne tworzą połączenie pomiędzy Obłokami zarówno w dwóch jak i trzech wymiarach. Ponadto wiek większości z nich zgodny jest z hipotezą, że zostały one uformowane w obszarze Mostu Magellana w wyniku ostatniego zbliżenia Obłoków. Dodane do próbki cefeidy anomalne rozłożone są bardziej równomiernie i nie tworzą wyraźnego połączenia.

Ostatni etap dotyczy szczegółowej analizy rozkładu gwiazd typu RR Lutni w obszarze Mostu Magellana (Jacyszyn-Dobrzeniecka i in., 2020, *The Astrophysical Journal*, 889, 26). W tej części pracy tej wykazałam, iż stare gwiazdy pulsujące obecne są w obszarze Mostu Magellana, lecz nie tworzą wyraźnego połączenia pomiędzy Obłokami, a ich rozkład raczej przypomina nakładające się na siebie rozległe halo. Dodatkowo przedstawiłam rekonstrukcję analizy wykonanej przez Belokurova i in. (2017, *Monthly Notices of the Royal Astronomical Society*, 466, 4711) wykazując, że nie da się odtworzyć uzyskanego przez nich połączenia pomiędzy Obłokami Magellana bez uwzględniania wielu niefizycznych artefaktów w końcowej próbce danych.

Contents

I	Synopsis of the thesis	9
	List of published scientific articles constituting the doctoral thesis	11
	Synopsis	13
1	Introduction	13
1.1	The Magellanic System	13
1.2	Structure of the Magellanic Clouds	14
1.3	The Magellanic Bridge area	15
2	The OGLE project	16
2.1	General information	16
2.2	The OGLE Collection of Variable Stars	16
3	Analysis	17
3.1	Samples and methods	17
3.2	The Large Magellanic Cloud	18
3.3	The Small Magellanic Cloud	19
3.4	The Magellanic Bridge	20
4	Impact of this study	22
5	Summary	23
	Bibliography	26
II	Full texts of published scientific articles	29
	List of figures	33
	List of tables	34
1	OGLE-ing the Magellanic System: Three-Dimensional Structure of the Clouds and the Bridge Using Classical Cepheids	35
1.1	Introduction	36
1.2	Data	39
1.2.1	The OGLE Collection of Classical Cepheids	39
1.2.2	The Sample Selection	39
1.3	Data Analysis	40
1.3.1	Period-Luminosity Relation	40
1.3.2	Distances	43
1.3.3	Coordinate Transformations	45
1.3.4	Model and Plane Fitting	47

1.4	The Large Magellanic Cloud	48
1.4.1	Three-Dimensional Structure	48
1.4.2	Ages	51
1.4.3	Substructures	52
1.4.4	Plane Fitting	57
1.5	The Small Magellanic Cloud	60
1.5.1	Three-Dimensional Structure	60
1.5.2	Ages	61
1.5.3	Substructures	64
1.6	The Magellanic Bridge	67
1.7	Discussion	71
1.7.1	Three-Dimensional Structure and Substructures: the LMC	71
1.7.2	Three-Dimensional Structure and Substructures: the SMC	74
1.7.3	LMC-SMC Interactions and the Magellanic Bridge	75
1.7.4	Ages	77
1.8	Conclusions	77
2	OGLE-ing the Magellanic System: Three-Dimensional Structure of the Clouds and the Bridge Using RR Lyrae Stars	83
2.1	Introduction	84
2.2	Data	85
2.2.1	The OGLE Collection of RR Lyr Stars	85
2.2.2	The Sample Selection	86
2.3	Data Analysis	89
2.3.1	Period–Luminosity Relation	89
2.3.2	Metallicities and Distances	90
2.3.3	Coordinate Transformations	90
2.3.4	Model and Ellipsoid Fitting	92
2.4	The Large Magellanic Cloud	94
2.4.1	Three-Dimensional Structure	94
2.4.2	Ellipsoid Fitting	96
2.4.3	Comparison with Previous Studies	100
2.5	The Small Magellanic Cloud	102
2.5.1	Three-Dimensional Structure	102
2.5.2	Ellipsoid Fitting	105
2.5.3	Comparison with Previous Studies	108
2.6	The Magellanic Bridge	110
2.7	Comparison with Distribution of the Classical Cepheids	111
2.7.1	The Large Magellanic Cloud	112
2.7.2	The Small Magellanic Cloud	114
2.7.3	The Magellanic Bridge	114
2.8	Conclusions	115
3	OGLE-ing the Magellanic System: Cepheids in the Bridge	119
3.1	Introduction	119
3.2	Observational Data	120
3.2.1	OGLE Collection of Variable Stars	120
3.3	Data Analysis	121
3.3.1	Period–Luminosity Relations and Individual Distances	121
3.3.2	Coordinate Transformations	121

3.4	Classical Cepheids	121
3.4.1	Updated Bridge Sample	121
3.4.2	Two- and Three-dimensional Analysis	123
3.4.3	Ages	124
3.4.4	Proper Motions	124
3.4.5	Different Distance Estimates	125
3.4.6	Reddening Parameters	128
3.5	Anomalous Cepheids	129
3.5.1	Final Sample and Basic Parameters	129
3.5.2	Two- and Three-dimensional Analysis	130
3.5.3	Proper Motions	130
3.6	Reclassified Cepheids	130
3.7	<i>Gaia</i> DR2 Cepheids in the Bridge	131
3.7.1	Comparison with OCVS	131
3.8	Conclusions	132
4	OGLE-ing the Magellanic System: RR Lyrae Stars in the Bridge	135
4.1	Introduction	135
4.2	Observational Data	136
4.2.1	OCVS	136
4.3	Data Analysis	136
4.3.1	Sample Selection	136
4.3.2	Individual Distances and Coordinates	136
4.4	OGLE RRL Sample	137
4.4.1	Three-dimensional Distribution	137
4.4.2	Numerical Analysis	137
4.5	A Reanalysis	139
4.5.1	No Evident Connection	139
4.6	B17 RRL Candidates from <i>Gaia</i> DR1	140
4.6.1	Selection Process	140
4.6.2	Two-dimensional Analysis	141
4.6.3	Comparison with OGLE and <i>Gaia</i> DR2	143
4.7	Comparison of Different Tracers Distribution	144
4.8	Conclusions	146

Part I

Synopsis of the thesis

List of published scientific articles constituting the doctoral thesis

1. *OGLE-ing the Magellanic System: Three-Dimensional Structure of the Clouds and the Bridge using Classical Cepheids (Paper I)*
A. M. Jacyszyn-Dobrzeńska, D. M. Skowron, P. Mróz, J. Skowron, I. Soszyński, A. Udalski, P. Pietrukowicz, S. Kozłowski, Ł. Wyrzykowski, R. Poleski, M. Pawlak, M. K. Szymański, K. Ulaczyk
ACTA ASTRONOMICA, 66, 149 (2016)
Impact Factor (as of 2019): 2.640
Number of points from the Polish Ministry of Science and Higher Education list of scientific journals: 140 (30 as based on years 2013-2016)
Number of citations (as of 29 June 2021 according to the NASA Astrophysics Data System Abstract Service): 71
2. *OGLE-ing the Magellanic System: Three-Dimensional Structure of the Clouds and the Bridge using RR Lyrae Stars (Paper II)*
A. M. Jacyszyn-Dobrzeńska, D. M. Skowron, P. Mróz, I. Soszyński, A. Udalski, P. Pietrukowicz, J. Skowron, R. Poleski, S. Kozłowski, Ł. Wyrzykowski, M. Pawlak, M. K. Szymański, K. Ulaczyk
ACTA ASTRONOMICA, 67, 1 (2017)
DOI: 10.32023/0001-5237/67.1.1
Impact Factor (as of 2019): 2.640
Number of points from the Polish Ministry of Science and Higher Education list of scientific journals: 140 (30 as based on years 2013-2016)
Number of citations (as of 29 June 2021 according to the NASA Astrophysics Data System Abstract Service): 57
3. *OGLE-ing the Magellanic System: Cepheids in the Bridge (Paper III)*
A. M. Jacyszyn-Dobrzeńska, I. Soszyński, A. Udalski, M. K. Szymański, D. M. Skowron, J. Skowron, P. Mróz, K. Kruszyńska, P. Iwanek, P. Pietrukowicz, R. Poleski, S. Kozłowski, K. Ulaczyk, K. Rybicki, M. Wrona
THE ASTROPHYSICAL JOURNAL, 889, 25 (2020)
DOI: 10.3847/1538-4357/ab61f1
Impact Factor (as of 2019): 5.580
Number of points from the Polish Ministry of Science and Higher Education list of scientific journals: 140 (40 as based on years 2013-2016)
Number of citations (as of 29 June 2021 according to the NASA Astrophysics Data System Abstract Service): 8
4. *OGLE-ing the Magellanic System: RR Lyrae Stars in the Bridge (Paper IV)*
A. M. Jacyszyn-Dobrzeńska, P. Mróz, K. Kruszyńska, I. Soszyński,

D. M. Skowron, A. Udalski, M. K. Szymański, P. Iwanek, J. Skowron, P. Pietrukowicz, R. Poleski, S. Kozłowski, K. Ulaczyk, K. Rybicki, M. Wrona

[THE ASTROPHYSICAL JOURNAL, 889, 26 \(2020\)](#)

DOI: [10.3847/1538-4357/ab61f2](https://doi.org/10.3847/1538-4357/ab61f2)

Impact Factor (as of 2019): 5.580

Number of points from the Polish Ministry of Science and Higher Education list of scientific journals: 140 (40 as based on years 2013-2016)

Number of citations (as of 29 June 2021 according to the NASA Astrophysics Data System Abstract Service): 7

Synopsis

1 Introduction

1.1 The Magellanic System

For many years the Magellanic Clouds were thought to be long-term satellites of the Milky Way. Their proper motions (PMs), measured precisely only a few years ago, changed this paradigm, as it turned out that the PMs are too high for the Clouds to be on a bound orbit around the Milky Way (Kallivayalil et al., 2013). The Magellanic System is thus plausibly approaching the Milky Way for the first time. This implies that many of the observed irregularities of the Magellanic System as well as an existence of its extragalactic structures need to be explained in the new context. Many scientific studies are now devoted to disentangling the interaction history of the Magellanic System. The study presented in this doctoral thesis is one of such and shows an original and unique analysis. It was led by myself in cooperation with the Optical Gravitational Lensing Experiment (OGLE) Team and under the “Diamond Grant” program by the Polish Ministry of Science and Higher Education in years 2014–2018.

When not taking into account the Sagittarius dwarf galaxy, the Magellanic Clouds are our closest galaxies. Together with surrounding structures they form the Magellanic System. These additional structures are an effect of interactions between both Clouds and also between the Clouds and the Milky Way (e.g. Gardiner et al., 1994; Gardiner and Noguchi, 1996; Yoshizawa and Noguchi, 2003; Connors et al., 2006; Růžicka et al., 2009, 2010; Besla et al., 2010, 2012; Diaz and Bekki, 2012; Guglielmo et al., 2012, Belokurov et al., 2017, hereafter B17; Zivick et al., 2019). Due to its proximity, the Magellanic System can be called our local laboratory in the context of interacting galaxies and plays an important role in understanding the history and future of the Milky Way. Both Magellanic Clouds are also very useful for studying many astrophysical properties of stellar populations and gas in different environments. These galaxies contain many different types of objects that are involved in various astrophysical processes.

The Magellanic System consists of the Large and Small Magellanic Cloud (LMC and SMC, respectively), Magellanic Bridge (MBR), Magellanic Stream and Leading Arm. The Magellanic Bridge constitutes a gaseous and stellar connection between the Clouds (e.g. Harris, 2007; Barger et al., 2013; Skowron et al., 2014; B17; Zivick et al., 2019, Jacyszyn-Dobrzeniecka et al. 2020a, hereafter Paper III, Jacyszyn-Dobrzeniecka et al. 2020b, hereafter Paper IV). A stream of gas spanning around 160° on the sky and following the galaxies on their past

trajectory is the Magellanic Stream (Nidever et al., 2008, 2010). The Leading Arm consists of four groups of high velocity clouds, which are already interacting with the Milky Way disk. In these clouds young stars were discovered (Nidever et al., 2008; McClure-Griffiths et al., 2008; Venzmer et al., 2012; Casetti-Dinsecu et al., 2014). Lately, the Leading Arm relationship with the Magellanic System has been put into doubt (Tepper-García et al., 2019).

1.2 Structure of the Magellanic Clouds

The Large Magellanic Cloud

Structures of both Magellanic Clouds reveal many irregularities and asymmetries, which are probably effects of interactions involving these galaxies. In the LMC, young and old stars are distributed differently. The former are clumped in substructures, while the latter have a rather regular distribution (Cioni et al., 2000; Bica et al., 2008; Haschke et al., 2012a; Subramanian and Subramanian, 2013; Joshi and Joshi, 2014, Jacyszyn-Dobrzyniecka et al. 2016, hereafter *Paper I*, Jacyszyn-Dobrzyniecka et al. 2017, hereafter *Paper II*). The LMC reveals an off-center bar that is an overdensity in both young and old stellar populations (Nikolaev et al., 2004; Subramanian and Subramanian, 2013; van der Marel and Kallivayalil, 2014). The galaxy also has one main spiral arm and a few additional less prominent arms visible in both stellar and gaseous component (Staveley-Smith et al., 2003; Nikolaev et al., 2004; Olsen and Massey, 2007; Bica et al., 2008; Moretti et al., 2014).

Classical Cepheids (CCs) were used by many authors to analyze the distribution of young stars in the LMC. It was shown that this galaxy's disk is warped and the bar stands out as an overdensity that is offset from the disk plane (Nikolaev et al., 2004; Persson et al., 2004; Haschke et al., 2012a). Moreover, the measured values of the viewing angle strongly depend on the adopted center, which is due to the deviations from the planar geometry.

Studies of the CCs distribution in the LMC before the publication of *Paper I* were based mainly on the OGLE-III data (Haschke et al., 2012a). The OGLE-III survey observed mostly the bar area in the LMC and did not cover the northern arm. The upgrade to the fourth phase of the OGLE project and a substantial extension of the observed area enabled me to make the first analysis of the distribution of CCs in the entire LMC disk area.

Numerous studies published before this research showed that the RR Lyrae (RRL) stars in the LMC have a regular distribution that can be described as a tri-axial ellipsoid (Pejcha and Stanek, 2009; Haschke et al., 2012a; Deb and Singh, 2014), with possibly two structures: a disk and halo (Subramanian and Subramanian, 2009; Deb and Singh, 2014). However, the existence of the disk has been questioned (Wagner-Kaiser and Sarajedini, 2013). Other studies suggested that the LMC RRL distribution reveals a bar (Subramanian and Subramanian, 2009; Haschke et al., 2012a). All of these studies were based on the OGLE-III data. With the update to the fourth phase of the OGLE project (OGLE-IV), we gained insight into farther areas and the entire LMC disk.

The Small Magellanic Cloud

Young stars in the SMC tend to be more concentrated in the central parts of the galaxy and in the Wing, which connects the SMC to the Bridge area (Cioni

et al., 2000; Nidever et al., 2011). Older stellar populations are distributed more uniformly and can be described as a tri-axial ellipsoid (Haschke et al., 2012b; Rubele et al., 2015). The SMC has a high optical depth especially in its eastern parts (Nidever et al., 2013; Deb et al., 2015). The galaxy is elongated almost along the line of sight (Scowcroft et al., 2016). This is consistent with predictions from numerical models of interactions between the Magellanic Clouds (Diaz and Bekki, 2012).

Similarly as for the LMC, CCs were often used to study the structure of the SMC. Haschke et al. (2012b) showed that the SMC has a significant optical depth along the line of sight. Subramanian and Subramaniam (2015) fitted a disk to the SMC CCs distribution and found extra-planar features on both sides of the disk. On the other hand, Scowcroft et al. (2016) showed that the SMC is elongated along the line of sight and that fitting a plane to this distribution is not a correct approach. As I showed in this analysis, the OGLE-IV data led to similar results as those of Scowcroft et al. (2016). The main difference is that the sample that I used is over 50 times more numerous than their sample.

A tri-axial ellipsoid is also a good description of the RRab stars distribution in the SMC (Haschke et al., 2012b; Subramanian and Subramaniam, 2012; Deb et al., 2015). Different parts of the SMC were found to have a significant line of sight depth, some of which were interpreted as a bulge (Kapakos et al., 2010; Haschke et al., 2012b; Deb et al., 2015). Moreover, aforementioned studies showed that the north-eastern part of the SMC is located closer and contains more metal-rich stars. Additionally, stars with different metallicities constitute different dynamical structures: metal-rich form a thick disk with a bulge, while metal-poor constitute a halo (Kapakos et al., 2011; Kapakos and Hatzidimitriou, 2012). These studies were also based on the OGLE-III database.

1.3 The Magellanic Bridge area

Spanning the area between the Clouds, the Magellanic Bridge is thought to be one of our closest extragalactic stellar populations that was formed as an effect of tidal interactions (Harris, 2007). The continuous connection between the Clouds was first found in neutral hydrogen (HI) by Hindman et al. (1963). Later, stars of different ages were found in the Bridge: young (Harris, 2007; Skowron et al., 2014; Paper I; B17; Mackey et al., 2017; Paper III), intermediate-age (Nöel et al., 2013, 2015; Skowron et al., 2014; Carrera et al., 2017) and old (Bagheri et al., 2013; B17; Carrera et al., 2017; Paper II; Paper IV). Numerical models predict that the Bridge was formed after the last encounter of the Magellanic Clouds that happened between 300 and 150 Myr ago (e.g. Gardiner et al., 1994; Gardiner and Noguchi, 1996; Růžička et al., 2010; Besla et al., 2012; Diaz and Bekki, 2012; Zivick et al., 2019).

Skowron et al. (2014) used the OGLE-IV data to show for the first time that young stars form a continuous connection between the Magellanic Clouds that follows the HI distribution. On the other hand, old stars are distributed more broadly and their distribution resembles two overlapping halos, showing a smooth transition between the LMC and SMC stellar populations in metallicities and distances (Bagheri et al., 2013; Skowron et al., 2014; Wagner-Kaiser and Sarajedini, 2017; Paper II; Zivick et al., 2019; Paper IV). Articles contributing this doctoral thesis gave an important insight into the topic of the distribution of classical pulsators in the Magellanic Bridge. I have shown that classical Cepheids

follow the young stellar and HI bridge, while anomalous Cepheids (ACs) and RR Lyrae stars reveal broad distributions typical for the older population (Paper I; Paper II; Paper III; Paper IV).

2 The OGLE project

2.1 General information

The OGLE survey was established in the early 1990s and since then the project has been monitoring the densest regions of the sky, concentrating on the Galactic bulge, disk and the Magellanic System. The project uses the 1.3-m Warsaw Telescope at Las Campanas Observatory in Chile. The current fourth phase, OGLE-IV, is in operation since 2010 with a 32-chip mosaic CCD camera, with the field of view of 1.4 deg^2 (Udalski et al., 2015). The OGLE-IV uses two passbands, I and V , from the Johnson-Cousins standard photometric system. Unprecedented quality of the OGLE data and long-term observations provided a unique database that led to numerous important discoveries in astrophysics, many of which were scientific milestones.

Currently, a vast area of more than 750 square degrees is observed by the OGLE project in the Magellanic System. It completely covers the Magellanic Bridge region, as well as very broad areas containing LMC and SMC halos. For the data used in these studies, a median number of observations is 500 in the I filter and 50 in the V filter per one classical pulsator. These factors make the OGLE database perfect for detailed Magellanic System studies.

2.2 The OGLE Collection of Variable Stars

Continuous observations of the densest areas of the sky led to the creation of the OGLE Collection of Variable Stars (OCVS) that contains more than a million objects (Soszyński, 2018), making the OGLE project one of the largest sky variability surveys worldwide. The parts of the Collection used in this study span more than 20 years (1997–2019). The pre-selection of variable stars is based on automatic algorithms, however the visual inspection of candidates' light curves plays a crucial role in a final classification. Different astrophysical parameters are also taken into account, i.e. location on the period–luminosity (PL) diagram or parameters of the Fourier light curve decomposition.

Cepheids

One of the most important and widely used parts of the OCVS is the Collection of Classical Cepheids. CCs are evolved young ($< 300 \text{ Myr}$) and massive ($3\text{--}20 M_{\odot}$) stars. Most of them cross the instability strip during their helium burning blue loop. They pulsate radially via the κ -mechanism. Their periods range from less than one day to more than 100 days (for fundamental mode pulsators), with a typical value of several days. First CCs discovered in the Magellanic Clouds played an important role in astronomy as they led Henrietta Leavitt to the discovery of the PL relation (the Leavitt law, Leavitt, 1908; Leavitt and Pickering, 1912). This made CCs the first standard candles and the base of the extragalactic distance scale ladder.

ACs represent the older population (as shown by the analysis of their three-dimensional distributions, [Iwanek et al. 2018](#)). These Cepheids are low-metallicity, intermediate mass (1–2 M_{\odot}) stars with periods typically between 0.3–3 days. ACs also obey the PL relations, thus can be used in structural studies.

In the analysis presented in this thesis I used the aforementioned properties of Cepheids to calculate individual distances and analyze the three-dimensional structure of the Magellanic Clouds. I used the OGLE-IV Collection of Cepheids in the Magellanic System ([Soszyński et al., 2015, 2017, 2019](#)). Taking into account the latest updates, the Collection includes 9650 CCs and 278 ACs. The completeness of both samples is more than 99% ([Soszyński et al., 2019](#)).

RR Lyrae Stars

The most numerous part of the OGLE Collection of classical pulsators consists of representatives of the old population: RR Lyrae stars. They are evolved, low mass stars located in the region of the Hertzsprung–Russell diagram where the instability strip intersects the horizontal branch.. They pulsate radially via the κ -mechanism. Their periods are typically between 0.2–1 day. RRL stars are numerous in many stellar environments. They are used to study the chemistry, dynamics and distribution of the oldest observable population of stars. RRL stars are also used to study galactic structures in the Local Group, as they obey the PL relations.

In this study, I used RRL stars published in the OCVS ([Soszyński et al., 2016, 2017, 2019](#)) to analyze the structure of the old stellar population in the Magellanic Clouds. The updated Collection includes 47 828 RRL stars in the Magellanic System and is 96% complete ([Soszyński et al., 2019](#)).

3 Analysis

3.1 Samples and methods

The first part of this study ([Paper I](#); [Paper II](#)) was based on 9535 classical Cepheids pulsating in the fundamental and first-overtone modes and 32 581 RRL stars of ab type from the early release of the OGLE-IV Collection of Variable Stars ([Soszyński et al., 2015, 2016](#)). The second part of my study ([Paper III](#); [Paper IV](#)) concentrates on the analysis of the Magellanic Bridge. Here, I used the updated and expanded OCVS samples consisting of 9554 CCs, 268 ACs and 34 177 RRab stars ([Soszyński et al., 2019](#)). Each of these samples was cleaned by iteratively rejecting outliers located farther than 3σ from the fitted period–luminosity relation. After calculating individual distances, I presented my results in two types of maps: two-dimensional projections of a three-dimensional Cartesian space and an equal-area Hammer projection of the celestial sphere.

Cepheids

For both classical and anomalous Cepheids, I fitted the PL relations using the reddening free Wesenheit index ([Madore, 1976](#)):

$$W_{I,V-I} = I - 1.55(V - I) \quad (1)$$

and a linear function:

$$W_{I,V-I} = a \log(P) + b \quad (2)$$

and applied the least-squares method. For the fundamental mode CCs, I additionally divided samples into two groups: one with $\log P \leq 0.4$ and the other with $\log P > 0.4$. I calculated individual distance to each Cepheid using the PL relation obtained for the LMC and the most accurate mean LMC distance (Pietrzyński et al., 2013, 2019). The median relative uncertainty of resulting distances was estimated to be around 3% (1.5 kpc for the LMC CCs).

RR Lyrae Stars

For RRab stars I calculated photometric metallicities using ϕ_{31} coefficient of a Fourier decomposition of OGLE light curves and a Nemeč et al. (2013) relation. In the next step I estimated absolute Wesenheit magnitudes based on relations from Braga et al. (2015) and obtained individual distance to each RRab star. The median uncertainty of the distances to individual RRab stars was around 1.5 kpc for the LMC (3% relative to the median distance).

The method of calculating individual distances used for RRab stars was different than that used for CCs. Many studies have shown that the effect of metallicity on CCs PL relations is negligible (i.e., Romaniello et al. 2008; Bono et al. 2008; Freedman and Madore 2011; Wielgórski et al. 2017; Gieren et al. 2018). For the RRL variables the metallicity influences the location of horizontal branch in relation to the instability strip (i.e., Catelan et al. 2004; Braga et al. 2015).

3.2 The Large Magellanic Cloud

Distribution of classical Cepheids

The three-dimensional distribution maps of CCs in the LMC (Figs. 4 and 5 in Paper I) show that these young stars are located mainly in the substructures in the LMC disk, namely the bar and the northern arm, which both are very prominent on the plots. Almost all CCs are concentrated in the inner 4 kpc around the LMC center. The closest CCs are located mainly in the eastern parts of the galaxy, especially the eastern part of the bar and the northern arm. This reflects the inclination of the LMC disk. Moreover, the most prominent structure is definitely the bar. It is connected with the northern arm in the western part of the LMC. Also, the plots suggest that the northern arm is located at a lower distance than the mean LMC distance. In this study I also showed that there exists an additional arm that is located at the north most part of the LMC disk and is connected to the main northern arm.

I divided the LMC sample into subsamples to analyze substructures in this galaxy (Fig. 7 in Paper I). I additionally divided the bar and the northern arm into two separate parts. The eastern part of the bar is the most prominent and densest area of the LMC and is usually referred to as the LMC bar (see Fig. 14 in Nikolaev et al., 2004 and Figs. 1 and 7 in Haschke et al., 2012a). My results suggest that the eastern and western parts of the bar belong to one structure. Both distance and age tomography show that there is a continuous distribution of stars in these two parts of the bar and there is no significant break in the distribution of any of the analyzed parameters. Moreover, when treating eastern

and western parts of the bar as one substructure, the dynamical center of the LMC (van der Marel and Kallivayalil, 2014) is in the center of the bar.

For the age estimation I used the period–age relation from Bono et al. (2005) for metallicity $Z = 0.01$. Most of LMC CCs are in the age range 50–130 Myr. The youngest CCs constitute the western part of the bar and are younger than 50 Myr. CCs in the age range 50–70 Myr are situated mainly in the central part of the bar. Older are located in the entire bar and the northern arm. The oldest CCs are spread around the entire LMC disk.

Distribution of RR Lyrae Stars

The distance tomography and the column density maps of the RRab stars distribution in the LMC (Figs. 6 and 7 in Paper II) reveals that in its closest parts the RRab stars are clumped in a slightly elongated structure. At distances close to the mean LMC distance and farther, the on-sky projection of RRab stars distribution is regular. Moreover, the eastern part of the LMC is located closer than the western part. The LMC *blend artifact* is very prominent on these maps. It is a non-physical structure that is formed by highly blended stars located in the LMC central parts, where the crowding effect plays an important role. Additionally, based on aforementioned maps I stated that the LMC RRab halo seems to be neither spheroidal, nor ellipsoidal. It is asymmetrical with its eastern part located closer to us.

I analyzed results of a tri-axial ellipsoid model fitting to the LMC RRab distribution (Fig. 9 in Paper II). The central part of the LMC was removed for this procedure to minimize the effect of the blend artifact. However, the axes ratio is the highest for the central parts of the LMC. This may not be physical because of the artifact. Larger ellipsoids, representing the LMC halo, are less elongated and more twisted towards the SMC.

3.3 The Small Magellanic Cloud

Distribution of classical Cepheids

The shape of the on-sky CCs distribution in the SMC (Fig. 12 in Paper I) is changing with the distance, becoming less symmetrical. At the same time the center of this shape is moving away from the SMC dynamical center (Stanimirović et al., 2004). The three-dimensional column density maps (Fig. 13 in Paper I) show that in the on-sky projection the densest concentration of CCs does not match the SMC dynamical center. Moreover, the SMC shape in three dimensions is best described as an elongated tri-axial ellipsoid with its longest axis located almost along the line of sight. The longest axis is 4–5 times longer than the other two axes. This is consistent with the stellar distribution gradient found by Scowcroft et al. (2016) as based on Diaz and Bekki (2012) model of Magellanic Clouds interactions.

I selected two substructures in the SMC (Fig. 16 in Paper I). Both south-western and northern substructures have ellipsoidal shapes and are off-axis with respect to the longest SMC ellipsoid axis. The northern structure is on average younger and located closer than the south-western, which is older and located farther. The OGLE data shows that the Wing is not prominent in CCs distribution, although there are some CCs located in its area.

I estimated ages of CCs in the SMC using period–age relation from [Bono et al. \(2005\)](#) for metallicity $Z = 0.004$. Young stars are more clumped and concentrated in the northern parts of the SMC, while old stars are more spread. Moreover, my study also revealed that there is a general tendency in the SMC, where young stars are on average located closer than old stars.

A comparison of CCs ages distribution in the LMC and SMC shows that on average the LMC CCs are significantly younger than those in the SMC. Also, the oldest SMC Cepheids are around 150 Myr older than the oldest LMC CCs. The CCs ages distribution in the SMC is bimodal, thus this galaxy probably had two epochs of star formation. The younger peak is located around 110 Myr, which is the value for the median CCs age in the LMC. This result is consistent with a study by [Subramanian and Subramanian \(2015\)](#).

Distribution of RR Lyrae Stars

In the SMC RRL stars distribution I did not observe an overcrowded area, in contrast to the LMC. The SMC reveals a very regular structure in RRAb stars in both two and three dimensions, as well as on the distance tomography maps (Figs. 4, 5 and 11 in [Paper II](#)). These maps also show that the center of RRAb distribution differs significantly from the SMC dynamical center and the mean distance. I did not find any evidence for substructures or other irregularities in the SMC RRAb distribution.

For the SMC, I also analyzed results of tri-axial ellipsoid model fitting (Fig. 14 from [Paper II](#)). The shape of inner and outer ellipsoids does not change and all ellipsoids have virtually the same axes ratio. All of them are elongated almost along the line of sight. The outer ellipsoids are slightly more twisted towards the LMC.

3.4 The Magellanic Bridge

Distribution of Cepheids

First CCs in the MBR area were discovered by [Soszyński et al. \(2015\)](#) and published as a part of the OCVS, that was later updated ([Soszyński et al., 2019](#)). I performed the first analysis of the three dimensional distribution of these objects. I selected the MBR sample from the entire CCs collection based on three-dimensional locations of the stars. The final sample consists of 10 objects.

The on-sky distribution of CCs in the Magellanic Bridge area (Fig. 3 in [Paper III](#)) reveals that these objects match the HI density contours, with only two CCs being slightly offset from the highest HI density value. Similarly, CCs also follow the distribution of young stars in the MBR ([Skowron et al., 2014](#)). In three dimensions (Fig. 4 in [Paper III](#)) two CCs are located close to the LMC and may constitute a connection between the LMC sample and the genuine Bridge members. Similarly, two CCs closest to the SMC may actually belong to the SMC Wing and connect this structure to the MBR. The other two CCs are located farther and they may constitute the Counter Bridge, predicted by numerical models ([Diaz and Bekki, 2012](#)). Summarizing, 8 out of 10 CCs in the final sample do form a bridge-like connection between the Magellanic Clouds in three dimensions.

In the final study, I used two age estimates to calculate ages of Bridge CCs. One is the same as I used in previous work ([Bono et al., 2005](#)), while the other

one is a more up-to-date model which includes stellar rotation (Anderson et al., 2016). For both estimates, I used period–age relations for the SMC metallicity. The ages resulting from applying the relation of Anderson et al. (2016) with average stellar rotation are approximately twice as large as the values obtained by using both period–age and period–age–color relations from Bono et al. (2005). In the more physical model with rotation, five out of ten Bridge CCs have ages of less than or equal to 300 Myr. This is consistent with a hypothesis that these stars were formed in-situ after the last encounter of the Magellanic Clouds. Moreover, these youngest CCs form a bridge-like connection between the Magellanic Clouds in three dimensions.

I analyzed proper motion data from *Gaia* Data Release 2 (DR2; *Gaia* Collaboration et al. 2018) for the Bridge CCs. Two CCs that are located close to the LMC also have very similar PMs to this galaxy. Similarly, two CCs located close to the SMC also have similar PMs to the SMC. For all other CCs from the MBR sample PMs have values between those for the LMC and SMC. According to Zivick et al. (2019) these are expected values for the Bridge population. In the LMC related frame the Bridge CCs seem to be co-moving with the SMC, while in the SMC related frame these objects are moving away from this galaxy.

I separately analyzed anomalous Cepheids (Soszyński et al., 2017, 2019) to select a Bridge sample based on three-dimensional locations. The final sample consists of 11 ACs. The on-sky view reveals that the ACs are far more spread than the CCs and the former do not form any evident substructures or streams as the latter do (Figs. 1 and 3 in Paper III). The ACs distribution does not match neither the HI nor the young stars distribution. In three dimensions, these stars form a continuous connection between the Magellanic Clouds, which is not an evident stream (Fig. 8 in Paper III).

Similarly as for CCs, I also analyzed *Gaia* DR2 proper motion data for the Bridge ACs. Their PMs have values that are typical for Bridge objects according to Zivick et al. (2019). Their absolute values are slightly lower than PMs of the LMC and SMC.

Distribution of RR Lyrae Stars

The initial study of the OGLE RRL stars in the Bridge (Paper II) revealed that these stars do not form an evident stream-like connection between the Magellanic Clouds and are rather two overlapping halos. After the OCVS sample was updated (Soszyński et al., 2019), I performed a more detailed analysis of the MBR RRL stars sample. Fig. 2 in Paper IV reveals that the RRab stars are present in the area between the Magellanic Clouds and their distribution is very spread. There is no evident bridge-like connection. Although the contours of the distribution density do connect, it only happens at a very low level (1 star per 1 kpc² and lower).

Additionally, I analyzed results of a multi-Gaussian mixture model applied to the RRL sample. For different numbers of Gaussians fitted none of them is centered in the Bridge area. Thus, there is no additional population or over-density. The Bridge RRab stars are located in Gaussians wings. Moreover, I used the multi-Gaussian procedure to model the distribution of RRab stars in the Magellanic System with an additional offset between the LMC and SMC added along the x axis. This analysis showed that the contours only connect when the Magellanic Clouds are located close enough to each other. Thus, the bridge

stream may not exist or be on a very low density level.

B17 presented a map of the OGLE-IV RRL distribution in the MBR area (their Fig. 18) that was not consistent with results from my first study and presented a stream of RRab stars between the Magellanic Clouds. I reconstructed their results by reanalyzing the entire OGLE sample using the method of B17. Only after using the same as their coordinates, sphere projections, method of calculation, bin sizes and ranges, and color-scale range I was able to reproduce the stream of RRab stars. When using other parameters, the stream was not visible. I called this a “plotting effect”.

I also decided to test the main result of B17, which was a discovery of RRL stars bridge between the Magellanic Clouds based on the *Gaia* Data Release 1 (DR1; *Gaia Collaboration et al. 2016*) and a selection algorithm presented by B17. I used a sample that was created by following their steps. The resulting maps revealed many spurious sources in the central Bridge area forming obvious stripes on the sky. The stripes reflect *Gaia* scanning law and are an effect of cross-match failures in *Gaia* DR1 (B17). However, B17 claimed that most of the stripes together with non-physical sources disappear after applying their method. I showed in this study that this is not the case, as I was not able to reproduce their results without obtaining many non-physical sources in the Bridge area. Interestingly, the stripes in the Bridge form a structure that resembles a stream when the data is binned, especially when the bin size is relatively large. Contours that I obtained using this sample are consistent with what B17 reported.

Also, a comparison between this final sample and the OGLE RRL distribution in the central Bridge area (for right ascension in the range $2^{\text{h}}-4^{\text{h}}$) revealed that only 15% of objects obtained using B17 method are genuine RRL stars. For the entire sample discussed in this subsection only more than 40% are RRL stars (based on both OCVS and *Gaia* DR2). This high level of contamination (60%) is not consistent with B17 who reported 30–40% for their entire sample. The completeness of B17 sample is around 11–12%, which is in agreement with what they estimated.

4 Impact of this study

The presented studies provide the first three-dimensional analysis of the structure of the Magellanic Clouds with classical pulsators, that cover the entire area of the Clouds as well as regions between and around them. The four publications constituting this doctoral thesis have been referenced 143 times (as of 29 June 2021 according to the NASA Astrophysics Data System Abstract Service). This number proves that my research has been of a significant importance and has influenced other scientific projects. Most of the citations reference the first part of the study, concerning the three-dimensional structure of the Magellanic System. Paper I and Paper II presented for the first time a very detailed analysis of the distribution of young and old stellar population representatives in both Magellanic Clouds. My studies were the first ones to use the almost complete OGLE-IV Collection of Variable Stars, covering very broad areas around the Magellanic Clouds, incomparable to those of OGLE-III, and will be a golden standard in the Magellanic System studies for years to come.

The results described in this thesis were presented at 19 different meetings in years 2016 – 2020 and led to many interesting discussions between researchers.

My studies were a base for an invited lecture “OGLE-ing the Magellanic System” that I gave during the Synoptic Magellanic Clouds conference in September 2019. I also presented the results at eight other international conferences, including four talks and four posters (three with flash talks). Additionally, I discussed the results during two international workshops and presented them at five seminars and one research group meeting. I also gave two lectures for students.

5 Summary

In this thesis I presented results of the project concerning the three-dimensional structure of the Magellanic System based on the OGLE-IV classical pulsators, that I have been working on during my doctoral studies. The unique results have been of significant impact on the astronomical society worldwide, as this was the first time the high-quality OGLE-IV data of a vast sky coverage were used to disentangle the structure of the Clouds and the Bridge.

I analyzed the distribution of classical Cepheids and RR Lyrae stars in both Magellanic Clouds. For CCs I fitted PL relations to the OGLE data using reddening-free Wesenheit index and calculated individual distances based on the mean LMC distance. For RR Lyrae stars I used relations including period and metallicity to obtain absolute magnitudes and then calculated individual distances. I presented the distribution of these variables on different types of maps, especially in three-dimensional Cartesian coordinates and Hammer equal-area projection of the sphere.

In the LMC, CCs are clumped in central substructures, mainly the bar and the northern spiral arm. Their overall distribution is disk-like. There is also an additional small northern arm connected to the main arm in the north. Moreover, I redefined the LMC bar by adding its western part based on distance and age distribution of CCs. I did not find any additional spiral arms in the southern parts of the LMC. In the SMC CCs reveal a very elongated distribution that resembles a tri-axial ellipsoid with its longest axis located almost along the line of sight. I also found two ellipsoidal off axis substructures in this galaxy. Moreover, CCs in the SMC revealed a trend where younger stars are located closer to us, while older ones farther.

RR Lyrae stars are very spread and form a regular structure that can be modeled as a tri-axial ellipsoid in each Magellanic Cloud. In the center of the LMC I encountered a problematic blend artifact that is a result of intense blending and crowding effects.

I performed a detailed analysis of classical pulsators in the Magellanic Bridge area. The final sample of CCs consists of 10 objects that form a connection between the LMC and SMC in three dimensions. At least half of these stars are around or younger than 300 Myr, which places them well within a hypothesis that these were formed in situ in the Bridge. The CCs distribution matches very well the neutral hydrogen and young stars bridges between the Magellanic Clouds. I also studied the sample of anomalous Cepheids in the MBR. Their distribution is different such that they do not form an evident stream, but are rather spread all over the area between the Magellanic Clouds.

RR Lyrae stars are present in the Bridge and their distribution resembles two overlapping halos. In the OGLE-IV data I did not find and evidence for

the existence of a stream. Moreover, I reanalysed the OGLE data and the final sample of B17 showing that it is not possible to reproduce their result of a RRL bridge without imposing special conditions on plots or without non-physical artifacts located in the central part of the Bridge.

Acknowledgments

This doctoral thesis would never have taken such a form had it not been for the help and support of many people. I would like to express my gratitude to the ones whose input has been of most significant importance for conducting studies presented in this thesis.

First of all I would like to thank my PhD advisors: dr Dorota Skowron, with whom I have been working since preparations of my bachelor thesis, and prof. dr hab. Igor Soszyński, who became my advisor when I started working on my “Diamond Grant” project. I appreciate every single minute of the countless hours and days that you have spent working with me. Thank you for all the conversations we had, for advising me, for showing me the right way when I was wrong, for all your corrections to my always very long manuscripts. But most of all, thank you for always believing in me, even in the toughest times in my life, when I myself was losing the faith. I am eternally grateful for your understanding and patience.

I am very thankful to prof. dr hab. Andrzej Udalski, the leader of the OGLE Project, for allowing me to use the unpublished OGLE data and to work with the OGLE Team. Thank you very much for this chance, which was life changing for me, and let me step into the world of highest quality scientific research.

I would like to thank all members of the OGLE Team, especially dr Przemek Mróz, dr hab. Szymon Kozłowski, dr Jan Skowron, dr hab. Paweł Pietrukowicz, prof. dr hab. Łukasz Wyrzykowski, prof. dr hab. Michał Szymański, dr Radosław Poleski. I appreciate your help and support, non-obvious solutions, original ideas, inspiring discussions. Thank you for being the people I could look up to and being a motivation to work harder. Thank you also for showing me how does the team work look like.

I am grateful to all employees and students of the Warsaw Astronomical Observatory, whom I was able to meet during my time spent there, especially my lecturers, colleagues and students I was teaching. I appreciate the friendly and family atmosphere created by all of you. Thank you for giving me a multi-faceted experience, which helped me become the scientist I am today.

I also would like to thank the Polish Ministry of Science and Higher Education for awarding me the “Diamond Grant” (No. DI2013 014843) for my project “Analysis of galaxies interactions in the Magellanic System” (pol. *Analiza oddziaływań galaktyk w Systemie Magellana*). Thanks to this grant I was able to conduct the high quality research that constitutes this doctoral thesis.

Bibliography

- Anderson, R.I., Saio, H., Ekström, S., Georgy, C., and Meynet, G. 2016, *A&A*, 591, A8
- Bagheri, G., Cioni, M.-R.L., and Napiwotzki, R. 2013, *A&A*, 551, A78
- Barger, K.A., Haffner, L.M., and Bland-Hawthorn, J. 2013, *ApJ*, 771, 132
- Belokurov, V., Erkal, D., Deason, A.J., et al. 2017, *MNRAS*, 466, 4711
- Besla, G., Kallivayalil, N., Hernquist, L., van der Marel, R.P., Cox, T.J., and Kereš, D. 2010, *ApJL*, 721, L97
- Besla, G., Kallivayalil, N., Hernquist, L., van der Marel, R.P., Cox, T.J., and Kereš, D. 2012, *MNRAS*, 421, 2109
- Bica, E.L.D., Bonatto, C., Dutra, C.M., and Santos J.F.C. 2008, *MNRAS*, 389, 678
- Bono, G., Marconi, M., Cassisi, S., Caputo, F., Gieren, W., and Pietrzyński, G. 2005, *ApJ*, 621, 966
- Bono, G., Caputo, F., Fiorentino, G., Marconi, M., and Musella, I. 2008, *ApJ*, 684, 102
- Braga, V.F., Dall’Ora, M., Bono, G., et al. 2015, *ApJ*, 799, 165
- Carrera, R., Conn, B.C., Noël, N.E.D., et al. 2017, *MNRAS*, 471, 4571
- Casetti-Dinescu, D.I., Bidin, C.M., Girard, T.M., et al. 2014, *ApJL*, 784, L37
- Catelan, M., Pritzl, B.J., and Smith, H.A. 2004, *ApJS*, 154, 633
- Cioni, M.-R.L., Habing, H.J., and Israel, F.P. 2000, *A&A*, 358, L9
- Connors, T.W., Kawata, D., Gibson, B.K. 2006, *MNRAS*, 371, 1, 108
- Deb, S., and Singh, H.P., 2014, *MNRAS*, 438, 2440
- Deb, S., Singh, H.P., Kumar, S., and Kanbur, S.M. 2015, *MNRAS*, 449, 2768
- Diaz, J.D., and Bekki, K. 2012, *ApJ*, 750, 36
- Freedman, W.L., and Madore, B.F. 2011, *ApJ*, 734, 46
- Gaia* Collaboration, Brown, A.G.A., et al. 2016, *A&A*, 595, A2
- Gaia* Collaboration, Brown, A.G.A., et al. 2018, *A&A*, 616, A1
- Gardiner, L.T., Sawa, T., and Fujimoto, M. 1994, *MNRAS*, 266, 567
- Gardiner, L.T., and Noguchi, M. 1996, *MNRAS*, 278, 191
- Gieren, W., Storm, J., Konorski, P., et al. 2018, *A&A*, 620, 99
- Guglielmo, M., Lewis, G.F., and Bland-Hawthorn, J. 2014, *MNRAS*, 444, 1759
- Harris, J. 2007, *ApJ*, 658, 345
- Haschke, R., Grebel, E.K., and Duffau, S. 2012a, *AJ*, 144, 106
- Haschke, R., Grebel, E.K., and Duffau, S. 2012b, *AJ*, 144, 107
- Hindman, J.V., Kerr, F.J., McGee, R.X. 1963, *AuJPh*, 16, 570
- Iwanek, P., Soszyński, I., Skowron, D., et al. 2018, *AcA*, 68, 213
- Jacyszyn-Dobrzyniecka, A.M., Skowron, D.M., Mróz, P., et al. 2016, *AcA*, 66, 149 ([Paper I](#))
- Jacyszyn-Dobrzyniecka, A.M., Skowron, D.M., Mróz, P., et al. 2017, *AcA*, 67, 1

(Paper II)

- Jacyszyn-Dobrzyniecka, A.M., Soszyński, I., Udalski, A., et al. 2020a, *ApJ*, 889, 25 (Paper III)
- Jacyszyn-Dobrzyniecka, A.M., Mróz, P., Kruszyńska, K., et al. 2020b, *ApJ*, 889, 26 (Paper IV)
- Joshi, Y.C., and Joshi, S. 2014, *NewA*, 28, 27
- Kallivayalil, N., van der Marel, R.P., Besla, G., Anderson, J., and Alcock, C. 2013, *ApJ*, 764, 161
- Kapakos, E., Hatzidimitriou, D., and Soszyński, I. 2010, *ASPC*, 424, 233
- Kapakos, E., Hatzidimitriou, D., and Soszyński, I. 2011, *MNRAS*, 415, 1366
- Kapakos, E., and Hatzidimitriou, D. 2012, *MNRAS*, 426, 2063
- Leavitt, H.S. 1908, *Annals of Harvard College Observatory*, 60, 87
- Leavitt, H.S., and Pickering, E.C. 1912, *Harvard College Observatory Circular*, 173, 1
- Mackey, A.D., Kuposov, S.E., Da Costa, G.S., et al. 2017, *MNRAS*, 472, 2975
- Madore, B.F. 1976, *Royal Greenwich Observatory Bulletins*, 182, 153
- McClure-Griffiths, N.M., Staveley-Smith, L., Lockman, F.J., et al. 2008, *ApJL*, 673, L143
- Moretti, M.I., Clementini, G., Muraveva, T., et al. 2014, *MNRAS*, 437, 2702
- Nemec, J.M., Cohen, J.G., Ripepi, V., Derekas, A., Moskalik, P., Sesar, B., Chadid, M., and Bruntt, H. 2013, *ApJ*, 773, 181
- Nidever, D.L., Majewski, S.R., and Butler Burton, W. 2008, *ApJ*, 679, 432
- Nidever, D.L., Majewski, S.R., Butler Burton, W., and Nigra, L. 2010, *ApJ*, 723, 1618
- Nidever, D.L., Majewski, S.R., Muñoz, R.R., et al. 2011, *ApJL*, 733, L10
- Nidever, D.L., Monachesi, A., Bell, E.F., et al. 2013, *ApJ*, 779, 145
- Nikolaev, S., Drake, A.J., Keller, S.C., et al. 2004, *ApJ*, 601, 260
- Nöel, N.E.D., Conn, B.C., Carrera, R., Read, I.J., Rix, H.-W., and Dolphin, A. 2013, *ApJ*, 768, 109
- Nöel, N.E.D., Conn, B.C., Read, I.J., Carrera, R., Dolphin, A., and Rix, H.-W. 2015, *MNRAS*, 452, 4222
- Olsen, K.A.G., and Massey, P. 2007, *ApJL*, 656, L61
- Pejcha, O., and Stanek, K.Z. 2009, *ApJ*, 704, 1730
- Pietrzyński, G., Graczyk, D., Gieren, W., et al. 2013, *Nature*, 495, 76
- Pietrzyński, G., Graczyk, D., Gallenne, A., et al. 2019, *Nature*, 567, 200
- Persson, S.E., Madore, B.F., Krzemiński, W., et al. 2004, *AJ*, 128, 2239
- Romaniello, M., Primas, F., Montini, M., et al. 2008, *A&A*, 488, 731
- Rubele, S., Girardi, L., Kerber, L., et al. 2015, *MNRAS*, 449, 639
- Růžička, A., Theis, C., and Palouš, J. 2009, *ApJ*, 691, 1807
- Růžička, A., Theis, C., and Palouš, J. 2010, *ApJ*, 725, 369
- Scowcroft, V., Freedman, W.L., Madore, B.F., et al. 2016, *ApJ*, 816, 49
- Skowron, D.M., Jacyszyn A.M., Udalski, A., et al. 2014, *ApJ*, 795, 108
- Skowron, D.M., Soszyński, I., Udalski, A., et al. 2016, *AcA*, 66, 269
- Soszyński, I., Udalski, A., Szymański, M.K., et al. 2015, *AcA*, 65, 297
- Soszyński, I., Udalski, A., Szymański, M.K., et al. 2016, *AcA*, 66, 131
- Soszyński, I., Udalski, A., Szymański, M.K., et al. 2017, *AcA*, 67, 103
- Soszyński, I. 2018, *Proceedings of the Polish Astronomical Society*, 7, 168
- Soszyński, I., Udalski, A., Szymański, M.K., et al. 2019, *AcA*, 69, 87
- Stanimirović, S., Staveley-Smith, L., and Jones, P.A. 2004, *ApJ*, 604, 176
- Staveley-Smith, L., Kim, S., Calabretta, M.R., Haynes, R.F., Kesteven, M.J.

2003, *MNRAS*, 339, 87

Subramanian, A., and Subramanian, S. 2009, *A&A*, 503, L9

Subramanian, S., and Subramanian, A. 2012, *ApJ*, 744, 128

Subramanian, S., and Subramanian, A. 2013, *A&A*, 552, A144

Subramanian, S., and Subramanian, A. 2015, *A&A*, 573, A135

Tepper-García, T., Bland-Hawthorn, J., Pawlowski, M.S., and Fritz, T.K. 2019, *MNRAS*, 488, 918

Udalski, A., Szymański, M.K., and Szymański, G. 2015, *AcA*, 65, 1

van der Marel, R.P., and Kallivayalil, N. 2014, *ApJ*, 781, 121

Venzmer, M.S., Kerp, J., and Kalberla, P.M.W. 2012, *A&A*, 547, A12

Wagner-Kaiser, R., and Sarajedini, A. 2013, *MNRAS*, 431, 1565

Wagner-Kaiser, R., and Sarajedini, A. 2017, *MNRAS*, 466, 4138

Wielgórski, P., Pietrzyński, G., Gieren, W., et al. 2017, *ApJ*, 842, 116

Yoshizawa, A.M., and Noguchi, M. 2003, *MNRAS*, 339, 1135

Zivick, P., Kallivayalil, N., Besla, G., et al. 2019, *ApJ*, 874, 78

Bibliographic journal abbreviations

<i>A&A</i>	<i>Astronomy and Astrophysics</i>
<i>AcA</i>	<i>Acta Astronomica</i>
<i>AJ</i>	<i>Astronomical Journal</i>
<i>ApJ</i>	<i>Astrophysical Journal</i>
<i>ApJL</i>	<i>Astrophysical Journal Letters</i>
<i>ApJS</i>	<i>Astrophysical Journal Supplement</i>
<i>ASPC</i>	<i>Astronomical Society of the Pacific Conference Series</i>
<i>AuJPh</i>	<i>Australian Journal of Physics</i>
<i>MNRAS</i>	<i>Monthly Notices of the Royal Astronomical Society</i>
<i>NewA</i>	<i>New Astronomy</i>

Part II

Full texts of published scientific articles

List of Figures

1.1	P-L relations for the Wesenheit magnitude for fundamental-mode and first-overtone CCs in the LMC and in the SMC	42
1.2	Three-dimensional map of CCs in the Magellanic System in Cartesian coordinates	44
1.3	Three-dimensional map of CCs in the Magellanic System in Hammer projection	46
1.4	Distance tomography of the LMC in the Hammer projection	49
1.5	Cepheid density maps in the LMC with Cepheid column density contours	50
1.6	Age tomography of the LMC	51
1.7	Substructures in the LMC	53
1.8	Distance histograms of the selected regions in the LMC	54
1.9	Age histograms of the selected regions in the LMC	55
1.10	The bar and the northern arm on the three-dimensional map of the CCs in the LMC in Cartesian coordinates	58
1.11	Distance-gradient of the best-fit plane for the entire LMC	58
1.12	Distance tomography of the SMC	61
1.13	Cepheid density in the SMC with Cepheid column density contours	62
1.14	Age tomography of the SMC	63
1.15	Three-dimensional map of the CCs in the SMC in Cartesian coordinates	64
1.16	Substructures in the SMC	65
1.17	Distance and age histograms for the SMC	66
1.18	CCs in the Magellanic Bridge area over the spatial density map of the Young Population stars	69
1.19	Three-dimensional map of CCs in the Magellanic Bridge	71
2.1	The Bailey diagram for RRL stars	86
2.2	P-L relations for the Wesenheit magnitude for RRL(ab) stars in the Magellanic System	87
2.3	Stellar density contours of the LMC RRL stars	88
2.4	The RRL stars in the Magellanic System in the Cartesian coordinates	88
2.5	The equal-area Hammer projection of the RRL stars in the Magellanic System with color-coded distances	91
2.6	Distance tomography of the RRL stars distribution in the LMC	95
2.7	RRL stars density maps in the LMC in the Cartesian coordinates	96
2.8	Parameters of the best-fit triaxial ellipsoids for the LMC RRL stars	97
2.9	Best-fit triaxial ellipsoids for the LMC data	98

2.10	Best-fit triaxial ellipsoid centers in Cartesian coordinates projections for the LMC data	100
2.11	Distance tomography of the RRL stars distribution in the SMC .	103
2.12	RRL stars column density maps in the SMC in the Cartesian coordinates	104
2.13	Parameters of the best-fit triaxial ellipsoids for the SMC RRL stars	105
2.14	Best-fit triaxial ellipsoids for the SMC data	107
2.15	Best-fit triaxial ellipsoids centers in the Cartesian coordinates projections for the SMC data	108
2.16	binned RRL stars distribution in the Magellanic Bridge area . . .	111
2.17	The equal-area Hammer projection of RRL stars and classical Cepheids in the Magellanic System	112
2.18	RRL stars and classical Cepheids in the Magellanic System in the Cartesian coordinates	113
3.1	On-sky locations of Cepheids in the Magellanic System	120
3.2	PL relations for classical and anomalous Cepheids in the Magellanic Clouds	122
3.3	On-sky locations of the central Bridge Cepheid sample	124
3.4	Three-dimensional distribution of classical Cepheids in the Magellanic System	125
3.5	Proper motions of Bridge Classical Cepheids	126
3.6	On-sky proper motions of Bridge Classical Cepheids	126
3.7	Three-dimensional distribution of CCs in the Magellanic System with different distance estimates	126
3.8	Three-dimensional distribution of anomalous Cepheids in the Magellanic System	130
3.9	Proper motions of Bridge Anomalous Cepheids	130
3.10	On-sky proper motions of Bridge Anomalous Cepheids	131
3.11	Three-dimensional distribution of CCs and ACs in the Magellanic System	132
3.12	Comparison of OGLE and <i>Gaia</i> DR2 Cepheids in the Magellanic Bridge area	132
4.1	On-sky locations of RRL stars in the Magellanic System	137
4.2	Top and front view of the RRab stars in the Magellanic System .	138
4.3	Centers of 32 fitted Gaussians overplotted on the three-dimensional distribution of RRab stars	138
4.4	Two-dimensional plots of three-dimensional Cartesian space projections showing points simulated using a multi-Gaussian fit . . .	138
4.5	Comparison of OGLE RRL distribution from this study and B17	140
4.6	Comparison of RRL stars distribution in different binning and projections	141
4.7	On-sky locations of RRL candidates using different versions of B17 cuts	142
4.8	Comparison of B17 candidates distribution with a reproduction from this study	143
4.9	Different binning of B17 reproduction	144
4.10	The CMDs of the B17 RRL candidates obtained in this section and the cleaned sample of OCVS RRL stars	144

4.11 Comparison of on-sky locations of different tracers in the MBR . 145

List of Tables

1.1	Classical Cepheids sample used in the analysis	40
1.2	P-L relations for CCs in the Magellanic Clouds	41
1.3	Classical Cepheids in the Magellanic System	47
1.4	Characteristics of the LMC substructures	52
1.5	Kolmogorov-Smirnov test results in the LMC	56
1.6	Best-fit parameters of the three-dimensional plane fitting procedure	57
1.7	LMC disk parameters from the literature	59
1.8	Characteristics of the SMC substructures	66
1.9	Kolmogorov-Smirnov test results in the SMC	67
1.10	Magellanic Bridge Cepheids	68
2.1	P-L relations for RRab stars in the Magellanic Clouds	89
2.2	RRL stars (ab) in the Magellanic System	92
2.3	Triaxial ellipsoid best-fit parameters for the LMC	99
2.4	Parameters of the LMC RRL stars modeling from literature	101
2.5	Triaxial ellipsoid best-fit parameters for the SMC	106
2.6	Parameters of the SMC RRL stars modeling from literature	109
3.1	PL Relations for CCs in the Magellanic System in the Wesenheit Magnitude	122
3.2	Magellanic Bridge Classical Cepheids: Basic Parameters	123
3.3	Magellanic Bridge Classical Cepheids: Ages	125
3.4	Magellanic Bridge Classical Cepheids: Distances	127
3.5	Magellanic Bridge Classical Cepheids: Absolute Magnitudes	127
3.6	Magellanic Bridge Classical Cepheids: Reddening Parameters	128
3.7	Magellanic Bridge Anomalous Cepheids: Basic Parameters	129
3.8	Period-luminosity relations for anomalous Cepheids in the Magellanic System in the Wesenheit Magnitude	129
3.9	Magellanic Bridge Cepheids: Reclassification	132
4.1	Number of RRL Stars in the Samples	137
4.2	B17 RRL Candidates from <i>Gaia</i> DR1: Cross-match	143

OGLE-ing the Magellanic System: Three-Dimensional Structure of the Clouds and the Bridge Using Classical Cepheids

A.M. Jacyszyn-Dobrzniecka¹, D.M. Skowron¹, P. Mróz¹,
J. Skowron¹, I. Soszyński¹, A. Udalski¹, P. Pietrukowicz¹,
S. Kozłowski¹, Ł. Wyrzykowski¹, R. Poleski^{1,2}, M. Pawlak¹,
M. K. Szymański¹ and K. Ulaczyk^{1,3}

¹Warsaw University Observatory, Al. Ujazdowskie 4, 00-478 Warszawa, Poland
e-mail: ajacyszyn@astrouw.edu.pl

²Department of Astronomy, Ohio State University, 140 W. 18th Ave.,
Columbus OH 43210, USA

³Department of Physics, University of Warwick, Gibbet Hill Road,
Coventry CV4 7AL, UK

Received March 1, 2016

ABSTRACT

We analyzed a sample of 9418 fundamental-mode and first-overtone classical Cepheids from the OGLE-IV Collection of Classical Cepheids. The distance to each Cepheid was calculated using the period–luminosity relation for the Wesenheit magnitude, fitted to our data.

The classical Cepheids in the LMC are situated mainly in the bar and in the northern arm. The eastern part of the LMC is closer to us and the plane fit to the whole LMC sample yields the inclination $i = 24.2 \pm 0.7$ and position angle $\text{P.A.} = 151.4 \pm 1.7$. We redefined the LMC bar by extending it in the western direction and found no offset from the plane of the LMC contrary to previous studies. On the other hand, we found that the northern arm is offset from a plane by about -0.5 kpc, which was not observed before. The age distribution of the LMC Cepheids shows one maximum at about 100 Myr.

We demonstrate that the SMC has a non-planar structure and can be described as an extended ellipsoid. We identified two large ellipsoidal off-axis structures in the SMC. The northern one is located closer to us and is younger, while the south-western is farther and older. The age distribution of the SMC Cepheids is bimodal with one maximum at 110 Myr, and another one at 220 Myr. Younger stars are located in the closer part of this galaxy while older ones are more distant.

We classified nine Cepheids from our sample as Magellanic Bridge objects. These Cepheids show a large spread in three-dimensions although five of them form a connection between the Clouds. The closest one is closer than any of the LMC Cepheids, while the farthest one – farther than any SMC Cepheid. All but one Cepheids in the Magellanic Bridge are younger than 300 Myr. The oldest one can be associated with the SMC Wing.

Key words: *Stars: fundamental parameters – Cepheids – Magellanic Clouds – Galaxies: statistics – Galaxies: structure*

1. Introduction

The Large Magellanic Cloud (LMC) and the Small Magellanic Cloud (SMC) are one of our closest galaxies. What makes the LMC–SMC pair even more interesting is that these galaxies have a common history. Their interactions led to formation of a few intriguing structures: the Magellanic Stream, the Leading Arm, and the Magellanic Bridge (Gardiner *et al.* 1994, Gardiner and Noguchi 1996, Yoshizawa and Noguchi 2003, Connors *et al.* 2006, Růžička *et al.* 2009, 2010, Besla *et al.* 2010, 2012, Diaz and Bekki 2011, 2012, Guglielmo *et al.* 2014). Together with the Magellanic Clouds they constitute the Magellanic System.

The Magellanic Stream is a 160° long stream of gas that seems to be trailing the Clouds' past orbit (Nidever *et al.* 2008, 2010). It has a double nature in terms of morphology, velocity and metallicity (*e.g.*, Putman *et al.* 2003, Nidever *et al.* 2008, Fox *et al.* 2010, 2013, Richter *et al.* 2013). The Leading Arm was formed together with the Stream (*e.g.*, Nidever *et al.* 2008). It comprises of four groups of High Velocity Cloud (Venzmer *et al.* 2012) and is interacting with matter in the Milky Way disk (McClure-Griffiths *et al.* 2008). It is known to have a young stellar component (Casetti-Dinescu *et al.* 2014).

The Magellanic Bridge (MBR), a connection between the two Clouds, was known as a gaseous feature since the work of Hindman *et al.* (1963). It is thought to be formed after the last encounter of the LMC and SMC that took place 200–300 Myr ago (*e.g.*, Gardiner *et al.* 1994, Gardiner and Noguchi 1996, Růžička *et al.* 2010, Diaz and Bekki 2012, Besla *et al.* 2012). The detailed analysis of neutral Hydrogen (HI) kinematics reveals that the Magellanic Bridge is connected with the western part of the LMC disk (Indu and Subramaniam 2015). Moreover, the velocity distribution suggests that the MBR is being sheared. Numerical models predict that the Bridge should have a stellar component (*e.g.*, Diaz and Bekki 2012, Besla *et al.* 2012, Guglielmo *et al.* 2014), that should be an important tracer of interactions between the LMC and SMC.

Young stars in the area between the Clouds were observed by Shapley (1940). Later, young stars were discovered farther from the SMC, in the direction to the LMC (Irwin *et al.* 1985, Demers and Battinelli 1998, Harris 2007, Noël *et al.* 2013, 2015). Finally, Skowron *et al.* (2014) showed that there exists a continuous connection between the Clouds formed by a young stellar population. Moreover, the Bridge also contains warm ionized gas (Barger *et al.* 2013). Intermediate age stars were also observed in the MBR (Noël *et al.* 2013, 2015), as well as candidates for an old stellar population (Bagheri *et al.* 2013). Recent studies of stellar clusters and associations suggest that these structures may be forming a tidal dwarf galaxy (Bica *et al.* 2015) that had already been proposed by Bica and Schmitt (1995). Such galaxies form from the gas pulled out of the interacting galaxies and can have their own star formation (SF) processes (Ploeckinger *et al.* 2014, 2015).

The interactions between the Magellanic Clouds have made a significant impact on both galaxies. The knowledge of their structure brings relevant implications for their common history as well as for other, more distant galaxy systems. The Clouds are our closest interacting galaxies, thus can be described as our “local laboratory”. Their structure is also essential for proper understanding of the nature of rare microlensing events detected toward the Clouds and their interpretation either as self-lensing or due to compact dark matter objects (*e.g.*, Wyrzykowski *et al.* 2011, Besla *et al.* 2013).

In the LMC younger and older stars have different spatial distributions although the overall shape of the galaxy is roughly regular (*e.g.*, Cioni *et al.* 2000, Bica *et al.* 2008, Joshi and Joshi 2014). Its disk is distorted, elongated and asymmetrical and can be divided into inner and outer parts with different inclination angles (van der Marel and Cioni 2001, van der Marel 2001, Olsen and Salyk 2002, Nikolaev *et al.* 2004, Haschke *et al.* 2012a, Subramanian and Subramanian 2013). The eastern parts of the disk and the halo are located closer to us because of the LMC’s inclination toward the SMC (van der Marel and Cioni 2001, Nikolaev *et al.* 2004, Persson *et al.* 2004, Pejcha and Stanek 2009, Koerwer 2009, Subramanian and Subramanian 2010, Rubele *et al.* 2012, Haschke *et al.* 2012a, Subramanian and Subramanian 2013, van der Marel and Kallivayalil 2014, Deb and Singh 2014).

The LMC has an off-center bar that appears as an overdensity in young and old stellar populations (Zhao and Evans 2000, Cioni *et al.* 2000, van der Marel 2001, Nikolaev *et al.* 2004, Subramanian and Subramanian 2013, van der Marel and Kallivayalil 2014) as well as in the numerical models of the off-center bar (Bekki 2009, Besla *et al.* 2012). The galaxy also has one prominent spiral arm and maybe two or three irregular and not very prominent arms (*e.g.*, Cioni *et al.* 2000, Nikolaev, *et al.* 2004, Bica *et al.* 2008, Moretti *et al.* 2014). HI maps reveal four spiral-like structures (Staveley-Smith *et al.* 2003) and the new ones have just been discovered (Indu and Subramanian 2015). Some of the LMC stars are kinematically associated with these HI arms rather than with the disk (Olsen and Massey 2007).

The SMC is an elongated irregular galaxy with a central concentration where young and old stars have slightly different distributions (*e.g.*, Cioni *et al.* 2000, Subramanian and Subramanian 2012, Haschke *et al.* 2012b, Rubele *et al.* 2015). The SMC is known to have several substructures, of which the most prominent is the Wing, that is a part of the galaxy that connects it with the Magellanic Bridge (*e.g.*, Cioni *et al.* 2000, Nidever *et al.* 2011). Older populations are more uniformly distributed while younger tend to concentrate in the central parts and in the Wing. Moreover, the Wing also comprises of many young stellar clusters (Piatti *et al.* 2015). Nidever *et al.* (2013) showed that the optical depth in the eastern part of the SMC is two times higher than in the western part, and the eastern part comprises of two groups of stars with different mean distances. The SMC is rotated toward the LMC and their closest parts on the sky are also the closest in the sense of distance (Scowcroft *et al.* 2016).

The classical Cepheids (CCs) represent a young stellar population and play an important role in structural studies of many extragalactic systems. In the LMC and SMC they are of exceptional significance. Henrietta Leavitt had discovered the famous Leavitt law studying the SMC Cepheids – period–luminosity (P-L) relation – Leavitt (1908).

Numerous studies of the LMC and SMC structure were based on the CCs. Nikolaev *et al.* (2004) analyzed more than 2000 MACHO Cepheids in the LMC and measured the viewing angles of this galaxy. They found that the results are strongly dependent on the adopted center of the LMC, due to deviations from the planar geometry. Moreover, they showed that the disk is warped, with the bar being offset from the disk plane. A similar study was performed by Persson *et al.* (2004) for 92 Cepheids observed in the near infrared passbands. Later, Haschke *et al.* (2012ab) investigated almost 2000 Cepheids from the OGLE-III data set. They constructed three-dimensional maps of the Clouds by using individual reddening estimates and determining distances to each Cepheid. They also detected mild twisting in the LMC disk and noticed that the bar stands out as an overdensity.

Subramanian and Subramaniam (2015) fitted a plane to the SMC young stellar “disk” and found extra-planar features in front of and in the back of the “disk”. The authors suggest that the former may be a tidal structure that connects the SMC with MBR and the latter may be a stellar counterpart of the Counter Bridge predicted by numerical models (Diaz and Bekki 2012). On the other hand Scowcroft *et al.* (2016) showed that the SMC is extremely elongated along the line of sight and they state that fitting a plane to such structure is incorrect. The elongation of the SMC is consistent with the significant optical depth values for this galaxy (*e.g.*, Nidever *et al.* 2013, Deb *et al.* 2015) and the numerical models predictions (Diaz and Bekki 2012).

The CCs were also used to study the star formation history (SFH) of the Magellanic Clouds. Both galaxies have had an active SFH during the last 2 Gyr (Harris and Zaritsky 2009, Inno *et al.* 2015) and the age distribution similarities between the LMC and SMC suggest that the galaxies must have had common SF episodes (Harris and Zaritsky 2009, Indu and Subramaniam 2011, Inno *et al.* 2015, Subramanian and Subramaniam 2015, Joshi *et al.* 2016).

In this paper we present results of a three-dimensional analysis of the Magellanic System using the OGLE Collection of Classical Cepheids recently published by Soszyński *et al.* (2015). The Collection is based on the OGLE-IV data (Udalski *et al.* 2015), covering about 650 square degrees in this area. Compared to the OGLE-III collection of Classical Cepheids, on which the studies described above were based, the OGLE-IV Classical Cepheids Collection includes the northern and southern parts of the LMC and extended outskirts of the SMC. This is the first time that we see a full picture of the Clouds with CCs from the OGLE project.

The sample completeness is over 99%, which makes it the most complete and least contaminated sample of CCs in the Magellanic Clouds and Bridge. Given

the vast OGLE-IV coverage of the Magellanic System, it is unlikely that many additional CCs will be discovered in this region, making this the ultimate collection of CCs in the Magellanic System.

The paper is organized as follows. In Section 2 we describe the OGLE-IV data and OGLE Collection of Classical Cepheids. In Section 3 we present the details of the analysis. Sections 4 to 6 contain results for the LMC, SMC, and the Bridge, respectively. We discuss and summarize the results in Sections 7 and 8.

2. Data

2.1. The OGLE Collection of Classical Cepheids

The OGLE Collection of Classical Cepheids in the Magellanic System (Soszyński *et al.* 2015) contains 9535 objects of which 4620 are located in the LMC and 4915 in the SMC OGLE-IV fields. Among those 5168 pulsate solely in the fundamental mode (F), 3530 solely in the first-overtone (1O), 117 oscillate only in the second-overtone (2O), 711 stars are double-mode pulsators, and nine pulsate in three modes.

The collection is based on the *I*- and *V*-band photometry from OGLE-IV (Udalski *et al.* 2015). The first step in variable star classification was the visual inspection of candidates' light curves. The selection of Cepheids was then based on the star's light curve shape, its location in the P-L diagram, and the ratio of periods, if multi-periodic. In some cases, the detailed inspection of the light curve was repeated, taking other parameters of the star into account. The final catalog contains CCs mean magnitudes in both bands, *I*-band amplitude, pulsation periods, epochs of maximum light, and Fourier parameters derived from the *I*-band light curves (Soszyński *et al.* 2015).

2.2. The Sample Selection

For our analysis we chose CCs pulsating in the fundamental mode and the first-overtone, including multi-mode pulsators, thus we excluded 117 stars oscillating solely in the second overtone from our sample. We were left with 9418 stars – 4593 in the LMC and 4825 in the SMC. Among those, 32 CCs (2 – LMC and – 30 SMC) are located in the genuine MBR fields, as defined by OGLE-IV field names, *i.e.*, within $RA\ 1^h54^m \lesssim \alpha \lesssim 4^h06^m$ (see green region in Fig. 19 of Udalski *et al.* 2015).

Next, we discarded Cepheids that did not have both *I*- and *V*-band magnitudes (50 objects from the LMC, 27 from the SMC and one from MBR). Then, during the procedure of fitting the P-L relations to our sample (see Section 3), we iteratively rejected Cepheids with the luminosity deviating from the fit by more than 3σ . This left us with 4222 Cepheids in the LMC, and 4663 in the SMC. We did not apply the fitting procedure to the MBR Cepheids separately.

Soszyński *et al.* (2015) state that at least five of the MBR CCs are truly located in the MBR. We carefully inspected 31 objects from the genuine MBR fields in terms of their location on the sky, distance from the observer and from the Magellanic Clouds. Indeed, 22 of them ($\alpha \lesssim 2^h$) are well correlated with the whole SMC sample, but nine are significantly offset from both galaxies. We reclassify those as MBR stars. Thus the final sample consists of 4222 Cepheids in the LMC, 4654 in the SMC and nine in the MBR. The final sample numbers are summarized in Table 1.

Table 1
Classical Cepheid sample used in the analysis

	All	F	1O	F1O&1O2O	F1O2O&1O2O3O
LMC	4222	2292	1589	337	4
SMC	4654	2646	1727	281	0
MBR	9	4	4	1	0
Total	8885	4942	3320	619	4

3. Data Analysis

3.1. Period-Luminosity Relation

The first step in obtaining distances to Cepheids was to fit the P-L relation to the LMC sample. In order to do this we first removed all the 1O Cepheids with $\log P < -0.3$ (we express P in days) from our sample. That is because they may represent a different sample with different chemical composition which is reflected in the P-L non-linearity near this value (Soszyński *et al.* 2008). Moreover, these stars are faintest, and most affected by crowding and blending effects, hence have greater luminosity uncertainty than the mean. For multi-mode pulsators we used the lowest pulsation mode. For fitting we used the reddening-independent Wesenheit magnitude (Madore 1976) for the V - and I -band photometry defined as:

$$W_{I,V-I} = I - 1.55 \cdot (V - I). \quad (1)$$

The coefficient 1.55 is calculated from a standard interstellar extinction curve dependence of the I -band extinction on $E(V - I)$ reddening (Schlegel, Finkbeiner and Davis 1998). We fitted a linear function in the form:

$$W_{I,V-I} = a \cdot \log(P) + b \quad (2)$$

using the least-squares method. In each iteration we rejected 3σ outliers until there were none. The majority of rejected outliers are due to blending and crowding effects.

In the case of fundamental-mode CCs we divided the sample into two groups: one with $\log P \leq 0.4$, and one with $\log P > 0.4$. A break in the P-L relation at this value was already reported in the literature (*e.g.*, Bauer *et al.* 1999, Udalski *et al.* 1999, Sharpee *et al.* 2002, Sandage *et al.* 2009, Soszyński *et al.* 2010). We also fitted the P-L relation to the *I*- and *V*-band magnitudes (without correcting for extinction). The same procedure was repeated for the SMC. Results are shown in Table 2 and in Fig. 1.

Table 2

P-L relations for CCs in the Magellanic Clouds

P-L for Wesenheit magnitude			$W_{I,V-I} = a \cdot \log P + b$					
Galaxy	P. mode	$\log P$	a	b [mag]	σ [mag]	χ^2/dof	N_{inc}	N_{rej}
LMC	F	≤ 0.4	-3.216 ± 0.033	15.864 ± 0.010	0.103	2.991	284	6
		> 0.4	-3.317 ± 0.007	15.890 ± 0.005	0.075	1.568	2103	87
		all	-3.313 ± 0.006	15.888 ± 0.004	0.078	1.686	2382	98
	1O	all	-3.414 ± 0.007	15.388 ± 0.002	0.079	1.714	1931	84
SMC	F	≤ 0.4	-3.488 ± 0.015	16.507 ± 0.004	0.157	6.920	1746	43
		> 0.4	-3.315 ± 0.009	16.379 ± 0.006	0.144	5.811	957	30
		all	-3.458 ± 0.005	16.492 ± 0.002	0.155	6.746	2708	68
	1O	all	-3.540 ± 0.007	15.959 ± 0.002	0.170	8.083	2010	30
P-L for <i>I</i> -band magnitude			$I = a \cdot \log(P) + b$					
Galaxy	P. mode	$\log P$	a	b [mag]	σ [mag]	χ^2/dof	N_{inc}	N_{rej}
LMC	F	≤ 0.4	-3.036 ± 0.032	16.865 ± 0.010	0.140	5.499	279	11
		> 0.4	-2.894 ± 0.007	16.810 ± 0.005	0.147	6.015	2093	97
		all	-2.911 ± 0.006	16.822 ± 0.004	0.146	5.959	2372	108
	1O	all	-3.240 ± 0.006	16.356 ± 0.002	0.159	7.065	1950	65
SMC	F	≤ 0.4	-3.147 ± 0.015	17.420 ± 0.004	0.208	12.104	1756	33
		> 0.4	-2.912 ± 0.009	17.241 ± 0.006	0.222	13.815	976	11
		all	-3.113 ± 0.005	17.401 ± 0.002	0.216	13.064	2734	42
	1O	all	-3.278 ± 0.007	16.813 ± 0.002	0.223	13.916	2007	33
P-L for <i>V</i> -band magnitude			$V = a \cdot \log(P) + b$					
Galaxy	P. mode	$\log P$	a	b [mag]	σ [mag]	χ^2/dof	N_{inc}	N_{rej}
LMC	F	≤ 0.4	-2.964 ± 0.032	17.526 ± 0.010	0.190	10.142	280	10
		> 0.4	-2.629 ± 0.007	17.399 ± 0.005	0.211	12.412	2090	100
		all	-2.672 ± 0.006	17.429 ± 0.004	0.207	11.986	2365	115
	1O	all	-3.133 ± 0.006	16.975 ± 0.002	0.223	13.983	1946	69
SMC	F	≤ 0.4	-2.914 ± 0.015	18.001 ± 0.004	0.254	18.003	1758	31
		> 0.4	-2.648 ± 0.009	17.792 ± 0.006	0.283	22.469	978	9
		all	-2.901 ± 0.005	17.984 ± 0.002	0.266	19.846	2734	42
	1O	all	-3.122 ± 0.007	17.361 ± 0.002	0.273	20.912	2004	36

N_{inc} is the number of objects included in the final fit, while N_{rej} is the number of rejected objects.

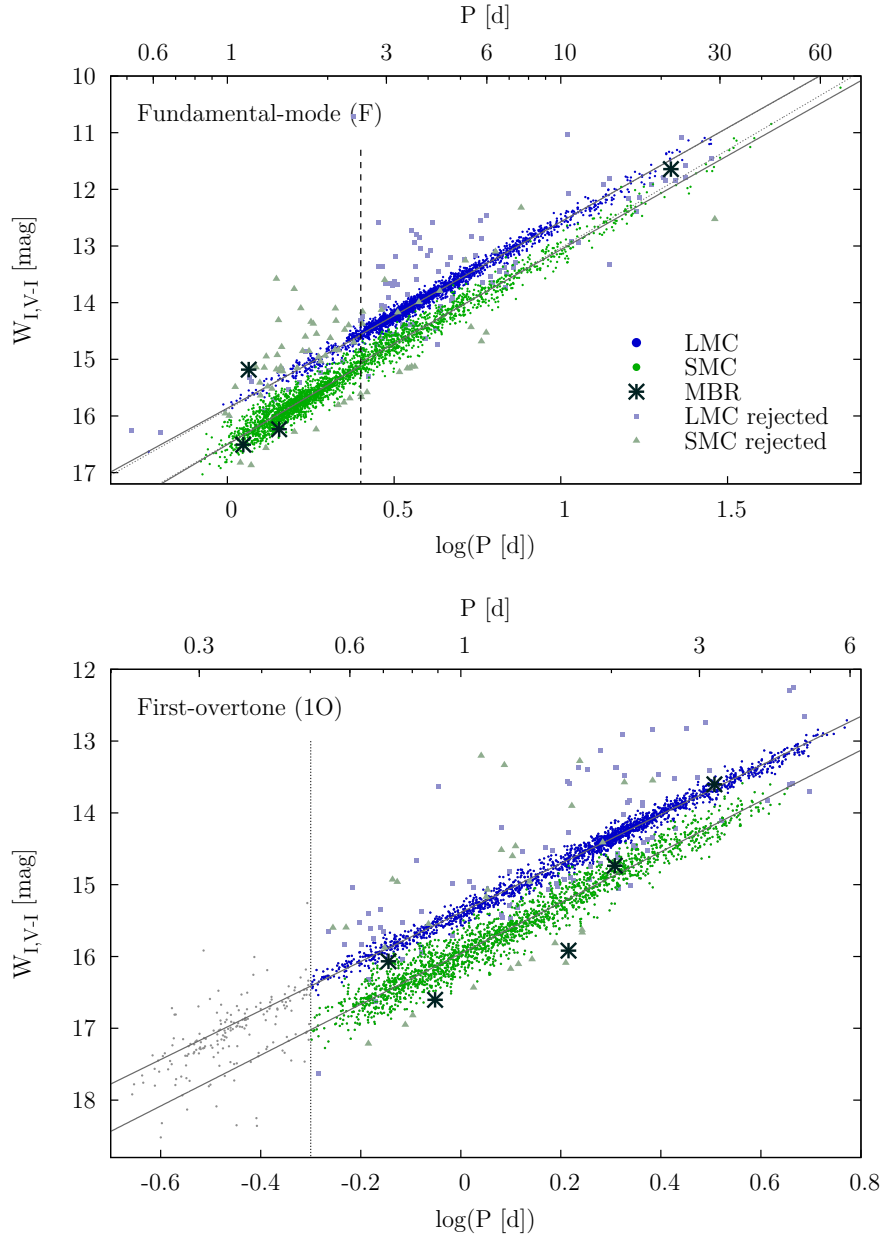


Fig. 1. P-L relations for the Wesenheit magnitude for fundamental-mode (*top panel*) and first-overtone (*bottom panel*) CCs in the LMC (blue dots) and in the SMC (green dots). The MBR Cepheids are marked with large stars. Gray points represent stars rejected during the iterative 3σ clipping when fitting the P-L relations. *Top panel*: Solid lines represent separate fits for two sets of F Cepheids divided at $\log P = 0.4$. The dotted lines show fits for the whole F sample in the LMC and SMC. The dashed vertical line represents the period at which the P-L relation breaks. *Bottom panel*: The solid lines show fits for 1O CCs. Small gray dots represent 1O Cepheids with $\log P < -0.3$ that were removed from our sample, as marked by the dotted vertical line.

The most accurate fits are obtained for the Wesenheit magnitude for the LMC Cepheids. They show the smallest scatter of only 0.08 mag. This is why we decided to use these relations for distance determinations in further analysis. In the case of the SMC, large values of χ^2/dof are a result of this galaxy's elongation almost along the line of sight – significant distance differences between the Cepheids account for the scatter in magnitudes.

The slopes of the P-L for the Wesenheit index for F Cepheids with $\log P > 0.4$ are identical for the LMC and SMC within 1σ errors, as expected (Ngeow *et al.* 2015). We cannot compare slopes for $\log P < 0.4$ for two reasons. First, the LMC sample is much less numerous than the SMC sample and so the comparison would be biased (Udalski *et al.* 1999). Second, the SMC may simply have a different value of the slope because of its different environment and Cepheids with shorter periods may have different chemical composition (Bauer *et al.* 1999, Soszyński *et al.* 2010). When calculating the distances we assume that the SMC $\log P < 0.4$ slope is identical as for the LMC.

3.2. Distances

In order to obtain both LMC and SMC Cepheid distances we used the mean distance to the LMC measured by Pietrzyński *et al.* (2013) from eclipsing-binaries, $d_{\text{LMC}} = 49.97 \pm 0.19$ (statistical) ± 1.11 (systematic) kpc. With 2.2% error it is the most accurate measurement of the mean LMC distance up to date.

For each object we calculated the reference magnitude W_{ref} , *i.e.*, the Wesenheit magnitude on the fitted P-L line (for the LMC) corresponding to its period P :

$$W_{\text{ref}} = a_{\text{LMC}} \cdot \log(P) + b_{\text{LMC}}. \quad (3)$$

We used a and b coefficients from Table 2, in the case of fundamental-mode Cepheids separately for $\log P \leq 0.4$ and > 0.4 . So the relative distance modulus is:

$$\delta\mu = W_{I,V-I} - W_{\text{ref}}. \quad (4)$$

And then the absolute distance simply:

$$d = d_{\text{LMC}} \cdot 10^{\frac{\delta\mu}{5}}. \quad (5)$$

Fig. 2 shows three-dimensional maps of the Magellanic System in the Cartesian space. Blue dots mark the LMC Cepheids, green dots SMC, and large dark teal dots show the Magellanic Bridge sample. Gray points mark the 3σ outliers rejected in the procedure of P-L fitting (see Fig. 1 for comparison). There is a distinct spread in the Cepheid distances along the line of sight that is mostly, but not entirely physical, and a part of it is due to errors in distance calculation. The errors are typically 1.2–1.6 kpc (median $\approx 3\%$ relative) for the LMC and 1.4–2.3 kpc (median $\approx 3\%$ relative) for the SMC. When calculating the uncertainties we used the error of zero points of the OGLE-IV photometry which is $\sigma_{I,V} = 0.02$ mag and the uncertainties

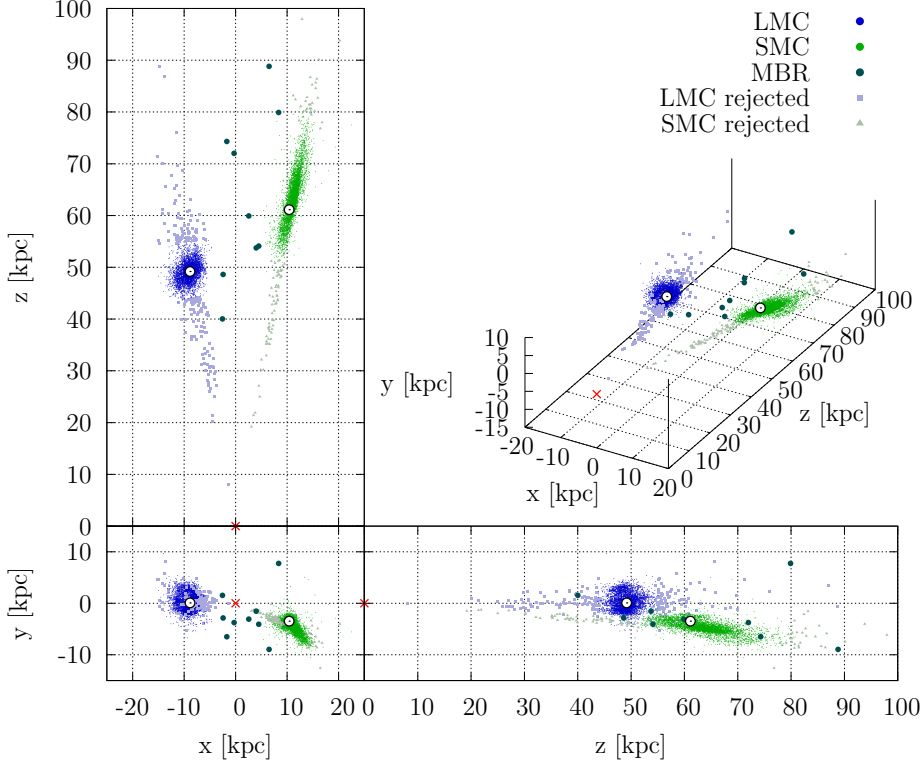


Fig. 2. Three-dimensional map showing the Magellanic System in Cartesian coordinates with the z axis pointing toward $\alpha_{\text{cen}} = 3^{\text{h}}20^{\text{m}}$, $\delta_{\text{cen}} = -72^{\circ}$. Blue dots represent the LMC, green dots SMC, and the large dark teal dots – MBR. Gray points show the 3σ outliers rejected in the P-L fitting procedure (see Fig. 1 for comparison). Red cross marks the observer’s location. White circles mark the LMC (Pietrzyński *et al.* 2013, van der Marel and Kallivayalil 2014) and SMC (Graczyk *et al.* 2014, Stanimirović *et al.* 2004) centers.

of the P-L fit which are shown in Table 2. We intentionally omitted the uncertainty of the LMC distance measurement because it would only increase Cepheid distance uncertainties without affecting the geometry. While the photometry error itself is not large $\sigma_{I,V} = 0.02$ mag, it translates at the LMC distance to $\sigma_{d,I,V} = 0.46$ kpc and $\sigma_{d,W} = 0.65$ kpc and this is the “natural spread” of the method. There is also a possibility, that even though we are using the reddening-free Wesenheit index, the differential and variable extinction within the LMC/SMC may add up to the error in Cepheid distances.

We have analyzed how much the adopted reddening law influences the distance uncertainties. For a Wesenheit index with a different coefficient:

$$W_{I,V-I} = I - 1.44 \cdot (V - I) \quad (6)$$

(Udalski 2003) we obtained slightly smaller uncertainties. In the case of the LMC the median distance uncertainty was about 1.38 kpc (2.8% relative) when using a coefficient of 1.55, and 1.31 kpc (2.6% relative) when using 1.44. In the case of

the SMC the numbers are: 1.79 kpc (2.8% relative) for 1.55, and 1.70 kpc (2.6% relative) for 1.44. We see that the choice of the reddening law coefficient does not influence the distance uncertainties in a significant way.

3.3. Coordinate Transformations

In this study we visualize the results with two types of maps. The first one is a two-dimensional sky map in a Hammer equal-area projection. The projection is rotated so that the z axis is pointing toward $\alpha_{\text{cen}} = 3^{\text{h}}20^{\text{m}}$, $\delta_{\text{cen}} = -72^\circ$. For each Cepheid, x_{Hammer} and y_{Hammer} are calculated from:

$$\alpha_{\text{b}} = \alpha + \left(\frac{\pi}{2} - \alpha_{\text{cen}} \right), \quad (7)$$

$$l = \arctan \left(\frac{\sin(\alpha_{\text{b}}) \cos(\delta_{\text{cen}}) + \tan(\delta) \sin(\delta_{\text{cen}})}{\cos(\alpha_{\text{b}})} \right), \quad l \in [-\pi; \pi], \quad (8)$$

$$\beta = \arcsin(\sin(\delta) \cos(\delta_{\text{cen}}) - \cos(\delta) \sin(\delta_{\text{cen}}) \sin(\alpha_{\text{b}})), \quad (9)$$

$$x_{\text{Hammer}} = -\frac{2\sqrt{2} \cdot \cos(\beta) \sin\left(\frac{l}{2}\right)}{\sqrt{1 + \cos(\beta) \cos\left(\frac{l}{2}\right)}}, \quad (10)$$

$$y_{\text{Hammer}} = \frac{\sqrt{2} \cdot \sin(\beta)}{\sqrt{1 + \cos(\beta) \cos\left(\frac{l}{2}\right)}}. \quad (11)$$

Fig. 3 shows the Hammer projection of the Magellanic System where the Cepheid distances are color-coded. The LMC is on the left, with a clearly visible bar and a northern arm, while the SMC is on the right. The Magellanic Bridge Cepheids between the two galaxies are marked with larger dots. Here we can clearly see the distance differences between the two galaxies. The bottom panels show close-ups of each of the Clouds. When looking at the LMC (left) we can clearly see the inclination of this galaxy – the western side of the LMC (the right side of the map) lies farther from us than the eastern side. In fact, it is rotated in the direction of the SMC. The right panel shows the SMC close-up. The large spread in Cepheid distances reflects the galaxy's significant elongation (see Fig. 2 for comparison).

The second type of maps used in this study are the three-dimensional Cartesian space (x, y, z) projections with different viewing angles. In this transformation the observer is always in $(0, 0, 0)$ while the z axis is pointing toward different equatorial coordinates: α_{cen} and δ_{cen} . The transformation equations were taken from van der Marel and Cioni (2001) and Weinberg and Nikolaev (2001):

$$x = -d \cdot \cos(\delta) \sin(\alpha - \alpha_{\text{cen}}), \quad (12)$$

$$y = d \cdot (\sin(\delta) \cos(\delta_{\text{cen}}) - \cos(\delta) \sin(\delta_{\text{cen}}) \cos(\alpha - \alpha_{\text{cen}})), \quad (13)$$

$$z = d \cdot (\cos(\delta) \cos(\delta_{\text{cen}}) \cos(\alpha - \alpha_{\text{cen}}) + \sin(\delta) \sin(\delta_{\text{cen}})), \quad (14)$$

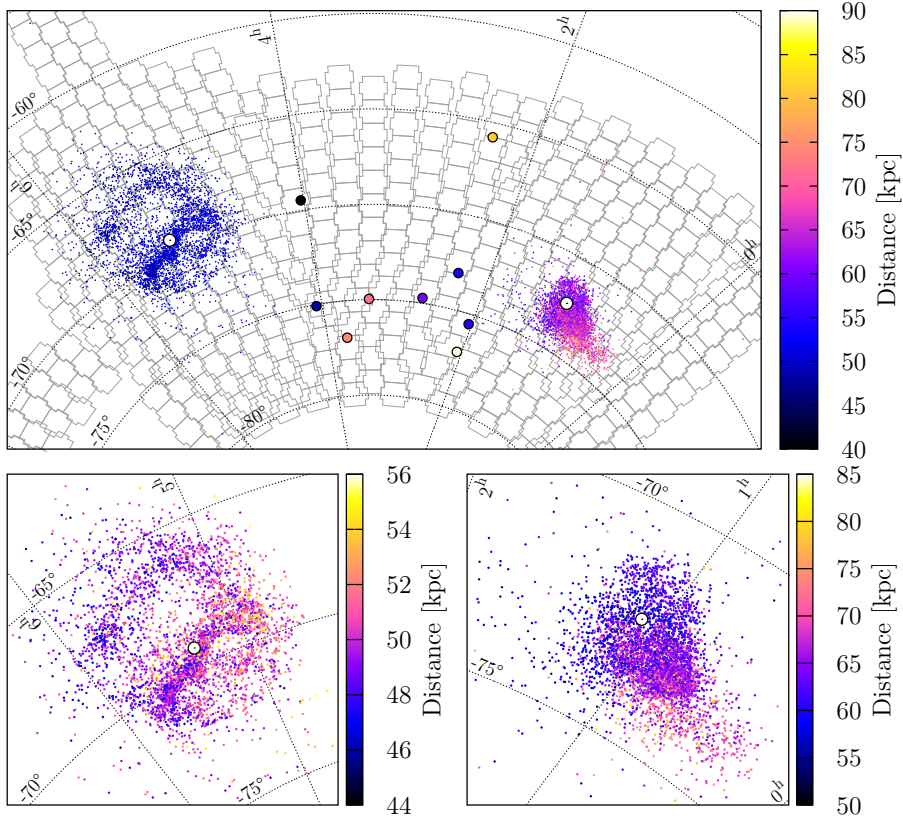


Fig. 3. Three-dimensional map of CCs in the Magellanic System in a Hammer projection with the z axis pointing toward $\alpha_{\text{cen}} = 3^{\text{h}}20^{\text{m}}$, $\delta_{\text{cen}} = -72^{\circ}$. Cepheid distances are color-coded. *Upper panel*: MBR Cepheids are marked with large dots. Gray contours represent OGLE-IV fields in the Magellanic System. *Lower left panel*: Close-up on the LMC. *Lower right panel*: Close-up on the SMC. Note the change in color range. White circles mark the LMC (van der Marel and Kallivayalil 2014) and SMC (Stanimirović *et al.* 2004) centers.

where d is the calculated distance to each Cepheid and α_{cen} , δ_{cen} are the map center coordinates. Maps showing only the LMC or only SMC are rotated so that the z axes are pointing toward their dynamical centers. For the LMC we adopt $\alpha_{\text{LMC-cen}} = 5^{\text{h}}20^{\text{m}}12^{\text{s}}$, $\delta_{\text{LMC-cen}} = -69^{\circ}18'$, which is for the whole population with a correction for young stars proper motions (van der Marel and Kallivayalil 2014). For the SMC we use $\alpha_{\text{SMC-cen}} = 1^{\text{h}}05^{\text{m}}$, $\delta_{\text{SMC-cen}} = -72^{\circ}25'12''$ (Stanimirović *et al.* 2004). We decided to use the dynamical centers of these galaxies because we think they are the most reliable. The same centers were used to calculate Magellanic Clouds' proper motions (see Kallivayalil *et al.* 2006ab, 2013 and van der Marel and Kallivayalil 2014).

The uncertainties of the Cartesian coordinates include the OGLE astrometric uncertainty which is $\sigma_{\alpha,\delta} = 0''.2$. Every coordinate is also dependent on the distance, so the uncertainties of x , y and z include the distance uncertainty. Their val-

ues are in the following ranges: $0.4 \text{ kpc} < \sigma_x < 1.3 \text{ kpc}$, $0.6 \text{ kpc} < \sigma_y < 1.3 \text{ kpc}$, and $1.3 \text{ kpc} < \sigma_z < 2.4 \text{ kpc}$.

The most important parameters of the CCs sample analyzed in this publication are available online from the OGLE website:

<http://ogle.astrouw.edu.pl>

Table 3 presents the first few lines of the data file.

Table 3
Classical Cepheids in the Magellanic System

Columns 1-7						
Location	OCVS Id	P. mode	P ^(a) [d]	I [mag]	V [mag]	W _{I,V-I} [mag]
LMC	OGLE-LMC-CEP-0004	1O	2.2296385	15.123	15.690	14.244
LMC	OGLE-LMC-CEP-0005	F	5.6119491	14.651	15.425	13.451
LMC	OGLE-LMC-CEP-0006	1O	3.2947501	14.707	15.366	13.686
LMC	OGLE-LMC-CEP-0007	1O	0.7090827	16.955	17.561	16.016
LMC	OGLE-LMC-CEP-0008	1O/2O	0.9728732	16.337	16.921	15.432
⋮	⋮	⋮	⋮	⋮	⋮	⋮
Columns 8-14						
RA	Dec	d [kpc]	x ^(b) [kpc]	y ^(b) [kpc]	z ^(b) [kpc]	Age ^(c) [Myr]
04 ^h 35 ^m 20 ^s 16	−69°48′07″.7	51.03 ± 1.40	−5.69 ± 0.43	1.06 ± 0.85	50.70 ± 1.50	102 ± 19
04 ^h 35 ^m 31 ^s 52	−69°44′05″.8	51.05 ± 1.41	−5.72 ± 0.43	1.11 ± 0.85	50.72 ± 1.50	66 ± 15
04 ^h 35 ^m 42 ^s 16	−69°43′29″.1	51.51 ± 1.42	−5.79 ± 0.43	1.13 ± 0.86	51.18 ± 1.51	75 ± 14
04 ^h 36 ^m 30 ^s 06	−68°37′35″.7	52.77 ± 1.45	−6.30 ± 0.46	2.10 ± 0.88	52.35 ± 1.55	256 ± 47
04 ^h 36 ^m 33 ^s 08	−69°18′43″.6	50.05 ± 1.38	−5.80 ± 0.43	1.42 ± 0.84	49.69 ± 1.47	199 ± 36
⋮	⋮	⋮	⋮	⋮	⋮	⋮

The electronic version of the whole sample used in this study is available online from the OGLE website. (a) For multi-mode Cepheids the longest period is provided. (b) The cartesian x , y and z coordinates. (c) The ages were calculated using PA relations from Bono *et al.* (2005).

3.4. Model and Plane Fitting

In the next step we attempt to characterize the LMC Cepheids in three dimensions. Here we use a Cartesian coordinate system with the origin in the LMC center and z axis oriented toward the observer.

$$x = d\tilde{x}(\alpha, \delta) = -d \cdot \cos(\delta) \sin(\alpha - \alpha_{\text{LMC-cen}}), \quad (15)$$

$$y = d\tilde{y}(\alpha, \delta) = d \cdot (\sin(\delta) \cos(\delta_{\text{LMC-cen}}) - \cos(\delta) \sin(\delta_{\text{LMC-cen}}) \cos(\alpha - \alpha_{\text{LMC-cen}})), \quad (16)$$

$$z = d_{\text{LMC}} - d\tilde{z}(\alpha, \delta) = d_{\text{LMC}} - d \cdot (\cos(\delta) \cos(\delta_{\text{LMC-cen}}) \cos(\alpha - \alpha_{\text{LMC-cen}}) + \sin(\delta) \sin(\delta_{\text{LMC-cen}})). \quad (17)$$

Structural parameters of the LMC disk (inclination, position angle) can be inferred from a plane fit to the data:

$$z = ax + by + c. \quad (18)$$

The coefficient c quantifies the shift of the best-fit plane from the adopted LMC center. The remaining two parameters can be transformed to the disk inclination i and position angle P.A.:

$$i = \arccos\left(1/\sqrt{a^2 + b^2 + 1}\right), \quad (19)$$

$$\text{P.A.} = \arctan\left(-\frac{a}{b}\right) + \frac{\pi}{2}\text{sgn}(b). \quad (20)$$

A simple linear least-squares fit to the plane equation can be biased, because the uncertainties of all coordinates (x, y, z) are not negligible, since they all contain distance measurement error. Hence, we propose a parametrization in which a line joining the observer and the i -th Cepheid intersects the fitted plane at a distance:

$$d_{\text{model}}(\alpha_i, \delta_i; a, b, c) = \frac{d_{\text{LMC}} - c}{\tilde{z}(\alpha_i, \delta_i) + a\tilde{x}(\alpha_i, \delta_i) + b\tilde{y}(\alpha_i, \delta_i)} \quad (21)$$

or a distance modulus:

$$\mu_{\text{model}}(\alpha_i, \delta_i; a, b, c) = 5 \log(d_{\text{model}}(\alpha_i, \delta_i; a, b, c)) + 10 \quad (22)$$

if d_{model} is expressed in kpc. We minimize the sum:

$$\chi^2(a, b, c) = \sum_i \left(\frac{\mu_i - \mu_{\text{model}}(\alpha_i, \delta_i; a, b, c)}{\sigma_{\mu,i}} \right)^2 \quad (23)$$

using the Nelder-Mead algorithm (Nelder and Mead 1965). The adopted uncertainties $\sigma_{\mu,i}$ include OGLE photometry uncertainties ($\sigma_{I,V} = 0.02$ mag) and the uncertainties of the P-L fit given in Table 2. The fitting procedure is iterative and after each step 3σ outliers are rejected. The typical deviation from the best-fit plane (1.5 kpc) is constrained by the accuracy of the P-L relation and the ‘‘natural spread’’ of the method of calculating distances as described above (0.65 kpc). We checked that the influence of the choice of d_{LMC} and $(\alpha_{\text{LMC-cen}}, \delta_{\text{LMC-cen}})$ on the best-fit parameters is negligible.

4. The Large Magellanic Cloud

4.1. Three-Dimensional Structure

Previous studies of the LMC CCs based on the OGLE-III data (*cf.* Fig. 1 from Haschke *et al.* 2012a) did not include the northern and southern parts of the galaxy. This is the first time that we see a full picture of the LMC with the OGLE Cepheids.

Fig. 3 shows that the disk of the LMC is inclined and rotated in the direction of its smaller neighbor, the SMC. This result is consistent with previous findings (van der Marel and Cioni 2001, Nikolaev *et al.* 2004, Persson *et al.* 2004, Pejcha and Stanek 2009, Koerwer 2009, Subramanian and Subramanian 2010, Haschke *et al.* 2012a, Subramanian and Subramanian 2013, van der Marel and Kallivayalil 2014, Deb and Singh 2014). We slice-up the galaxy into distance intervals in Fig. 4 to see the details of this tilt. Top three panels show LMC parts that are closer than 50 kpc, while bottom three panels that are farther than 50 kpc (which is very close to the mean distance to the LMC $d_{\text{LMC}} = 49.97$ kpc from Pietrzyński *et al.* 2013). There is a clear difference between the top and the bottom row – the closest LMC stars are located mainly in the eastern parts of the galaxy, especially the eastern part of the bar and the northern arm, while the farthest parts of the LMC are in the west. Moreover, the northern arm seems to lie closer to us than the rest of the galaxy. The bar will be discussed in detail in Section 5.

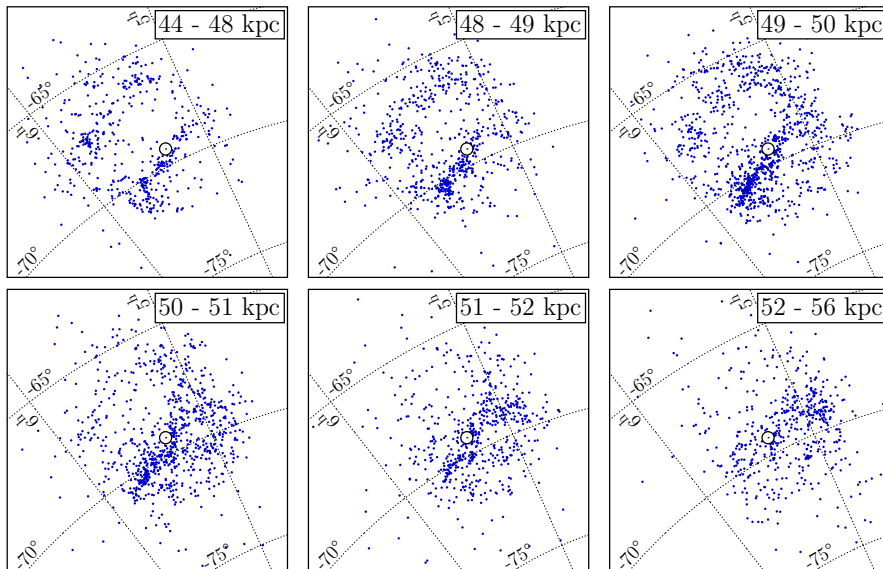


Fig. 4. Distance tomography of the LMC in the Hammer projection. Note that the *first* and the *last panel* distance range is 4 kpc, the *intermediate panels* – 1 kpc. White circle marks the LMC center (van der Marel and Kallivayalil 2014).

In Fig. 5 we show Cepheid column density maps. The top map is visualized in the Hammer projection and the bottom three in the Cartesian planes xy , xz and yz , with the z axis pointing toward the LMC center. The most prominent feature is the bar – especially its eastern part – and the northern arm. The northern arm shows a number of overdensities: one is connected with the bar, another two are on the northmost side of the LMC and the fourth one is at the tip of the arm. We also see two Cepheid overdensities in the southern part of the LMC, which may indicate a presence of another arm. The larger of these overdensities seems to be connected

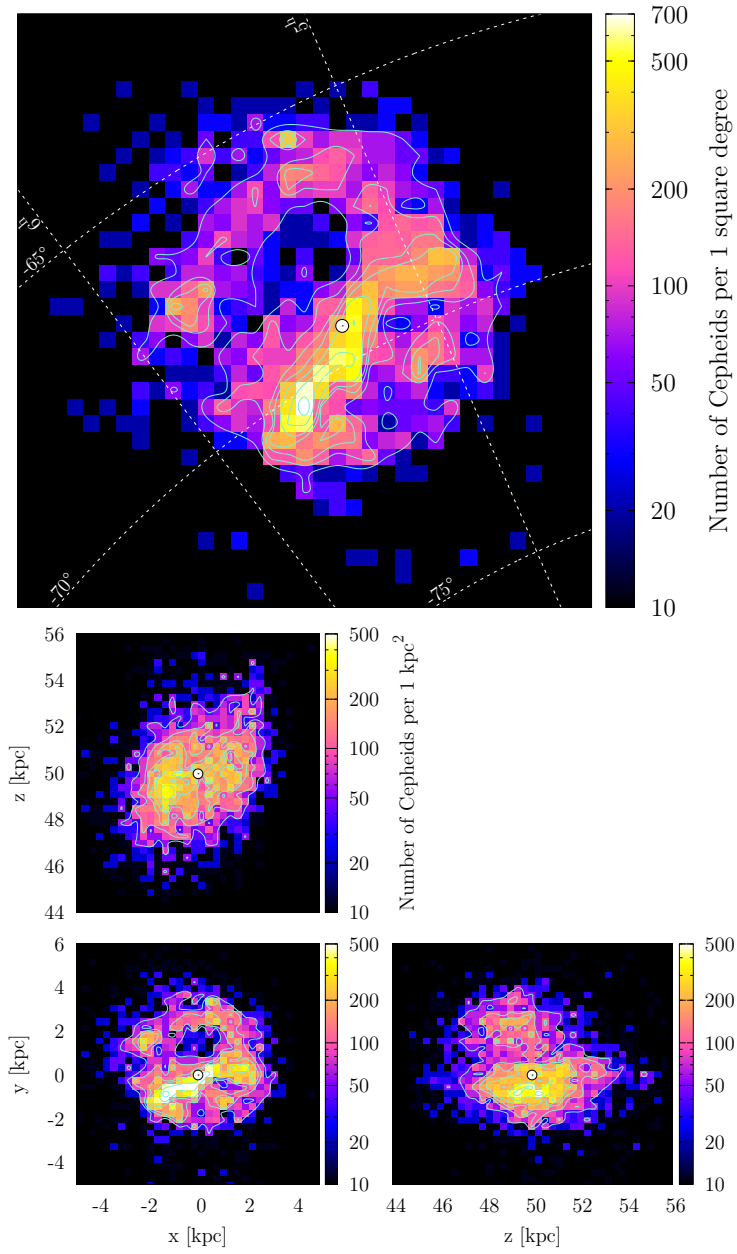


Fig. 5. Cepheid density maps in the LMC with Cepheid column density contours. *Top map*: Map in the Hammer projection. The bin size is 0.0001 in units of Hammer projection coordinates x_{Hammer} and y_{Hammer} in both directions. Contour levels are: 50, 100, 150, 200, 300, 500, 700 Cepheids per 1 square degree. *Bottom set of three maps*: Maps in the Cartesian coordinates projections with the z axis pointing toward the LMC center. The bin size is 0.3 kpc in x , y and z . Contour levels on the xy plane are 50, 100, 150, 250, 500, 800, on the xz plane 50, 100, 150, 200, 250, 300 and on the yz plane 50, 100, 150, 200, 300, 400 Cepheids per 1 kpc^2 . The white circle marks the LMC center (Pietrzyński *et al.* 2013, van der Marel and Kallivayalil 2014).

with and coming out of the bar at its east end – this is also visible in the first panel of Fig. 4. The other southern overdensity is separated from the bar.

The bottom set of three maps in Fig. 5 shows bins in the Cartesian projections, see figure caption for a full description. The map showing the xy plane is very similar to the top map. The bar has the largest column density and its eastern part is the most prominent feature of the galaxy. The northern arm and its overdensities, as well as the southern structures, are also well distinguishable. The xz plane (view “from the top”) shows that the inclination of the LMC is very evident. The eastern part of the LMC lies closer to us and is more numerous than the western part. The yz plane (view “from the side”) shows two almost separate parts: the northern and the southern, that comprise with the LMC northern arm and the bar, respectively. This projection clearly shows that the arm is closer to us than the LMC, as implied in Fig. 4. On the other hand, the southern part is at a similar distance as the mean LMC distance. Contrary to previous studies (*e.g.*, Zhao and Evans 2000, Nikolaev *et al.* 2004, Subramanian and Subramanian 2013, van der Marel and Kallivayalil 2014 and numerical model of the off-center bar in Bekki 2009 and Besla *et al.* 2012), we do not see that the bar is located closer to us than the LMC.

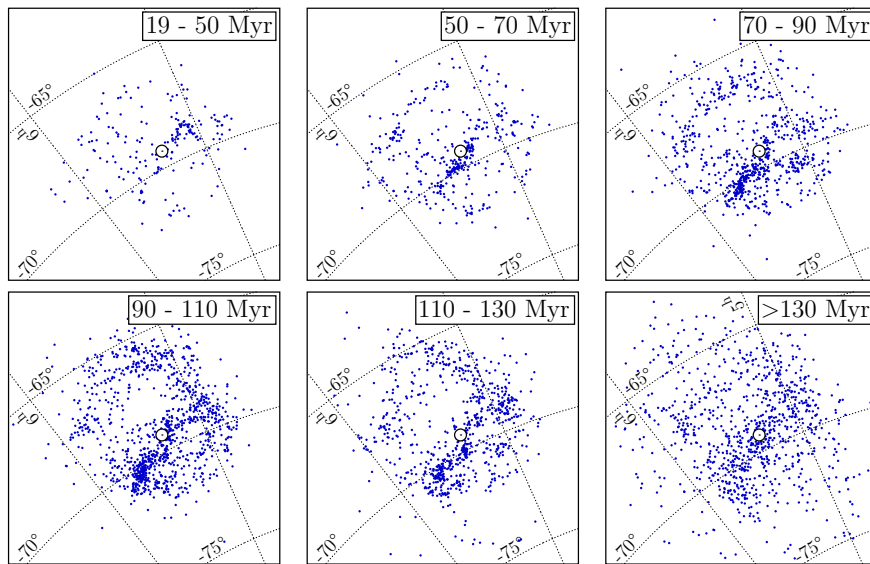


Fig. 6. Age tomography of the LMC using the relation from Bono *et al.* (2005) for a constant metallicity $Z = 0.01$. The maps are in the Hammer projection. Note that the *first panel* shows an interval of 51 Myr, *last* – 263 Myr, *the other ones* – 20 Myr. White circle marks the LMC center (van der Marel and Kallivayalil, 2014).

4.2. Ages

We estimated ages of the LMC Cepheids using the period–age relation from Bono *et al.* (2005) for a constant metallicity $Z = 0.01$. Some studies suggest that LMC has a metallicity gradient (Cioni 2009, Feast *et al.* 2010, Wagner-Kaiser and

Sarajedini 2013), but a recent study by Deb and Singh (2014) shows that there is no such gradient or it is too small to be detected with techniques used.

The on-sky distribution of Cepheids in different age intervals is presented in Fig. 6. Most of the stars fall into the age range of 50–130 Myr. The youngest Cepheids are found in the western part of the bar at $\alpha \approx 5^{\text{h}}$ and are younger than 50 Myr. In the age interval of 50–70 Myr the central part of the bar emerges. Then the eastern part of the bar shows up along with the western part and the northern arm. The eastern and western areas of the bar were formed at similar times and thus should be treated as parts of one coherent structure. Cepheids older than 130 Myr are scattered along the bar and the arm and are spread all over the LMC disk.

Soszyński *et al.* (2015) noticed that there is a difference between the distributions of fundamental and first-overtone Cepheids in the LMC, such that 1O stars are more spread than F-mode stars (see their Fig. 4). This can be explained by age differences between these types – the 1O Cepheids are slightly older and so had time to spread.

4.3. Substructures

To investigate properties of the bar, the arm, and other structures of the LMC we divided the galaxy into several regions shown in Fig. 7. The left panel illustrates selection areas for main structures: the whole bar and the whole arm as well as two southern regions. We further divided the bar and the arm each into two subregions – eastern and western bar, and northern arm 1 and northern arm 2, as shown in the right panel. Basic parameters of all substructures, such as the median distance and age, standard deviations and number of stars in each group, are listed in Table 4.

Table 4

Characteristics of the LMC substructures

Substructure	$\langle \text{dist} \rangle$ [kpc]	σ_{dist} [kpc]	$\langle \text{age} \rangle$ [Myr]	σ_{age} [Myr]	N
All Cepheids	49.93	1.79	104	53	4222
Bar	50.03	1.74	100	48	1662
Eastern Bar	49.86	1.65	100	49	1318
Western Bar	51.03	1.82	104	45	344
Northern Arm	49.39	1.66	106	48	965
Northern Arm 1	49.43	1.70	105	50	820
Northern Arm 2	49.13	1.35	108	34	143
Southern Region 1	49.96	1.73	106	46	236
Southern Region 2	50.78	1.39	101	52	190

The table lists median distance and age together with standard deviations, and a number of stars in each substructure.

When constructing the selection areas for each structure we followed the density contours for binned data shown in Fig. 5. The choice was also based on distri-

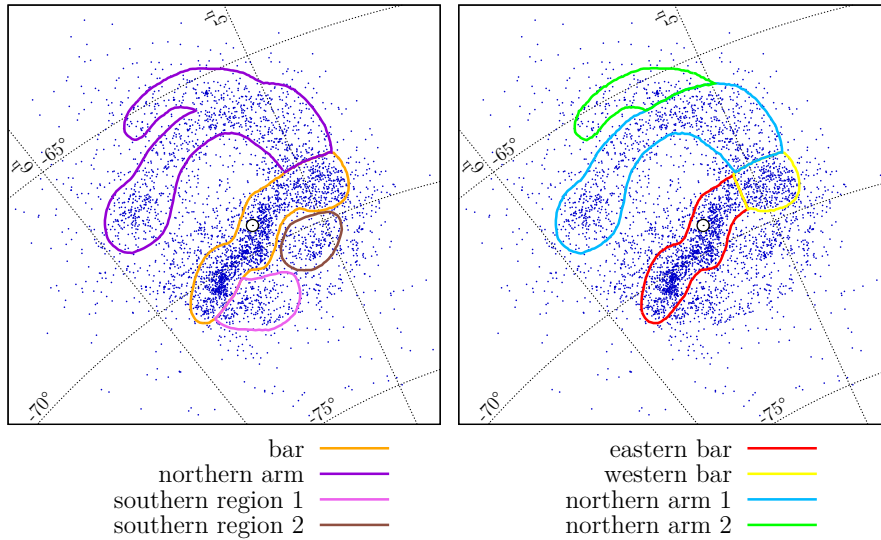


Fig. 7. The maps show the LMC Cepheids in the Hammer projection. *Left*: Main regions are presented: the whole bar, the whole northern arm and two southern regions. *Right*: The map shows divisions of the bar and the arm into two subregions: eastern and western bar, northern arm 1 and northern arm 2. White point with dot in the middle marks the LMC center (van der Marel and Kallivayalil 2014).

butions of stars in different age intervals (see Fig. 6). The age-space distributions were discussed in detail in Section 4.2. Here we concentrate on justification of the selected regions and their properties.

The selection of the bar area was performed in a few stages. The density contours suggest that the bar may consist of two parts: eastern, making up almost the whole bar in terms of star counts, and western. The eastern bar which is regarded as the “classical” LMC bar (see Fig. 14 in Nikolaev *et al.* 2004 and Figs. 1 and 7 in Haschke *et al.* 2012a) is the densest and the brightest part of the LMC. It is also located about 0.5 kpc closer than the rest of this galaxy (*e.g.*, Zhao and Evans 2000, Cioni *et al.* 2000, Nikolaev *et al.* 2004, Subramanian and Subramanian 2013, van der Marel and Kallivayalil 2014 and numerical models of the off-center bar in Bekki 2009 and Besla *et al.* 2012). However, Fig. 4 suggests that the entire bar should consist of both the eastern and the western part. There is a fairly continuous band of stars between the parts and there is no significant break between these parts at any of the distance slices. Even though the first two panels of Fig. 4 show mainly the eastern bar, the third map (distance interval 49–50 kpc) shows a western counterpart. At larger distances we see that the eastern area fades and the western is more visible. The age-tomography (Fig. 6) leads to very similar conclusions: the maps showing age intervals 90–110 Myr and 110–130 Myr represent the most evident connection between the eastern and western area of the bar. Moreover, the dynamical center of the LMC, marked in Fig. 7 with a white circle, is located in the middle of the whole bar, not its eastern part.

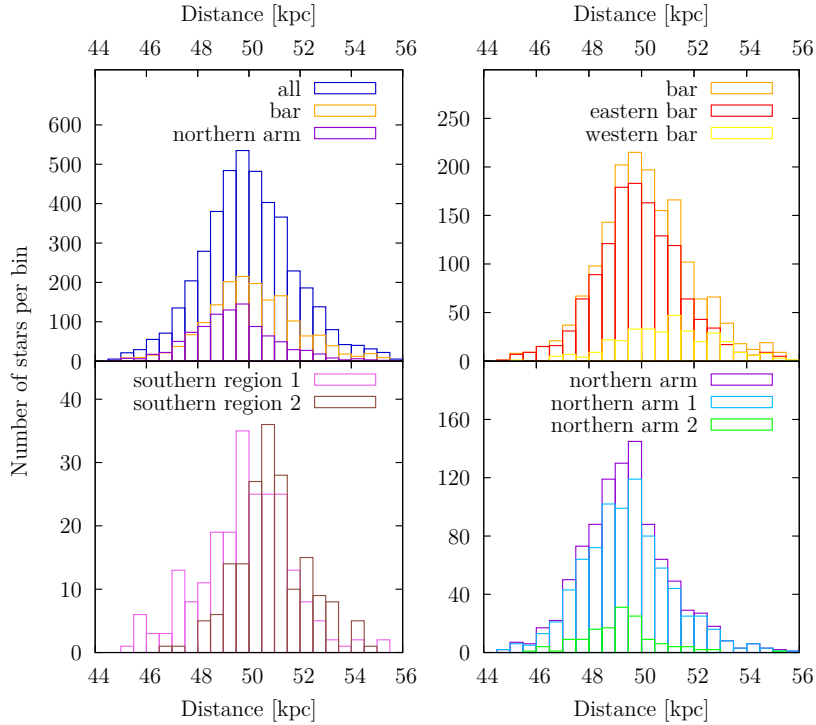


Fig. 8. Distance histograms of the selected regions in the LMC. *Left panel, top*: Comparison of all LMC Cepheids with the main structures – the bar and the northern arm. *Left panel, bottom*: Southern regions 1 and 2. *Right panel, top*: Comparison of the whole bar with its eastern and western parts. *Right panel, bottom*: Comparison of the whole northern arm with its parts 1 and 2.

A histogram showing the comparison of the distance distribution in the whole LMC and the bar (as well as the northern arm) is in the top left panel of Fig. 8. We perform a series of Kolmogorov-Smirnov (KS) tests for the null hypothesis that the two samples come from the same distribution, and the test results for various samples are listed in Table 5. In the case of the whole LMC and the bar we obtained $D = 0.039$ and a p -value = 0.048. This means that the hypothesis can be rejected at a significance level $\alpha = 0.05$. However, according to Sellke *et al.* (2001), the error rate associated with a p -value of ≈ 0.05 is at least 23% and typically $\approx 50\%$ (which is the probability that a true null hypothesis has been rejected). In the case of the p -value = 0.01, the error rate is at least 7% and typically $\approx 15\%$, thus in the following analysis we will assume that the null hypothesis can be rejected only if p -value ≤ 0.01 . According to the KS test results, and median distances from Table 4 we again see that the bar does not lie closer to us than the LMC, when defined as described in the previous paragraph. The top right panel of Fig. 8 shows a histogram of the entire bar and separately its eastern and western parts. Here we can see that the eastern part does lie closer to us than the western part, which is supported by their median distances (49.86 kpc and 51.03 kpc, respectively) and

the KS test results at significance level $\alpha = 0.001$ ($D = 0.287$, p -value = 0). If we treat the bar in a “classical” way, *i.e.*, as its eastern part, then there is no strong evidence that it is located closer to us than the LMC (the offset is only 0.07 kpc, see Table 4). Also, the significance level at which we could reject the hypothesis of the two distributions coming from the same sample is only $\alpha = 0.1$ ($D = 0.039$, p -value = 0.089).

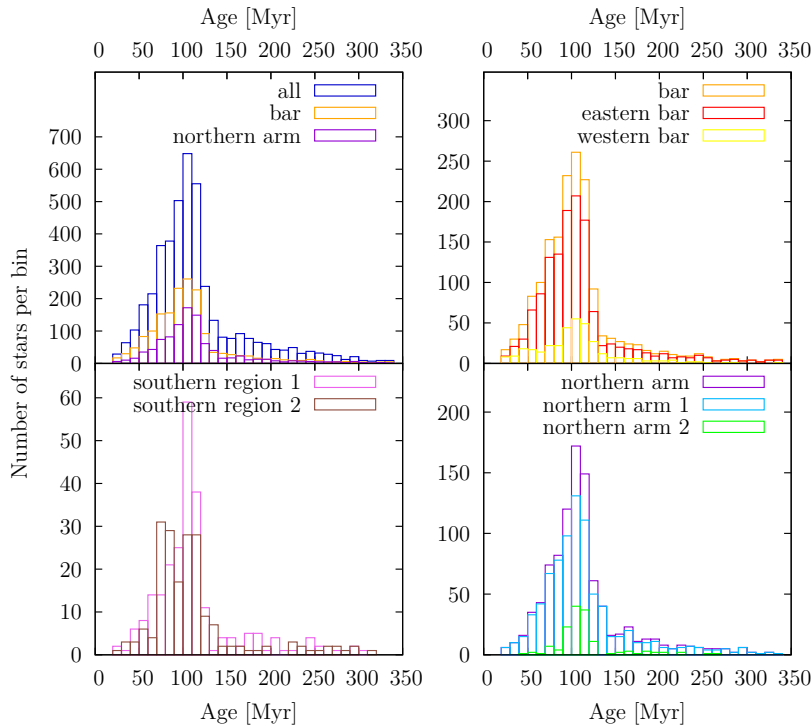


Fig. 9. Age histograms of the selected regions in the LMC. *Left panel, top*: Comparison of all LMC Cepheids with the main structures – the bar and the northern arm. *Left panel, bottom*: Southern regions 1 and 2. *Right panel, top*: Comparison of the whole bar with its eastern and western parts. *Right panel, bottom*: Comparison of the whole northern arm with its parts 1 and 2.

The age histograms in the top left panel of Fig. 9 show that Cepheids’ age distribution in the bar is fairly similar to the age distribution of the entire galaxy, as supported by median ages in Table 4, but the KS test results presented in Table 5 allow us to reject this hypothesis at a significance level $\alpha = 0.001$ ($D = 0.069$, p -value = 0). The top right panel suggests that the western part of the bar is slightly older than the eastern part, but since p -value = 0.042, we cannot reject that they come from the same age distribution. This further supports our choice of the bar region.

The northern arm selection area was based on density contours (Fig. 5). We divided the arm into two parts that we named northern arm 1 and northern arm 2 (hereafter NA1 and NA2). The NA1 is the most prominent part of the whole

Table 5
Kolmogorov-Smirnov test results in the LMC

Sample 1	Sample 2	DISTANCE			AGE		
		D	p -value	α^*	D	p -value	α^*
all	bar	0.039	0.048	0.050	0.069	0.000	0.001
all	bar-E	0.039	0.089	0.100	0.079	0.000	0.001
all	arm-N	0.165	0.000	0.001	0.041	0.133	—
arm-N	bar	0.193	0.000	0.001	0.098	0.000	0.001
bar	bar-E	0.060	0.009	0.025	0.017	0.980	—
bar	bar-W	0.227	0.000	0.001	0.066	0.159	—
bar-E	bar-W	0.287	0.000	0.001	0.083	0.042	0.050
SR1	SR2	0.295	0.000	0.001	0.139	0.031	0.050
arm-N	arm-N1	0.025	0.942	—	0.031	0.781	—
arm-N	arm-N2	0.146	0.009	0.025	0.173	0.001	0.005
arm-N1	arm-N2	0.171	0.001	0.005	0.204	0.000	0.001

* α is a significance level at which a null hypothesis that the two samples come from the same distribution can be rejected. No value means that $\alpha \geq 0.100$ and the hypothesis cannot be rejected. Due to our strict approach we treat values only below $\alpha = 0.010$ as significant and allowing us to reject the hypothesis.

northern arm. It is connected with the western part of the bar and stretches out to the northern and eastern side of the LMC. The NA2 is located in the northmost part of the LMC and is connected with NA1. It is visible as the brightest overdensity in the northern part of Fig. 5. Soszyński *et al.* (2015) noticed that it is only visible in fundamental mode Cepheids.

The distance histogram in the top left panel of Fig. 8 shows that the northern arm is located closer to us than the whole LMC at a significance level $\alpha = 0.001$ (see Table 5). The bottom right panel compares distance distributions of NA1 and NA2. Their distances are consistent with an overall distance of the northern arm, but the KS test shows a difference in their distributions at level $\alpha = 0.005$. On the other hand, the age histograms and KS test results in Table 5 lead to a conclusion that the arm is slightly older than the bar (top left panel of Fig. 9), but there is no age difference between the northern arm and the LMC.

The first map in the top panel of Fig. 4 suggests that there might be another arm in the southern part of the LMC. It seems to be connected with the bar at its south-east end.

We subdivide this region into two parts: southern region 1 (SR1) and southern region 2 (SR2) shown in Fig. 7. Their mean distances (Table 4) are consistent with the inclination of the LMC disk. The SR1, which is located in the eastern part of

the LMC, is also closer to us than SR2, that is located in the western part of the galaxy, at significance level $\alpha = 0.001$ (Table 5). Interestingly, SR2 seems to be younger than SR1, but the significance of this claim is low ($\alpha = 0.05$), thus we do not treat this result as relevant.

4.4. Plane Fitting

We performed a three-dimensional plane fitting to the LMC Cepheids as described in Section 3.4. We used Cartesian coordinates x, y, z although in the plane-fitting model the coordinate system center is placed in the LMC center and z axis points in the opposite direction than on our map projections. We separately fit CCs in the bar, in the northern arm and for the entire LMC. The three-dimensional selection areas for the bar and the arm are shown in Fig. 10. We do realize that fitting a simple plane is a great oversimplification, especially in the case of the bar, but the scope of this paper is a rough estimation of the global parameters for which a simple plane fitting is sufficient.

The best-fit parameters are listed in Table 6, where a, b and c are plane equation coefficients, i and P.A. are inclination and position angle respectively. There are separate sets of parameters for all LMC Cepheids, for all except the bar, for the bar, and for the northern arm. All fits have *rms* values of about 1.5 kpc, which is a result of the inaccuracy of distance determination.

Table 6

Best-fit parameters of the three-dimensional plane fitting procedure

LMC data	a	b	c [kpc]	N
All Cepheids	-0.395 ± 0.014	0.215 ± 0.013	-0.005 ± 0.021	4190
All except bar	-0.354 ± 0.016	0.237 ± 0.014	-0.013 ± 0.031	2458
Bar	-0.414 ± 0.039	-0.048 ± 0.095	-0.094 ± 0.045	1731
Northern arm	-0.378 ± 0.032	0.571 ± 0.082	-0.463 ± 0.170	756
LMC data	i	P.A.	χ^2/dof	<i>rms</i> [kpc]
All Cepheids	$24^\circ 2 \pm 0^\circ 7$	$151^\circ 4 \pm 1^\circ 7$	1.355	1.5
All except bar	$23^\circ 1 \pm 0^\circ 8$	$146^\circ 1 \pm 2^\circ 0$	1.323	1.5
Bar	$23^\circ 1 \pm 1^\circ 5$	$187^\circ 2 \pm 12^\circ 6$	1.376	1.5
Northern arm	$34^\circ 4 \pm 2^\circ 9$	$123^\circ 8 \pm 3^\circ 8$	1.163	1.2

The coefficients were calculated using the Markov chain Monte Carlo method.

In the case of all LMC Cepheids, we obtain $i = 24^\circ 2 \pm 0^\circ 7$ and P.A. = $151^\circ 4 \pm 1^\circ 7$ that correlate well with values from the literature (see comparison in Table 7). The parameter c , which is an offset of the fitted plane from the LMC center along z axis in kpc, is very small and consistent with the two centers being identical. Fig. 11 shows the z coordinate gradient and therefore the direction of LMC's tilt.

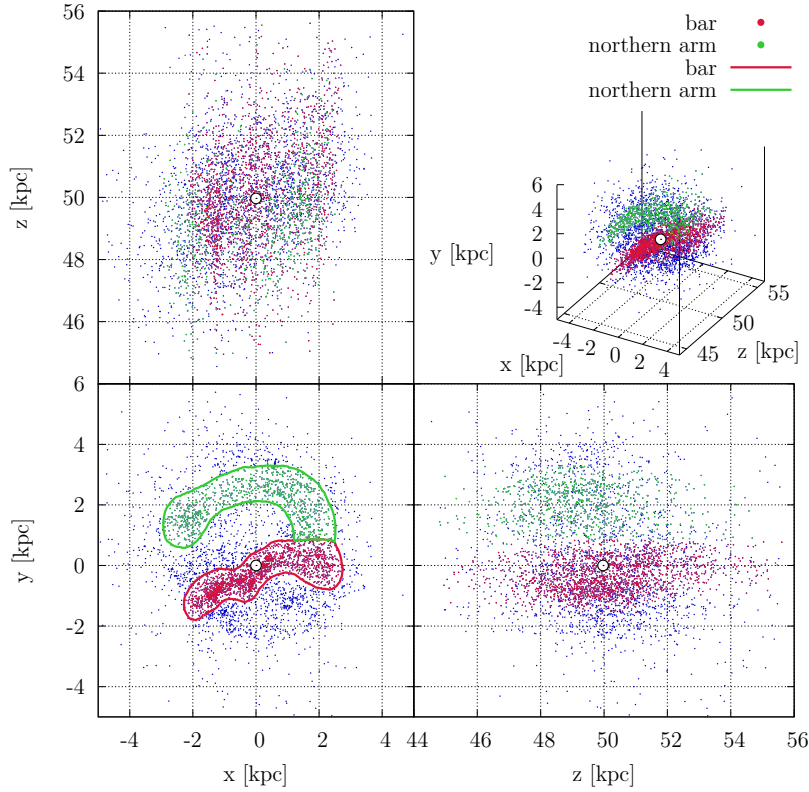


Fig. 10. Three-dimensional map of the CCs in the LMC in Cartesian coordinates with the z axis pointing toward the LMC center. Blue dots represent the entire LMC Cepheid population, red dots the bar and green dots northern arm. The xy plane shows the selection regions for the bar and for the northern arm for plane-fitting. White circle marks the LMC center (Pietrzyński *et al.* 2013, van der Marel and Kallivayalil 2014).

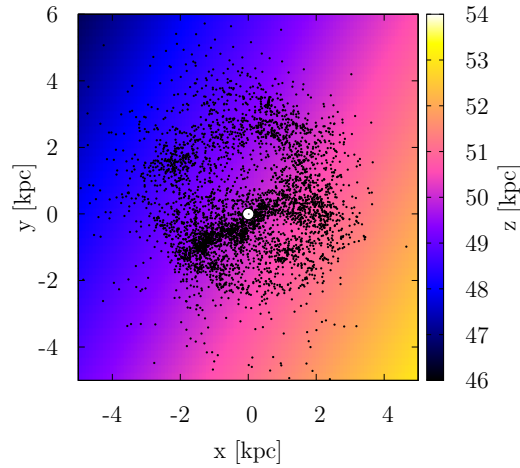


Fig. 11. Distance-gradient of the best-fit plane for the entire LMC (color-coded) in Cartesian xy coordinates with the z axis pointing toward the LMC center. Black dots show all LMC Cepheids. White circle marks the LMC center (van der Marel and Kallivayalil 2014).

The fit to all Cepheids except those in the bar gives identical values of i and P.A. (within 1σ errors for i and 2.26σ for P.A.), showing that the bar does not influence the fit. This is also consistent with the result from Subramanian and Subramaniam (2013) who analyzed the red clump stars in the LMC and found that the bar is a co-planar structure, although it may be offset from the plane by up to 0.5 kpc in the direction of the observer. This offset is not reflected in parameter c of our fit, which for the bar is -0.094 ± 0.045 kpc and this value is statistically insignificant within 3σ uncertainty. As discussed in previous sections, this is an effect of the bar selection criteria.

Table 7

LMC disk parameters from the literature

Cepheids and young population			
Reference	i	P.A.	Data
This work: all	$24^\circ 2 \pm 0^\circ 7$	$151^\circ 4 \pm 1^\circ 7$	OGLE-IV CCs
This work: bar only	$23^\circ 1 \pm 1^\circ 5$	$187^\circ 2 \pm 12^\circ 6$	OGLE-IV CCs
This work: arm only	$34^\circ 4 \pm 2^\circ 9$	$123^\circ 8 \pm 3^\circ 8$	OGLE-IV CCs
Caldwell and Coulson (1986)	$29^\circ \pm 7^\circ$	$142^\circ \pm 8^\circ$	Cepheids
Laney and Stobie (1986)	$45^\circ \pm 7^\circ$	$145^\circ \pm 17^\circ$	Cepheids
van der Marel and Cioni (2001)	$34^\circ 7 \pm 6^\circ 2$	$122^\circ 5 \pm 8^\circ 3$	AGB stars
Nikolaev <i>et al.</i> (2004)	$30^\circ 7 \pm 1^\circ 1$	$151^\circ 0 \pm 2^\circ 4$	Cepheids
Persson <i>et al.</i> (2004)	$27^\circ 0 \pm 6^\circ 0$	$127^\circ \pm 10^\circ$	Cepheids
Haschke <i>et al.</i> (2012a)	$32^\circ \pm 4^\circ$	$115^\circ \pm 15^\circ$	OGLE-III CCs
van der Marel and Kallivayalil (2014)	$26^\circ 2 \pm 5^\circ 9$	$154^\circ 5 \pm 2^\circ 1$	PM + young pop. LOS velocity
Other tracers			
Reference	i	P.A.	Data
Koerwer (2009)	$23^\circ 5 \pm 0^\circ 4$	$154^\circ 6 \pm 1^\circ 2$	Red clump
Subramanian and Subramaniam (2010)	$23^\circ 0 \pm 0^\circ 8$	$163^\circ 6 \pm 1^\circ 5$	OGLE-III RR Lyr
Subramanian and Subramaniam (2010)	$37^\circ 4 \pm 2^\circ 3$	$141^\circ 2 \pm 3^\circ 7$	MCPS data
Rubele <i>et al.</i> (2012)	$26^\circ 2 \pm 2^\circ 0$	$129^\circ 1 \pm 13^\circ 0$	VMC data
Haschke <i>et al.</i> (2012a)	$32^\circ \pm 4^\circ$	$116^\circ \pm 18^\circ$	OGLE-III RR Lyr
Subramanian and Subramaniam (2013)	$25^\circ 7 \pm 1^\circ 6$	$141^\circ 5 \pm 4^\circ 5$	Red clump outer disk ($r > 3^\circ$)
van der Marel and Kallivayalil (2014)	$39^\circ 6 \pm 4^\circ 5$	$147^\circ 4 \pm 10^\circ 0$	Proper motion (PM) data
van der Marel and Kallivayalil (2014)	$34^\circ 0 \pm 7^\circ 0$	$139^\circ 1 \pm 4^\circ 1$	PM + old pop. LOS velocity
Deb and Singh (2014)	$24^\circ 20$	$176^\circ 01$	OGLE-III RR Lyr (ellipsoid)
Deb and Singh (2014)	$36^\circ 43$	$149^\circ 08$	OGLE-III RR Lyr (plane)

The fit to the northern arm Cepheids reveals a different nature of this distribution. Both the inclination and position angle are inconsistent with the literature within 3σ errors. The angle between the best-fit planes for the LMC disk and the northern arm is about 40° . The c parameter indicates that the northern arm is

shifted by up to -0.463 ± 0.170 kpc (significant within 3σ errors) with respect to the LMC center and thus it is located closer to us. This is consistent with conclusions from previous sections.

Table 7 presents a comparison of our results with values from the literature. The inclination and position angle for the whole LMC sample are consistent with most of the results for young stars within the errors, although i is the lowest of all from Cepheid and young population studies. On the contrary, the P.A. is well correlated with higher values. Surprisingly, there is a significant difference between our results based on the OGLE-IV data, and results of Haschke *et al.* (2012a) who used the OGLE-III Cepheids. As was already mentioned, the OGLE-III collection of CCs did not contain most of the northern arm and the southern structures. This would indicate that the fit to the OGLE-III data should yield similar results as our bar-only sample. The case is totally opposite – our inclination angle for the bar only is much lower than that of Haschke *et al.* (2012a), while the P.A. is much higher. To check their i and P.A. values we selected a similar sample from our data. We picked the F-mode Cepheids located in OGLE-IV fields coinciding with OGLE-III fields. Our fitting procedure resulted in values very similar to those obtained for the entire LMC OGLE-IV Cepheid sample.

Results presented in this paper are also consistent with the parameter values for the intermediate-age and older stellar populations (the second part of Table 7).

5. The Small Magellanic Cloud

5.1. Three-Dimensional Structure

The three-dimensional structure of the SMC is shown in Fig. 2. The galaxy is elongated almost along the line of sight and its longitudinal dimension (along the z axis) is about 4–5 times greater than transverse dimensions in both x and y coordinates. This is perfectly consistent with the latest findings by Scowcroft *et al.* (2016). The SMC shape is best described as an extended ellipsoid with additional off-axis structures that are also ellipsoidal. Note that the Wing is not clearly visible in our data although in Figs. 2 and 3 we do see some Cepheids located in that area. On the other hand, CCs are distributed all around the SMC.

To show the change of shape of the SMC with increasing distance we have performed the distance tomography. Fig. 12 shows sections of this galaxy in different distance intervals. The closest part of the SMC ($d < 59$ kpc) has a round shape on the sky. The farther we look the less symmetrical it becomes. Moreover, the Cepheids seem to move away from the dynamical center of the SMC, marked with a white circle, to the south-western direction.

The second and the third map in the top row reveal an additional substructure located in the north, that fades at a distance of about 65 kpc. At a similar distance range another substructure appears in the south-west and is best visible on the second and the third map in the bottom row.

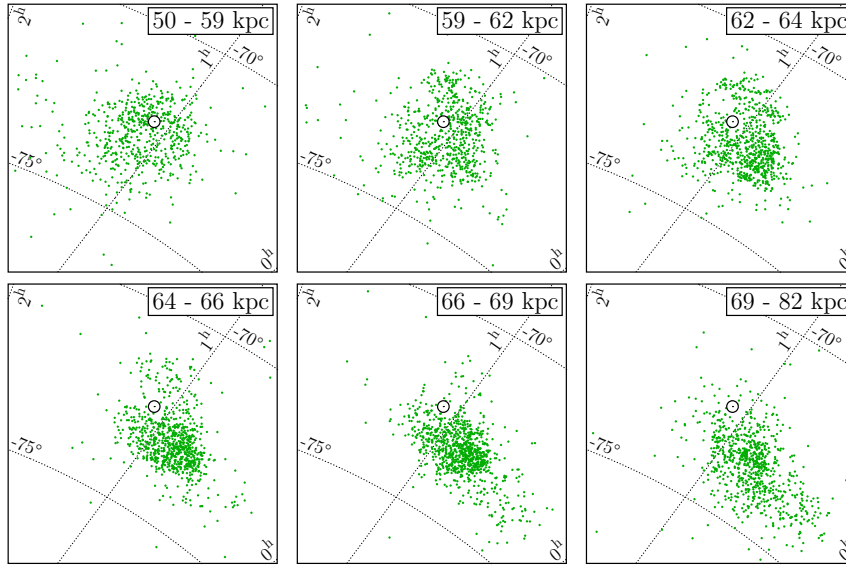


Fig. 12. Distance tomography of the SMC in the Hammer projection. Note that the distance intervals are, starting from the upper left, 9, 3, 2, 2, 3, 13 kpc. White circle marks the SMC center (Stanimirović *et al.* 2004).

To better visualize the SMC subtle structures we binned the data both in the Hammer projection and in the Cartesian space projections. The top map in Fig. 13 shows the on-sky projection of the binned data with stellar density contours overlaid. Interestingly, the higher density contours omit the dynamical SMC center. We can see that the SMC is actually heart-shaped with a curved tail in its south-western part. The top of the “heart” also suggests the existence of an additional substructure. This part and the tail in the south-west were not clearly visible in the OGLE-III Cepheid data (compare with Fig. 1 from Haschke *et al.* 2012b).

The bottom set of three maps in Fig. 13 shows Cepheid density in the Cartesian space (see figure caption for a full description). The bottom left map, in the xy plane, resembles the map with the Hammer projection although the contours are more smooth and the additional structures are not clearly visible. The projection on the xz plane does not show any evident substructures. The densest region of the SMC is located farther than the mean galaxy distance and falls between distances 62–70 kpc. The yz plane yields a more compelling evidence for the existence of the northern substructure, situated in the closer part of the SMC. Fig. 2 from Haschke *et al.* (2012b) shows that this substructure was not clearly visible in the OGLE-III Cepheid data, although it somewhat emerges in their Fig. 3.

5.2. Ages

We estimated ages of Cepheids in the SMC using the period–age relations from Bono *et al.* (2005) for a constant metallicity $Z = 0.004$. We again assumed that

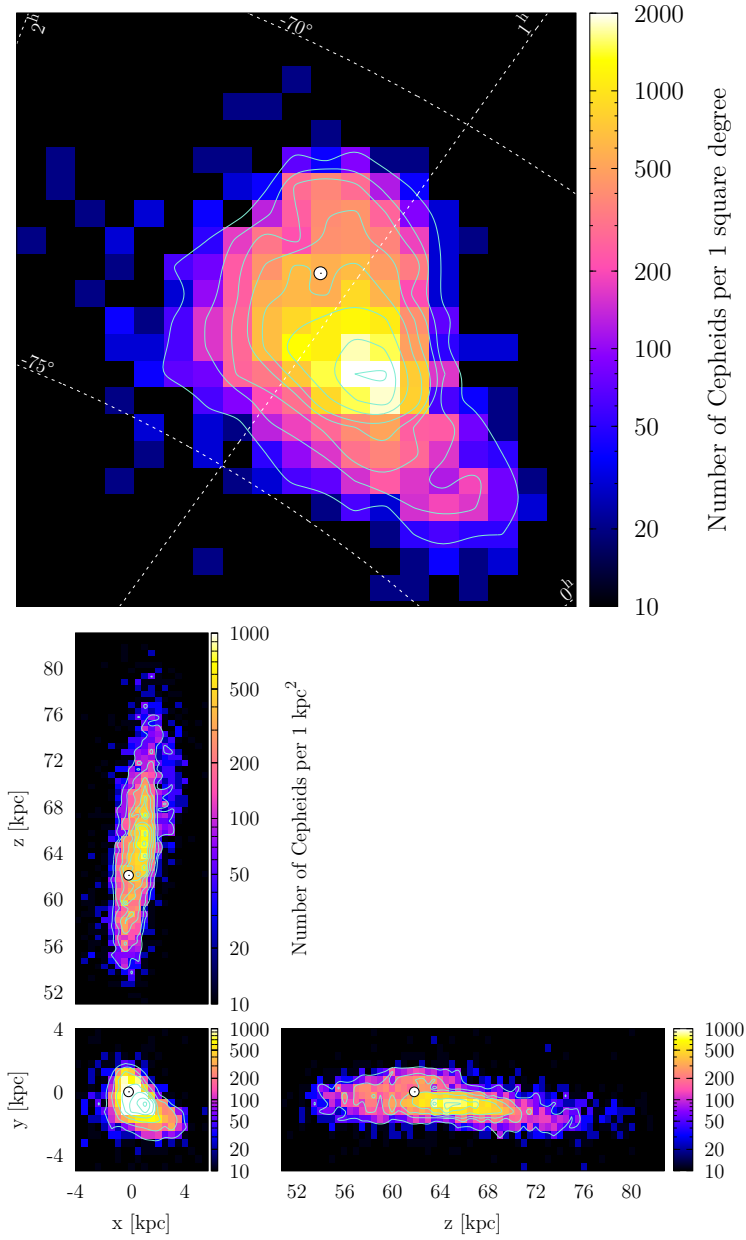


Fig. 13. Cepheid density in the SMC with Cepheid column density contours. *Top map*: Map in the Hammer projection. The bin size is 0.0001 in units of Hammer projection coordinates x_{Hammer} and y_{Hammer} in both directions. Contour levels are: 50, 150, 250, 400, 600, 1000, 1500, 2000 Cepheids per 1 square degree. *Bottom set of three maps*: Maps in the Cartesian coordinates projections with the z axis pointing toward the SMC center. The bin size is 0.5 kpc in x , y and z . Contour levels on the xy plane are 50, 200, 500, 1000, 1700, 2500, 3500, on the xz plane 50, 100, 200, 300, 400, 500, 650 and on the yz plane 50, 150, 250, 400, 600, 800 Cepheids per 1 kpc^2 . White circle marks the SMC center (Graczyk *et al.* 2014, Stanimirović *et al.* 2004).

there is no metallicity gradient in the SMC, which is supported by recent studies (Cioni 2009, Parisi *et al.* 2009, Deb and Singh 2014). However, some suggest that the SMC may have a low metallicity gradient (Carrera *et al.* 2008, Kapakos and Hatzidimitriou 2012, Dobbie 2014), and if this was the case, it may have somewhat influenced our age estimates. Romaniello *et al.* (2008) found a metallicity spread $\Delta[\text{Fe}/\text{H}] \approx 0.2$ dex for 12 Cepheids in this galaxy. This would translate to a metallicity range of $Z \in (0.003, 0.005)$. We made a rough estimate by interpolating PA relations from Bono *et al.* (2005) and found that such a spread in metallicity would introduce differences in age calculations at the level of up to $\sim 10\%$ for first-overtone, and up to $\approx 6\%$ for fundamental mode pulsators.

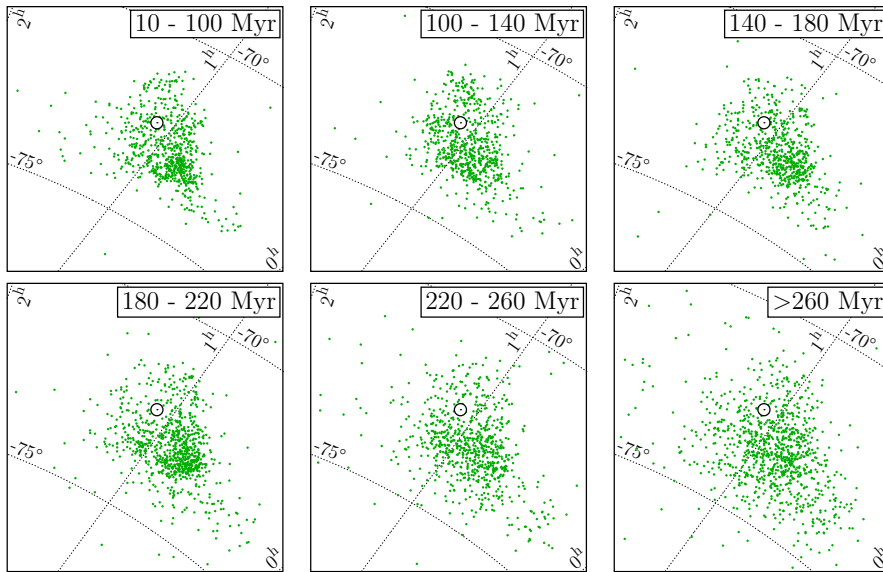


Fig. 14. Age tomography of the SMC using the relation from Bono *et al.* (2005) for a constant metallicity $Z = 0.004$. The maps are in the Hammer projection. Note that the *first panel* shows an interval of 90 Myr, *last* – 278 Myr, the *other ones* – 40 Myr. White circle marks the SMC center (Stanimirović *et al.* 2004).

In Fig. 14 we show the on-sky view of Cepheids in different age intervals. The age range is larger than in the LMC, which means that the SMC CCs population is older than that of the LMC. Young and intermediate age Cepheids form similar structures, although young stars are more concentrated in the north than older stars (second map in the top row). The older the Cepheids the more they concentrate in the south-western parts of the SMC (second map in the bottom row). The oldest stars in our sample are rather evenly spread and do not form any obvious structures. Our Cepheid age-tomography matches well with Fig. 13 from Rubele *et al.* (2015) where the star formation rates (SFRs) for the VMC data are shown. Recently formed stars have a “heart-like” structure while the older ones are more uniformly distributed.

The differences in the distribution of younger and older stars are even better visible in Fig. 15. The maps show Cartesian space projections and the transformation is rotated so that the z axis is pointing toward the SMC center. Cepheids are divided into two groups: younger than 150 Myr and older than 150 Myr. The former group is represented with red dots and the latter with blue dots. We clearly see that younger Cepheids are located mainly in the closer part of this galaxy while the older ones are distinctly farther.

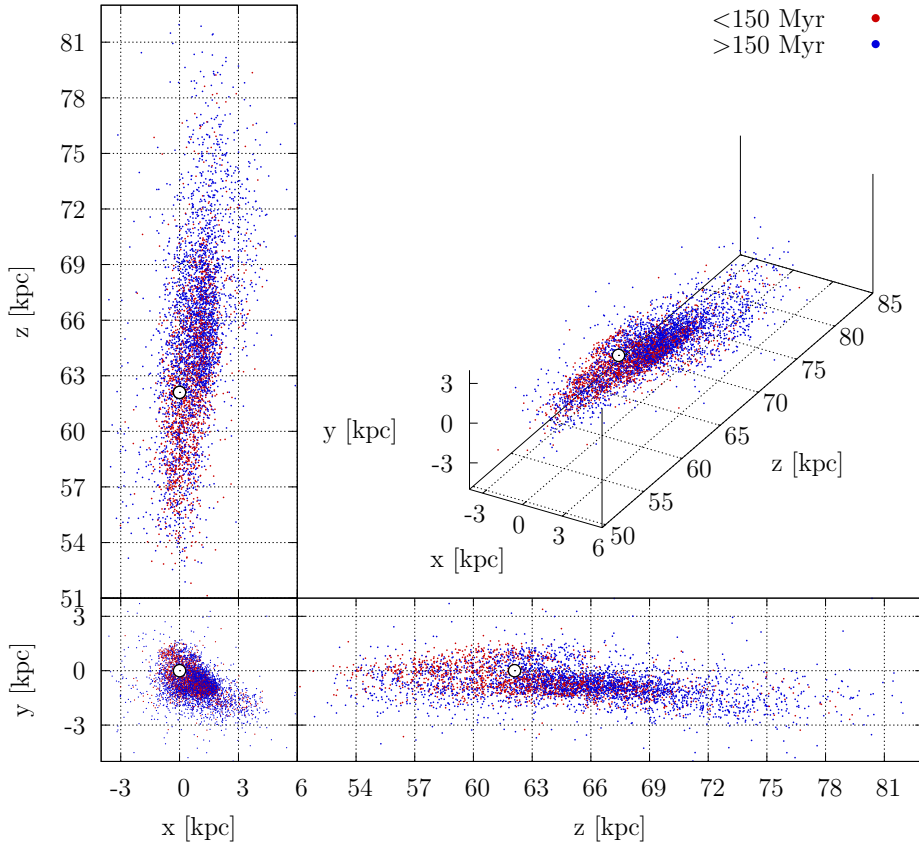


Fig. 15. Three-dimensional map of the CCs in the SMC in Cartesian coordinates with the z axis pointing toward the SMC center. Red dots represent Cepheids younger than 150 Myr and blue dots stand for Cepheids in the age interval of 150–300 Myr. White circle marks the SMC center (Graczyk *et al.* 2014, Stanimirović *et al.* 2004).

5.3. Substructures

In order to investigate the structure of the SMC in more detail we selected two subregions and named them south-western and northern region. The selected areas are shown in Fig. 16. The substructures are also visible in Fig. 12. The northern one is best visualized in the second and third top panels and also in the first bottom

panel. The south-western region emerges in the first bottom panel and is even more clear in the following panels. We see that the south-western region is located in the more distant half of the SMC while the northern region is in the closer part of this galaxy. The latter is consistent with Subramanian and Subramaniam (2012) who stated that the north-eastern part of the SMC is located closer to us, based on red clump and RR Lyr stars. Both substructures are distinct on the three-dimensional SMC maps as well as on the contour maps.

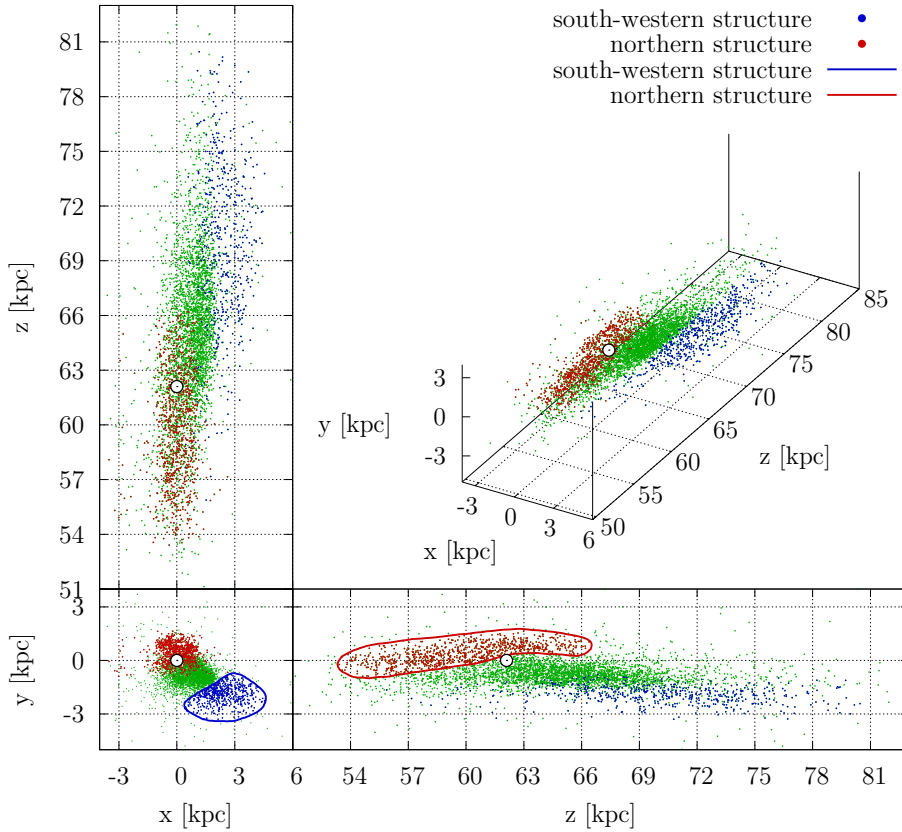


Fig. 16. Three-dimensional map of the CCs in the SMC in Cartesian coordinates with the z axis pointing toward the SMC center. The map shows selected areas for the south-western and northern regions marked with blue line and dots, and red line and dots, respectively. White circle marks the SMC center (Graczyk *et al.* 2014, Stanimirović *et al.* 2004).

Table 8 lists median distances and ages of the SMC and its substructures, together with standard deviations and sample numbers. Fig. 17 shows distance and age distributions for the whole SMC as compared with its two substructures (left panels) and with the LMC (right panels). We again see that the south-western structure is situated in the farther half of the SMC while the northern region is situated closer. The bottom left panel also reveals that the latter is younger than the for-

Table 8
Characteristics of the SMC substructures

Substructure	$\langle \text{dist} \rangle$ [kpc]	σ_{dist} [kpc]	$\langle \text{age} \rangle$ [Myr]	σ_{age} [Myr]	N
All Cepheids	64.62	4.95	193	89	4654
Northern Structure	59.90	3.00	152	84	868
South-Western Structure	70.18	4.44	233	88	525

Table lists median distance and age together with standard deviations, and a number of stars in each substructure.

mer and the KS test results (Table 9) reject the hypothesis of samples coming from the same distributions at significance level $\alpha = 0.001$. This is also consistent with our conclusions from Section 5.2, *i.e.*, that the SMC closest parts were formed later than its more distant areas.

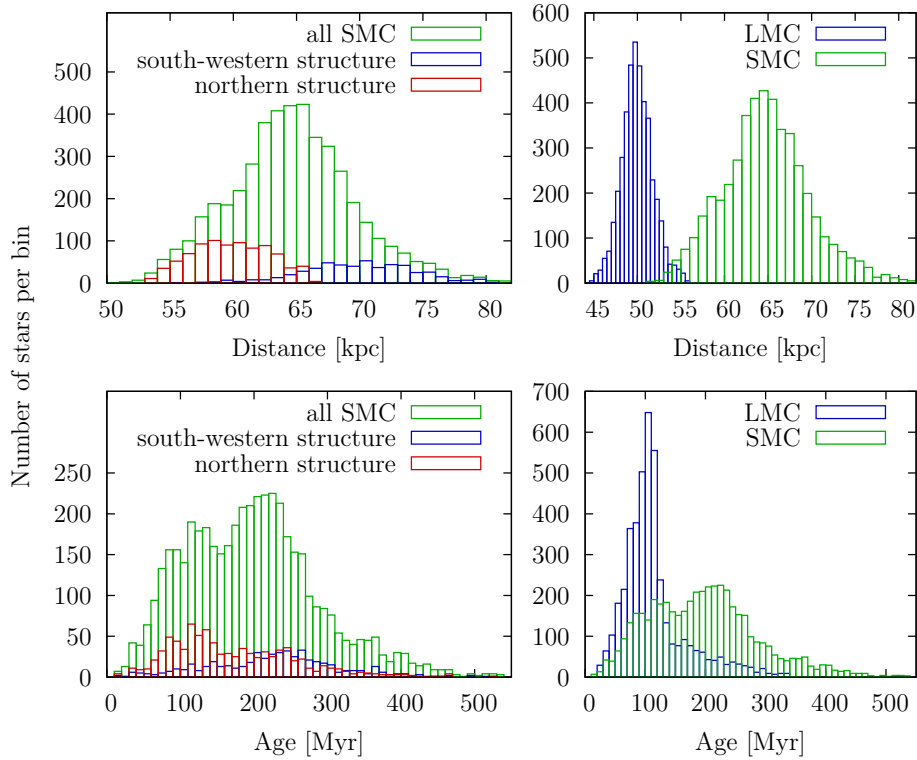


Fig. 17. Distance (*top row*) and age (*bottom row*) histograms for the SMC. *Left panel:* Histograms for the whole SMC Cepheid sample (green) and separately the two selected substructures: the south-western (blue) and northern (red) regions. *Right panel:* Comparison of the SMC (green) with the LMC (blue).

Table 9

Kolmogorov-Smirnov test results in the SMC

Sample 1	Sample 2	DISTANCE			AGE		
		D	p -value	α^*	D	p -value	α^*
all	northern	0.471	0.000	0.001	0.168	0.000	0.001
all	south-western	0.460	0.000	0.001	0.200	0.000	0.001
northern	south-western	0.839	0.000	0.001	0.334	0.000	0.001

* α is a significance level at which a null hypothesis that the two samples come from the same distribution can be rejected.

The right panels illustrate differences between the LMC and the SMC. The top panel shows that both galaxies have Gaussian-like distance distributions although the SMC has a bump on the left side of the maximum. The age histogram in the bottom panel shows that the LMC Cepheids are on average significantly younger than the SMC objects. The oldest LMC Cepheids are ≈ 390 Myr old, while the oldest SMC stars are ≈ 540 Myr old.

The SMC must have had two epochs of star formation. It is reflected in its bimodal Cepheid age distribution. The younger bump has its maximum close to the LMC peak ages (around 110 Myr) while the second bump is at the age of about 220 Myr. The two SMC peaks are separated by the local minimum at about 150 Myr. Fig. 15 shows differences in their spatial distribution, *i.e.*, the youngest Cepheids are closer to us than the older ones.

The two-peak nature of the age distribution in the SMC was also detected by Subramanian and Subramaniam (2015). Their Fig. 9 is very similar to ours in the context of the maxima, the peak separation and the age range. The spatial distribution of different-age Cepheids is consistent in both studies (see Fig. 10 from Subramanian and Subramaniam 2015 and Fig. 14 in this work), even though Subramanian and Subramaniam (2015) used the period–age–color relations from Bono *et al.* (2005) for dereddened data, while we used the simpler period–age relation.

On the other hand, there is only one episode of extensive Cepheid formation in the LMC, coincident with the younger SMC bump, followed by a slow decline toward older ages. This shows that Clouds had a different Cepheid formation history, possibly with a common episode. At the same time it does not mean that the Clouds had a different SFH, since we only concentrate on CCs in this paper. Moreover, because the SMC has lower metallicity than LMC, the Cepheids in the former galaxy may be more massive and thus older.

6. The Magellanic Bridge

From our initial sample of Cepheids in the Magellanic System we decided to classify nine as the Magellanic Bridge objects. Their parameters are listed in Ta-

ble 10. We provide Cepheids' ID from the OGLE Collection of Variable Stars along with the local ID that we use in this work (M1, ..., M9), pulsation period P , I - and V -band magnitudes, equatorial coordinates for epoch J2000.0, distance d and estimated age. The distance uncertainty does not include the mean LMC distance uncertainty (from Pietrzyński *et al.* 2013 $d_{\text{LMC}} = 49.97 \pm 0.19$ (statistical) ± 1.11 (systematic) kpc). The list contains four fundamental-mode Cepheids, four first-overtone pulsators and one double-mode oscillator (1O2O) for which we analyzed its lowest mode (1O).

Table 10
Magellanic Bridge Cepheids

P. mode	OCVS ID							
	Loc. ID	P [d]	I [mag]	V [mag]	RA	Dec	d [kpc] ^(a)	Age [Myr]
F	OGLE-SMC-CEP-4956 M1	1.1162345	17.372	17.930	3 ^h 23 ^m 24 ^s .90	-74°58'07".3	72.11 ± 2.01	283 ± 58
	OGLE-SMC-CEP-4957 M2	1.4300017	17.376	18.112	3 ^h 43 ^m 04 ^s .54	-76°56'02".6	74.61 ± 2.08	232 ± 48
	OGLE-LMC-CEP-3376 ^(*) M3	1.1589986	15.892	16.350	4 ^h 01 ^m 38 ^s .02	-69°28'40".5	40.13 ± 1.12	275 ± 56
	OGLE-SMC-CEP-4953 ^(*) ^(b) M4	21.3856946	12.967	13.821	2 ^h 20 ^m 49 ^s .46	-73°05'08".3	53.93 ± 1.50	27 ± 5
1O	OGLE-SMC-CEP-4955 ^(*) M5	2.0308924	15.675	16.281	2 ^h 42 ^m 28 ^s .88	-74°43'17".6	60.04 ± 1.65	120 ± 19
	OGLE-LMC-CEP-3377 ^(*) M6	3.2144344	14.629	15.291	4 ^h 04 ^m 28 ^s .88	-75°04'47".1	48.76 ± 1.34	73 ± 12
	OGLE-SMC-CEP-4952 M7	1.6414839	16.901	17.535	2 ^h 04 ^m 09 ^s .38	-77°04'38".4	89.51 ± 2.46	151 ± 24
	OGLE-SMC-CEP-4954 M8	0.8883941	17.156	17.512	2 ^h 21 ^m 28 ^s .45	-65°45'22".4	80.71 ± 2.22	291 ± 47
1O2O	OGLE-SMC-CEP-4951 ^(*) M9	0.7170500	16.769	17.222	2 ^h 02 ^m 33 ^s .88	-75°30'48".0	54.44 ± 1.50	366 ± 59

(*)These stars form a continuous-like connection between the Magellanic Clouds. ^(a) The distance uncertainty does not include the mean LMC distance uncertainty from Pietrzyński *et al.* (2013) $d_{\text{LMC}} = 49.97 \pm 0.19$ (statistical) ± 1.11 (systematic) kpc. ^(b) The OGLE-IV Collection of Classical Cepheids provides only the V -band magnitude for this object. The star is saturated on the standard OGLE-IV I -band reference image. Presented here I -band magnitude and more accurate period determination comes from dedicated re-reduction of the OGLE images.

Soszyński *et al.* (2015) classified five Cepheids as MBR objects. Our Bridge sample contains four more objects than their sample, which is not surprising, as our classification was based not only on the on-sky projected locations of the Cepheids (see Fig. 18), but also on their three-dimensional distribution (see Fig. 19). Even

so one can argue about the classification of M9 Cepheid. This object is close to the whole SMC sample and could be assigned to the SMC Wing. Nevertheless, we believe that this object is connecting the SMC Wing with the Bridge and may as well be classified as a Bridge Cepheid.

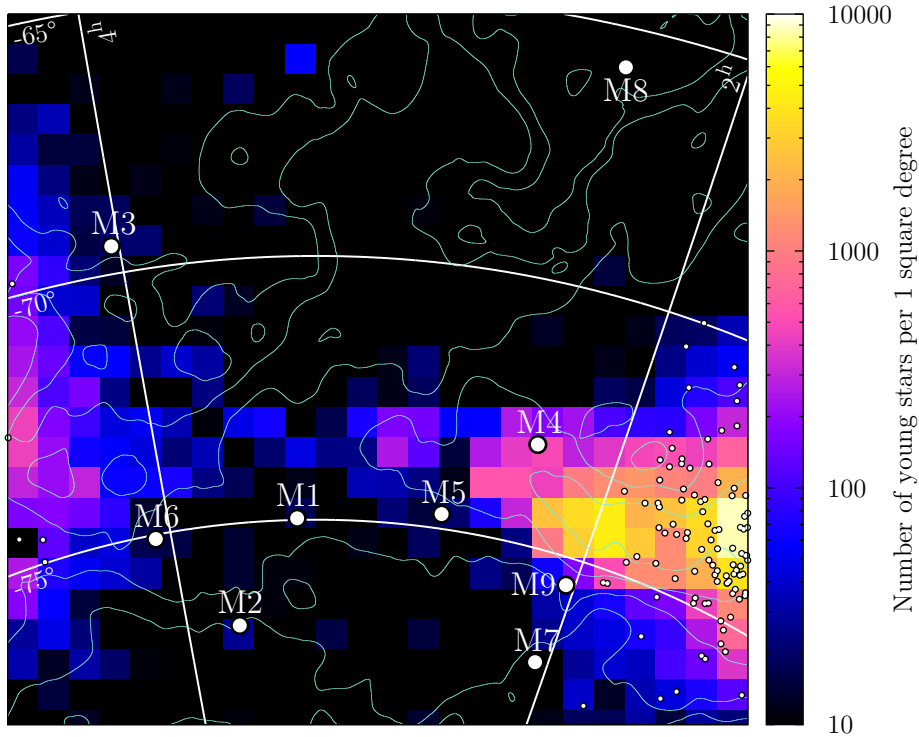


Fig. 18. CCs in the Magellanic Bridge area over the spatial density map of the Young Population stars from Skowron *et al.* (2014). Labels M1–M9 represent the Cepheids’ local IDs from Table 7. The map is represented in a Hammer equal-area projection centered at $\alpha_{\text{cen}} = 3^{\text{h}}18^{\text{m}}$, $\delta_{\text{cen}} = -70^{\circ}$. The color-coded value of each “pixel” is a logarithm of the number of stars per square degree area, while each “pixel” area is ≈ 0.335 square degrees. Light green contours mark neutral hydrogen (HI) emission integrated over the velocity range $80 < v < 400$ km/s, where each contour represents the HI column density twice as large as the neighboring contour. HI column densities are in the range $10^{20} - 4 \times 10^{21}$ cm^{-2} . Data were taken from the LAB survey of Galactic HI (Kalberla *et al.* 2005).

Fig. 18 shows the location of our Cepheids with respect to the HI density contours (Kalberla *et al.* 2005) and the young stellar population discovered by Skowron *et al.* (2014). Almost all Cepheids’ locations are well correlated with the HI contours and with the young stellar population space density distribution. Especially M4, which is also the youngest Cepheid in our MBR sample, is located in one of the densest young population regions from Skowron *et al.* (2014) near the SMC.

Skowron *et al.* (2014) showed that there exists a continuous connection between the two Magellanic Clouds built up of the young stars (age < 1 Gyr). The on-sky distribution of Bridge Cepheids also forms a continuous connection and adds to

the overall distribution of the young population. These are Cepheids named M6, M1, M5, M4, M9 (see Fig. 18). If we look at their three-dimensional distribution in Fig. 19, they fall along a line between the Clouds in the xy plane. The xz and yz planes show that M6, M5, M4 and M9 indeed form a connection between the Clouds. M3 may also contribute to this structure. On the other hand, M1 and M2 lie significantly farther. Moreover, they are located in the outskirts of the young population density contours from Skowron *et al.* (2014) which may indicate their different origin. Similarly, M7 and M8 are located even farther from both Clouds and also far from the young population density contours, thus they do not belong to the genuine Bridge population. These two Cepheids may contribute to the Counter Bridge predicted in numerical simulations (Diaz and Bekki 2012). We discuss this in details in Section 7.

The Cepheids in the Magellanic Bridge are very spread along the line of sight. The closest star (M3) is located at $d \approx 40$ kpc thus it is closer to us than any LMC Cepheid. The farthest (M7) is at almost 90 kpc and this is farther than any SMC Cepheid. This again shows that not all MBR Cepheids form a continuous connection between the Clouds, and rises a question about their origin and how they got to their current location. On the other hand, we do observe stars located far from the LMC and SMC all around these galaxies (*i.e.*, see the LMC Cepheid at $\alpha \approx 5^{\text{h}}30^{\text{m}}$, $\delta \approx -56^\circ$ or SMC Cepheid at $\alpha \approx 23^{\text{h}}30^{\text{m}}$, $\delta \approx -68^\circ$ in Fig. 3). These objects were probably ejected from the galaxies in random directions. Some of our MBR Cepheids may belong to the outliers population.

The ages of Bridge Cepheids were again calculated using the period–age relation from Bono *et al.* (2005). There are different relations for different metallicities. In the case of the Bridge the gas metallicity is about $Z_{\text{MBR}} \approx 0.1 Z_{\odot}$ (Lehner *et al.* 2008) or slightly higher ($-0.5 < \log(Z_{\text{MBR}}/Z_{\odot}) < -1$ from Misawa *et al.* 2009, although this was measured along the line of sight in an area that is possibly not mixed with metal-poor gas, as it is in other regions of the Bridge). Moreover, the 0.1 solar metallicity in the MBR is consistent with the Magellanic Stream metallicity (Fox *et al.* 2013). Thus we can assume $Z_{\text{MBR}} = 0.002$ for the Bridge Cepheids (if we first assume that they were formed *in-situ*). Note that Bono *et al.* (2005) do not provide the period–age relation for this metallicity – the lowest value is $Z = 0.004$ (typical for the SMC). We therefore use this relation for the MBR Cepheids, keeping in mind that it is just a rough estimate.

The youngest Cepheid is M4 and its age estimate is 27 Myr. Its location is well correlated with the young population density contours from Skowron *et al.* (2014). This star was probably formed together with other young stars in the Bridge. Another young Cepheid is M6 and its age estimate is 74 Myr. This star is located at a distance close to the mean LMC distance and is ≈ 7.1 kpc from the center of the LMC, which is much farther than any other LMC Cepheid. The oldest Cepheid is M9 and it is ≈ 370 Myr old. This star is located fairly close to the SMC Wing and may be classified as the Wing object. Two Cepheids are aged between 100–

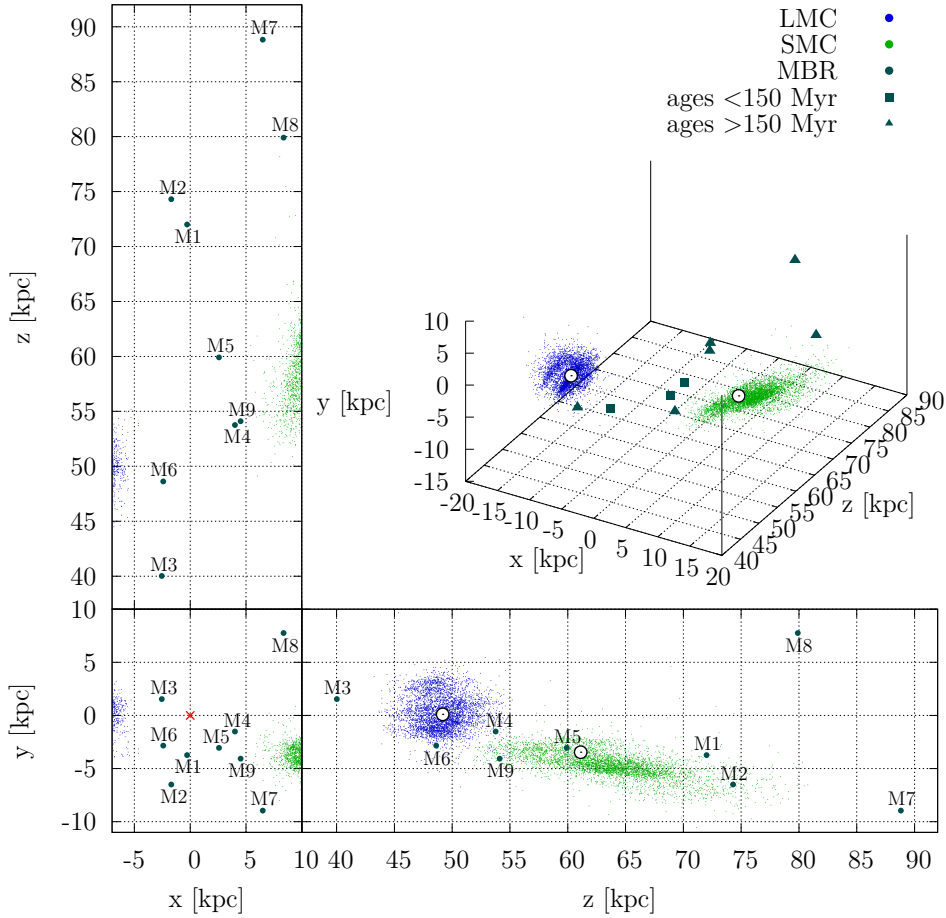


Fig. 19. Three-dimensional map of CCs in the Magellanic Bridge in Cartesian coordinates with the z axis pointing toward $\alpha_{\text{cen}} = 3^{\text{h}}20^{\text{m}}$, $\delta_{\text{cen}} = -72^{\circ}$. Blue dots represent the LMC, green dots SMC and the large dark teal dots – the MBR. Labels M1–M9 represent the Cepheids’ local IDs from Table 7. Red cross stands for the observer’s location. White circle marks the LMC (Pietrzyński *et al.* 2013, van der Marel and Kallivayalil 2014) and SMC (Graczyk *et al.* 2014, Stanimirović *et al.* 2004) centers.

200 Myr. One of them is the farthest one – M7, which is about 150 Myr old. The other four Cepheids are in the ages range 200–300 Myr. One of them is the closest object, the other three are located at distances 72–81 kpc.

7. Discussion

7.1. Three-Dimensional Structure and Substructures: the LMC

The LMC has a bar that is thought to be offset from the center of this galaxy by about 0.5 kpc. First suggestions that the bar may not be aligned with the disk plane were based on the microlensing events (Zhao and Evans 2000). The offset of

about 0.5 kpc was measured and used in many studies (*e.g.*, Nikolaev *et al.* 2004, Subramanian and Subramanian 2013, van der Marel and Kallivayalil 2014). The offset had also been predicted by numerical models, *e.g.*, Bekki (2009) concludes that it is not the bar that is offset but the entire disk population. Besla *et al.* (2012) had reproduced not only the off-center bar but also the spiral structure of the LMC with one arm.

In this work we redefine the idea of the LMC bar. By examining the distance and age distributions of the central parts of the LMC we argue that the bar comprises of not only the central-eastern region considered to be the “classical” bar, but also of the western region, as shown in Fig. 7. In the distance and age regime both parts are continuously connected, making the homogeneous, though asymmetrical, structure. The redefinition of the bar moves the dynamical center of the LMC to the center of the bar.

The mean distance of the redefined bar is close to the mean LMC distance and we do not observe any significant offset. That is not consistent with the value of 0.5 kpc from the literature, and the reason may be a different definition of the bar region (see Fig. 14 in Nikolaev *et al.* 2004, Fig. 2 in Subramanian and Subramanian 2009 and Figs. 1 and 7 in Haschke *et al.* 2012a – bar areas are consistent with our eastern part of the bar from Fig. 7). However, if we use the “classical” LMC bar, we still do not see a significant offset from the galaxy center (the “classical” bar is located closer to us by only ≈ 0.07 kpc), contrary to the cited studies.

We fitted a plane to the entire Cepheid population in the LMC as well as to its substructures. The whole LMC sample shows no offset along the line of sight as compared to the mean LMC distance from Pietrzyński *et al.* (2013) and that is expected from a correct fitting procedure. The obtained inclination and position angles are consistent with values from the literature (see Table 7). The *rms* of our fit is about 1.5 kpc, which is partly a “natural spread” of the method described in Section 3, and partly a contribution of the extra-planar features of the LMC. Nikolaev *et al.* (2004) found that the disk is warped, with a distortion amplitude $\gtrsim 0.3$ kpc. This warp explains high χ^2/dof values for planar disk in our fits. On the other hand, Subramanian and Subramanian (2013) found that the disk can be divided into two differently inclined parts – the inner and the outer – separated at the radial distance from the LMC center of 3° . The inner disk would be more warped than the outer. They also concluded that the bar is offset but is still a co-planar feature. They classified structures as extra-planar if their deviation is > 1.5 kpc. Olsen and Salyk (2002) had previously identified warps in the disk in similar locations. The detailed modeling of the extraplanar features of the LMC disk is beyond the scope of this paper.

We also fitted a plane to Cepheids in the redefined bar and found a small offset of about -0.09 kpc from the mean LMC distance which is statistically insignificant within 3σ uncertainty. We are aware that fitting a plane to the bar is not the best approach because of the nonplanar nature of this structure. Nikolaev *et al.*

(2004) suggest caution when deriving parameters such as viewing angles for the inner LMC structures. Also Subramanian and Subramaniam (2013) stated that the structure of the bar is not smooth and some of its parts are located closer to us than other.

Interestingly, when fitting a plane to the northern arm sample we found an offset of about -0.48 kpc. This means that the arm is located closer to us than the whole LMC. Moreover, the arm lies in a different plane (has different inclination and position angle) than the whole LMC sample and this result is statistically significant.

The OGLE-IV CCs data set clearly shows the bar and the main northern arm of the LMC. We also tried to localize less prominent structures in other parts of this galaxy. In the north we identified an additional small spiral arm (NA2, see Section 4.3). This finding is consistent with the latest results from Besla *et al.* (2016) who analyzed deep optical images of the LMC and identified multiple spiral arms. Both structures are at precisely the same location – compare our northern arm 2 in Fig. 7 with multiple spiral arms in Fig. 3 from Besla *et al.* (2016). The structures that we see in the southern part of the LMC are not as prominent and do not form a spiral arm, which is also consistent with conclusions from Besla *et al.* (2016). However, it does not exclude the possibility that there exists a sparse spiral arm connected with the south-eastern part of the bar which is not clearly visible in the CCs distribution.

We compare our results to those obtained by Haschke *et al.* (2012a) from the OGLE-III Cepheid data. What is striking – the distances they derived are substantially larger than ours. Cepheid distances fall in the range of 44–56 kpc in this work, and 45–60 kpc in the work of Haschke *et al.* (2012a). This discrepancy is also reflected in their mean LMC distance of 53.9 ± 1.8 kpc which is not consistent with the literature (as highlighted by de Grijs *et al.* 2014). The method of determining distances was similar in both studies, but we used a reddening-free Wesenheit index and determined distances relative to the most accurate LMC distance measurement (Pietrzyński *et al.* 2013), while Haschke *et al.* (2012a) calculated absolute distances based on the *I*- and *V*-band magnitudes corrected for extinction. Thus the problem could lie in the dereddening method or the reddening maps used, as also suggested by de Grijs *et al.* (2014).

It is also worth noting that the OGLE-III collection of Cepheids in the LMC used by Haschke *et al.* (2012a) did not include the northern arm and some of the southern parts of this galaxy. For comparison see the lower-right panel in Fig. 12 of Moretti *et al.* (2014) where they compare the OGLE-III CCs with the EROS-2 data. Nevertheless, the results that did not include the northern arm should also be consistent with ours, since the northern arm is closer to us than the rest of the galaxy, while the southern parts are at approximately the same distance.

7.2. Three-Dimensional Structure and Substructures: the SMC

We find that the SMC is extremely elongated almost along the line of sight. Its size along the z Cartesian axis is about 4–5 times larger than along the x and y axes. This is consistent with the latest structural analysis of the SMC performed by Scowcroft *et al.* (2016), based on mid-infrared Spitzer data for 92 Cepheids. The comparison of Fig. 6 in Scowcroft *et al.* (2016) with our Fig. 15 or 16 shows a similar spread along each of the axes, although the substructures are only visible in the OGLE-IV data, as the sample is about 50 times more numerous.

We agree with Scowcroft *et al.* (2016) that the standard parameters such as the inclination and position angle are not adequate for describing a galaxy with such an elongated shape, even though such parameters were determined in many studies (*e.g.*, Stanimirović *et al.* 2004, Subramanian and Subramanian 2012, Haschke *et al.* 2012b, Subramanian and Subramanian 2015). Scowcroft *et al.* (2016) claim that the shape of the SMC can be best characterized as a cylinder. We would rather describe it as a tri-axial elongated ellipsoid, although the existence of the “off-axis” structures makes it even more complicated and separate fits for the main body and the substructures might be necessary (see Fig. 16).

We would expect our results to be coherent with those of Haschke *et al.* (2012b), based on the OGLE-III CCs catalog, as the number of Cepheids is similar and the main body of the SMC is clearly visible in both data sets (Fig. 1 in Haschke *et al.* 2012b and Fig. 13 in this work). Any differences in conclusions would be a result of different methods of distance determinations, as noted in Section 7.1. They obtained the median distance to the SMC for the Cepheid sample of 63.1 ± 3.1 kpc which is consistent with the literature (de Grijs and Bono 2015) and with the median SMC distance of 64.6 ± 4.9 kpc derived from our sample.

However, the bottom map in Fig. 3 of Haschke *et al.* (2012b) suggests that the SMC is not very elongated along the line of sight and rather has a disk-like structure, although the spread in distances of about 30 kpc is consistent with our results, so it is only an effect of the chosen projection. The difference is in the distance range, which is about 50 kpc to 80 kpc in this study, and 45 kpc to 75 kpc in Fig. 5 of Haschke *et al.* (2012b).

We also compare our results with those of Subramanian and Subramanian (2015), who analyzed Cepheids from the OGLE-III catalog. Their Fig. 7 shows similar SMC geometry as our Fig. 15, although one has to keep in mind that the x and y are swapped with respect to our plots, and the resolution is different for each of their axes, which gives a false impression about the shape of this galaxy. Fig. 6 of Subramanian and Subramanian (2015) shows the fitted plane along the axis of the steepest gradient and the z axis. Note that here the scale of the z axis is 10 times smaller than the scale of the axis of the steepest gradient, thus rising a question about the relevance of such fit. The gradient they observe is rather an effect of the northern substructure being closer to us (see Fig. 16 in this paper), than the SMC having an inclined plane in the xy projection.

Subramanian and Subramaniam (2015) also detected some extra-planar features in their sample, under the assumption that there is an actual SMC plane. We do not support this scenario, as we show that there is no SMC plane as such, and the galaxy can be described as a tri-axial ellipsoid, elongated along the z axis. In this case, the reported extra-planar features would simply be parts of the main body of the SMC or one of the substructures shown in Fig. 16.

7.3. LMC-SMC Interactions and the Magellanic Bridge

The OGLE-IV Cepheid data show that the Magellanic Clouds are rotated toward each other (see Fig. 2). In fact, the closest SMC Cepheids are at similar distances as the farthest LMC objects in our sample. Moreover, the Clouds' closest on-sky locations are also the closest in the sense of distances and three-dimensional distribution. That is perfectly consistent with Scowcroft *et al.* (2016).

The collision model by Besla *et al.* (2012) predicts that the Clouds had a close interaction about 200–300 Myr ago (see Gardiner *et al.* 1994, Gardiner and Noguchi 1996, Růžička *et al.* 2010, Diaz and Bekki 2012). Both galaxies should have trails due to such interaction. It is also possible that the co-rotation of the Magellanic Clouds has the same origin (Scowcroft *et al.* 2016). Fig. 10 in Scowcroft *et al.* (2016) shows the predicted SMC spheroid distribution (a model by Diaz and Bekki 2012) along with the analyzed Cepheids. We compare it to our xz projection in Fig. 16 where the z axis is along the distance and the x axis – along the right ascension (for this comparison see Fig. 6 in Scowcroft *et al.* 2016). We see that our Cepheids extend even farther but still along the gradient predicted by the model.

A model by Besla *et al.* (2012) predicts that there should exist a stellar counterpart to the gaseous Magellanic Bridge, in the area between the Clouds. It should mainly consist of a young population of stars formed *in-situ*. Such young stars were already observed in the MBR (Irwin *et al.* 1985, Demers and Battinelli 1998, Harris 2007, Noël *et al.* 2013, 2015, Skowron *et al.* 2014), as well as intermediate-age stars (Noël *et al.* 2013, 2015) and older population candidates (Bagheri *et al.* 2013). Moreover, Skowron *et al.* (2014) showed that there is a continuous connection between the two Clouds made of young stars (ages < 1 Gyr). According to Besla *et al.* (2012), the stars in the Bridge should follow the Clouds past trajectories.

In Fig. 18 we compared the OGLE-IV Cepheid locations in the Bridge with the young stellar stream from Skowron *et al.* (2014). The on-sky locations are well correlated – most of the Bridge Cepheids are situated within the contours of young population column densities. However, Fig. 19 shows that only five of nine stars from our sample form a coherent structure in three-dimensions. This raises questions about origin of the other four Cepheids and makes an important constraint for numerical models of the Magellanic Clouds interactions. On the other hand, these Cepheids may be the LMC or SMC outliers ejected from these galaxies in random directions that we now observe in the Bridge area.

Moreover, ages of our Bridge Cepheids are compatible with the assumption that the Bridge was created during the last interaction of the Clouds (*e.g.*, Gardiner *et al.* 1994, Gardiner and Noguchi 1996, Růžička *et al.* 2010, Diaz and Bekki 2012, Besla *et al.* 2012). Models predict that this interaction happened 200–300 Myr ago and most of our Cepheids are younger than that. This indicates that they were formed outside of the Clouds – in the Bridge.

Diaz and Bekki (2012) model predicts not only the existence of the Magellanic Bridge but also another structure, that they named the Counter Bridge. It is a tidal feature of the same origin as the “classical” Bridge. The model reveals it as a dense and clearly defined stream that extends away from the SMC up to the distances of about 85 kpc. Authors conclude that the location of the Counter Bridge may cause higher levels of optical depth in the SMC and especially in its north-eastern parts. Because of the significant SMC elongation along the line of sight, the farthest stars belonging to the SMC population may be mixed with the unbound stars that should be properly classified as Counter Bridge objects.

Nidever *et al.* (2013) discovered a distance bimodality in the eastern SMC using red clump stars, but mean distances of both components were too low to be a stellar counterpart of the Counter Bridge, although the authors argue, that the closer structure located in front of the main SMC body forms a connection between the Magellanic Bridge and the SMC.

Subramanian and Subramaniam (2015) claim to have detected the stellar counterpart of the Counter Bridge. They have classified it based on the fitted plane and the extra-planar structures that they discovered in front of as well as behind the plane (see Figs. 7 and 14 in Subramanian and Subramaniam 2015). As we previously argued, the plane fitting in the case of the SMC is illegitimate, making the claims about the stellar part of the Counter Bridge an overstatement.

However, if the Counter Bridge was visible in the OGLE-III data set (analyzed by Subramanian and Subramaniam 2015) it should also be detectable in our sample. Fig. 2 shows all the fundamental-mode and first-overtone CCs from the OGLE Collection of Variable Stars, many of which are much farther (or closer) than the mean SMC distance, and these are marked with gray dots. These stars were classified as outliers from the P-L relation and removed from our sample in further analysis. While most of them are blends, we cannot rule out the possibility that some of these stars may be candidates for the Counter Bridge population (distances > 80 kpc), especially that two genuine Bridge Cepheids are located near or farther than 80 kpc.

Diaz and Bekki (2012) concluded that the Counter Bridge stars may mix with the SMC population. If this is the case, then it is possible that we observe the Counter Bridge as a stellar structure but we are unable to separate it from the SMC sample.

7.4. Ages

Indu and Subramaniam (2011) suggested that the LMC perigalactic passage about 200 Myr ago pulled out the HI to the north of this galaxy. Because of the LMC's motion through the Galaxy halo the star-forming processes began. One of the SFR peaks that they detected is at about 90–100 Myr, which coincides with the age peak for the LMC Cepheids in our sample at 104 Myr. Harris and Zaritsky (2009) also detected a peak in the age distribution in the LMC around 100 Myr, although there are different maxima in different parts of this galaxy – the SFH of the LMC is not uniform. The peak at about 100 Myr is observed mainly in the bar, and this is consistent with our results, as most of the Cepheids are located in the bar. On the other hand, Joshi and Joshi (2014) detected an intensified SF episode about 125–250 Myr ago, which is slightly older than 100 Myr found in this analysis, but is still consistent within errors. The difference is most probably due to different PA relations used.

The bottom right panel of Fig. 17 also shows that the younger age peak of the SMC at about 120 Myr correlates with the LMC peak, which suggests a common SF episode. This result is consistent with Inno *et al.* (2015) who discovered that the Clouds had an active SFH during the last 400 Myr and that there are age distribution similarities between the two galaxies. Another common SF maxima in the Clouds were already seen at 500 Myr and 2 Gyr (Harris and Zaritsky 2009).

In the case of the the SMC, Indu and Subramaniam (2011) detected the shift in the center of the population of stars younger than 500 Myr in the north-east direction. That is the direction toward the LMC. We also noticed that younger stars from our sample tend to clump in the north. The authors also showed that the rate of this shift changed at 200 Myr and was faster from that time on suggesting this may be caused by the perigalactic passage of the Clouds and the Galaxy's gravitational attraction. This coincides with the second age maximum in the SMC at about 220 Myr.

The age distributions of Cepheids in the OGLE-III data analyzed by Subramanian and Subramaniam (2015) and in our OGLE-IV sample are consistent. We observe a very similar age distribution with two peaks and the age tomographies are also alike (see Fig. 14 and Fig. 10 in Subramanian and Subramaniam 2015). The analysis of SMC CCs by Joshi *et al.* (2016) showed a SF peak at 250 ± 50 Myr which is consistent with our older Cepheid SF peak in this galaxy. They have also detected a second peak at about 160 Myr in the eastern part of the SMC which is consistent with our conclusion from Fig. 15, that the eastern part of this galaxy is younger.

8. Conclusions

In this work we analyzed a total sample of 9418 fundamental-mode and first-overtone CCs in the Magellanic System from the OGLE Collection of Classical

Cepheids based on the OGLE-IV data (Udalski *et al.* 2015, Soszyński *et al.* 2015). We fitted the P-L relations to the data using the Wesenheit index for the *I*- and *V*-band photometry. Fundamental-mode Cepheids with $\log P \leq 0.4$ were treated separately. The best fits for the Wesenheit, the *I*- and *V*-band magnitudes are presented, for both the LMC and SMC.

We calculated relative distances to each Cepheid using the reddening-free Wesenheit index and the most accurate measurement of the mean LMC distance from Pietrzyński *et al.* (2013) as a reference. The results are presented on three-dimensional maps in the Hammer equal-area projection and in the Cartesian space.

The Cepheids in the LMC are present mainly in the bar and the northern arm. Both structures, as well as the whole galaxy, are inclined such that the eastern parts are closer to us. We fitted a plane to the LMC sample and obtained the inclination and position angles of $i = 24.2 \pm 0.6$ and P.A. = 151.4 ± 1.5 that are consistent with the literature. The *rms* of our sample is 1.5 kpc and it reflects the significant scatter of the sample along the line of sight.

The age distribution of the LMC Cepheids reveals one peak at about 100 Myr. Younger Cepheids tend to be clumped in the bar and the northern arm, while older stars are spread all over the LMC disk. The northern arm seems to be younger than the bar that has a similar age distribution as the whole galaxy.

We redefined the LMC bar such that it spans almost the whole width of the LMC. Both the classical bar (the central and eastern part of our bar) and the newly added western part form one coherent structure that is clearly visible in Cepheid density contours. Although the western part of the bar is less numerous the two parts are connected both in their distance and age on-sky distributions. Moreover, after the redefinition of the bar the dynamical center of the LMC is now located in the center of the bar.

We separately fitted a plane to the bar Cepheids, despite the fact that this may not be a proper physical model of the bar, although should yield a reasonable offset. The offset for the new bar is consistent with that for the whole galaxy which means that the bar is not located closer to us than the galaxy. On the other hand the distance distributions show that the “classical” bar that we call the eastern bar also is not offset from the LMC plane, contrary to previous studies.

The LMC northern spiral arm is a very prominent feature in the Cepheid distribution. We fitted a plane to the northern arm and found that this structure is offset from the whole LMC sample by about 0.5 kpc toward us, and lies in a different plane described by $i = 34.4 \pm 2.9$ and P.A. = 123.8 ± 3.8 .

Our data does not reveal any other spiral arms in the central or southern parts of this galaxy although we do see an additional spiral arm in the north. We suppose that there may be another arm connected with the bar on its south-eastern side, but there are too few Cepheids in that region to provide strong evidence.

The unusual elongation of the SMC is confirmed in this study. The SMC is elongated almost along the line of sight and its longitudinal dimension is 4–5 times

greater than the transverse dimension. The north-eastern part of the SMC is located closer to us than its south-western part. Note that both Clouds are inclined toward each other.

The age distribution of the SMC Cepheids reveals two peaks, one at about 100 Myr, which is very similar to the LMC peak, suggesting a common star formation episode, that could be due to LMC-SMC interaction, and another one at about 220 Myr. Moreover, younger and older Cepheids are differently distributed, supporting this hypothesis – the former group is located in the closer part of this galaxy, while the latter – in the farther.

The SMC shape may be described as an extended ellipsoid with two additional prominent off-axis structures that are also ellipsoidal. One is located in the north of the SMC and is closer than the SMC main body and significantly younger than the other one, which is located in the south-western part of the SMC and hence farther.

The Wing of the SMC is not reflected in the Cepheid distribution, although there are stars spread all over the galaxy and some of them in the eastern part belonging to the Wing. Moreover, we see Cepheids at very large distances (≈ 80 kpc), that may be a stellar counterpart to the Counter Bridge that is mixed with the SMC population.

The on-sky locations of most of the nine Magellanic Bridge Cepheids are correlated with the young stellar population density contours. Moreover, they seem to form a connection between the LMC and SMC. On the other hand, the three-dimensional distribution of the Bridge CCs reveals that four of the nine objects are located far from this connection, at very diverse distances – the closest one being closer to us than any of the LMC objects, and the farthest one farther than any SMC Cepheid. This is an important constraint for models of the Magellanic Clouds interactions.

All Bridge Cepheids except one have ages < 300 Myr which is consistent with the time of MBR formation and indicates that these stars were born *in-situ*. The oldest MBR Cepheid may be connected with the SMC Wing because of its nearby location.

Acknowledgements. We would like to thank Profs. M. Kubiak and G. Pietrzyński, former members of the OGLE team, for their contribution to the collection of the OGLE photometric data over the past years. We thank the anonymous referee for comments and suggestions that greatly improved this publication. A.M.J.-D. is supported by the Polish Ministry of Science and Higher Education under “Diamond Grant” No. 0148/DIA/2014/43. D.M.S. is supported by the Polish National Science Center under the grant no. 2013/11/D/ST9/03445. I.S. is supported by the Polish Ministry of Science and Higher Education through the program “Ideas Plus” award No. IdP2012 000162. The OGLE project has received funding from the National Science Center, Poland, grant MAESTRO 2014/14/A/ST9/00121 to AU.

REFERENCES

- Bagheri, G., Cioni, M.-R.L., and Napiwotzki, R. 2013, *A&A*, **551**, A78.
- Barger, K.A., Haffner, L.M., and Bland-Hawthorn, J. 2013, *ApJ*, **771**, 132.
- Bauer, F., *et al.* (EROS collaboration) 1999, *A&A*, **348**, 175.
- Bekki, K. 2009, *MNRAS*, **393**, L60.
- Besla, G., Kallivayalil, N., Hernquist, L., van der Marel, R.P., Cox, T.J., and Kereš, D. 2010, *ApJ*, **721**, L97.
- Besla, G., Kallivayalil, N., Hernquist, L., van der Marel, R.P., Cox, T.J., and Kereš, D. 2012, *MNRAS*, **421**, 2109.
- Besla, G., Hernquist, L., and Loeb, A. 2013, *MNRAS*, **428**, 2342.
- Besla, G., Martinez-Delgado, D., van der Marel, R.P., Beletsky, Y., Seibert, M., Schlafly, E.F., Grebel, E.K., and Neyer, F. 2016, *ApJ*, **825**, 20.
- Bica, E.L.D., and Schmitt, H.R. 1995, *ApJS*, **101**, 41.
- Bica, E.L.D., Bonatto, C., Dutra, C.M., and Santos J.F.C. 2008, *MNRAS*, **389**, 678.
- Bica, E.L.D., Santiago, B., Bonatto, C., Garcia-Dias, R., Kerber, L., Dias, B., Barbuy, B., and Balbinot, E. 2015, *MNRAS*, **453**, 3190.
- Bono, G., Marconi, M., Cassisi, S., Caputo, F., Gieren, W., and Pietrzyński, G. 2005, *ApJ*, **621**, 966.
- Caldwell, J.A.R., and Coulson, I.M. 1986, *MNRAS*, **218**, 223.
- Carrera, R., Gallart, C., Aparicio, A., Costa, E., Méndez, R.A., and Noël, N.E.D. 2008, *AJ*, **136**, 1039.
- Casetti-Dinescu, D.I., Bidin, C.M., Girard, T.M., Méndez, R.A., Vieira, K., Korchagin, V.I., and van Altena, W.F. 2014, *ApJ*, **784**, L37.
- Cioni, M.-R.L., Habing, H.J., and Israel, F.P. 2000, *A&A*, **358**, L9.
- Cioni, M.-R.L. 2009, *A&A*, **506**, 1137.
- Connors, T.W., Kawata, D., and Gibson, B.K. 2006, *MNRAS*, **371**, 108.
- Deb, S., and Singh, H.P. 2014, *MNRAS*, **438**, 2440.
- Deb, S., Singh, H.P., Kumar, S., and Kanbur, S.M. 2015, *MNRAS*, **449**, 2768.
- de Grijs, R., Wicker, J.E., and Bono, G. 2014, *ApJ*, **147**, 122.
- de Grijs, R., and Bono, G. 2015, *AJ*, **149**, 179.
- Demers, S., and Battinelli, P. 1998, *AJ*, **115**, 154.
- Diaz, J.D., and Bekki, K. 2011, *MNRAS*, **413**, 2015.
- Diaz, J.D., and Bekki, K. 2012, *ApJ*, **750**, 36.
- Dobbie, P.D., Cole, A.A., Subramaniam, A., and Keller, S. 2014, *MNRAS*, **442**, 1680.
- Feast, M.W., Abedigamba, O.P., and Whitelock, P.A. 2010, *MNRAS*, **408**, L76.
- Fox, A.J., Wakker, B.P., Smoker, J.V., Richter, P., Savage, B.D., and Sembach, K.R. 2010, *ApJ*, **718**, 1046.
- Fox, A.J., Richter, P., Wakker, B.P., Lehner, N., Howk, J.C., Ben Bekhti, N., Bland-Hawthorn, J., and Lucas, S. 2013, *ApJ*, **772**, 110.
- Gardiner, L.T., Sawa, T., and Fujimoto, M. 1994, *MNRAS*, **266**, 567.
- Gardiner, L.T., and Noguchi, M. 1996, *MNRAS*, **278**, 191.
- Graczyk, D., *et al.* 2014, *ApJ*, **780**, 59.
- Guglielmo, M., Lewis, G.F., and Bland-Hawthorn, J. 2014, *MNRAS*, **444**, 1759.
- Harris, J. 2007, *ApJ*, **658**, 345.
- Harris, J. and Zaritsky, D. 2009, *ApJ*, **138**, 1243.
- Haschke, R., Grebel, E.K., and Duffau, S. 2012a, *AJ*, **144**, 106.
- Haschke, R., Grebel, E.K., and Duffau, S. 2012b, *AJ*, **144**, 107.
- Hindman, J.V., Kerr, F.J., and McGee, R.X. 1963, *Australian Journal of Physics*, **16**, 570.
- Indu, G., and Subramaniam, A. 2011, *A&A*, **535**, A115.
- Indu, G., and Subramaniam, A. 2015, *A&A*, **573**, A136.
- Inno, L., *et al.* 2015, *ASP Conf. Series*, **491**, 265.
- Irwin, M.J., Kunkel, W.E., and Demers, S. 1985, *Nature*, **318**, 160.
- Joshi, Y.C., and Joshi, S. 2014, *New Astronomy*, **28**, 27.

- Joshi, Y.C., Mohanty, A.P., and Joshi, S. 2016, *Research in Astronomy and Astrophysics*, **16**, 9.
- Kalberla, P.M.W., Burton, W.B., Hartmann, D., Arnal, E.M., Bajaja, E., Morras, R., and Pöppel, W.G.L. 2005, *A&A*, **440**, 775.
- Kallivayalil, N., van der Marel, R.P., Alcock, C., Axelrod, T., Cook, K.H., Drake, A.J., and Geha, M. 2006a, *ApJ*, **638**, 772.
- Kallivayalil, N., van der Marel, R.P., and Alcock, C. 2006b, *ApJ*, **652**, 1213.
- Kallivayalil, N., van der Marel, R.P., Besla, G., Anderson, J., and Alcock, C. 2013, *ApJ*, **764**, 161.
- Kapakos, E., and Hatzidimitriou, D. 2012, *MNRAS*, **426**, 2063.
- Koerwer, J.F. 2009, *AJ*, **138**, 1.
- Laney, C.D., and Stobie, R.S. 1986, *MNRAS*, **222**, 449.
- Leavitt, H.S. 1908, *Annals of Harvard College Observatory*, **60**, 87.
- Lehner, N., Howk, J.C., Keenan, F.P., and Smoker, J.V. 2008, *ApJ*, **678**, 219.
- Madore, B.F. 1976, *Royal Greenwich Observatory Bulletins*, **182**, 153.
- McClure-Griffiths, N.M., *et al.* 2008, *ApJ*, **673**, L143.
- Misawa, T., Charlton, J.C., Kobulnicky, H.A., Wakker, B.P., and Bland-Hawthorn, J. 2009, *ApJ*, **695**, 1382.
- Moretti, M.I., *et al.* 2014, *MNRAS*, **437**, 2702.
- Nelder, J.A., and Mead R. 1965, *Computer Journal*, **7**, 308.
- Ngeow, C., Kanbur, S.M., Bhardwaj, A., and Singh, H.P. 2015, *ApJ*, **808**, 67.
- Nidever, D.L., Majewski, S.R., and Butler Burton, W. 2008, *ApJ*, **679**, 432.
- Nidever, D.L., Majewski, S.R., Butler Burton, W., and Nigra, L. 2010, *ApJ*, **723**, 1618.
- Nidever, D.L., Majewski, S.R., Muñoz, R.R., Beaton, R.L., Patterson, R.J., and Kunkel, W.E. 2011, *ApJ*, **733**, L10.
- Nidever, D.L., Monachesi, A., Bell, E.F., Majewski, S.R., Muñoz, R.R., and Beaton, R.L. 2013, *ApJ*, **779**, 145.
- Nikolaev, S., Drake, A.J., Keller, S.C., Cook, K.H., Dalal, N., Griest, K., Welch, D.L., and Kanbur, S.M. 2004, *ApJ*, **601**, 260.
- Nöel, N.E.D., Conn, B.C., Carrera, R., Read, I.J., Rix, H.-W., and Dolphin, A. 2013, *ApJ*, **768**, 109.
- Nöel, N.E.D., Conn, B.C., Read, I.J., Carrera, R., Dolphin, A., and Rix, H.-W. 2015, *MNRAS*, **452**, 4222.
- Olsen, K.A.G., and Salyk, C. 2002, *AJ*, **124**, 2045.
- Olsen, K.A.G., and Massey, P. 2007, *ApJ*, **656**, L61.
- Parisi, M.C., Grocholski, A.J., Geisler, D., Sarajedini, A., and Clariá, J.J. 2009, *AJ*, **138**, 517.
- Pejcha, O., and Stanek, K.Z. 2009, *ApJ*, **704**, 1730.
- Persson, S.E., Madore, B.F., Krzemiński, W., Freedman, W.L., Roth, M., and Murphy, D.C. 2004, *AJ*, **128**, 2239.
- Piatti, A.E., de Grijs, R., Rubele, S., Cioni, M.-R.L., Ripepi, V., and Kerber, L. 2015, *MNRAS*, **450**, 552.
- Pietrzyński, G., *et al.* 2013, *Nature*, **495**, 76.
- Ploekinger, S., Hensler, G., Recchi, S., Mitchell, N., and Kroupa, P. 2014, *MNRAS*, **437**, 3980.
- Ploekinger, S., Recchi, S., Hensler, G., and Kroupa, P. 2015, *MNRAS*, **447**, 2512.
- Putman, M.E., Staveley-Smith, L., Freeman, K.C., Gibson, B.K., and Barnes, D.G. 2003, *ApJ*, **586**, 170.
- Richter, P., Fox, A.J., Wakker, B.P., Lehner, N., Howk, J.C., Bland-Hawthorn, J., Ben Bekhti, N., and Fechner, C. 2013, *ApJ*, **772**, 111.
- Romaniello, M., *et al.* 2008, *A&A*, **488**, 731.
- Rubele, S., *et al.* 2012, *A&A*, **537**, A106.
- Rubele, S., *et al.* 2015, *MNRAS*, **449**, 639.
- Růžička, A., Theis, C., and Palouš, J. 2009, *ApJ*, **691**, 1807.
- Růžička, A., Theis, C., and Palouš, J. 2010, *ApJ*, **725**, 369.
- Sandage, A., Tammann, G.A., and Reindl, B. 2009, *A&A*, **493**, 471.
- Schlegel, D.J., Finkbeiner, D. and Davis, M. 1998, *ApJ*, **500**, 525.

- Scowcroft, V., Freedman, W.L., Madore, B.F., Monson, A., Persson, S.E., Rich, J., Seibert, M., and Rigby, J.R. 2016, *ApJ*, **816**, 49.
- Sellke, T., Bayarri, M.J., and Berger, J.O. 2001, *The American Statistician*, **55**, 1.
- Shapley, H. 1940, *Harvard College Observatory Bulletin*, **914**, 8.
- Sharpee, B., Stark, M., Pritzl, B., Smith, H., Silbermann, N., Wilhelm, R., and Walker, A. 2002, *AJ*, **123**, 3216.
- Skowron, D.M., *et al.* 2014, *ApJ*, **795**, 108.
- Soszyński, I., *et al.* 2008, *Acta Astron.*, **58**, 163.
- Soszyński, I., *et al.* 2010, *Acta Astron.*, **60**, 17.
- Soszyński, I., *et al.* 2015, *Acta Astron.*, **65**, 297.
- Stanimirović, S., Staveley-Smith, L., and Jones, P.A. 2004, *ApJ*, **604**, 176.
- Staveley-Smith, L., Kim, S., Calabretta, M.R., Haynes, R.F., and Kesteven, M.J. 2003, *MNRAS*, **339**, 87.
- Subramaniam, A., and Subramanian, S. 2009, *ApJ*, **703**, L37.
- Subramanian, S., and Subramaniam, A. 2010, *A&A*, **520**, A24.
- Subramanian, S., and Subramaniam, A. 2012, *ApJ*, **744**, 128.
- Subramanian, S., and Subramaniam, A. 2013, *A&A*, **552**, A144.
- Subramanian, S., and Subramaniam, A. 2015, *A&A*, **573**, A135.
- Udalski, A., Szymański, M.K., Kubiak, M., Pietrzyński, G., Soszyński, I., Woźniak, P., and Żebruń, K. 1999, *Acta Astron.*, **49**, 201.
- Udalski, A. 2003, *ApJ*, **590**, 284.
- Udalski, A., Szymański, M.K., and Szymański, G. 2015, *Acta Astron.*, **65**, 1.
- van der Marel, R.P., and Cioni, M.-R.L. 2001, *AJ*, **122**, 1807.
- van der Marel, R.P. 2001, *AJ*, **122**, 1827.
- van der Marel, R.P., and Kallivayalil, N. 2014, *ApJ*, **781**, 121.
- Venzmer, M.S., Kerp, J., and Kalberla, P.M.W. 2012, *A&A*, **547**, A12.
- Wagner-Kaiser, R., and Sarajedini, A. 2013, *MNRAS*, **431**, 1565.
- Weinberg, M.D., and Nikolaev, S. 2001, *ApJ*, **548**, 712.
- Wyrzykowski, Ł., *et al.* 2011, *MNRAS*, **416**, 2949.
- Yoshizawa, A.M., and Noguchi, M. 2003, *MNRAS*, **339**, 1135.
- Zhao, H., and Evans, N.W. 2000, *ApJ*, **545**, L35.

OGLE-ing the Magellanic System: Three-Dimensional Structure of the Clouds and the Bridge using RR Lyrae Stars

A.M. Jacyszyn-Dobrzeńska¹, D.M. Skowron¹, P. Mróz¹,
I. Soszyński¹, A. Udalski¹, P. Pietrukowicz¹, J. Skowron¹,
R. Poleski^{1,2}, S. Kozłowski¹, Ł. Wyrzykowski¹, M. Pawlak¹,
M.K. Szymański¹ and K. Ulaczyk³

¹Warsaw University Observatory, Al. Ujazdowskie 4, 00-478 Warszawa, Poland
e-mail: ajacyszyn@astrouw.edu.pl

²Department of Astronomy, Ohio State University, 140 W. 18th Ave., Columbus,
OH 43210, USA

³Department of Physics, University of Warwick, Gibbet Hill Road,
Coventry, CV4 7AL, UK

Received November 29, 2016

ABSTRACT

We present a three-dimensional analysis of a sample of 22 859 type ab RR Lyr stars in the Magellanic System from the OGLE-IV Collection of RR Lyr stars. The distance to each object was calculated based on its photometric metallicity and a theoretical relation between color, absolute magnitude and metallicity.

The LMC RR Lyr distribution is very regular and does not show any substructures. We demonstrate that the bar found in previous studies may be an overdensity caused by blending and crowding effects. The halo is asymmetrical with a higher stellar density in its north-eastern area, which is also located closer to us. Triaxial ellipsoids were fitted to surfaces of a constant number density. Ellipsoids farther from the LMC center are less elongated and slightly rotated toward the SMC. The inclination and position angle change significantly with the a axis size. The median axis ratio is 1 : 1.23 : 1.45.

The RR Lyr distribution in the SMC has a very regular, ellipsoidal shape and does not show any substructures or asymmetries. All triaxial ellipsoids fitted to surfaces of a constant number density have virtually the same shape (axis ratio) and are elongated along the line-of-sight. The median axis ratio is 1 : 1.10 : 2.13. The inclination angle is very small and thus the position angle is not well defined.

We present the distribution of RR Lyr stars in the Magellanic Bridge area, showing that the Magellanic Clouds' halos overlap.

A comparison of the distributions of RR Lyr stars and Classical Cepheids shows that the former are significantly more spread and distributed regularly, while the latter are very clumped and form several distinct substructures.

Key words: Stars: fundamental parameters – Stars: variables: RR Lyrae – Magellanic Clouds – Galaxies: statistics – Galaxies: structure

1. Introduction

The Magellanic System consists of the Large Magellanic Cloud (LMC) and Small Magellanic Cloud (SMC) along with a few structures that were formed as a result of the Clouds' interactions. These structures are: the Magellanic Stream, the Leading Arm, and the Magellanic Bridge (MBR) (Gardiner *et al.* 1994, Gardiner and Noguchi 1996, Yoshizawa and Noguchi 2003, Connors *et al.* 2006, Růžička *et al.* 2009, 2010, Besla *et al.* 2010, 2012, Diaz and Bekki 2011, 2012, Guglielmo *et al.* 2014). For more information on the Magellanic System and especially the Magellanic Clouds morphology see Introduction in Jacyszyn-Dobrzyniecka *et al.* (2016) (hereafter Paper I). Here we concentrate on an analysis based on the RR Lyr (RRL) type variable stars.

The RRL stars are pulsating stars of great importance. They obey the period–luminosity law, which together with their well established luminosities, makes them good standard candles and allows for precise distance determinations to globular clusters and nearby galaxies. The RRL stars represent the old population and due to their large numbers in most stellar systems, they serve as tracers of the three-dimensional structure, metallicity distribution, and star formation history of galaxies. There was a great number of studies that analyzed the Magellanic Clouds' morphology with RRL variables, and we will summarize their main results below. All studies were based on the third part of the Optical Gravitational Lensing Experiment (OGLE) Catalog of Variable Stars (OCVS) containing over 17 000 RRL type ab (RRab) stars in the LMC (Soszyński *et al.* 2009) and almost 2000 RRab stars in the SMC (Soszyński *et al.* 2010). However that dataset did not cover the extended area around the Magellanic Clouds, in contrary to the OGLE-IV data that we use here.

The RRL stars distribution in the LMC is known to be roughly regular, and has been often modeled as a triaxial ellipsoid (Pejcha and Stanek 2009, Deb and Singh 2014), which is rotated such that the eastern side of this galaxy is closer to us than the western side (Pejcha and Stanek 2009, Haschke *et al.* 2012a). Some studies suggested that the RRL population of the LMC has two components: the disk and the halo (Subramaniam and Subramaniam 2009, Deb and Singh 2014), although the existence of the disk has been questioned (Wagner-Kaiser and Sarajedini 2013). It was also proposed, that the LMC has a bar-like structure in the center which stands out as a RRL stars overdensity (Subramaniam and Subramaniam 2009), and is almost 5 kpc in front of the main body of the LMC disk (Haschke *et al.* 2012a).

The RRL stars distribution in the SMC also has a regular, ellipsoidal shape (Haschke *et al.* 2012b) that can be modeled as a triaxial ellipsoid extended along the line-of-sight (Subramaniam and Subramaniam 2012, Deb *et al.* 2015). The central part of the SMC was found to have a large line-of-sight depth (Haschke *et al.* 2012b), which has been interpreted as a bulge (Deb *et al.* 2015). The north-eastern side of the RRL stars distribution seems to have a larger depth (Kapakos *et al.* 2010). It is also closer to us than the main SMC body (Subramaniam and Subrama-

niam 2012, Deb *et al.* 2015) and contains more metal-rich stars (Deb *et al.* 2015). A study by Kapakos *et al.* (2011) and Kapakos and Hatzidimitrou (2012) showed that stars with different metallicities seem to belong to different dynamical structures. The metal-rich objects constitute a thick disk with a bulge, while the metal-poor stars form a halo.

In the area between the Magellanic Clouds – the Magellanic Bridge – intermediate age stars were observed by Nöel *et al.* (2013, 2015). Moreover, candidates for an old stellar population were found by Bagheri *et al.* (2013). They used 2MASS and WISE near-infrared catalogs and found RGB and AGB stars in an on-sky stripe between the Clouds. Authors were unable to identify whether these objects are genuine Bridge members or they belong to the LMC or SMC halo.

Soszyński *et al.* (2016ab) recently released the newest part of the OGLE Collection of RRL stars that enabled us to analyze the three-dimensional morphology of the Magellanic System that we present here. The Collection is based on the OGLE-IV data (Udalski *et al.* 2015) that cover about 650 square degrees in this region. This area is significantly greater than that of the OGLE-III survey, on which the studies described above were based. The extended coverage of the OGLE-IV Collection includes the outskirts of the Magellanic Clouds and the Magellanic Bridge. This allows us to deduce the actual shape of these galaxies although the farthest outskirts, especially in the LMC area, are still not entirely covered by observations.

We organized the paper as follows. Section 2 gives description of the OGLE-IV data and OGLE Collection of RRL stars. In Section 3, the technical details of the analysis are presented. We then describe the three-dimensional structure of the LMC, SMC and Magellanic Bridge in Sections 4, 5 and 6, respectively. Section 7 presents comparison of the RRL stars and CCs distribution from Paper I. We summarize our results in Section 8.

2. Data

2.1. The OGLE Collection of RR Lyr Stars

The newest part of the OGLE Collection of RRL stars (Soszyński *et al.* 2016ab) contains 45 453 objects in total and is the largest published catalog of RRL stars up to date. The classification was based on the period search for almost all *I*-band light curves in the OGLE database (Udalski *et al.* 2015). Then light curves with periods from 0.2 to 1 day were selected and automatic and manual classification was performed. Finally, each light curve was inspected visually. When the case was doubtful other parameters, like the position of the object in the color–magnitude diagram, were taken into account. About 40% of the RRL stars were not included in the previous versions of the OGLE Collection of RRL stars. Almost all of them are located in the extended region covered by OGLE-IV that was not observed during earlier phases of the OGLE project.

The Collection includes 32 581 RRab, 10 246 RRc, and 2624 RRd stars, with 22 anomalous RRd stars. Of those 39 082 are located in the LMC, whereas 6369 – in the SMC. The boundary between these galaxies was set at $RA = 2^{\text{h}}48^{\text{m}}$ because of a local minimum of the number of RRL stars. This value is only an approximation because it is not possible to separate the Magellanic Clouds due to their overlapping halos. Similarly, it is not possible to entirely separate the Magellanic Clouds’ RRL stars from Milky Way halo’s RRL stars so the sample possibly contains some number of the latter ones. The completeness of the OGLE Collection of RRL stars is about 96%. The gaps between CCD chips in the OGLE-IV camera are responsible for the loss of about 7% of stars from the fields that were not covered by the OGLE-III.

2.2. The Sample Selection

Our analysis is based on RRL stars pulsating in the fundamental mode (RRab). Among 32 581 RRab stars 27 620 are located in the LMC and 4961 in the SMC. Hereafter when we write about our RRL stars sample we mean these RRab stars. We applied the same cuts to our sample as described in Skowron *et al.* (2016). We rejected the objects that did not have the V -band magnitude because these stars were useless for the Wesenheit magnitude calculations. Then we removed RRL stars with large uncertainties of phase parameters that were later used to calculate photometric metallicities. In the next step, 20% of objects with the largest scatter of the light curve around the Fourier decomposition were excluded from the sample.

After this procedure we were left with 20 573 RRL stars in the LMC and 3560 in the SMC. Next, we made a cut on the Bailey diagram in order to better eliminate blends from our sample and excluded stars with peak-to-peak amplitude lower than

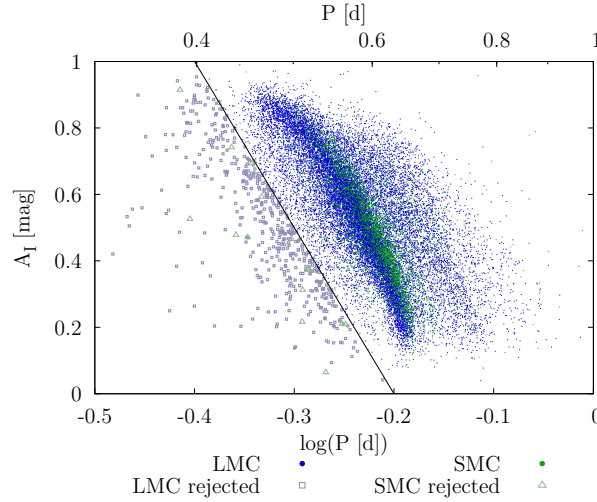


Fig. 1. The Bailey diagram for RRL stars (ab). Black line denotes the adopted limit for a blend rejection. The SMC RRL stars are overplotted on the LMC RRL stars. The rejected SMC RRL stars are marked with large triangles while the rejected LMC RRL stars – with squares.

for a typical RRL stars at a given period P in the I -band, *i.e.*, we removed objects for which $A_I < -5 \cdot \log(P) - 1$ (see Fig. 1). Then we fitted the period–luminosity relation (P-L) to our sample and iteratively removed RRL stars with luminosities deviating more than 3σ from the fit (see Fig. 2). The results are described in Section 2.3. This left us with the final sample consisting of 19401 RRL stars in the LMC and 3458 stars in the SMC.

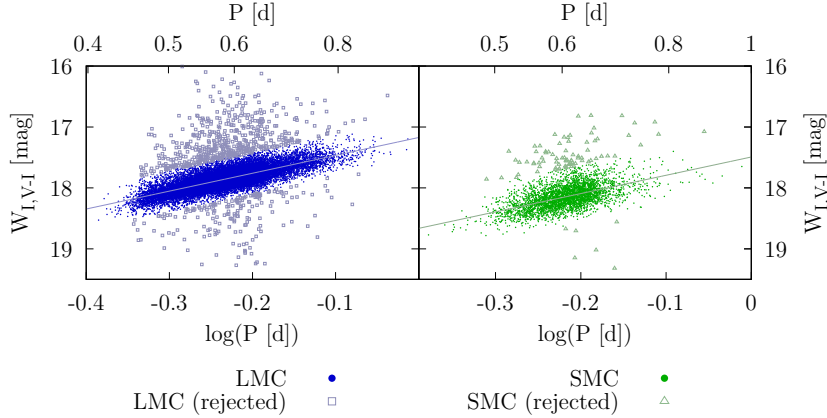


Fig. 2. P-L relations for the Wesenheit magnitude for RRL(ab) stars in the Magellanic System showing objects rejected as 3σ outliers during the fitting procedure. *Left panel:* The fit for the LMC. Rejected objects are marked with squares. *Right panel:* The fit for the SMC. Rejected objects are marked with triangles.

After all these restrictive cuts we expected that we would see no blends in our data. Unfortunately, three-dimensional maps of the LMC still show a non-physical feature – an elongation in the LMC structure along the line-of-sight coming out of the center of this galaxy and visible on its both sides (hereafter we refer to it as the LMC blend-artifact). Fig. 3 illustrates this effect on the xz and the yz planes in the Cartesian projection, that will be described in Section 3.3. Red contours represent all RRL stars, before any sample cuts were done, while black contours show the cleaned, final sample. The elongated central structure has decreased, but not vanished entirely. Its cone-like shape and orientation exactly toward the observer at $(0,0,0)$ indisputably point to its non-physical nature. The LMC blend-artifact is also well visible on the xz plane in Fig. 4. Unfortunately, it is very difficult to separate all the blends from unblended stars because these objects are mixed together in every parameter space. We tried to make additional and more restrictive cuts on diagrams including color, magnitude, amplitude, period, but none of these made a significant difference and the non-physical feature remained. Instead, normal, unblended RRL stars were removed. For this reason we refrain from performing additional cuts as this can falsify the two-dimensional maps and distributions and lead to a lower than real RRL stars column density. The existence of the LMC blend-artifact requires that any analysis of the LMC center adopts a very careful approach to the sample selection and analysis processes.

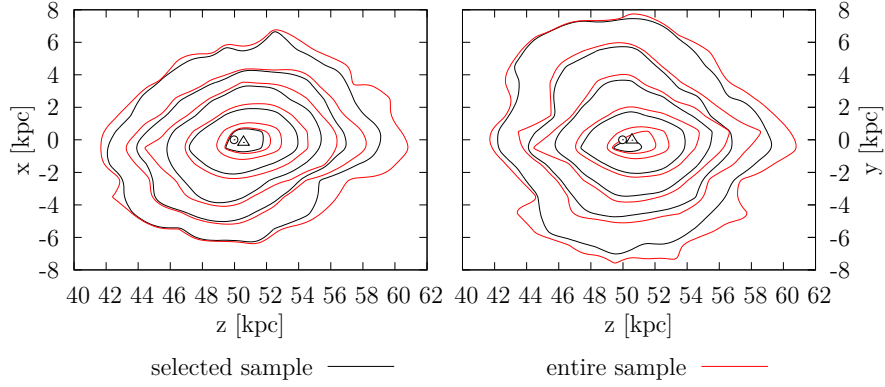


Fig. 3. Stellar density contours of the LMC RRL stars for the entire RRL sample – red (objects lacking I - or V -band magnitude are not included in this plot) and the cleaned sample – black, on the xz and yz planes in the Cartesian projection. Contour levels are the same in *both panels*.

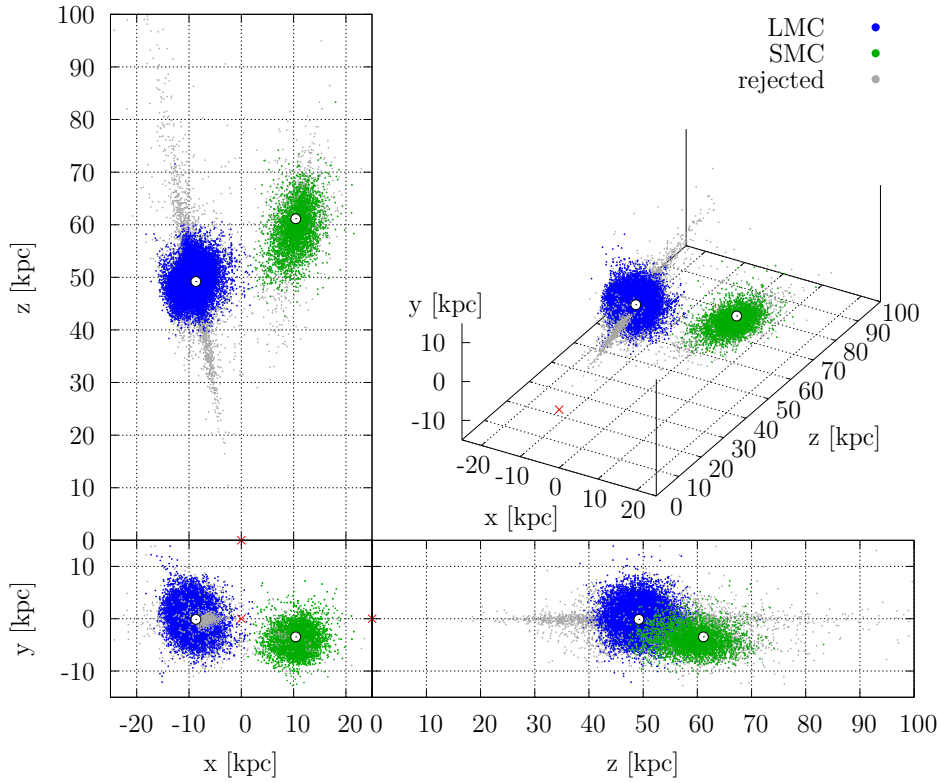


Fig. 4. The RRL stars in the Magellanic System in the Cartesian coordinates. The LMC stars are marked with blue dots, while the SMC stars – with green dots. Additionally, all the rejected RRL stars are shown with gray color (the RRL stars lacking I - or V -band magnitude are not included in this plot). Red cross marks the location of the observer. White circle denotes the LMC (Pietrzyński *et al.* 2013, van der Marel and Kallivayalil 2014) and SMC (Stanimirović *et al.* 2004, Graczyk *et al.* 2014) dynamical centers on this and the following maps.

3. Data Analysis

3.1. Period–Luminosity Relation

After removing objects with $A_I < -5 \cdot \log(P) - 1$ on the Bailey diagram we fitted a period–luminosity relation to our sample. We used the reddening-independent Wesenheit index (Madore 1976) for the V - and I -band photometry:

$$W_{I,V-I} = I - 1.55 \cdot (V - I) \quad (1)$$

The value of the coefficient (1.55) was calculated based on the dependence of the I -band extinction on $E(V - I)$ reddening (Schlegel *et al.* 1998). We used the least-squares method to fit the linear function in the form:

$$W_{I,V-I} = a \cdot \log(P) + b \quad (2)$$

separately to the LMC and SMC sample. In each iteration we rejected RRL stars that were 3σ outliers until there were none. The rejected objects are mostly blends, additionally affected by crowding. The results for the Wesenheit magnitude as well as for the I - and V -band magnitudes are shown in Table 1. Fig. 2 shows the fit for the Wesenheit magnitude and the rejected stars.

Table 1
P-L relations for RRab stars in the Magellanic Clouds

P-L for Wesenheit magnitude			$W_{I,V-I} = a \cdot \log(P) + b$			
Galaxy	a	b [mag]	σ [mag]	χ^2/dof	N_{inc}	N_{rej}
LMC	-2.933 ± 0.009	17.172 ± 0.003	0.114	3.605	19 401	720
SMC	-3.001 ± 0.028	17.492 ± 0.007	0.158	6.980	3 458	86
P-L for I -band magnitude			$I = a \cdot \log(P) + b$			
Galaxy	a	b [mag]	σ [mag]	χ^2/dof	N_{inc}	N_{rej}
LMC	-1.680 ± 0.009	18.374 ± 0.003	0.142	5.587	19 704	417
SMC	-1.709 ± 0.028	18.673 ± 0.007	0.153	6.557	3 482	62
P-L for V -band magnitude			$V = a \cdot \log(P) + b$			
Galaxy	a	b [mag]	σ [mag]	χ^2/dof	N_{inc}	N_{rej}
LMC	-0.910 ± 0.009	19.139 ± 0.003	0.187	9.768	19 625	496
SMC	-0.934 ± 0.028	19.422 ± 0.007	0.167	7.786	3 475	69

N_{inc} is the number of objects included in the final fit, while N_{rej} is the number of rejected objects.

3.2. Metallicities and Distances

The photometric metallicity of each RRL star in our sample was calculated the same way as in Skowron *et al.* (2016). The ϕ_{31}^I phase parameter from the Fourier decomposition of the *I*-band light curve was transformed to the phase parameter in the Kepler band ϕ_{31}^{Kp} and then the photometric metallicity relation of Nemeč *et al.* (2013) was applied. For more details on the metallicity calculation see Section 5 in Skowron *et al.* (2016). To calculate the distance we first transformed the metallicity from Jurcsik (1995) scale to the Carretta *et al.* (2009) scale using the relation from Kapakos *et al.* (2011):

$$[\text{Fe}/\text{H}]_C = 1.001 \cdot [\text{Fe}/\text{H}]_J - 0.112. \quad (3)$$

Then we used the coefficients from Table 5 in Braga *et al.* (2015) to calculate the absolute Wesenheit magnitude of each RRL star:

$$W_{I,V-I,abs} = a_W + b_W \cdot \log(P) + c_W([\text{Fe}/\text{H}]_C + 0.04) \quad (4)$$

where $a_W = -1.039 \pm 0.007$, $b_W = -2.524 \pm 0.021$ and $c_W = 0.147 \pm 0.004$.

Finally, the distance in pc is given by:

$$d = 10^{(W_{I,V-I} - W_{I,V-I,abs} + 5)/5}. \quad (5)$$

The distance uncertainty includes the OGLE photometric uncertainty which is $\sigma_{I,V} = 0.02$ mag and the uncertainty of the calculated metallicity. The median distance uncertainty for the LMC is 1.46 kpc (3% relative to the median distance) and for the SMC 1.78 kpc (3% relative to the median distance). Fig. 4 shows the RRL stars in the Magellanic System in three dimensions. The LMC stars are marked with blue dots, while the SMC stars – with green dots. Additionally, all the rejected RRL stars are shown with gray dots.

3.3. Coordinate Transformations

In this paper, we present our results using two types of maps. The first one is a two-dimensional equal-area Hammer projection. The z axis is pointing toward $\alpha_{\text{cen}} = 3^{\text{h}}20^{\text{m}}$, $\delta_{\text{cen}} = -72^\circ$. For each RRL star, x_{Hammer} and y_{Hammer} coordinates are calculated from the formulae used in Paper I. Fig. 5 shows the Magellanic System in the Hammer projection, where the distance is color-coded.

The second type of maps that we use shows stellar positions in the Cartesian three-dimensional space: (x, y, z) . We use different viewing angles although the observer is always at $(0, 0, 0)$. The z axis is pointing toward different equatorial coordinates: α_{cen} and δ_{cen} . The transformation equations are the same as used in Paper I and were taken from van der Marel and Cioni (2001) and Weinberg and Nikolaev (2001). Fig. 4 shows RRL stars in the Magellanic System in the Cartesian coordinates.

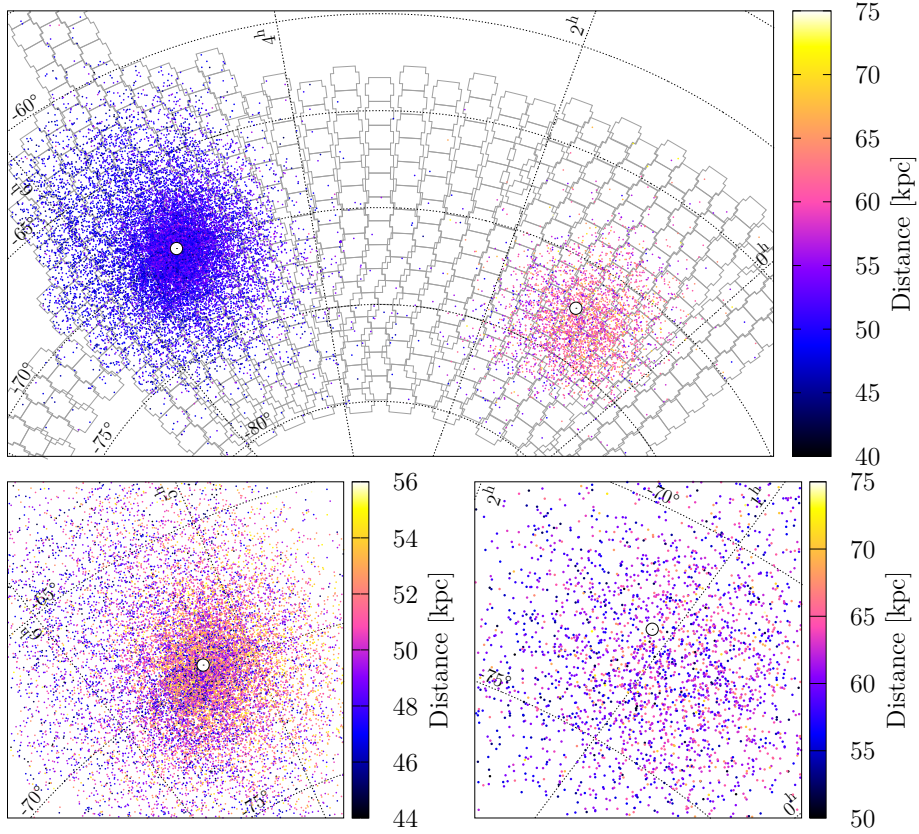


Fig. 5. The equal-area Hammer projection of the RRL stars in the Magellanic System with color-coded distances. Note the change in distance range between the panels. *Upper panel:* The LMC is on the left while the SMC is on the right. Gray contours represent the OGLE-IV fields. *Lower left panel:* Close-up on the LMC. *Lower right panel:* Close-up on the SMC (the dots representing RRL stars are one and half times larger than on other panels). White circles mark galaxies' dynamical centers.

Maps showing the entire Magellanic System are centered at $\alpha_{\text{cen}} = 3^{\text{h}}20^{\text{m}}$, $\delta_{\text{cen}} = -72^{\circ}$, while maps showing only the LMC or SMC are centered at their dynamical centers, similarly as in Paper I. For the LMC we adopted slightly different coordinates: $\alpha_{\text{LMC-cen}} = 5^{\text{h}}19^{\text{m}}31.2$, $\delta_{\text{LMC-cen}} = -69^{\circ}35'24''$, which are for the whole population with a correction for older stars proper motions (van der Marel and Kallivayalil 2014). For the SMC we use the same centering as in Paper I: $\alpha_{\text{SMC-cen}} = 1^{\text{h}}05^{\text{m}}$, $\delta_{\text{SMC-cen}} = -72^{\circ}25'12''$ (Stanimirović *et al.* 2004). The center of each galaxy, that is marked on our maps with a white circle, is composed of the dynamical on-sky center (α_{cen} , δ_{cen}) combined with the mean distance (d). For the LMC we use the distance $d_{\text{LMC}} = 49.97 \pm 0.19$ (statistical) ± 1.11 (systematic) kpc, calculated by Pietrzyński *et al.* (2013) which is the most accurate LMC distance up to date. For the SMC we adopted $d_{\text{SMC}} = 62.1 \pm 1.9$ kpc from Graczyk *et al.* (2014). These dynamical centers are shown in order to aid comparison with

other studies (*e.g.*, Paper I), even though they do not comply with RRL distribution centers.

The OGLE astrometric uncertainty is included in the Cartesian coordinates uncertainties. This astrometric uncertainty is $\sigma_{\alpha,\delta} = 0''.2$. The distance uncertainty is also included. The values of x, y and z position uncertainties are as follows: $0.1 \text{ kpc} < \sigma_x < 0.9 \text{ kpc}$, $0.1 \text{ kpc} < \sigma_y < 0.7 \text{ kpc}$, and $1.3 \text{ kpc} < \sigma_z < 4.1 \text{ kpc}$.

The most important parameters of the RRL stars sample analyzed in this publication are available on-line in a tabular form from the OGLE website:

<http://ogle.astrouw.edu.pl>

Table 2 presents the first few lines of the file.

Table 2
RRL stars (ab) in the Magellanic System

Columns 1–6						
Location	OCVS Id	P [d]	I [mag]	V [mag]	$W_{I,V-I}$ [mag]	
LMC	OGLE-LMC-RRLYR-00001	0.6347521	18.772	19.455	17.713	
LMC	OGLE-LMC-RRLYR-00003	0.6564971	18.649	19.306	17.631	
LMC	OGLE-LMC-RRLYR-00005	0.6433519	18.942	19.613	17.902	
⋮	⋮	⋮	⋮	⋮	⋮	
Columns 7–13						
$[\text{Fe}/\text{H}]_N$	RA	Dec	d [kpc]	$x^{(a)}$ [kpc]	$y^{(a)}$ [kpc]	$z^{(a)}$ [kpc]
-1.63 ± 0.12	04 ^h 27 ^m 45 ^s .45	−70°43′12″.0	50.23 ± 1.46	-4.83 ± 0.39	0.44 ± 0.85	49.99 ± 1.54
-1.41 ± 0.11	04 ^h 28 ^m 08 ^s .50	−70°21′22″.8	48.44 ± 1.39	-4.77 ± 0.38	0.71 ± 0.82	48.20 ± 1.48
-1.14 ± 0.42	04 ^h 28 ^m 21 ^s .06	−70°08′54″.5	53.33 ± 2.13	-5.32 ± 0.45	0.96 ± 0.90	53.06 ± 2.19
⋮	⋮	⋮	⋮	⋮	⋮	⋮

The electronic version of the entire sample used in this study is available on-line from the OGLE website. (a) The Cartesian x, y , and z coordinates.

3.4. Model and Ellipsoid Fitting

In the next step, we modeled the RRL stars spatial distribution by fitting triaxial ellipsoids to surfaces of a constant number density, to the LMC and SMC three-dimensional data in the Cartesian coordinate space. First, we calculated the local density of RRL stars in a $2 \times 2 \times 2$ kpc cube around each star, which was up to 338 and 29 stars per kpc^3 in the LMC and SMC, respectively. The cube size was chosen as a trade-off between the resolution and smoothness of the resulting star

density distribution. Subsequently, we divided both samples of RRL stars into bins of nearly constant star density and then fitted triaxial ellipsoids to these subsamples using an algorithm proposed by Turner *et al.* (1999), described below.

We aimed to find the parameters of an ellipsoid given its quadratic form:

$$ax^2 + by^2 + cz^2 + dxy + exz + fyz + gx + hy + kz + l = 0. \quad (6)$$

We found the best-fit ellipsoid by minimizing the sum of squared distances between the data points and the modeled ellipsoid. The resulting quadratic forms were then transformed to obtain parameters of the ellipsoid: coordinates of the center, length of semi-axes, and their orientation. The uncertainties were estimated using the bootstrap method. To aid the comparison with previous works, we provide two parameters describing the orientation of ellipsoids: inclination and position angle of the longest axis.

If an ellipsoid is centered at the origin, then its quadratic form is $\mathbf{X}^T \mathbf{A} \mathbf{X} = C$, where $C > 0$ and \mathbf{A} is a symmetric matrix with positive eigenvalues, $\mathbf{X}^T = [x, y, z]$. From the principal axis theorem, we know that eigenvectors of a matrix \mathbf{A} form an orthonormal basis such as $\mathbf{P}^T \mathbf{A} \mathbf{P} = \mathbf{D}$, where \mathbf{D} is a diagonal matrix and \mathbf{P} is a square matrix consisting of the eigenvectors corresponding to the eigenvalues in \mathbf{A} . In that basis, the quadratic form is simply $\mathbf{X}^T \mathbf{A} \mathbf{X} = \sum_i \lambda_i x_i^2 = C$, and hence the semi-axes of the ellipsoid are equal to $\sqrt{C/\lambda_i}$, where λ_i are eigenvalues of \mathbf{A} . Eigenvectors of \mathbf{A} span the semi-axes.

It can be straightforwardly shown that:

$$\mathbf{A} = \begin{bmatrix} a & d/2 & e/2 \\ d/2 & b & f/2 \\ e/2 & f/2 & c \end{bmatrix}$$

For the ellipsoid centered at \mathbf{X}_0 :

$$(\mathbf{X} - \mathbf{X}_0)^T \mathbf{A} (\mathbf{X} - \mathbf{X}_0) = \mathbf{X}^T \mathbf{A} \mathbf{X} - 2\mathbf{X}^T \mathbf{A} \mathbf{X}_0 + \mathbf{X}_0^T \mathbf{A} \mathbf{X}_0 = C. \quad (7)$$

Hence, the origin of the ellipsoid

$$\mathbf{X}_0 = -\frac{1}{2} \mathbf{A}^{-1} \begin{bmatrix} g \\ h \\ k \end{bmatrix}$$

while $C = \mathbf{X}_0^T \mathbf{A} \mathbf{X}_0 - l$.

4. The Large Magellanic Cloud

4.1. Three-Dimensional Structure

The RRL stars distribution in the LMC is known to be roughly regular, or ellipsoidal, possibly with a bar (Pejcha and Stanek 2009, Subramanian and Subramanian 2012, Haschke *et al.* 2012a, Wagner-Kaiser and Sarajedini 2013, Deb and Singh 2014).

We have estimated the sample center parameters using the maxima of the Right Ascension, Declination and distance of the RRL stars distribution which are $\tilde{\alpha}_{\text{LMC}} = 5^{\text{h}}21^{\text{m}}31^{\text{s}}.2$, $\tilde{\delta}_{\text{LMC}} = -69^{\circ}36'36''$, $\tilde{d}_{\text{LMC}} = 50.56$ kpc (hereafter the distribution center). The median LMC RRL stars distance based on our data is $d_{\text{LMC,med}} = 50.64$ kpc. This is slightly different than the dynamical center coordinates derived by van der Marel and Kallivayalil (2014) which were $\alpha_{\text{LMC-cen}} = 5^{\text{h}}19^{\text{m}}31^{\text{s}}.2$, $\delta_{\text{LMC-cen}} = -69^{\circ}35'24''$ and the mean LMC distance from Pietrzyński *et al.* (2013) derived from eclipsing binaries: $d_{\text{LMC}} = 49.97 \pm 0.19$ (statistical) ± 1.11 (systematic) kpc.

Fig. 4 shows the Magellanic System in the Cartesian coordinates where the LMC reveals its regular, although not entirely symmetrical, shape in three dimensions. The most protruding “substructure” is the LMC blend-artifact – a non-physical structure build up of the RRL stars seemingly drawn-out of the galaxy along the line-of-sight. These stars are mostly blends, additionally affected by crowding effects and are located in the dense LMC center. Because of their relatively low luminosity, RRL stars are very prone to such blending and crowding effects. As we have already described in Section 2.2 it is impossible to remove all the blends from our sample because many of them are not distinguishable from unblended RRL stars based solely on their light curves. An attempt to do so would lead to non-physical results.

The on-sky projection of the LMC seems to be roughly regular (see Fig. 5). To further investigate the three-dimensional structure of this galaxy we show its distance tomography in Fig. 6. The upper row represents the closest RRL stars in the LMC. There is a well visible clump at the center, elongated in the east-west direction and concentrated more on the eastern side of the distribution and dynamical center (first panel). It may seem to constitute the LMC bar, similarly as in Fig. 5 from Haschke *et al.* (2012a), but in fact this is a reflection of the non-physical LMC blend-artifact. On the other hand, we see that the LMC extended halo and the closest parts of it are definitely concentrated in the north-eastern parts of this galaxy. The LMC halo is not symmetrical with respect to the distribution and the dynamical center of this galaxy.

The middle row shows RRL stars near the average LMC distance. Here, the central parts of the LMC have a more regular shape. Again, we see that the LMC RRL stars halo is more numerous in the north-eastern parts of this galaxy. The lowest row represents the farthest LMC RRL stars. The RRL stars in the central

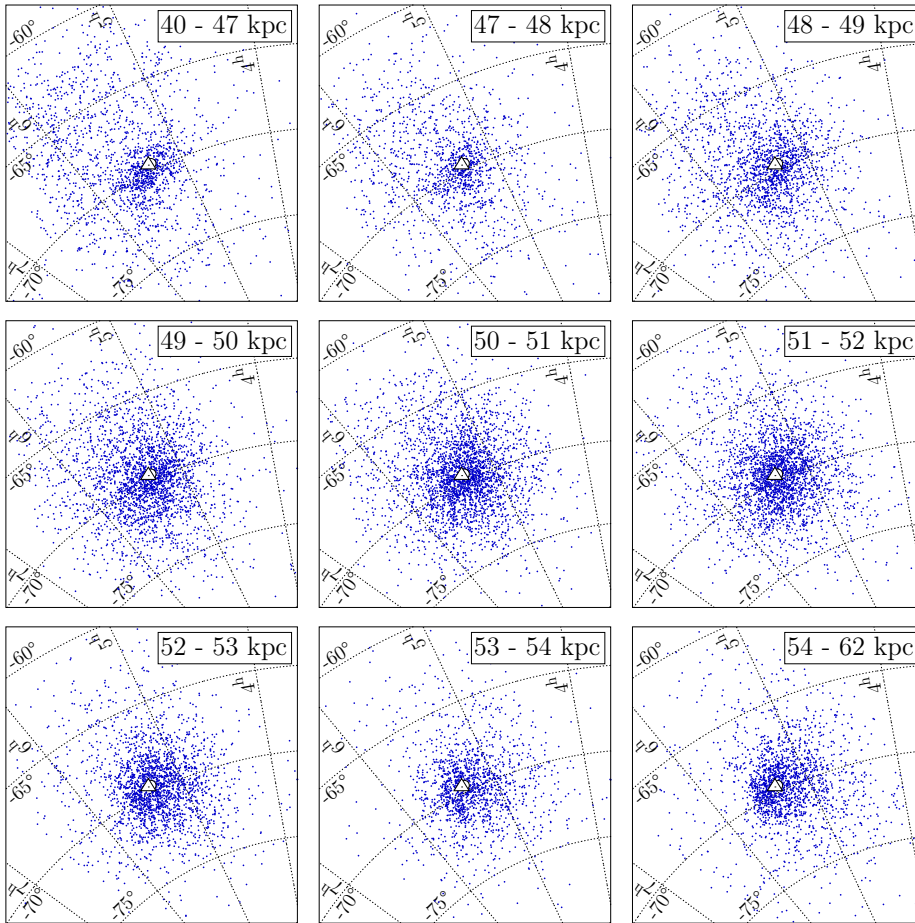


Fig. 6. Distance tomography of the RRL stars distribution in the LMC in the Hammer equal-area projection. Note different distance ranges. White circle marks the LMC dynamical center. White triangle marks the RRL stars distribution maxima along the RA, Dec and distance axes.

regions are more clumped on the eastern side but this is again due to the LMC blend-artifact as it is consistent with the distribution maximum. Interestingly, the LMC halo's farthest parts are more numerous on the western side. This is the direction toward the SMC. The distance tomography of the LMC suggests that the eastern part of the LMC is closer than the western part.

Column density maps in three Cartesian dimensions are shown in Fig. 7. The bin size is 0.5 kpc along each axis. On the xz and yz planes the LMC blend-artifact is clearly visible as a longitudinal structure that is elongated along the line-of-sight. The “view from the top” – xz plane – shows that the LMC outskirts are asymmetrical with the eastern side located closer to us than the western side. The LMC halo seems to be neither spheroidal nor ellipsoidal, which is also prominent on the yz plane.

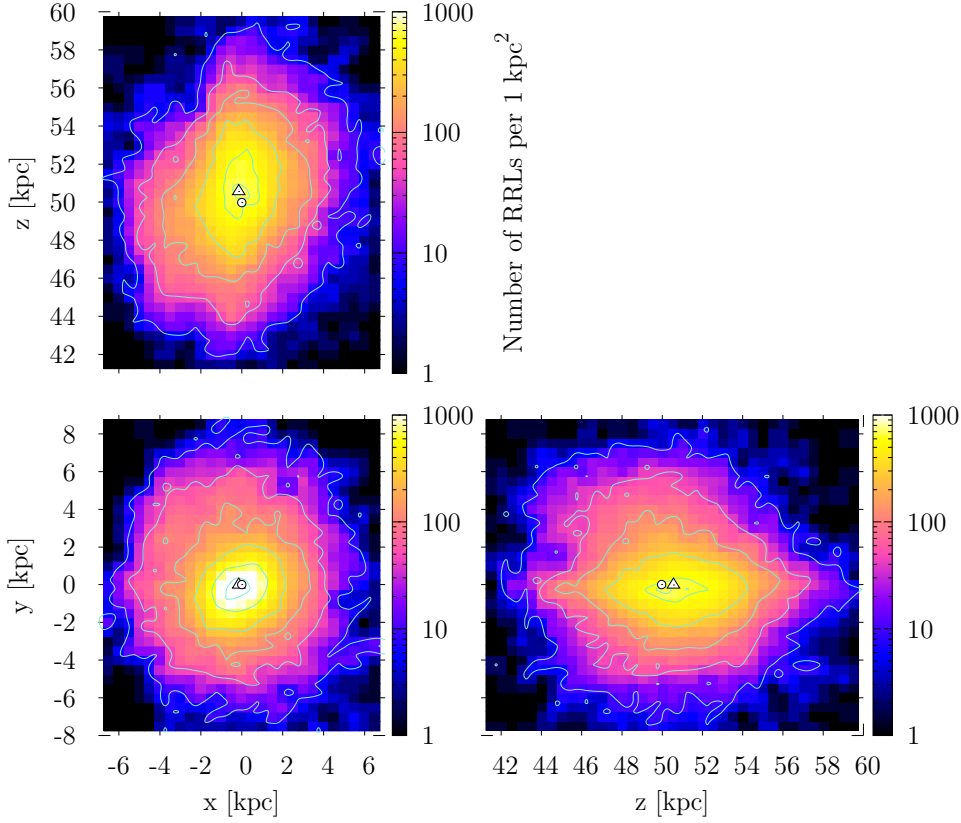


Fig. 7. RRL stars density maps in the LMC in the Cartesian coordinates (the z axis is pointing toward the LMC dynamical center). Bin size is 0.5 kpc in x , y and z axis. Contour levels on the xy plane are 10, 50, 120, 300, 700, 1300, on the xz and yz 10, 50, 120, 300, 600, 700 RRL stars per 1 kpc². Note the LMC blend-artifact clearly visible on the xz and yz planes. White circle and triangle mark the LMC dynamical and distribution centers, respectively.

4.2. Ellipsoid Fitting

As a result of the analysis based on the two- and three-dimensional maps we decided to model the LMC RRL stars distribution as a triaxial ellipsoid. The LMC RRL stars were divided into 21 subsamples consisting of 135 to 963 objects. The technical details of the modeling procedure were described in Section 3.4. The fitting results are presented in Figs. 8, 9, and 10 and in Table 3. To minimize the influence of the non-physical LMC blend-artifact, we decided to exclude the central region of the LMC from the fit and the following analysis. We removed RRL stars located within an angular on-sky radius of $1^{\circ}5$ from the LMC distribution center, *i.e.*, all RRL stars along the line-of-sight in a cone (see Fig. 9).

The innermost LMC ellipsoid corresponds to the star density of $\log(n) = 2.15 - 2.2 \text{ kpc}^{-3}$. The axis ratio $a : b : c$ is $1 : 1.168 : 1.950$ and it is the ellipsoid with the highest c/a ratio. The inclination is relatively small ($i = 7^{\circ}03$), while the

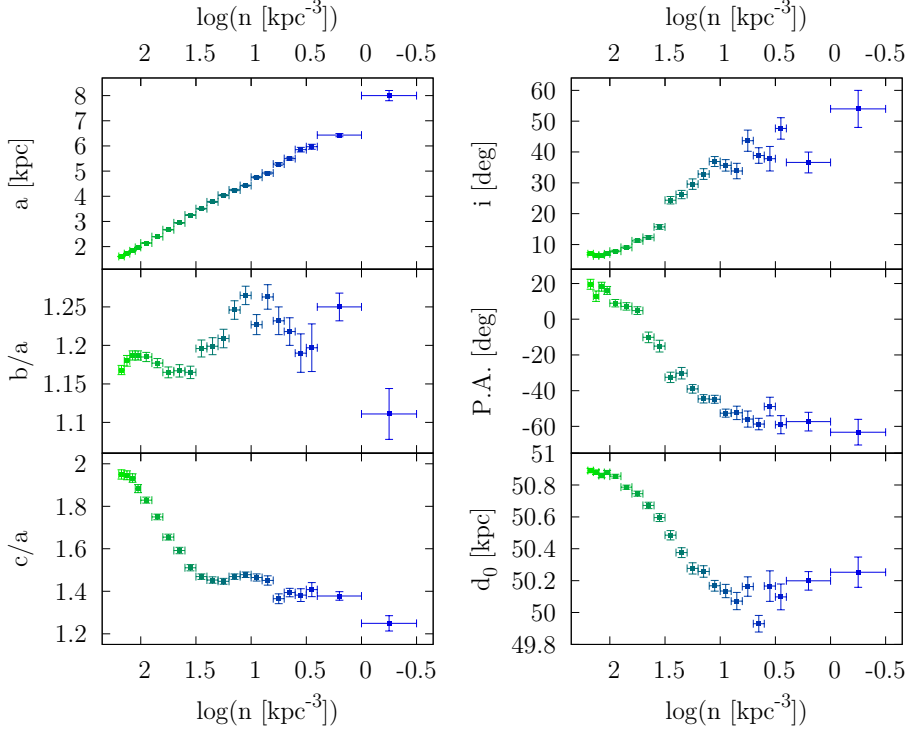


Fig. 8. Parameters of the best-fit triaxial ellipsoids for the LMC RRL stars. We excluded objects located within an angular radius of $1^{\circ}5$ from the LMC center because of the LMC blend-artifact. Green points represent the innermost ellipsoids while blue points – the outermost.

position angle is large ($\text{P.A.} = 19^{\circ}57$). As the number density n decreases (*i.e.*, a increases), c/a ratios are decreasing while b/a ratios do not show any trend (see Table 3 and Fig. 8). This shows that the innermost region of the LMC has the most elongated shape. This effect may not be entirely physical due to the residual blends which may cause the central ellipsoids to be more elongated along the line-of-sight. It is not possible to state how big this effect is, and whether it is entirely due to the crowding and blending effects, or the inner parts of the LMC are truly elongated as shown in the plots.

The largest ellipsoid has axis ratio $1 : 1.250 : 1.378$. We intentionally chose $\log(n) = 0.0 - 0.4 \text{ kpc}^{-3}$ as the largest ellipsoid because $\log(n) = -0.5 - 0.0 \text{ kpc}^{-3}$ stretches farther than the OGLE-IV fields and may not represent physical results. With increasing a , i is also increasing, but P.A. is decreasing (see Fig. 8). For $\log(n) = 0.0 - 0.4 \text{ kpc}^{-3}$: $i = 36^{\circ}61$ and $\text{P.A.} = -57^{\circ}32$. The largest ellipsoids are less stretched, their longest axes are more inclined and rotated differently. The median axis ratio is $1 : 1.23 : 1.45$.

Fig. 9 shows projections of the ellipsoids in the Cartesian space. Red line connects the LMC and SMC distribution centers. Larger ellipsoids do not evidently twist toward the SMC although the increasing P.A. suggests so. On the other hand,

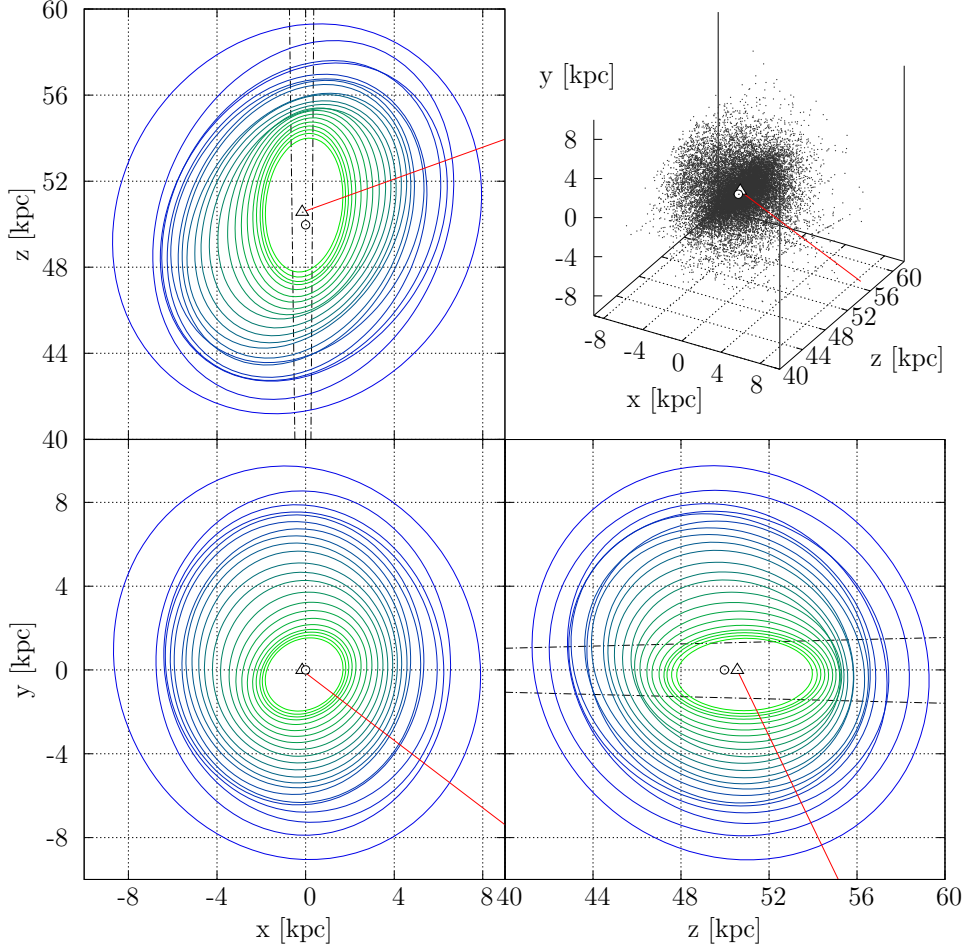


Fig. 9. Best-fit triaxial ellipsoids for the LMC data. Dash-dotted lines on the xz and yz planes represent area from where the RRL stars were excluded ($1^\circ 5$ angular radius from the LMC distribution center). Colors are compatible with Fig. 8. White circle and triangle mark the LMC dynamical and distribution centers, respectively. Red line connects the LMC and SMC distribution centers.

the xz and yz projections demonstrate that the LMC halo is stretched toward its smaller neighbor more than the inner parts.

The last three columns of Table 3 represent Right Ascension, Declination and distance of the ellipsoids' centers. We have additionally presented the Cartesian space projections of those centers in Fig. 10. Red line connects the LMC and SMC centers while the black line denotes the LMC – Milky Way centers connection. Green points stand for the smallest ellipsoids, while blue points for the largest. From Fig. 10 it is clearly visible that with increasing RRL stars number the center moves farther away from the SMC – in the opposite direction. This is consistent with our conclusions from Section 4.3. The LMC's farthest parts are more numerous in north-eastern parts of this galaxy.

Table 3
Triaxial ellipsoid best-fit parameters for the LMC

$\log(n \text{ [kpc}^{-3}\text{]})$	a [kpc]	b/a	c/a	i [deg]	P.A. [deg]	α_0 [deg]	δ_0 [deg]	d_0 [kpc]
2.15–2.2	1.606 ± 0.006	1.168 ± 0.006	1.950 ± 0.022	7.03 ± 0.37	19.57 ± 2.79	80.100 ± 0.014	−69.833 ± 0.005	50.891 ± 0.014
2.1–2.15	1.721 ± 0.006	1.180 ± 0.007	1.946 ± 0.021	6.30 ± 0.30	12.90 ± 2.93	80.107 ± 0.015	−69.842 ± 0.005	50.881 ± 0.014
2.05–2.1	1.833 ± 0.007	1.187 ± 0.006	1.933 ± 0.020	6.61 ± 0.34	18.21 ± 2.51	80.077 ± 0.018	−69.835 ± 0.006	50.860 ± 0.014
2.0–2.05	1.967 ± 0.007	1.187 ± 0.006	1.883 ± 0.019	6.95 ± 0.37	16.15 ± 2.22	80.094 ± 0.018	−69.838 ± 0.006	50.879 ± 0.013
1.9–2.0	2.143 ± 0.007	1.185 ± 0.006	1.829 ± 0.014	7.86 ± 0.32	8.95 ± 2.08	80.073 ± 0.018	−69.837 ± 0.006	50.856 ± 0.012
1.8–1.9	2.394 ± 0.008	1.177 ± 0.006	1.750 ± 0.013	9.10 ± 0.40	7.17 ± 2.08	80.090 ± 0.019	−69.835 ± 0.006	50.787 ± 0.013
1.7–1.8	2.671 ± 0.011	1.165 ± 0.007	1.655 ± 0.014	11.21 ± 0.47	4.82 ± 2.17	80.074 ± 0.024	−69.779 ± 0.008	50.746 ± 0.016
1.6–1.7	2.941 ± 0.012	1.167 ± 0.008	1.592 ± 0.015	12.32 ± 0.52	−10.15 ± 2.95	80.128 ± 0.026	−69.724 ± 0.011	50.672 ± 0.020
1.5–1.6	3.251 ± 0.014	1.165 ± 0.008	1.511 ± 0.015	15.69 ± 0.77	−15.06 ± 3.32	80.199 ± 0.032	−69.633 ± 0.013	50.596 ± 0.025
1.4–1.5	3.504 ± 0.021	1.196 ± 0.011	1.469 ± 0.013	24.36 ± 1.19	−32.53 ± 2.91	80.447 ± 0.036	−69.505 ± 0.016	50.485 ± 0.029
1.3–1.4	3.778 ± 0.024	1.199 ± 0.011	1.453 ± 0.015	26.22 ± 1.34	−30.21 ± 3.20	80.681 ± 0.046	−69.460 ± 0.019	50.376 ± 0.031
1.2–1.3	4.041 ± 0.027	1.209 ± 0.012	1.447 ± 0.014	29.60 ± 1.70	−39.00 ± 2.39	80.906 ± 0.046	−69.393 ± 0.021	50.277 ± 0.035
1.1–1.2	4.249 ± 0.030	1.246 ± 0.012	1.469 ± 0.013	32.86 ± 1.73	−44.59 ± 2.32	80.975 ± 0.052	−69.268 ± 0.023	50.258 ± 0.036
1.0–1.1	4.424 ± 0.027	1.265 ± 0.012	1.478 ± 0.013	36.91 ± 1.62	−44.82 ± 2.23	81.159 ± 0.050	−69.207 ± 0.024	50.168 ± 0.034
0.9–1.0	4.755 ± 0.035	1.227 ± 0.013	1.465 ± 0.017	35.67 ± 1.85	−52.58 ± 2.28	81.202 ± 0.069	−69.141 ± 0.032	50.135 ± 0.042
0.8–0.9	4.921 ± 0.046	1.263 ± 0.016	1.451 ± 0.022	33.84 ± 2.51	−52.43 ± 3.78	81.229 ± 0.090	−69.131 ± 0.038	50.072 ± 0.054
0.7–0.8	5.277 ± 0.060	1.232 ± 0.018	1.365 ± 0.023	43.65 ± 3.44	−55.88 ± 4.50	81.072 ± 0.104	−69.152 ± 0.044	50.163 ± 0.061
0.6–0.7	5.495 ± 0.059	1.218 ± 0.018	1.394 ± 0.020	38.86 ± 2.51	−58.67 ± 3.22	81.116 ± 0.125	−69.033 ± 0.039	49.930 ± 0.052
0.5–0.6	5.851 ± 0.091	1.190 ± 0.025	1.382 ± 0.030	37.82 ± 3.99	−48.89 ± 5.23	80.527 ± 0.208	−69.162 ± 0.069	50.166 ± 0.096
0.4–0.5	5.967 ± 0.099	1.197 ± 0.031	1.408 ± 0.033	47.63 ± 3.48	−59.03 ± 5.08	80.147 ± 0.250	−69.243 ± 0.080	50.098 ± 0.081
0.0–0.4	6.430 ± 0.064	1.250 ± 0.018	1.378 ± 0.020	36.61 ± 3.37	−57.32 ± 5.21	80.216 ± 0.169	−69.215 ± 0.062	50.199 ± 0.058
−0.5–0.0*	8.001 ± 0.204	1.111 ± 0.033	1.249 ± 0.036	53.99 ± 6.00	−63.25 ± 7.19	81.201 ± 0.682	−69.181 ± 0.156	50.253 ± 0.095

*This ellipsoid may not represent physical results due to its size extending farther than the OGLE-IV sky coverage in the east.

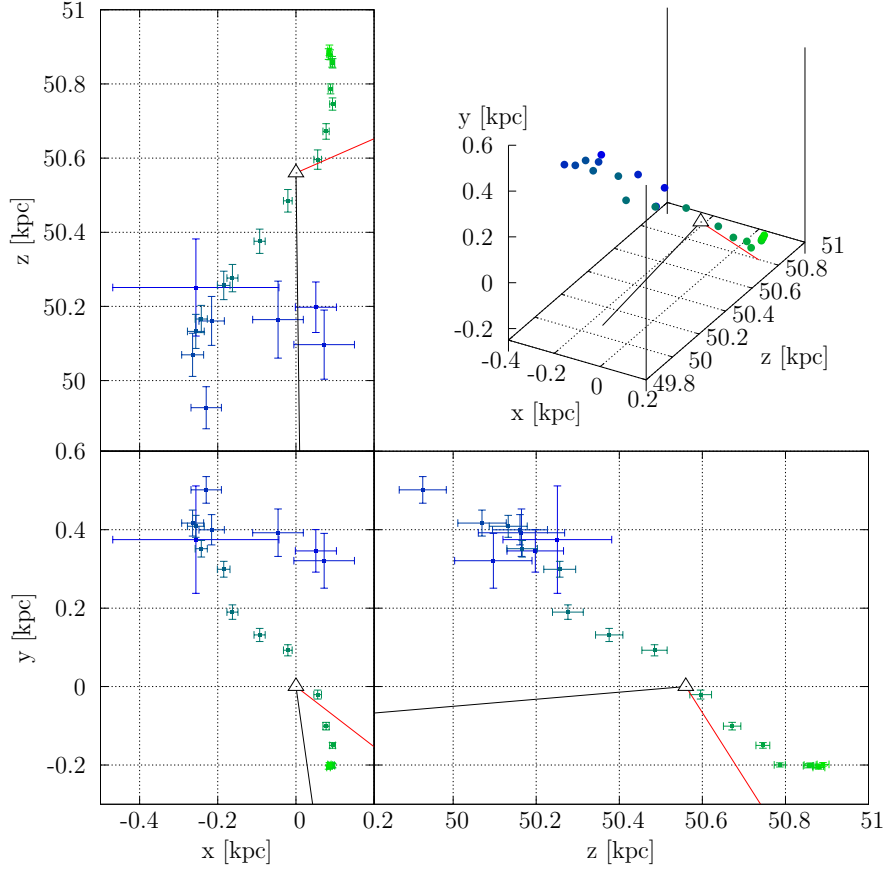


Fig. 10. Best-fit triaxial ellipsoid centers in Cartesian coordinates projections for the LMC data. Colors are compatible with Figs. 8 and 9. White triangle marks the RRL stars distribution center. Red line connects the LMC and SMC distribution centers and black line connects the LMC distribution center with the Milky Way center (Boehle *et al.* 2016).

4.3. Comparison with Previous Studies

Table 4 shows a comparison of RRL stars sample modeling parameters in different studies. The b/a ratio obtained from the OGLE-III data was larger than values presented in this work even for the smallest ellipsoids (*i.e.*, $\log(n) = 2.15 - 2.2 \text{ kpc}^{-3}$). The closest result to ours was presented by Pejcha and Stanek (2009) by removing RRL stars outside 250 per square degree contour. The differences may also be caused by the removal of stars located within the angular radius of $1^\circ 5$ from the LMC center from our sample.

The c/a ratio (of the shortest to the longest ellipsoid axis) is also smaller in our analysis, *i.e.*, our ellipsoids are less stretched, and this difference is even more prominent. It may be due to the restricted OGLE-III coverage or/and the LMC blend-artifact that may distort the results. The inclination angle for larger ellipsoids

Table 4
Parameters of the LMC RRL stars modeling from literature

Reference	b/a	c/a	i [deg]	P.A. [deg]	Data
Pejcha and Stanek (2009)	2.00	3.50	6	113.4	OGLE-III RRab Removed RRab outside 250 per square degree contour Additional color cut
	1.36	3.53	3	–	
	1.99	3.14	9	–	
Subramaniam and Subramanian (2009)	–	–	31.3 ± 3.5	125 ± 17	OGLE-III RRL stars on-sky projection Included extra-planar features
	–	–	20.8 ± 3.5	–	
Haschke <i>et al.</i> (2012a)	–	–	32 ± 4	114 ± 13	OGLE-III RRab on-sky projection Innermost 3° from optical center RRL stars $\in (3^\circ, 7^\circ)$ from optical center
	–	–	–	102 ± 21	
	–	–	–	122 ± 32	
Deb and Singh (2014)	1.67	4.07	24.20	176.01	OGLE-III RRab OGLE-III RRab plane fitting $ z = 10$ kpc
	–	–	36.43	149.08	
van der Marel and Kallivayalil (2014)	–	–	34.0 ± 7.0	139.1 ± 4.1	Proper motions + old pop. LOS velocity
This work: $\log(n) = 2.15-2.2 \text{ kpc}^{-3}$ This work: $\log(n) = 1.3-1.4 \text{ kpc}^{-3}$ This work: $\log(n) = 0.0-0.4 \text{ kpc}^{-3}$	1.168 ± 0.006	1.950 ± 0.022	7.03 ± 0.37	19.57 ± 2.79	OGLE-IV RRab
	1.199 ± 0.011	1.453 ± 0.015	26.22 ± 1.34	-30.21 ± 3.20	
	1.250 ± 0.018	1.378 ± 0.020	36.61 ± 3.37	-57.32 ± 5.21	

For comparison with other tracers see Table 7 in Paper I.

is well correlated with the literature values, not only for the RRL stars but also for other tracers (see Table 7 in Paper I). The position angle is slightly correlated only for larger ellipsoids.

Fig. 4 from Pejcha and Stanek (2009) shows a bar-like structure, that seems to emerge from the center of the LMC and is elongated along the line-of-sight (along the z axis). Other studies showed that there is an evident overdensity in the LMC center (Subramaniam and Subramanian 2009, Haschke *et al.* 2012a). Fig. 2 from Haschke *et al.* (2012a) also seems to show that this overdensity is elongated along the line-of-sight and forms a bar-like structure (see Fig. 5 in Haschke *et al.* 2012a where the RRL stars in the closer bins seem to form the bar). Subramaniam and Subramanian (2009) state that this RRL bar-like structure may also aid understanding the LMC bar evolution suggesting that there must have been a prominent star formation episode that led to the formation of the LMC disk. Moreover, that study suggested that the LMC RRL stars were formed in the disk rather than in the halo.

Our analysis sheds new light on these conclusions based on the central LMC regions. Because the LMC blend-artifact is very prominent and hard to remove, and was not easily distinguishable within the OGLE-III data, it may have been mistakenly treated as the LMC bar. We argue that the LMC RRL stars distribution does not have a bar, or if there is one, it is not as prominent as previously thought and a very careful analysis is needed to extract it from the crowded central areas of the galaxy.

Subramaniam and Subramanian (2009) obtained the inclination and position angle of their RRL stars sample very similar to that of the LMC disk and concluded that most of the LMC RRL stars constitute a non-spherical structure, while the rest form an inflated structure. This double-structured RRL stars distribution was later confirmed by Deb and Singh (2014) based on the metallicity analysis of the LMC RRL stars. They found that the RRL stars form the disk and the inner halo. The LMC RRL stars inner halo was also suggested by Subramaniam and Subramanian (2009). Our analysis of the three-dimensional distribution of the RRL stars does not support these findings. Similarly as Pejcha and Stanek (2009) and Haschke *et al.* (2012a), we do not see any extra-planar substructures toward north-east that could be an extension of the disk. On the other hand, change in the elongation between the innermost and outermost ellipsoids may reflect the double nature of the LMC RRL stars distribution (the disk and the inner halo), but our innermost ellipsoids are not disk-like (see Fig. 9). Again, the elongation of the central ellipsoids along the line-of-sight may be affected by residual blends in our data.

5. The Small Magellanic Cloud

5.1. Three-Dimensional Structure

In the case of the SMC, RRL stars density in the center is much lower, so crowding and blending effects are mild, allowing us to study the galaxy's central regions in detail and compare our results with the literature. Similarly as its larger

neighbor, the SMC also has a regular, ellipsoidal or nearly spheroidal shape (Kapakos *et al.* 2011, Subramanian and Subramanian 2012, Kapakos and Hatzidimitrou 2012, Haschke *et al.* 2012b, Deb *et al.* 2015). In this section, we concentrate on the three-dimensional analysis of the SMC using the OGLE-IV Collection of RRL stars which, in contrast to the OGLE-III Catalog, covers a very extended area around the SMC (see upper panel in Fig. 5 where the OGLE-IV fields sky coverage and the SMC are presented).

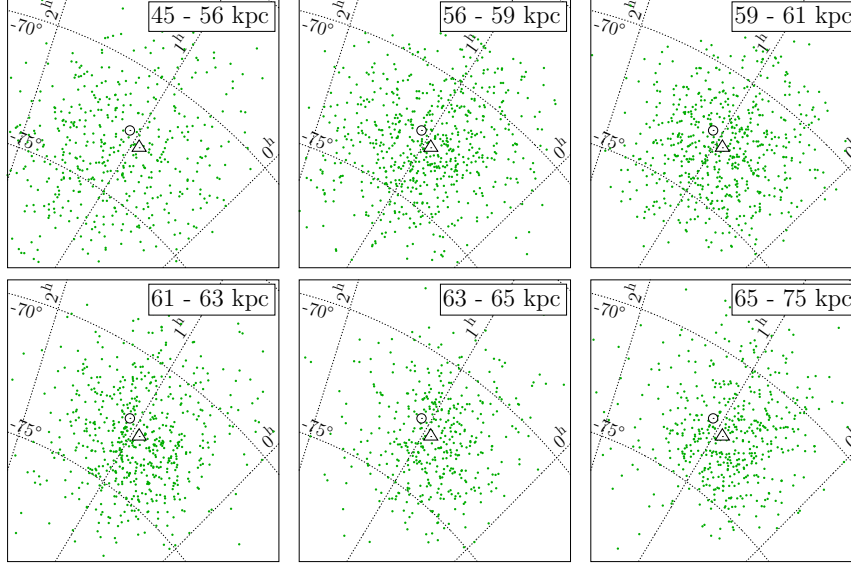


Fig. 11. Distance tomography of the RRL stars distribution in the SMC in the Hammer equal-area projection. Note different distance ranges. White circle marks the SMC dynamical center. White triangle marks the RRL stars distribution maxima along the RA and Dec axes.

Our data show that the SMC has a very regular shape in three-dimensions (see Fig. 4). Also, the on-sky projection of the SMC does not present any evident irregularities (see Fig. 5). We decided to slice-up this galaxy in distance bins in order to see its genuine structure along the line-of-sight. The distance tomography is shown in Fig. 11. White circle shows the SMC dynamical center (Stanimirović *et al.* 2004) while white triangle shows the SMC RRL stars distribution center. The latter was estimated in three dimensions using the maxima of the Right Ascension, Declination and distance RRL stars distribution which are $\tilde{\alpha}_{\text{SMC}} = 0^{\text{h}}55^{\text{m}}48^{\text{s}}0$, $\tilde{\delta}_{\text{SMC}} = -72^{\circ}46'48''$, $\tilde{d}_{\text{SMC}} = 60.45$ kpc. The median SMC RRL stars distance based on our data is $d_{\text{SMC,med}} = 60.58$ kpc. The on-sky distribution center parameters are significantly shifted with respect to the dynamical SMC center which are: $\alpha_{\text{SMC-cen}} = 1^{\text{h}}05^{\text{m}}$, $\delta_{\text{SMC-cen}} = -72^{\circ}25'12''$ (Stanimirović *et al.* 2004). The distribution distance maximum and the median RRL stars distance are also different from the mean SMC distance obtained from eclipsing binaries by Graczyk *et al.* (2014), which is $d_{\text{SMC}} = 62.1 \pm 1.9$ kpc.

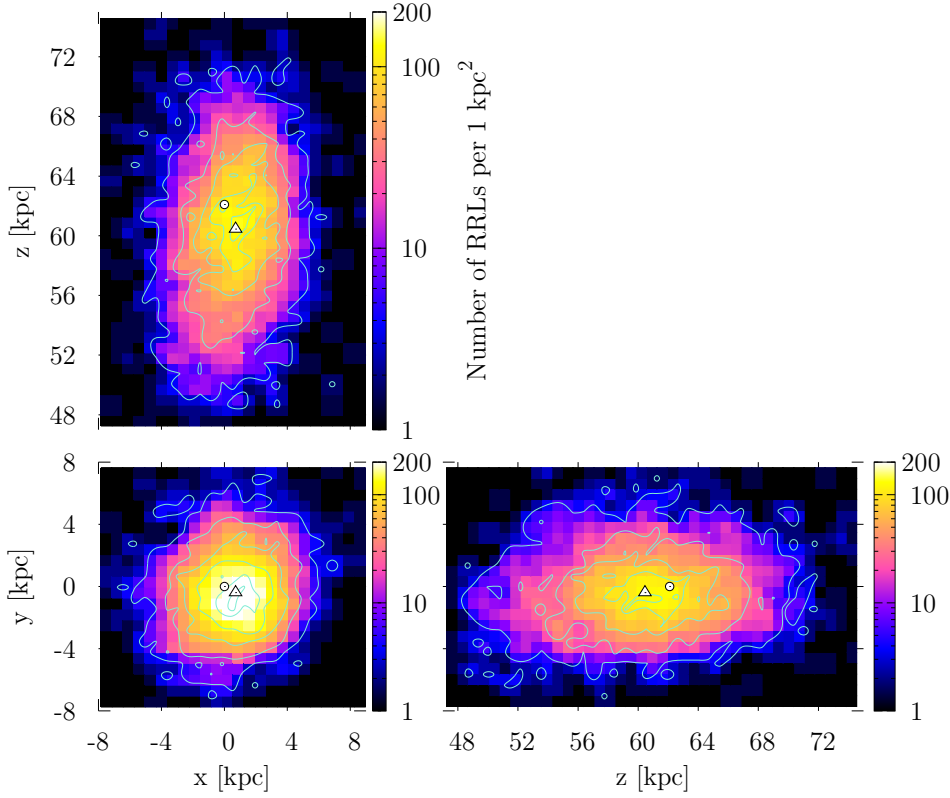


Fig. 12. RRL stars column density maps in the SMC in the Cartesian coordinates (the z axis is pointing toward the SMC dynamical center). Bin size is 0.7 kpc in x , y , and z axis. Contour levels on the xy plane are 5, 30, 70, 120, 200, 260, on the xz and yz 5, 30, 60, 100, 130 RRL stars per 1 kpc². White circle and triangle mark the SMC dynamical and distribution centers, respectively.

The closest RRL stars in the SMC are spread evenly on the sky – this is shown in the first panel of Fig. 11. Next three panels presenting RRL stars around the SMC mean distance do not suggest any asymmetries or substructures. Last two panels showing the most distant SMC RRL stars reveal that they are slightly more numerous in the south-western part of the galaxy than in the north-eastern part.

Fig. 12 shows RRL stars distribution in three dimensions. Bottom left panel shows the SMC as a regularly, near spheroidally shaped galaxy. *Soszyński et al.* (2010, see their Fig. 7) and *Haschke et al.* (2012b, see their Fig. 1) noticed that there are two overdensities in the SMC center, on-sky projection. A similar feature is visible in the on-sky projection in the OGLE-IV data (see Fig. 16), but it is not seen in the three-dimensional Cartesian column density maps (see Fig. 12). Thus this may be a projection effect. Views “from the top” (xz plane) and “from the side” (yz plane) demonstrate an elongation of the SMC. This galaxy is stretched almost along the line-of-sight and its shape is ellipsoidal. No substructures or evident irregularities can be derived from Fig. 12.

5.2. Ellipsoid Fitting

As a result of the analysis from Section 5.1, we decided to model the SMC RRL stars distribution as a triaxial ellipsoid. The details of the fitting procedure are given in Section 3.4. We divided the SMC RRL stars into eleven bins consisting of 126 to 356 stars. The detailed results of the modeling are presented in Table 5 and in Figs. 13, 14, and 15.

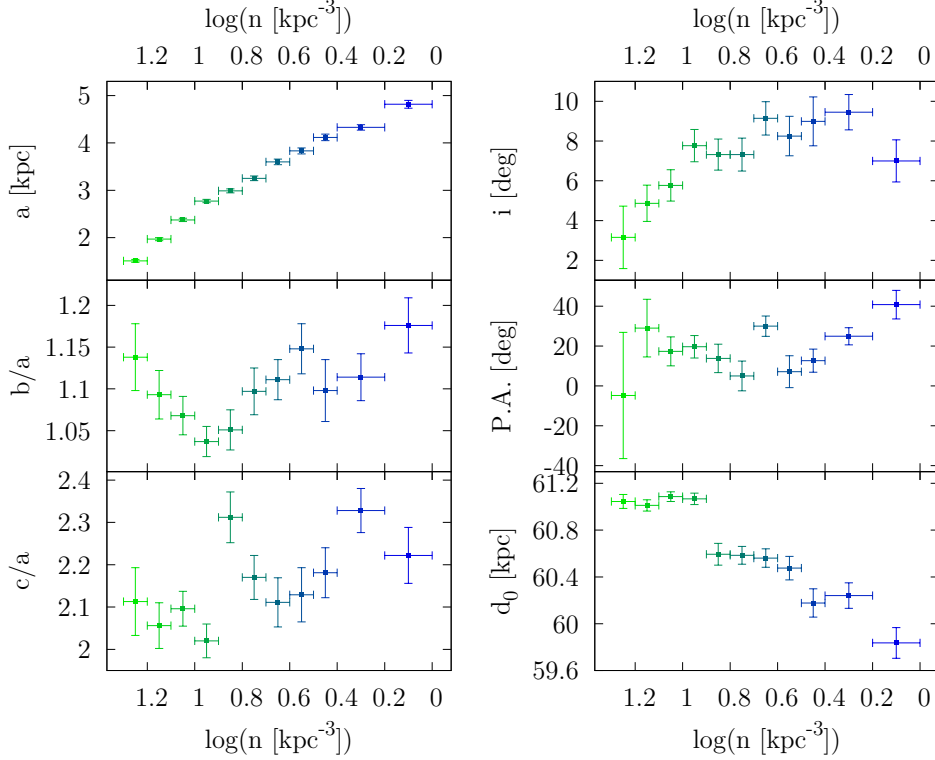


Fig. 13. Parameters of the best-fit triaxial ellipsoids for the SMC RRL stars. Green points represent the innermost ellipsoids while blue points – the outermost.

From Table 5 and Fig. 13 we see that for ellipsoids with decreasing $\log(n)$ (increasing a axis size) both b/a and c/a ratios neither increase nor decrease and do not change significantly. This means that all ellipsoids have virtually the same shape. The median axis ratio is 1 : 1.10 : 2.13. The inclination angle appears to slightly decrease from 9° to 3° in the central regions of the SMC. Because the inclination is small, the position angle (P.A.) of the major axis is not well-defined, varying from -5° to 41° .

Fig. 14 shows a three dimensional Cartesian space projections of the SMC ellipsoids. Both xy and xz planes suggest that the outer parts of the SMC are more rotated toward the LMC than the inner parts, although the difference is not very significant and is not visible on a yz plane. The SMC ellipsoids are elongated al-

Table 5

Triaxial ellipsoid best-fit parameters for the SMC

$\log(n [\text{kpc}^{-3}])$	a [kpc]	b/a	c/a
1.2–1.3	1.510 ± 0.031	1.138 ± 0.040	2.113 ± 0.080
1.1–1.2	1.969 ± 0.033	1.093 ± 0.029	2.056 ± 0.054
1.0–1.1	2.375 ± 0.034	1.068 ± 0.023	2.096 ± 0.041
0.9–1.0	2.773 ± 0.035	1.037 ± 0.018	2.020 ± 0.040
0.8–0.9	2.987 ± 0.042	1.051 ± 0.024	2.312 ± 0.060
0.7–0.8	3.253 ± 0.049	1.097 ± 0.028	2.170 ± 0.052
0.6–0.7	3.600 ± 0.059	1.111 ± 0.024	2.111 ± 0.058
0.5–0.6	3.832 ± 0.063	1.148 ± 0.030	2.129 ± 0.064
0.4–0.5	4.117 ± 0.069	1.098 ± 0.037	2.181 ± 0.059
0.2–0.4	4.328 ± 0.058	1.114 ± 0.028	2.328 ± 0.052
0.0–0.2	4.817 ± 0.083	1.176 ± 0.033	2.222 ± 0.066
$\log(n [\text{kpc}^{-3}])$	i [deg]	P.A. [deg]	
1.2–1.3	3.16 ± 1.57	-4.82 ± 31.68	
1.1–1.2	4.87 ± 0.91	29.00 ± 14.44	
1.0–1.1	5.77 ± 0.79	17.33 ± 7.29	
0.9–1.0	7.77 ± 0.81	19.65 ± 5.62	
0.8–0.9	7.32 ± 0.78	13.82 ± 7.13	
0.7–0.8	7.32 ± 0.83	5.00 ± 7.49	
0.6–0.7	9.14 ± 0.84	29.97 ± 5.10	
0.5–0.6	8.25 ± 0.99	7.13 ± 8.03	
0.4–0.5	8.99 ± 1.23	12.68 ± 5.80	
0.2–0.4	9.45 ± 0.89	24.91 ± 4.28	
0.0–0.2	7.00 ± 1.06	40.77 ± 7.15	
$\log(n [\text{kpc}^{-3}])$	α_0 [deg]	δ_0 [deg]	d_0 [kpc]
1.2–1.3	13.452 ± 0.115	-72.987 ± 0.023	61.045 ± 0.060
1.1–1.2	13.581 ± 0.084	-72.993 ± 0.026	61.011 ± 0.048
1.0–1.1	13.534 ± 0.085	-72.985 ± 0.023	61.086 ± 0.041
0.9–1.0	13.320 ± 0.095	-72.958 ± 0.026	61.067 ± 0.049
0.8–0.9	13.951 ± 0.113	-73.000 ± 0.036	60.594 ± 0.093
0.7–0.8	14.009 ± 0.116	-72.985 ± 0.035	60.585 ± 0.076
0.6–0.7	14.068 ± 0.133	-72.894 ± 0.037	60.561 ± 0.079
0.5–0.6	13.929 ± 0.149	-72.874 ± 0.047	60.475 ± 0.101
0.4–0.5	14.427 ± 0.221	-73.048 ± 0.065	60.177 ± 0.121
0.2–0.4	14.697 ± 0.187	-72.876 ± 0.050	60.240 ± 0.109
0.0–0.2	14.727 ± 0.195	-72.877 ± 0.070	59.836 ± 0.131

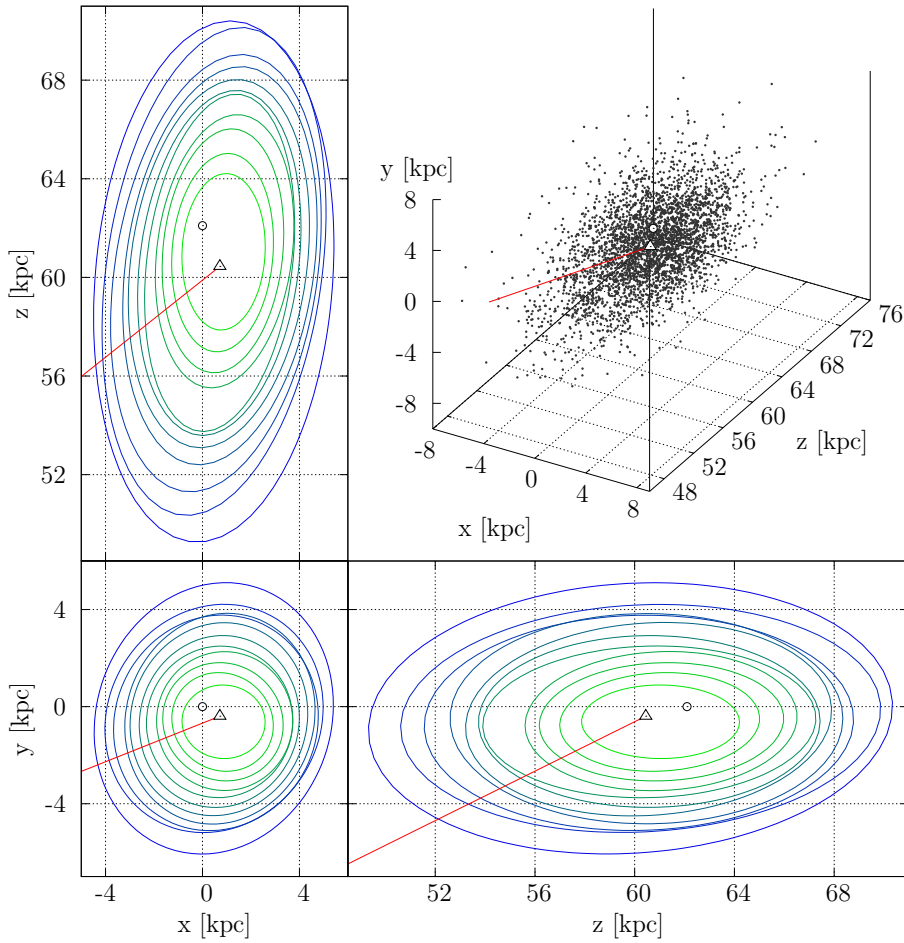


Fig. 14. Best-fit triaxial ellipsoids for the SMC data. Colors are compatible with Fig. 13. White circle and triangle mark the SMC dynamical and distribution centers, respectively. Red line connects LMC and SMC distribution centers.

most along the line-of-sight, as already shown in Fig. 12. Moreover, rotation of larger ellipsoids on the xy plane toward the LMC may also suggest that there is an overdensity located near the SMC Wing.

The Cartesian space projections of the ellipsoid centers are shown in Fig. 15. Green points denote the smallest ellipsoids while blue – the largest. It is clearly visible that the larger the ellipsoid is the closer its center is located to the observer (see also Table 5 and Fig. 13). Moreover, with increasing a axis size the Right Ascension of the ellipsoid center rises while the Declination does not show tendency to increase or decrease distinctly. This is reflected in the Cartesian space projections where centers of larger ellipsoids are located closer to the LMC. This trend may be caused by the overdensity in the SMC Wing area or/and the interactions between the Magellanic Clouds.

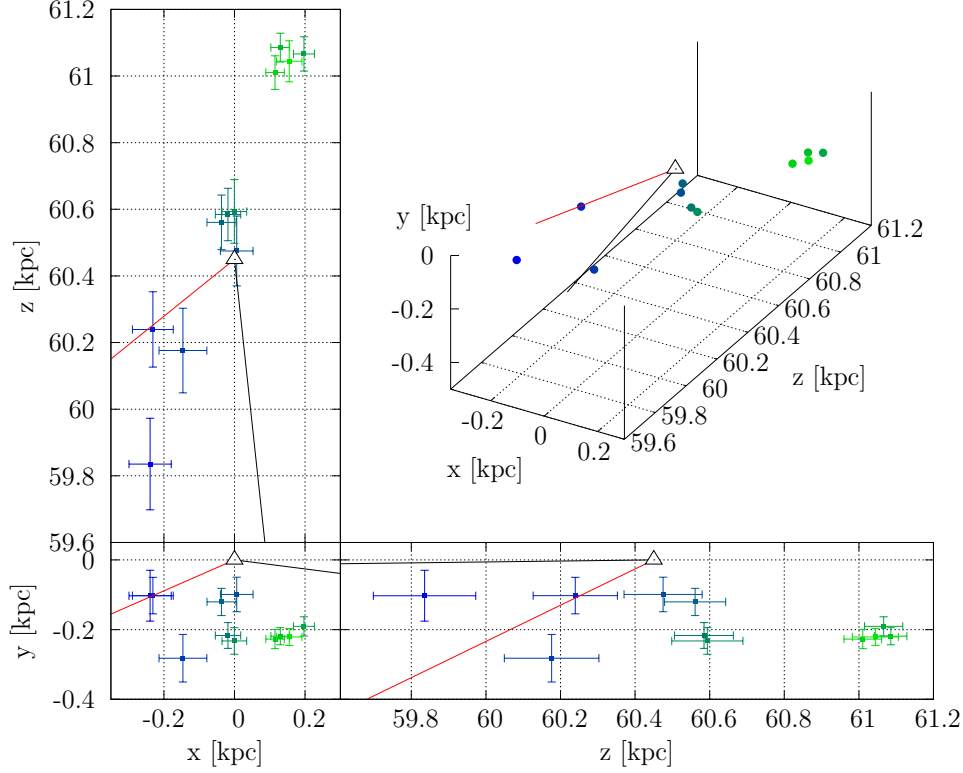


Fig. 15. Best-fit triaxial ellipsoids centers in the Cartesian coordinates projections for the SMC data. Colors are compatible with Fig. 13 and 14. White triangle marks the RRL stars distribution center. Red line connects the LMC and SMC distribution centers and black line connects the SMC center with the Milky Way center (Boehle *et al.* 2016).

5.3. Comparison with Previous Studies

A comparison between results obtained in this work and in other studies is presented in Table 6. Our value of b/a ratio is quite well compatible with those calculated for the OGLE-III RRL stars data. The best correlation is for restricted samples (*i.e.*, RRL stars within $r < 0.75$ in Subramanian and Subramanian 2012 or the SMC main body in Deb *et al.* 2015). The differences are caused by the limited OGLE-III sky coverage. On the other hand, c/a ratio is not that well correlated. The closest values were also the ones obtained for restricted samples (*i.e.*, RRL stars located within equal extent in x , y , and z in Subramanian and Subramanian 2012 or within spherical cells in Kapakos and Hatzidimitrou 2012). Other values suggested very elongated ellipsoids. This is probably again due to the smaller area observed by OGLE-III.

We also compare tilt parameters in Table 6. The inclination angle calculated for the OGLE-IV data is compatible with values obtained for the OGLE-III data. These values fall into the range $0^\circ - 7^\circ$. As we have already mentioned, small value

Table 6

Parameters of the SMC RRL stars modeling from literature

Reference	b/a	c/a	i [deg]	P.A. [deg]	Data
Subramanian and Subramaniam (2012)	1.17	1.28	4.2	67.5	OGLE-III RRL stars equal extent in x, y and z : $r < 2^\circ 0$
	1.24	1.39	3.3	69.5	Equal extent in x, y and z : $r < 2^\circ 5$
	1.33	1.61	2.6	70.2	Equal extent in x, y and z : $r < 3^\circ 0$
	1.07	20.01	0.5	48.84	$r < 0^\circ 75$
	1.30	8.00	0.1	64.87	$r < 2^\circ 00$
	1.33	6.47	0.3	74.40	$r < 3^\circ 00$
	1.05	19.84	0.4	78.83	Excluded 3 NW fields, $r < 0^\circ 75$
	1.34	8.21	0.1	66.00	Excluded 3 NW fields, $r < 2^\circ 00$
	1.57	7.71	0.4	65.96	Excluded 3 NW fields, $r < 3^\circ 00$
	Haschke <i>et al.</i> (2012b)	–	–	7 ± 15	83 ± 21
Kapakos and Hatzidimitrou (2012)	1.21	1.57	–	–	OGLE-III RRab within spherical cell 2.5 kpc
	1.18	1.53	–	–	Within spherical cell 3 kpc
	1.23	1.80	–	–	Within spherical cell 3.5 kpc
Deb <i>et al.</i> (2015)	1.310 ± 0.029	8.269 ± 0.934	2.265 ± 0.784	74.307 ± 0.509	OGLE-III RRab
	1.185 ± 0.001	9.411 ± 0.860	0.507 ± 0.287	55.966 ± 0.814	The SMC main body
This work: $\log(n) = 1.2-1.3 \text{ kpc}^{-3}$	1.138 ± 0.040	2.113 ± 0.080	3.16 ± 1.57	-4.82 ± 31.68	OGLE-IV RRab
	1.097 ± 0.028	2.170 ± 0.052	7.32 ± 0.83	5.00 ± 7.49	
	1.176 ± 0.033	2.222 ± 0.066	7.00 ± 1.06	40.77 ± 7.15	

of i makes P.A. not well defined and we should not rely on a comparison of this parameter. Even though, the P.A. derived from our sample seems to be smaller than the ones from the OGLE-III RRL stars.

We do not see any indicators of a bulge or a bar, similarly to Subramanian and Subramanian (2012) and Haschke *et al.* (2012b). Our equal-density ellipsoids based on the OGLE-IV data that cover a very extended area around the SMC are all elongated along the line-of-sight and have almost the same axis ratio. This means that the shape of the distribution does not change with distance from the center (see Fig. 14). Thus the elongation along the line-of-sight and so the higher line-of-sight depth might not indicate the presence of a bulge as Deb *et al.* (2015) stated, and as Subramanian and Subramanian (2009) deduced from their analysis of the red clump and RRL stars depth profile.

Many studies revealed that the north-eastern part of the SMC is located closer to us than the SMC main body (Subramanian and Subramanian 2012, Haschke *et al.* 2012b, Deb *et al.* 2015). Our data do not support this as we do not see any irregularities in the SMC structure that may cause a difference in the mean distance between some part of this galaxy and the rest (see *i.e.*, Fig. 12). This may be caused by the extended OGLE-IV sky coverage in comparison to the OGLE-III. On the other hand, we do see some asymmetries of the equal-density contours (Figs. 12 and 14) that may cause such effect.

6. The Magellanic Bridge

We do see some RRL stars located between the Magellanic Clouds (see Figs. 4 and 5), although they seem to belong to the halos of the two galaxies. This is not the first time old stars are observed there (Bagheri *et al.* 2013), although we are the first to show a three dimensional distribution of an old population in the Magellanic Bridge, represented by RRL stars. Because of the LMC's halo irregularities and the OGLE-IV limited sky coverage around the outskirts of this galaxy that we described above it is very difficult to statistically analyze the area between the Clouds. That is, it is practically impossible to separate the Bridge RRL stars from the LMC and SMC halos without having a good model of the LMC outermost halo, especially that the density of RRL stars in the MBR area is small and any deviations from the LMC halo density profile would be lost in the noise. We can only state that these two halos are overlapping.

A column density map of the Magellanic Bridge (MBR) is shown in the left panel of Fig. 16 as an on-sky projection. The RRL stars column density is color-coded. The overdensity near the SMC Wing is visible on the right, at $\alpha \approx 2^{\text{h}}$, $\delta \approx -75^\circ$. There may seem to be an overdensity connecting the Clouds along $\text{Dec} \approx -75^\circ$ although as we have mentioned it is very difficult to analyze this area statistically and spectroscopic observations will be needed to tell the true origin of these RRL stars.

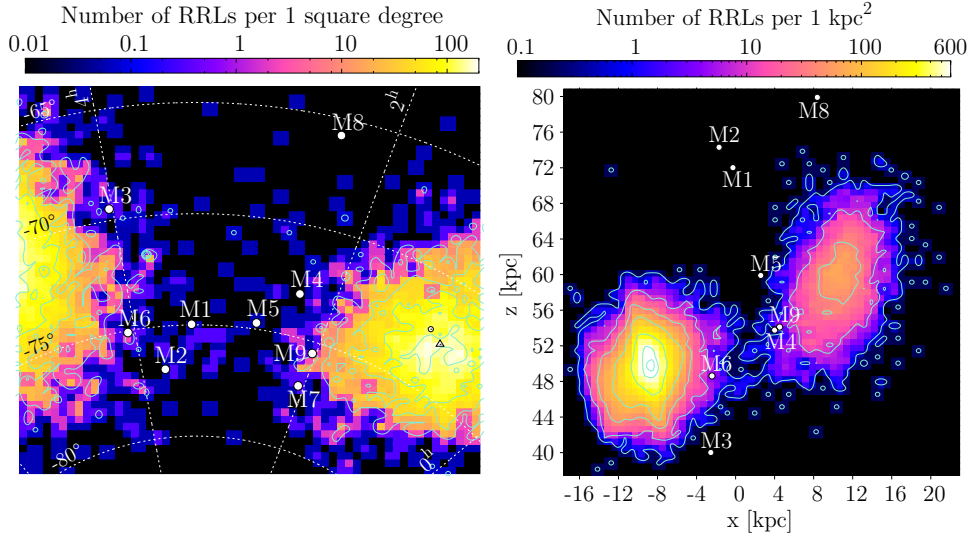


Fig. 16. *Left panel:* The on-sky projection of the binned RRL stars distribution in the Magellanic Bridge area (using Hammer equal-area projection). The RRL stars column density is color-coded. Additionally, the Classical Cepheids from Paper I are marked with white dots. The MBR CCs are represented with larger dots and labeled M1–M9 as in Paper I. *Right panel:* The xz plane of the Cartesian projection of RRL stars in the Magellanic System (view “from the top”). Bin size is 0.7 kpc in x , y , and z axis. Light green lines represent density contours, which levels are: 1, 10, 40, 100, 300, 600, 700 RRL stars per 1 kpc^2 .

Another view of the MBR area is presented in the right panel of Fig. 16. A column density map of the xz Cartesian space projection shows a “view from the top” of the entire Magellanic System. Additionally, density contours are plotted with light green lines. Extended SMC halo is fully pictured while the LMC outskirts reveal limited OGLE-IV sky coverage in the eastern parts of this galaxy. Without seeing the entire LMC outskirts we are unable to say if the stars that we see between the Clouds constitute the genuine MBR. Even though, we can definitely say that the LMC and SMC halos are overlapping.

7. Comparison with Distribution of the Classical Cepheids

In this section we compare the discussed distribution of the RRL stars with the distribution of the Classical Cepheids (CCs) that we analyzed in Paper I. The RRL stars represent an old stellar population while the CCs are young stars. Both types of objects in the entire Magellanic System are shown in Figs. 17 and 18. The former presents data in an on-sky equal-area Hammer projection, the latter in the three-dimensional Cartesian space projections.

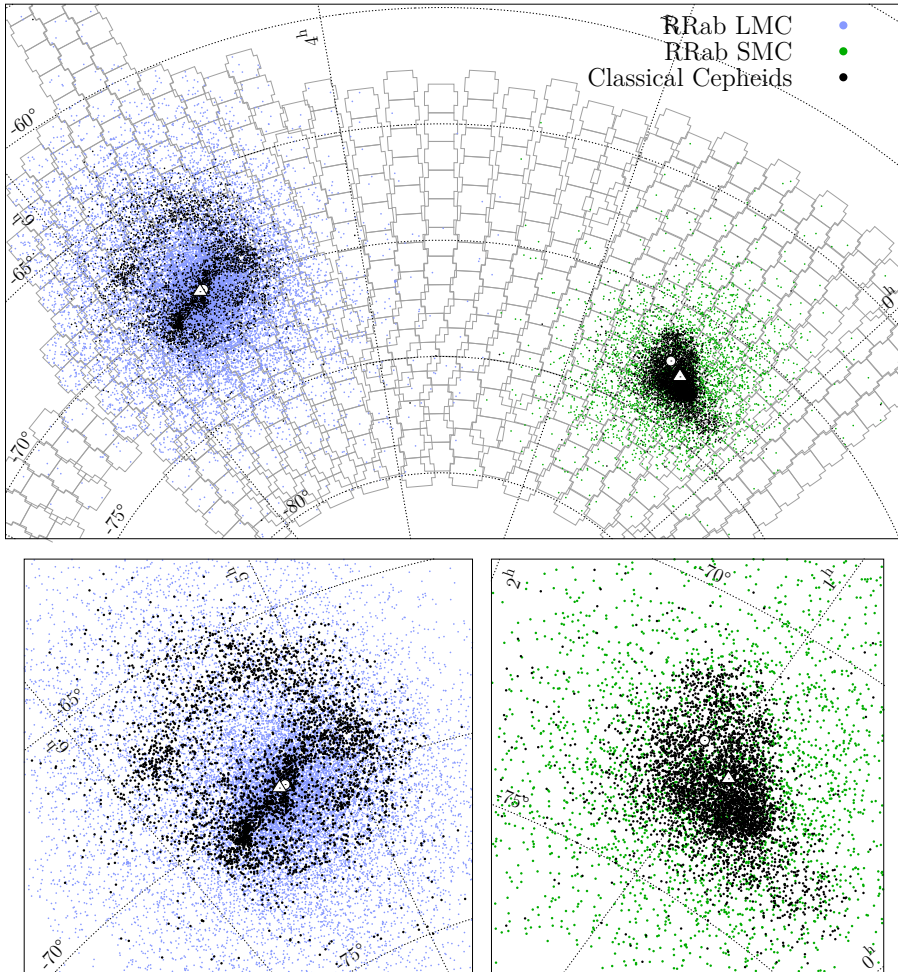


Fig. 17. The equal-area Hammer projection of the RRL stars in the Magellanic System – similar to Fig. 5 but Classical Cepheids from Paper I are overplotted with black dots. Blue dots mark the LMC RRL stars and green dots – the SMC RRL stars. White circles mark galaxies’ dynamical centers (Stanimirović *et al.* 2004, van der Marel and Kallivayalil 2014). White triangles mark RRL stars distribution centers.

7.1. The Large Magellanic Cloud

The most obvious difference between the CCs and RRL stars distributions in the LMC is their spread in the on-sky projection (see Fig. 17). The CCs are less spread than the RRL stars and are concentrated toward the galaxy center. The RRL stars are present in every OGLE-IV field and seem to be located even farther. There are more CCs than the RRL stars in the northern parts of the inner LMC, because of the well populated northern arm of this galaxy. The on-sky projection in Fig. 17 also shows that the CCs are located mainly in the LMC substructures: the bar and

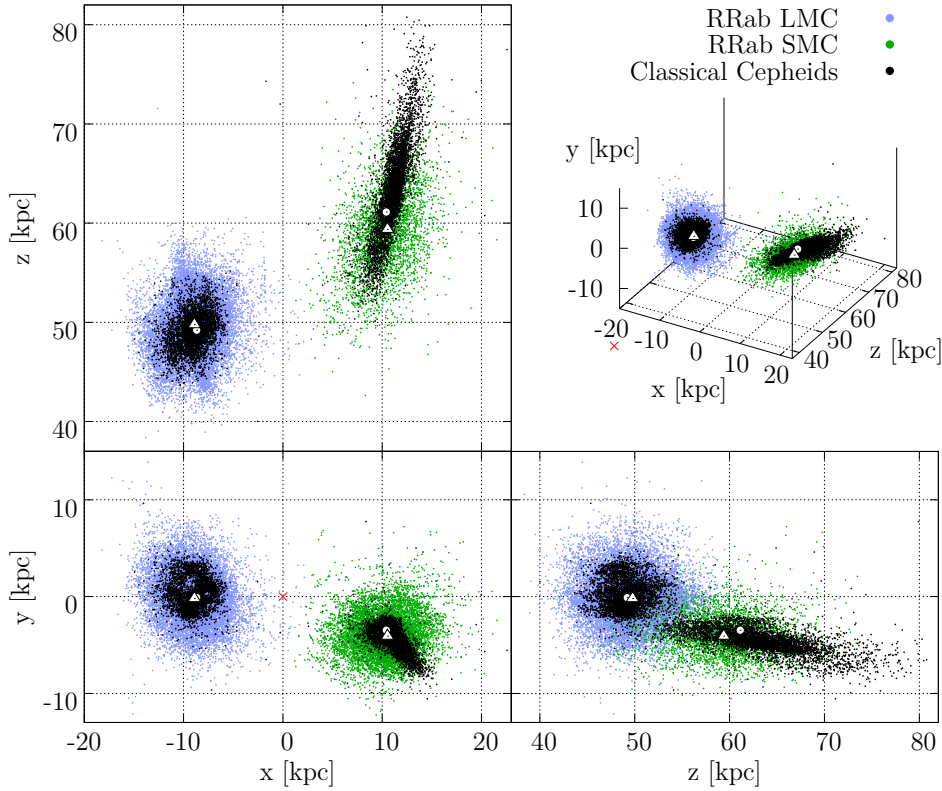


Fig. 18. The RRL stars in the Magellanic System in the Cartesian coordinates. The LMC stars are marked with blue dots, while the SMC stars – with green dots. Additionally, the Classical Cepheids from Paper I are overplotted with black dots. The white circle denotes the LMC (Pietrzyński *et al.* 2013, van der Marel and Kallivayalil 2014) and SMC (Stanimirović *et al.* 2004, Graczyk *et al.* 2014) dynamical centers. White triangles mark RRL stars distribution centers.

northern arm. The RRL stars are distributed definitely more smoothly and regularly and we do not see any evident substructures. The CCs distribution in the LMC can be modeled with a plane (see Paper I), while the RRL stars distribution is modeled as a triaxial ellipsoid that is far from being flat and so the LMC RRL stars may not be described as a plane.

The three-dimensional Cartesian space projections in Fig. 18 also show differences between the CCs and RRL stars distributions. The median distance of the LMC RRL stars is $d_{\text{RRL,med}} = 50.64$ kpc, while for the Cepheids it was $d_{\text{CC,med}} = 49.93$ kpc (see Table 4 in Paper I). These values are in good agreement within distance mean uncertainties and distance standard deviations, and a similar conclusion was reached by Haschke *et al.* (2012a). The xy plane represents a similar view to the on-sky projection from Fig. 18 that we have described above. View “from the top” (xz plane) again shows that the RRL stars distribution could not be described properly as a disk. Moreover, the CCs in the LMC were not as affected by crowding

and blending effects (see *i.e.*, Fig. 5 in Paper I) as the RRL stars. This is probably due to the fact that the RRL stars are fainter and have higher column density in the LMC center than the CCs. The yz plane only shows that the RRL stars are more spread than the CCs.

7.2. The Small Magellanic Cloud

Similarly as in the LMC, the RRL stars and CCs in the SMC are distributed differently. Again, older stars are more spread and form a regular structure in the on-sky projection, while younger stars are more clumped and concentrated near the galaxy center (see Fig. 17). The CCs seem to be more numerous in the southwestern part of the SMC.

The Cartesian coordinates projections in Fig. 18 show great differences between the RRL stars and CCs distributions in the SMC. The median distance of the RRL stars is $d_{\text{RRL,med}} = 60.58$ kpc and for the CCs it was $d_{\text{CC,med}} = 64.62$ kpc (see Table 8 in Paper I). This time the difference is larger than for the LMC and these values are not correlated within median distance uncertainties. Even though, they are within distance standard deviations. The difference may also be an effect of different methods of distance calculations for the CCs and RRL stars. The former were calculated relative to the LMC distance from Pietrzyński *et al.* (2013), assuming the same zeropoint of the P-L relation in both the LMC and SMC, while the latter were obtained independently of any other distance estimations. However, other studies show that the mean distance calculated for the RRLs is smaller than that for the CCs (Haschke *et al.* 2012b, de Grijs and Bono 2015) and this is in good agreement with our results.

The xy plane confirms that the RRL stars are more spread and constitute a very regular shape, while the CCs form a structure that is very elongated. The xz and yz projections demonstrate the SMC CCs shape that is stretched along the line-of-sight. In this direction the RRL stars do not reach that far and are less elongated than CCs, which is reflected in median distance differences.

7.3. The Magellanic Bridge

The RRL stars on-sky column density map of the Magellanic Bridge area showing also CCs locations is presented in the left panel of Fig. 16. The Bridge Cepheids are marked with large white dots and labeled M1–M9 (as in Paper I). Interestingly, their positions seem to be correlated with slightly higher RRL stars densities, especially those located along Declination $\approx -75^\circ$.

A very different picture is presented in the Cartesian coordinates x and z projection of the same area that is shown in the right panel of Fig. 16. The Bridge Cepheids are very spread along the z axis (along the line-of-sight). Only three of them fall into higher RRL stars density contour at the level of 1 RRL star per kpc^2 (M4, M6, and M9) and two other are quite close (M3 and M5). The highest number of RRL stars per 1 kpc^2 in the Bridge area is reached strictly between the Clouds

and we would expect to find the genuine MBR RRL stars right there. However, even if we account for the errors in distance estimations, the locations of MBR CCs and RRL stars situated between the Clouds are not correlated.

8. Conclusions

In this work, we present the analysis based on a sample 19 401 RRab selected from the newest release of the OGLE Collection of RRL stars in the Magellanic System (Soszyński *et al.* 2016a) based on the OGLE-IV data (Udalski *et al.* 2015).

The LMC has a regular shape in three dimensions and no prominent substructures are distinguishable. Even though, the LMC halo is slightly asymmetrical with larger number of RRL stars in its north-eastern part, which is also located closer to us than the entire LMC. We argue that the putative LMC bar in RRL stars is in fact an effect of strong blending and crowding effects in the LMC center, and it was not possible to distinguish before the OGLE-IV extensive data were available. Triaxial ellipsoids were fitted to surfaces of constant number density, excluding the densest central region. Smaller ellipsoids have higher axis ratio and are elongated along the line-of-sight, which is probably not physical due to the residual blends. Larger ellipsoids are slightly more rotated toward the SMC although not entirely. The inclination and position angle change substantially with the a axis size. The ellipsoid centers move away from the SMC and from the observer and Milky Way center with increasing a axis size.

The SMC is mostly free from the blending and crowding effects, due to a significantly smaller number of RRL stars in this galaxy. The SMC has a very regular shape in three-dimensions and we do not see any substructures or asymmetries. We only see a slightly higher column density near the SMC Wing. The distribution center is very different from the dynamical center, which was not the case for the LMC. All ellipsoids fitted to surfaces of constant number density have virtually the same shape (*i.e.*, axis ratios). The inclination angle is very small thus the position angle is not well defined. In contrary to the LMC, SMC ellipsoids centers move toward the LMC, the observer and the Milky Way center with increasing a axis size.

We show, for the first time, a three dimensional distributions of the RRL stars in the extended area between the Magellanic Clouds – the Magellanic Bridge. Unfortunately, we are unable to separate two Clouds' halos from each other and thus we cannot differentiate the genuine Bridge RRL stars from those belonging to the LMC or SMC. This is mostly because of the limited OGLE-IV sky coverage on the eastern side of the LMC. With the LMC halo being asymmetrical and not fully covered it is very difficult to analyze the Bridge area statistically, especially that the RRL stars numbers in the Bridge are small and most probably any deviations from the LMC/SMC halo profile would be lost in the noise. We can only state that the Clouds' halos are overlapping.

A comparison with the results from Paper I clearly shows that the Classical Cepheids and the RRL stars are distributed differently in both Magellanic Clouds. The younger stars are clumped and constitute substructures while the older are more spread and distributed regularly. For the LMC we have obtained a very similar median distance for the CCs and RRL stars, in contrary to the SMC, where the difference is ≈ 4 kpc. The CCs distribution is definitely showing signs of Clouds' interaction, while it is not easy to find such evidence in the RRL stars distribution. In the Magellanic Bridge area on-sky projection, CCs seem to be located near the highest column density of RRL stars between the Clouds. On the other hand, Cartesian xz projection shows that the three-dimensional correlation is very small and while the RRL stars are located mainly between the Clouds, the CCs tend to spread far beyond.

Acknowledgements. A.M.J.-D. is supported by the Polish Ministry of Science and Higher Education under “Diamond Grant” No. 0148/DIA/2014/43. D.M.S. is supported by the Polish National Science Center under the grant 2013/11/D/ST9/03445 and the Polish Ministry of Science and Higher Education under the grant “Iuventus Plus” No. 0420/IP3/2015/73. The OGLE project has received funding from the National Science Center, Poland, grant MAESTRO 2014/14/A/ST9/00121 to AU.










REFERENCES

- Bagheri, G., Cioni, M.-R.L., and Napiwotzki, R. 2013, *A&A*, **551**, A78.
- Besla, G., Kallivayalil, N., Hernquist, L., van der Marel, R.P., Cox, T.J., and Kereš, D. 2010, *ApJ*, **721**, L97.
- Besla, G., Kallivayalil, N., Hernquist, L., van der Marel, R.P., Cox, T.J., and Kereš, D. 2012, *MNRAS*, **421**, 2109.
- Boehle, A., *et al.* 2016, *ApJ*, **830**, 17.
- Braga, V.F., *et al.* 2015, *ApJ*, **799**, 165.
- Carretta, E., Bragaglia, A., Gratton, R., D’Orazi, V., and Lucatello, S. 2009, *A&A*, **508**, 695.
- Connors, T.W., Kawata, D., and Gibson, B.K. 2006, *MNRAS*, **371**, 108.
- Deb, S., and Singh, H.P. 2014, *MNRAS*, **438**, 2440.
- Deb, S., Singh, H.P., Kumar, S., and Kanbur, S.M. 2015, *MNRAS*, **449**, 2768.
- de Grijs, R., and Bono, G. 2015, *AJ*, **149**, 179.
- Diaz, J.D., and Bekki, K. 2011, *MNRAS*, **413**, 2015.
- Diaz, J.D., and Bekki, K. 2012, *ApJ*, **750**, 36.
- Gardiner, L.T., Sawa, T., and Fujimoto, M. 1994, *MNRAS*, **266**, 567.
- Gardiner, L.T., and Noguchi, M. 1996, *MNRAS*, **278**, 191.
- Graczyk, D., *et al.* 2014, *ApJ*, **780**, 59.
- Guglielmo, M., Lewis, G.F., and Bland-Hawthorn, J. 2014, *MNRAS*, **444**, 1759.
- Haschke, R., Grebel, E.K., and Duffau, S. 2012a, *AJ*, **144**, 106.
- Haschke, R., Grebel, E.K., and Duffau, S. 2012b, *AJ*, **144**, 107.
- Jacyszyn-Dobrzeniecka, A.M., *et al.* 2016, *Acta Astron.*, **66**, 149 (Paper I).
- Jurcsik, J. 1995, *Acta Astron.*, **45**, 653.
- Kapakos, E., Hatzidimitriou, D., and Soszyński, I. 2010, *ASPC*, **424**, 233.
- Kapakos, E., Hatzidimitriou, D., and Soszyński, I. 2011, *MNRAS*, **415**, 1366.

- Kapakos, E., and Hatzidimitriou, D. 2012, *MNRAS*, **426**, 2063.
- Madore, B.F. 1976, *Royal Greenwich Observatory Bulletins*, **182**, 153.
- Nemec, J.M., Cohen, J.G., Ripepi, V., Derekas, A., Moskalik, P., Sesar, B., Chadid, M., and Bruntt, H. 2013, *ApJ*, **773**, 181.
- Nöel, N.E.D., Conn, B.C., Carrera, R., Read, I.J., Rix, H.-W., and Dolphin, A. 2013, *ApJ*, **768**, 109.
- Nöel, N.E.D., Conn, B.C., Read, I.J., Carrera, R., Dolphin, A., and Rix, H.-W. 2015, *MNRAS*, **452**, 4222.
- Pejcha, O., and Stanek, K.Z. 2009, *ApJ*, **704**, 1730.
- Pietrzyński, G., *et al.* 2013, *Nature*, **495**, 76.
- Růžička, A., Theis, C., and Palouš, J. 2009, *ApJ*, **691**, 1807.
- Růžička, A., Theis, C., and Palouš, J. 2010, *ApJ*, **725**, 369.
- Schlegel, D.J., Finkbeiner, D., and Davis, M. 1998, *ApJ*, **500**, 525.
- Skowron, D.M., *et al.* 2016, *Acta Astron.*, **66**, 269.
- Soszyński, I., *et al.* 2009, *Acta Astron.*, **59**, 1.
- Soszyński, I., Udalski, A., Szymański, M.K., Kubiak, M., Pietrzyński, G., Wyrzykowski, Ł., Ulaczyk, K., and Poleski, R. 2010, *Acta Astron.*, **60**, 165.
- Soszyński, I., *et al.* 2016a, *Acta Astron.*, **66**, 131.
- Soszyński, I., *et al.* 2016b, *MNRAS*, **463**, 1332.
- Stanimirović, S., Staveley-Smith, L., and Jones, P.A. 2004, *ApJ*, **604**, 176.
- Subramanian, A., and Subramanian, S. 2009, *A&A*, **503**, L9.
- Subramanian, S., and Subramanian, A. 2009, *A&A*, **496**, 399.
- Subramanian, S., and Subramanian, A. 2012, *ApJ*, **744**, 128.
- Turner, D.A., Anderson, I.J., Mason, J.C., and Cox, M.G. 1999, Technical Report RR9803, “School of Computing and Mathematics”, University of Huddersfield.
- Udalski, A., Szymański, M.K., and Szymański, G. 2015, *Acta Astron.*, **65**, 1.
- van der Marel, R.P., and Cioni, M.-R.L. 2001, *AJ*, **122**, 1807.
- van der Marel, R.P., and Kallivayalil, N. 2014, *ApJ*, **781**, 121.
- Wagner-Kaiser, R., and Sarajedini, A. 2013, *MNRAS*, **431**, 1565.
- Weinberg, M.D., and Nikolaev, S. 2001, *ApJ*, **548**, 712.
- Yoshizawa, A.M., and Noguchi, M. 2003, *MNRAS*, **339**, 1135.



OGLE-ing the Magellanic System: Cepheids in the Bridge*

Anna M. Jacyszyn-Dobrzeńicka^{1,2} , Igor Soszyński¹ , Andrzej Udalski¹, Michał K. Szymański¹, Dorota M. Skowron¹, Jan Skowron¹ , Przemek Mróz^{1,5} , Katarzyna Kruszyńska¹, Patryk Iwanek¹ , Paweł Pietrukowicz¹ , Radosław Poleski³ , Szymon Kozłowski¹ , Krzysztof Ulaczyk⁴ , Krzysztof Rybicki¹, and Marcin Wrona¹

¹ Astronomical Observatory, University of Warsaw, Al. Ujazdowskie 4, 00-478 Warszawa, Poland; jacyszyn@uni-heidelberg.de

² Astronomisches Rechen-Institut, Zentrum für Astronomie der Universität Heidelberg, Mönchhofstr. 12-14, D-69120 Heidelberg, Germany

³ Department of Astronomy, Ohio State University, 140 West 18th Avenue, Columbus, OH 43210, USA

⁴ Department of Physics, University of Warwick, Coventry CV4 7AL, UK

⁵ Division of Physics, Mathematics, and Astronomy, California Institute of Technology, Pasadena, CA 91125, USA

Received 2019 April 18; revised 2019 December 5; accepted 2019 December 8; published 2020 January 22

Abstract

We present a detailed analysis of the Magellanic Bridge Cepheid sample constructed using the Optical Gravitational Lensing Experiment Collection of Variable Stars. Our updated Bridge sample contains 10 classical and 13 anomalous Cepheids. We calculate their individual distances using optical period–Wesenheit relations and construct three-dimensional maps. Classical Cepheid (CC) on-sky locations match very well neutral hydrogen and young stars distributions; thus, they add to the overall young Bridge population. In three dimensions, 8 out of 10 CCs form a bridge-like connection between the Magellanic Clouds. The other two are located slightly farther away and may constitute the Counter Bridge. We estimate ages of our Cepheids to be less than 300 Myr for from 5 up to 8 out of 10, depending on whether the rotation is included. This is in agreement with a scenario where these stars were formed in situ after the last encounter of the Magellanic Clouds. Cepheids’ proper motions reveal that they are moving away from both Large and Small Magellanic Clouds. Anomalous Cepheids are more spread than CCs in both two and three dimensions, even though they form a rather smooth connection between the Magellanic Clouds. However, this connection does not seem to be bridge-like, as there are many outliers around both Magellanic Clouds.

Unified Astronomy Thesaurus concepts: [Magellanic Clouds \(990\)](#); [Cepheid variable stars \(218\)](#)

1. Introduction

The Magellanic Bridge (MBR), which undoubtedly is direct evidence of the Magellanic Clouds’ interactions, has been a subject of interest of many research projects. Though observations of the Bridge area started with Shapley’s first discovery of young stars located in the SMC Wing (Shapley 1940), the Bridge as a structure was discovered as a hydrogen feature (Hindman et al. 1963). Numerical models predict that the connection between the Large and Small Magellanic Clouds (LMC and SMC, respectively) was formed after their last encounter, about 200–300 Myr ago (e.g., Gardiner et al. 1994; Gardiner & Noguchi 1996; Růžička et al. 2010; Besla et al. 2012; Diaz & Bekki 2012) or, as recent study shows, slightly later—about 150 Myr ago (Zivick et al. 2019).

Different studies of the gaseous counterpart of the MBR showed that it is a rather complicated, multiphase structure (D’Onghia & Fox 2016 and references therein). The neutral hydrogen (HI) kinematics reveal that the Bridge is connected with the western parts of the LMC disk (Indu & Subramaniam 2015) and, moreover, is also being sheared. Other studies showed that the Bridge also contains warm ionized gas (Barger et al. 2013). Moreover, Wagner-Kaiser & Sarajedini (2017) found evidence of dust in the MBR, concluding that it has probably been pulled out of either or both Magellanic Clouds during their interactions.

Here we present a detailed analysis of classical and anomalous Cepheids in the Bridge area. Different stellar components of the Bridge have been discovered. This is in agreement with numerical model predictions (e.g., Besla et al. 2012;

Diaz & Bekki 2012; Guglielmo et al. 2014). Many studies were devoted to searching for young stars between the Magellanic Clouds and found evidence of their presence therein (Shapley 1940; Irwin et al. 1985; Demers & Battinelli 1998; Harris 2007; Noël et al. 2013, 2015; Skowron et al. 2014; Belokurov et al. 2017; Mackey et al. 2017; Zivick et al. 2019). Skowron et al. (2014) showed, using the Optical Gravitational Lensing Experiment (OGLE) data, that young stars form a continuous bridge-like connection and that their distribution is clumped. This was confirmed by Belokurov et al. (2017), who tested young main-sequence stars from *Gaia* and *GALEX*, as well as Mackey et al. (2017), who used Dark Energy Camera data. Young ages of some of these stars strongly suggest an in situ formation. Zivick et al. (2019) found a correlation between the young population and HI. Moreover, studies of stellar proper motions (PMs) for both young and old populations (Oey et al. 2018; Zivick et al. 2019) show that the Bridge is moving away from the SMC and toward the LMC.

The clumped pattern of stellar associations’ distribution between the Magellanic Clouds may suggest an ongoing process of forming a tidal dwarf galaxy (Bica & Schmitt 1995; Ploekinger et al. 2014, 2015, 2018; Bica et al. 2015). Recently, a dwarf galaxy was found located in the on-sky Bridge area, though it is located halfway between the Sun and the Magellanic System (Koposov et al. 2018).

Classical pulsators were also studied in the MBR. Soszyński et al. (2015b), as part of the OGLE Collection of Variable Stars (OCVS), published a list of classical Cepheids (CCs), including new discoveries located in the MBR. Jacyszyn-Dobrzeńicka et al. (2016, hereafter Paper I) studied their three-dimensional distribution and classified nine as MBR members. Five of these

* Draft version prepared on 2019 December 5.

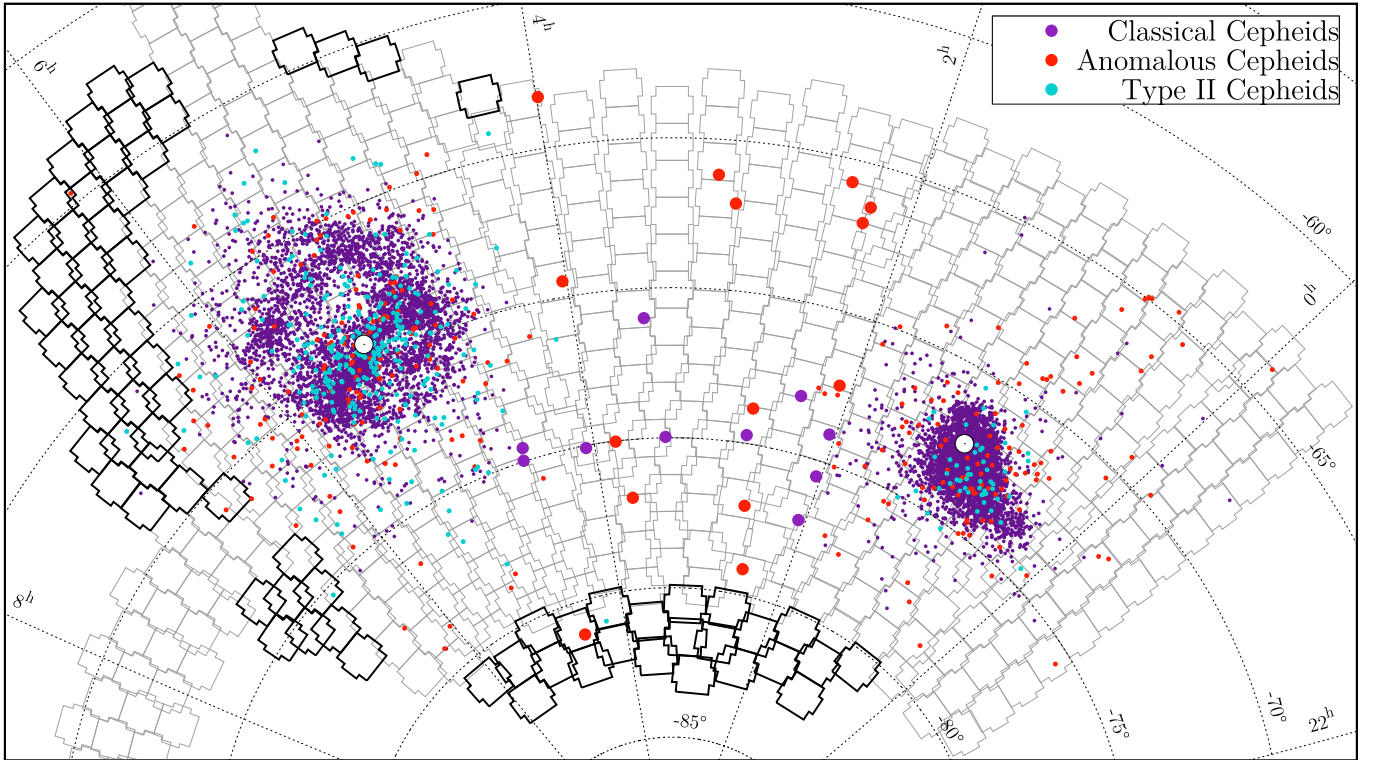


Figure 1. On-sky locations of Cepheids in the Magellanic System. The selected Bridge sample is featured with larger circles. Black contours show the newest addition to the OGLE-IV fields, while gray contours show main OGLE-IV fields in the Magellanic System that were already observed before 2017 July. White circles mark the LMC (van der Marel & Kallivayalil 2014) and SMC (Stanimirović et al. 2004) centers.

objects seem to form a bridge-like connection between the Magellanic Clouds, while the others are more spread in three dimensions. Ages of these CCs suggest that they were formed in situ, as almost all are under 300 Myr.

The evidence was found for intermediate-age and old stars between the Magellanic Clouds (Bagheri et al. 2013; Noël et al. 2013, 2015; Skowron et al. 2014; Carrera et al. 2017). Classical pulsators belonging to the latter group, the RR Lyrae stars, are also present in the MBR, and their distribution was thoroughly tested (Jacyszyn-Dobrzniecka et al. 2017, hereafter Paper II; Belokurov et al. 2017; Wagner-Kaiser & Sarajedini 2017). Also Mira candidates were searched for in the MBR (Deason et al. 2017). Another paper in the series of using OCVS to analyze the three-dimensional structure of the Magellanic System (Jacyszyn-Dobrzniecka et al. 2020, hereafter Paper IV), following closely this paper, summarizes and updates the current knowledge of RR Lyrae stars’ distribution in the Bridge. For more information on the old stellar counterpart of the MBR, see the Introduction in Paper IV.

In this work we present an analysis of Cepheids in the MBR using the updated, corrected, and extended OGLE data. We studied three-dimensional distributions of CCs, anomalous Cepheids (ACs), and type II Cepheids (T2Cs), though we did not classify any of the latter as MBR members. For CCs and ACs we also present a detailed analysis of many parameters and a comparison of different methods used. In this paper we also compare our sample to *Gaia* Data Release 2 (DR2) Cepheids and for the first time present their distribution in the Bridge.

We organized the paper as follows. In Section 2 we present the OCVS, as well as the latest changes and updates applied to the collection. Section 3 presents methods of calculating individual distances and coordinates’ transformation. A

detailed analysis of CC and AC distributions is included in Sections 4 and 5, respectively. In Section 6 we discuss the influence of the recent reclassification of four Cepheids on their parameters. For the first time we present *Gaia* DR2 Cepheids in the Bridge and compare them to the OCVS Cepheids in Section 7. We summarize and conclude the paper in Section 8.

2. Observational Data

2.1. OGLE Collection of Variable Stars

In this study we use data from the fourth phase of the OGLE project (Udalski et al. 2015). In particular, we use Cepheids from the OCVS in the Magellanic System (Soszyński et al. 2015b, 2017), including the latest updates (Soszyński et al. 2019). Most of the updates come from the newly added OGLE fields that are marked with black contours in Figure 1. Moreover, the updates also concerned a reclassification of types and modes of pulsation for four Cepheids from the MBR area that were presented in Paper I. This is due to their light-curve Fourier decomposition parameters suggesting different classification (Soszyński et al. 2015a). One Cepheid was moved from first-overtone to fundamental-mode CC. Three CCs were reclassified as ACs.

For one CC in our sample, namely, OGLE-SMC-CEP-4986, the *V*-band magnitude was not available in the OGLE database. Thus, we used the ASAS-SN Sky Patrol light curve (Schapsee et al. 2014; Kochanek et al. 2017) to calculate its mean magnitude in the *V* band. To make sure it is properly calibrated, we selected 10 reference stars located in the same detector (OGLE operates a 32-chip mosaic camera) as the Cepheid. These objects were nonvariables and had the closest magnitude and color to OGLE-SMC-CEP-4986, as well as good-quality

magnitude measurement in the OGLE database (many epochs). For the reference stars we compared magnitudes in the OGLE and ASAS-SN Sky Patrol and calculated a correction, which was on the order of 0.08 mag.

3. Data Analysis

3.1. Period–Luminosity Relations and Individual Distances

To calculate individual distances of Cepheids, we used the entire Magellanic System samples and applied the same technique as in Paper I (see Section 3.1 therein for more details). We did this separately for CCs and ACs. Using Wesenheit magnitudes (Madore 1982), we fitted period–luminosity (PL) relations (Leavitt law) to the LMC sample (see Equations (1) and (2) in Paper I). Together with the least-squares method, we applied 3σ clipping to the data. We note, however, that this approach may not be the most appropriate for studying distances (Deb et al. 2018), as Nikolaev et al. (2004) showed that the error distribution is not normal for Wesenheit index at a given period. On the other hand, many studies proved this technique to be very robust in the case of the Magellanic System (e.g., Haschke et al. 2012a, 2012b; Moretti et al. 2014; Paper I; Inno et al. 2016; Ripepi et al. 2017).

For fundamental-mode CCs we included a break in the PL relation at $\log P = 0.4$. For first-overtone CCs we excluded objects with $\log P < -0.3$ (see Section 3.1 in Paper I and Soszyński et al. 2008). Figure 2 shows separate PL relations for the final LMC and SMC CC and AC samples with Bridge Cepheids overplotted on each panel using larger symbols. Each type and mode is plotted using a different point type. Additionally, the bottom row highlights the four reclassified Cepheids and shows their local IDs (labels consisting of an “M” with a number that we started using in Paper I). The parameters of our fits are consistent with those from Paper I and are shown in Table 1. The number of stars included in the fits is slightly smaller than in Paper I because this time we did not complement our final set with OGLE-III observations.

We then followed our previous technique as described in detail in Section 3.2 of Paper I. We assumed that the fitted PL relation corresponds to the mean LMC distance and the individual distances were calculated with respect to the best fit (see Equations (3), (4), (5) in Paper I). As a reference distance we have used the most accurate up-to-date result obtained by Pietrzyński et al. (2019). The resulting three-dimensional distribution of CCs is discussed in the next section.

3.2. Coordinate Transformations

In this study we again use Hammer equal-area sky projection as we did in Papers I and II. The projection is rotated so that the z -axis is pointing toward $\alpha_{\text{cen}} = 3^{\text{h}}20^{\text{m}}$, $\delta_{\text{cen}} = -72^{\circ}$. This time we have introduced one small correction to Equations (7)–(11) from Paper I that leads to a coordinate system with an x -axis that is symmetrical with respect to α_{cen} . We have also added a coefficient of $-\frac{\pi}{2}$ when normalizing l that was missing in our original equations:

$$\alpha_{\text{b}} = \alpha + \left(\frac{\pi}{2} - \alpha_{\text{cen}} \right) \quad (1)$$

$$l = \arctan \left(\frac{\sin(\alpha_{\text{b}})\cos(\delta_{\text{cen}}) + \tan(\delta)\sin(\delta_{\text{cen}})}{\cos(\alpha_{\text{b}})} \right) \quad (2)$$

$$\beta = \arcsin(\sin(\delta)\cos(\delta_{\text{cen}}) - \cos(\delta)\sin(\delta_{\text{cen}})\sin(\alpha_{\text{b}})), \quad (3)$$

where l and β are auxiliary variables. We normalize the coordinates so that $l - \frac{\pi}{2} \in (-\pi, \pi)$ and $\beta \in \left(-\frac{\pi}{2}, \frac{\pi}{2}\right)$:

$$x_{\text{Hammer}} = -\frac{2\sqrt{2}\cos(\beta)\sin(l/2)}{\sqrt{1 + \cos(\beta)\cos(l/2)}} \quad (4)$$

$$y_{\text{Hammer}} = \frac{\sqrt{2}\sin(\beta)}{\sqrt{1 + \cos(\beta)\cos(l/2)}}. \quad (5)$$

4. Classical Cepheids

4.1. Updated Bridge Sample

In this section we present a detailed analysis of the updated sample of CCs in the Magellanic System in the context of the MBR. The sample of Bridge CCs was first presented by Soszyński et al. (2015b) and included five objects. Later, in Paper I we have enlarged that sample to nine and discussed their three-dimensional locations in detail (see Section 6 therein). We labeled the objects M1–M9 (see Table 10 in Paper I). Since then, Soszyński et al. (2017) have already added one classical Cepheid to the OGLE Bridge sample, making it the 10th one (M10).

Later, Soszyński et al. (2019) reclassified M7 from first-overtone CC to fundamental-mode CC. Moreover, three objects were moved from the CC sample to the AC sample, namely, M2, M3, and M8. The applied corrections influenced Cepheids’ distances, decreasing them by even up to ~ 20 kpc. Thus, the three-dimensional distribution of the Bridge sample has significantly changed as compared to Paper I.

We have constructed our final Bridge Cepheid sample based on the on-sky and three-dimensional locations of Cepheids in relation to the LMC and SMC entire samples. We decided to add two objects located close to the LMC (M12 and M13) to the Bridge sample. These CCs were already included in the first OGLE-IV Collection of CCs by Soszyński et al. (2015b) as LMC stars, though we did not incorporate these in the Paper I sample. All of the four outlier Cepheids, located both on the SMC side (M9 and M11; M11 was added by Soszyński et al. 2017 and was not present in the Paper I sample) and on the LMC side (M12, M13), are connecting the Clouds’ samples to the genuine MBR sample.

Due to these updates and corrections, our final Bridge CC sample consists of 10 objects. The list of CCs and their basic parameters is included in Table 2, which provides the object’s OCVS ID, local ID used in Paper I and this work, pulsation period P , mean magnitudes from both OGLE passbands (I and V), R.A. and decl. (epoch J2000.0), distance d (details on the method used—see Section 3.1), and age estimated using the period–age relation from Anderson et al. (2016) (including average rotation) and Bono et al. (2005) (without rotation). The list comprises five fundamental-mode pulsators, four first-overtone pulsators, and one double-mode Cepheid (pulsating simultaneously in the first and second overtone), for which we used its first-overtone period in this analysis.

Our Bridge Cepheid sample also consists of ACs that we discuss in Section 5. We note that we did not classify any of the recently published T2Cs in the Magellanic System (Soszyński et al. 2018) as a Bridge candidate, as these stars do not seem to form any bridge-like connection and none are located in the direct area of interest.

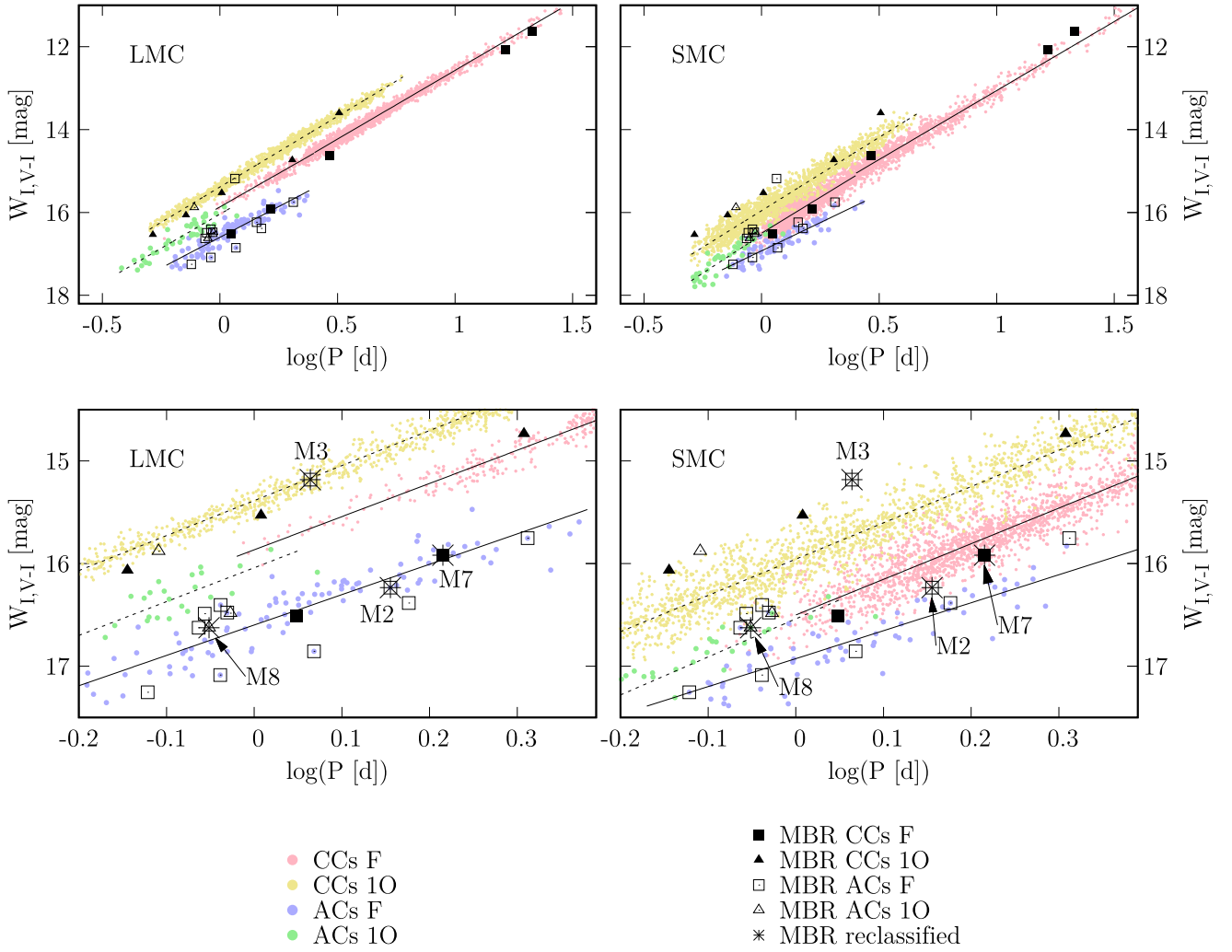


Figure 2. PL relations for classical and anomalous Cepheids in the LMC (left column) and SMC (right column). CCs are marked with smaller circles than ACs. The entire Bridge sample is overplotted on the presented PL relations in every panel, with each type marked separately. Additionally, bottom panels highlight four Cepheids that were reclassified and are marked with a star and their local ID. M7 was reclassified from first-overtone CC to fundamental-mode CC; M2 and M3, from fundamental-mode CCs to fundamental-mode ACs; and M8, from first-overtone CC to first-overtone AC. Plots do not show 3σ outliers, as these were removed from the final sample. The fit for fundamental-mode ACs in the SMC has significantly different slope than all of the other relations. Note, however, that we do not use the SMC AC PL relations and that these are only plotted here for comparison.

Table 1
PL Relations for CCs in the Magellanic System in the Wesenheit Magnitude

$W_{I,V-I} = a \log P + b$								
Galaxy	Puls. Mode	$\log P$	a	b (mag)	σ (mag)	χ^2/dof	N_{inc}	N_{rej}
LMC	F	≤ 0.4	-3.234 ± 0.033	15.866 ± 0.010	0.104	3.029	273	6
		> 0.4	-3.315 ± 0.008	15.888 ± 0.005	0.076	1.613	2042	85
		all	-3.311 ± 0.006	15.885 ± 0.004	0.079	1.714	2308	98
	1O	all	-3.411 ± 0.007	15.387 ± 0.003	0.077	1.634	1772	85
SMC	F	≤ 0.4	-3.470 ± 0.015	16.501 ± 0.004	0.162	7.362	1698	38
		> 0.4	-3.330 ± 0.008	16.389 ± 0.006	0.149	6.170	935	28
		all	-3.453 ± 0.005	16.489 ± 0.002	0.159	7.106	2636	63
	1O	all	-3.535 ± 0.007	15.957 ± 0.002	0.171	8.198	1879	30

Note. N_{inc} is the number of objects included in the fit, while N_{rej} is the number of objects rejected during the 3σ -clipping procedure.

It is noteworthy, however, that Iwanek et al. (2018) studied three-dimensional distributions of ACs and T2Cs in the context of the stellar evolution theory. They found that T2Cs are probably members of old and intermediate-age populations,

while ACs seem to belong to the old population as is demonstrated by their spread on-sky view.

In Figure 3 we compare the on-sky distribution of different tracers in the central Bridge area. The plot shows classical

Table 2
Magellanic Bridge Classical Cepheids: Basic Parameters

Mode	OCVS ID Loc. ID	P (day)	$\langle I \rangle$ (mag)	$\langle V \rangle$ (mag)	R.A.	Decl.	d (kpc) ^{a,b}	Age (Myr)	
								rot. ^c	no-rot. ^d
F	OGLE-SMC-CEP-4956								
	M1	1.1162345	17.372	17.930	03 ^h 23 ^m 24 ^s .90	−74°58′07″.3	71.53 ± 2.00	567	283 ± 59
	OGLE-SMC-CEP-4953								
	M4	21.3856352	12.965	13.824	02 ^h 20 ^m 49 ^s .46	−73°05′08″.3	53.28 ± 1.49	48	27 ± 6
	OGLE-SMC-CEP-4952 ^e								
	M7	1.6414839	16.901	17.535	02 ^h 04 ^m 09 ^s .38	−77°04′38″.4	69.99 ± 1.97	410	209 ± 44
	OGLE-SMC-CEP-4987 ^f								
M10	2.9284749	15.738	16.458	03 ^h 31 ^m 34 ^s .40	−70°59′38″.2	56.45 ± 1.56	252	132 ± 28	
OGLE-SMC-CEP-4986 ^g									
M11	16.4454990	13.480	14.378	02 ^h 02 ^m 59 ^s .72	−74°03′24″.7	54.87 ± 1.53	59	34 ± 8	
10	OGLE-SMC-CEP-4955								
	M5	2.0308924	15.675	16.281	02 ^h 42 ^m 28 ^s .88	−74°43′17″.6	59.58 ± 1.64	297	120 ± 20
	OGLE-LMC-CEP-3377								
	M6	3.2144344	14.629	15.291	04 ^h 04 ^m 28 ^s .88	−75°04′47″.1	48.38 ± 1.34	191	74 ± 13
	OGLE-LMC-CEP-3380								
	M12	1.0178714	16.485	17.101	04 ^h 35 ^m 32 ^s .89	−74°33′46″.7	53.62 ± 1.48	576	252 ± 41
OGLE-LMC-CEP-3381 ^h									
M13	0.5188341	17.230	17.677	04 ^h 37 ^m 03 ^s .69	−74°58′25″.3	53.84 ± 1.49	1101	519 ± 84	
1020	OGLE-SMC-CEP-4951 ^h								
	M9	0.7170500	16.769	17.222	02 ^h 02 ^m 33 ^s .88	−75°30′48″.0	54.06 ± 1.49	807	367 ± 60

Notes. All Cepheids except M1 and M7 form a continuous-like connection between the Magellanic Clouds.

^a The distance uncertainty does not include the mean LMC distance uncertainty from Pietrzyński et al. (2019) $d_{\text{LMC}} = 49.59 \pm 0.09$ (statistical) ± 0.54 (systematic) kpc.

^b For comparison of distance estimates using different techniques, see Table 4.

^c This age value was estimated using the period–age relation for average instability strip crossing and including average initial rotation from Anderson et al. (2016).

^d This age determination was estimated using the period–age relation from Bono et al. (2005). For other estimates see Table 3.

^e This Cepheid was reclassified from first-overtone to fundamental-mode pulsator.

^f This Cepheid was added to the sample by Soszyński et al. (2017).

^g V-band magnitude for this Cepheid was calculated using ASAS-SN Sky Patrol (Schapsee et al. 2014; Kochanek et al. 2017).

^h Ages of short-period Cepheids may not be calculated properly (see details in Section 4.3).

(white circles), anomalous (red circles), and type II (green circles) Cepheids compared to the distribution of young stars from Skowron et al. (2014), as well as neutral hydrogen density contours from the Galactic All Sky HI Survey (McClure-Griffiths et al. 2009; Kalberla et al. 2010; Kalberla & Haud 2015). Larger circles distinguish the selected Bridge sample, while smaller circles show other Magellanic System Cepheids. Note that there is only one T2C in the highlighted area. Labels M1–M13 mark the CC sample from Paper I, as well as new CCs that we added to the final Bridge sample. Note that three of these objects were reclassified as ACs.

4.2. Two- and Three-dimensional Analysis

The on-sky locations of CCs in the MBR are presented using large white circles in Figure 3. Their locations match well with the HI density contours. Only two Cepheids, namely, M7 and M10, lie slightly offset from the peak HI density, though still well within contours showing the densest regions. Actually, the MBR CCs are forming an on-sky connection between the Magellanic Clouds following young stars’ distribution (Skowron et al. 2014). Based on the on-sky locations, we conclude that all of our CCs in the Bridge match results from Paper I, where we stated that the CCs add to the overall distribution of the young population. For comparison we also show in Figure 3 ACs, which are marked with large red circles. ACs are definitely more spread out and do not follow the young stars’ distribution, as was

also already shown by other studies (Fiorentino & Monelli 2012; Iwanek et al. 2018).

Figure 4 shows three-dimensional distribution of CCs in the Magellanic System. Four out of five CCs that we listed in Paper I as constituting a genuine connection between the Magellanic Clouds, specifically M4, M5, M6, and M9, have not been reclassified, and their locations are the same as we presented therein. One out of these five, M3, was reclassified as AC. The four CCs that were lately added to the sample, M10–M13, add to the bridge-like structure. However, M12 and M13 may plausibly not belong to the genuine Bridge population, as they seem to be the LMC outliers located in the extended LMC structure. Similarly, M9 and M11 are located very close to the SMC Wing and thus may also be the Wing stars. On the other hand, the four LMC/SMC outliers may also add to the main MBR sample. Taking that into account, we report here that 8 out of 10 CCs in our updated sample contribute to a bridge-like connection between the Magellanic Clouds.

The farthest CCs in our sample are M1 and M7. M7 is one of the two CCs that are located slightly offset from the HI contours and the young population density distribution (see Figure 3). This suggests that M7 and M10 may have a different origin than CCs discussed in the previous paragraph. Yet, they may still constitute the genuine Bridge population. To test that, other parameters than discussed in this paper need to be taken into account (i.e., chemical composition). However, these Cepheids could also be members of the Counter Bridge, predicted by the numerical

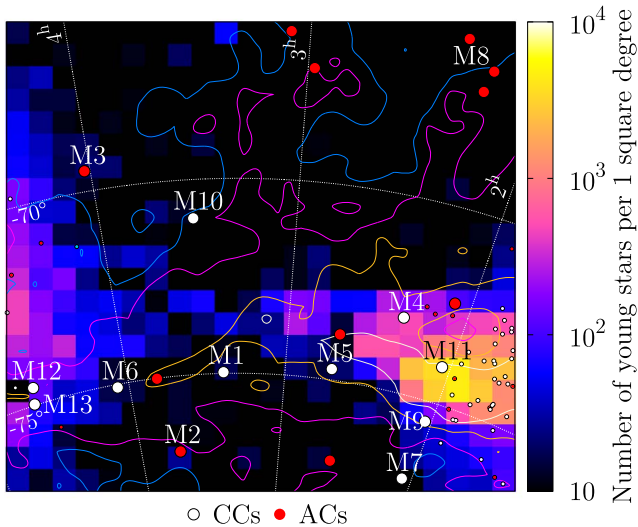


Figure 3. On-sky locations of the central Bridge Cepheid sample as compared to the color-coded young stars’ column density from Skowron et al. (2014) and neutral hydrogen density contours from the Galactic All Sky HI Survey (McClure-Griffiths et al. 2009; Kalberla et al. 2010; Kalberla & Haud 2015). Different types of Cepheids are marked with different colors. The selected Bridge sample is featured with larger circles, while smaller circles show LMC and SMC Cepheids. Labels M1–M9 mark the classical Cepheid sample from Paper I, and M10–M13 are new classical Cepheids that we added to the final MBR sample. M2, M3, and M8 were lately reclassified as anomalous Cepheids. The HI is integrated over the velocity range $80 \text{ km s}^{-1} < v < 400 \text{ km s}^{-1}$. Contours are on the levels (1, 2, 4, 8) $\cdot 10^{20} \text{ cm}^{-2}$. The color-coded value of each box is a logarithm of the number of young stars per square degree area (each pixel is $\approx 0.335 \text{ deg}^2$). The map is represented in a Hammer equal-area projection centered at $\alpha_{\text{cen}} = 3^{\text{h}}18^{\text{m}}$, $\delta_{\text{cen}} = -70^\circ$. This plot is an updated version of Figure 18 from Paper I.

model by Diaz & Bekki (2012). This structure was already discussed in Paper I in terms of the three-dimensional distribution of our previous sample, where we classified two CCs as plausible members of the Counter Bridge. Both were reclassified—M8 as AC and M7 as first-overtone CC—from fundamental-mode CC to first-overtone pulsator (Section 6). With the updated sample we do not have as evident candidates as before, though M1 and M7 are located near the borders of the Counter Bridge (see Figure 17 in Ripepi et al. 2017).

Our Bridge sample is not as spread out in terms of distances as the sample presented in Paper I. All of the CCs are located in between the Magellanic Clouds, being farther than the closest LMC Cepheid and closer than the farthest SMC Cepheid. On the other hand, not all of the Bridge CCs form an evident, bridge-like connection. Some of these stars may also be ejected from the LMC and/or SMC instead of forming the genuine Bridge. Indeed, we do see some individual objects spread over in different directions near these galaxies. The origin of our Bridge CCs will not be fully understood until further analyses are carried out taking into account different parameters than the ones we present in this paper. Of special importance are spectroscopic observations that could lead to a definite classification of these objects.

4.3. Ages

Ages of our CCs were estimated using the period–age relation from Anderson et al. (2016) and Bono et al. (2005). The main difference between these two is that the former

includes average rotation, while the latter does not include stellar rotation at all. As we have already discussed in Paper I (see Section 6 therein), the Bridge has metallicity similar to or smaller than the SMC (Lehner et al. 2008; Misawa et al. 2009). Neither Anderson et al. (2016) nor Bono et al. (2005) provide any relation for metallicity smaller than the SMC; thus, we applied to our Bridge sample the relation for the SMC metallicity. Calculated values are presented in Tables 2 and 3.

Table 3 presents the age estimates based on the period–age relation from Anderson et al. (2016) and Bono et al. (2005), as well as values obtained using the period–age–color relation (we used relations for the SMC metallicity). The relations from Anderson et al. (2016) were derived from theoretical models including rotation. Age values that they provide are approximately twice as large as values obtained using Bono et al. (2005) relations. This should not be surprising, as rotation induces mixing in stellar interiors, which leads to refreshing the core hydrogen supplies. Thus, a rotating star can be burning hydrogen for a longer time than a nonrotating one. As a result, the star can remain on the main sequence for a longer period of time and then cross the instability strip and become a Cepheid at an older age. Results from both relations from Bono et al. (2005) match well within the error bars.

Including rotation, 5 out of 10 CCs in our Bridge sample are younger than 300 Myr. This is in agreement with an assumption that these objects were formed in situ after the last encounter of the Magellanic Clouds (e.g., Gardiner et al. 1994; Gardiner & Noguchi 1996; Růžička et al. 2010; Besla et al. 2012; Diaz & Bekki 2012; Zivick et al. 2019). All of these five CCs are constituting a connection between the LMC and SMC, as we have described in the previous section. These are the CCs indexed M4, M5, M6, M10, and M11.

Two CCs in our sample are younger than 60 Myr. These are M4 (48 Myr) and M11 (59 Myr), which are located close to the SMC. Both may be stars ejected from this galaxy. The two oldest CCs in our sample, M9 and M13, are also the shortest-period pulsators. The age determination is 807 Myr for M9 and 1101 Myr for M13. These values seem rather large and could be incorrect owing to the fact that models do not predict ages of objects with such short periods. That is why we treat these estimates as rather rough.

4.4. Proper Motions

We used *Gaia* DR2 (Gaia Collaboration et al. 2018) to analyze PMs of our Bridge CCs. Following Kallivayalil et al. (2013) and Zivick et al. (2018, 2019), we use here $\mu_N = \mu_\delta$ and $\mu_W = -\mu_\alpha \cos \delta$, where α , δ are R.A., decl., respectively. We compare our results to the LMC and SMC PMs (Kallivayalil et al. 2013; Zivick et al. 2018) in Figures 5 and 6. CC PMs follow the general on-sky movement of the Magellanic System. PMs of M12 and M13 are relatively very similar to the LMC PM, while PMs of M9 and M11 are relatively very similar to the SMC PM. This supports our conclusions from the previous subsection that these Cepheids are probably LMC and SMC outliers. All of the other Bridge CC PM values fall in between those of LMC and SMC. This is what we would expect for a Bridge population (see Figure 3 in Zivick et al. 2019).

Figure 6 shows PMs of Bridge CCs, as well as the LMC and SMC PMs, plotted as vectors on the sky. CC PMs as related to the LMC or SMC are rather low and comparable to the Clouds’ relative PM. In the LMC-related frame all CCs are moving away from this galaxy. For the SMC-related PMs the situation

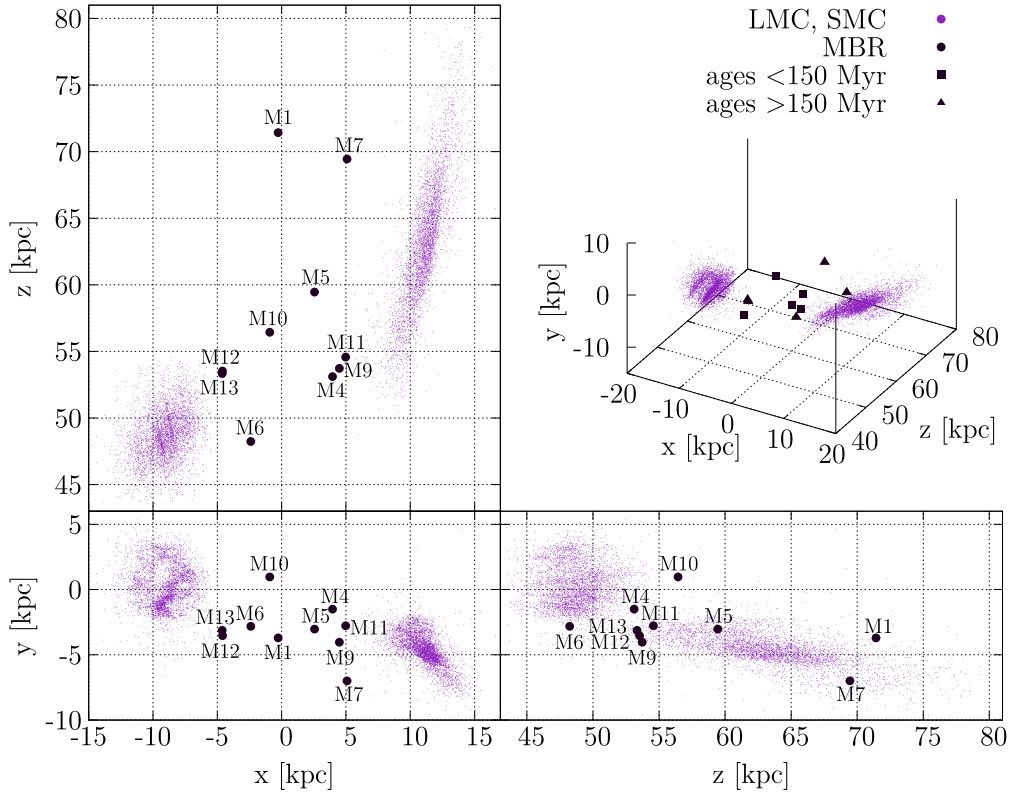


Figure 4. Three-dimensional distribution of classical Cepheids in the Magellanic System, with the MBR sample marked with large circles. Labels show local IDs of these objects (see Table 2). The map is represented in Cartesian coordinates with the observer located at (0, 0, 0). Ages were calculated using relations from Bono et al. (2005).

Table 3
Magellanic Bridge Classical Cepheids: Ages

Mode	Loc. ID	P (day) ^a	Age _{tot} (Myr) ^b	Age _{PA} (Myr) ^c	Age _{PAC} (Myr) ^d
F	M1	1.1	567	283 ± 59	271 ± 63
	M4	21.4	48	27 ± 6	27 ± 8
	M7	1.6	410	209 ± 44	207 ± 50
	M10	2.9	252	132 ± 28	110 ± 26
	M11	16.4	59	34 ± 8	35 ± 10
10	M5	2.0	297	120 ± 20	123 ± 22
	M6	3.2	191	74 ± 13	79 ± 15
	M12	1.0	576	252 ± 41	279 ± 50
	M13 ^e	0.5	1101	519 ± 84	475 ± 77
1020	M9 ^e	0.7	807	367 ± 60	329 ± 54

Notes.

^a Find a more precise period determination in Table 2.

^b Calculated using the period–age relation from Anderson et al. (2016) that includes average stellar rotation on an average instability strip crossing.

^c Calculated using the period–age relation from Bono et al. (2005).

^d Calculated using the period–age–color relation from Bono et al. (2005).

^e Ages of short-period Cepheids may not be calculated properly (see details in Section 4.3).

is similar. This means that the Bridge CCs are moving away from both Clouds.

4.5. Different Distance Estimates

The Cepheid PL relation has an intrinsic dispersion caused by a finite width of the instability strip (e.g., Anderson et al. 2016) and/or depth effects (e.g., Inno et al. 2013; Scowcroft et al. 2016; Paper I). This implies that the PL relations are more useful for

estimating the sample’s mean distance than individual distances of each Cepheid. The natural spread of PL relations is significantly smaller in the infrared (e.g., Storm et al. 2011; Ngeow et al. 2015; Scowcroft et al. 2016; Gallenne et al. 2017; Madore et al. 2017). However, one can obtain useful PL relations in the optical regime with Wesenheit magnitude that combines two passbands and includes a color term (Udalski et al. 1999; Fouqué et al. 2007; Soszyński et al. 2008; Ngeow 2012; Lemasle et al. 2013; Anderson et al. 2016; Paper I). Ngeow (2012) showed

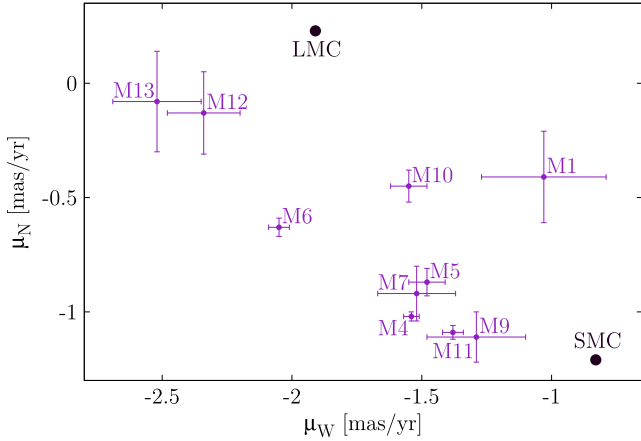


Figure 5. PMs of Bridge CCs as compared to the PM of the LMC (Kallivayalil et al. 2013) and SMC (Zivick et al. 2018). All 10 CCs from our sample are marked with their local IDs.

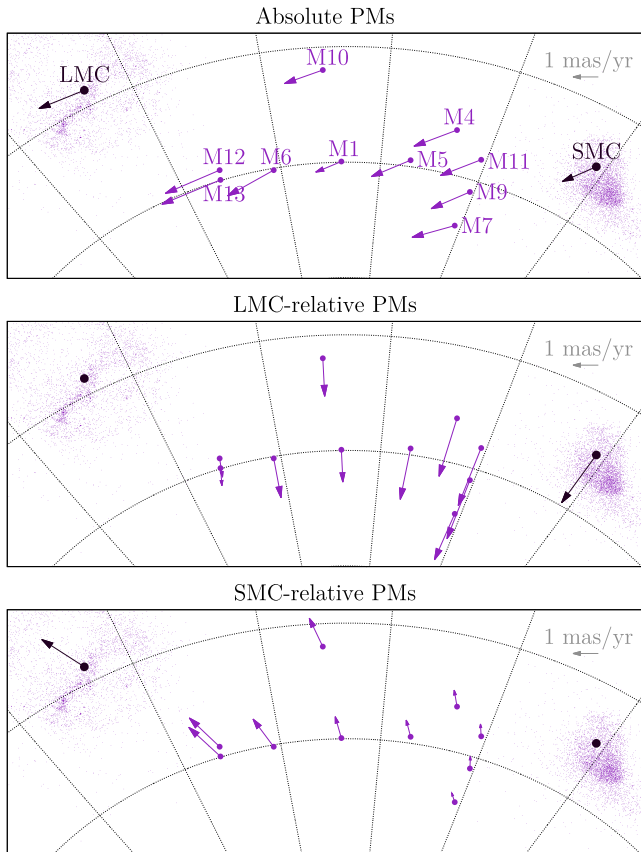


Figure 6. PMs of Bridge CCs, as well as LMC (Kallivayalil et al. 2013) and SMC (Zivick et al. 2018), shown as vectors on the sky. The top panel presents absolute PMs, while the middle and bottom panels present the LMC- and SMC-related frame, respectively. We adopted the LMC center of van der Marel & Kallivayalil (2014) and the SMC center of Stanimirović et al. (2004).

that the period–Wesenheit relations can be used to determine individual distances of Galactic Cepheids. Here we have also tried other techniques to calculate individual distances of our MBR CC sample. The results are shown in Table 4 and Figure 7 and discussed in this section.

As described in Section 3.1, our basic method of calculating distances is the same as we used in Paper I. It relies on the

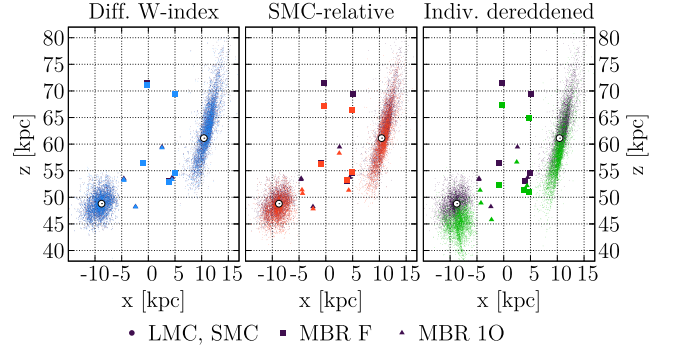


Figure 7. Three-dimensional distribution of CCs in the Magellanic System in Cartesian x - z plane projection. The distribution obtained using our basic distance estimates (as described in Section 3.1) is marked with black in every panel. Overplotted are, for comparison, different distributions marked with colored circles (see text for details). The Bridge CC sample is highlighted with larger symbols. In all of the panels white circles mark LMC (Pietrzyński et al. 2019; van der Marel & Kallivayalil 2014) and SMC (Graczyk et al. 2014; Stanimirović et al. 2004) centers.

Wesenheit PL relation for the LMC and an assumption that the fit corresponds to the mean LMC distance (Pietrzyński et al. 2019). We called this distance estimate d_{LMC} , as it is related to the LMC, and show it in the fourth column in Table 4 (as well as in Table 2). The resulting uncertainty does not include uncertainty from Pietrzyński et al. (2019), as it would only lead to a systematic error, which would be the same for our entire sample. In order to test how the adopted reddening law influences individual distances, we also calculated distances the same way but with a different color term coefficient in the Wesenheit index. Instead of 1.55 we used 1.44 (see Equation (6) in Paper I and Udalski 2003). The results are shown as $d_{\text{LMC},W44}$ (fifth column in Table 4) and match very well our basic distances, although the former are slightly smaller. For comparison, see also the left panel of Figure 7, where the three-dimensional distribution obtained with basic distances is marked with black circles, while with that a different reddening law is marked with blue circles and is overplotted on the former. This also means that the adopted reddening law does not have much impact on the Bridge Cepheids’ distances. This is in agreement with the fact that the reddening toward the MBR is low (Schlegel et al. 1998; Wagner-Kaiser & Sarajedini 2017; Skowron et al. 2019, in preparation).

We also calculated distances in relation to the SMC (d_{SMC} ; sixth column in Table 4). We used the same technique as in our basic approach but adopted the SMC fit and the SMC mean distance as a reference (Graczyk et al. 2014). The resulting distances are smaller than our basic values, and the difference is up to 5 kpc in some cases, even though the geometry of the entire LMC and SMC samples does not differ much using both approaches. This is shown in the middle panel of Figure 7, where we overplotted the three-dimensional distribution relative to the SMC (red) on that relative to the LMC (black). This incoherence may be caused by the fact that our SMC sample reveals a slightly larger mean distance when using our basic method than that from Graczyk et al. (2014). Thus, when we changed the reference point to the SMC, the entire sample moved slightly closer.

Having magnitudes in both OGLE passbands, I and V , we could also deredden our data. This is the same approach as used by Haschke et al. (2012a, 2012b). First, we calculated absolute magnitudes using PL relations from Sandage et al. (2004, 2009) that were derived for the LMC and SMC data

Table 4
Magellanic Bridge Classical Cepheids: Distances

Mode	Loc. ID	P (day) ^a	d_{LMC} (kpc) ^b	$d_{\text{LMC, W44}}$ (kpc) ^b	d_{SMC} (kpc) ^c	d_{red} (kpc)
F	M1	1.1	71.53 ± 2.00	71.17 ± 1.89	67.22 ± 1.86	67.37 ± 10.83
	M4	21.4	53.28 ± 1.49	53.00 ± 1.41	53.43 ± 1.50	51.53 ± 7.46
	M7	1.6	69.99 ± 1.97	69.87 ± 1.87	66.98 ± 1.85	65.40 ± 10.25
	M10	2.9	56.45 ± 1.56	56.45 ± 1.49	56.29 ± 1.56	52.39 ± 7.73
	M11	16.4	54.87 ± 1.53	54.80 ± 1.46	55.30 ± 1.55	51.24 ± 7.36
1O	M5	2.0	59.58 ± 1.64	59.42 ± 1.56	58.39 ± 1.61	56.74 ± 8.33
	M6	3.2	48.38 ± 1.34	48.31 ± 1.27	47.95 ± 1.33	45.91 ± 6.40
	M12	1.0	53.62 ± 1.48	53.61 ± 1.40	51.66 ± 1.43	49.18 ± 7.51
	M13	0.5	53.84 ± 1.49	53.47 ± 1.40	51.01 ± 1.41	51.62 ± 8.21
1O2O	M9	0.7	54.06 ± 1.49	53.66 ± 1.41	51.63 ± 1.42	52.50 ± 8.14

Notes.^a Find a more precise period determination in Table 2.^b The distance uncertainty does not include the mean LMC distance uncertainty from Pietrzyński et al. (2019) $d_{\text{LMC}} = 49.59 \pm 0.09$ (statistical) ± 0.54 (systematic) kpc.^c The distance uncertainty does not include the mean LMC distance uncertainty from Graczyk et al. (2014) $d_{\text{SMC}} = 62.1 \pm 1.9$ kpc.

Table 5
Magellanic Bridge Classical Cepheids: Absolute Magnitudes

Loc. ID	M_I (mag) ^a	$M_{I,2}$ (mag) ^b	M_V (mag) ^a	$M_{V,2}$ (mag) ^b	$E(V - I)$ (mag)	$E(V - I)_2$ (mag)
M1	-1.984 ± 0.028	-1.742 ± 0.184	-1.524 ± 0.036	-1.175 ± 0.209	0.098 ± 0.053	-0.009 ± 0.280
M4	-5.654 ± 0.054	-5.504 ± 0.057	-4.842 ± 0.070	-4.644 ± 0.063	0.048 ± 0.093	-0.001 ± 0.089
M7	-2.463 ± 0.029	-2.233 ± 0.159	-1.957 ± 0.037	-1.628 ± 0.181	0.128 ± 0.054	0.029 ± 0.242
M10	-3.183 ± 0.032	-2.971 ± 0.123	-2.608 ± 0.041	-2.308 ± 0.139	0.145 ± 0.059	0.057 ± 0.188
M11	-5.327 ± 0.051	-5.170 ± 0.052	-4.547 ± 0.065	-4.336 ± 0.058	0.118 ± 0.087	0.072 ± 0.082
M5	-3.140 ± 0.032	-2.928 ± 0.125	-2.569 ± 0.041	-2.268 ± 0.141	0.035 ± 0.059	-0.053 ± 0.191
M6	-3.723 ± 0.036	-3.525 ± 0.097	-3.096 ± 0.046	-2.819 ± 0.109	0.035 ± 0.065	-0.044 ± 0.149
M12	-2.264 ± 0.028	-2.029 ± 0.170	-1.777 ± 0.036	-1.440 ± 0.192	0.129 ± 0.054	0.027 ± 0.258
M13	-1.410 ± 0.028	-1.153 ± 0.215	-1.004 ± 0.036	-0.633 ± 0.243	0.042 ± 0.054	-0.074 ± 0.325
M9	-1.820 ± 0.028	-1.574 ± 0.193	-1.375 ± 0.036	-1.020 ± 0.219	0.009 ± 0.053	-0.101 ± 0.293

Notes. For first-overtone pulsators we used fundamentalized periods.^a Calculated using relations from Sandage et al. (2004, 2009).^b Calculated using relations from Gieren et al. (2018).

separately. We applied the SMC relations to the MBR sample, as the Bridge metallicity is close to or slightly lower than the SMC metallicity (e.g., Lehner et al. 2008; Misawa et al. 2009; Carrera et al. 2017; Wagner-Kaiser & Sarajedini 2017). We used relations not including the PL break at $\log P = 1$, as the samples used to derive these relations only consisted of Cepheids with $\log P > 0.4$. Half of our Bridge sample are CCs with shorter periods; thus, we extrapolate these PL relations. Moreover, it was shown that the break at $\log P = 1$ is not significant, at least for the SMC (Bhardwaj et al. 2016).

The PL relations that we used for the LMC (Sandage et al. 2004) are

$$M_I = (-2.949 \pm 0.020) \log P - (1.936 \pm 0.015) \quad (6)$$

$$M_V = (-2.701 \pm 0.035) \log P - (1.491 \pm 0.027). \quad (7)$$

Those for the SMC (Sandage et al. 2009) are

$$M_I = (-2.862 \pm 0.028) \log P - (1.847 \pm 0.022) \quad (8)$$

$$M_V = (-2.588 \pm 0.045) \log P - (1.400 \pm 0.035). \quad (9)$$

These relations were derived only for the fundamental-mode pulsators. For the first-overtone CCs in our sample we

fundamentalized the periods using the relation between periods from Alcock et al. (1995) (as in Groenewegen & Oudmaijer 2000):

$$P_{1O}/P_F = 0.733 - 0.034 \log P_F, \quad 0.1 < \log P_F \leq 0.7. \quad (10)$$

We have simplified the above equation and used the following form:

$$P_F = P_{1O}/(0.728 - 0.034 \log P_{1O}). \quad (11)$$

This relation does not account for metallicity dependence of the ratio of the fundamental-mode and the first-overtone periods (Sziládi et al. 2007, 2018). We used data for double-mode Cepheids in the LMC and SMC (Soszyński et al. 2015b) to verify the possible error that could arise from this simplification. We found that the median difference between the real fundamental mode of the Cepheid and the one calculated from its first-overtone period is 0.2% in the case of the LMC and 1.3% in the case of the SMC. This translates to differences in distance of order $\sim 1\%$, which do not influence this analysis.

It is noteworthy that relations for the LMC were derived using a significantly different mean distance modulus to this

Table 6
Magellanic Bridge Classical Cepheids: Reddening Parameters

Loc. ID	A_I (mag) ^a	$A_{I,W44}$ (mag) ^b	$A_{I,t}$ (mag) ^c	A_V (mag) ^a	$A_{V,W44}$ (mag) ^b	$A_{V,t}$ (mag) ^c
M1	0.083 ± 0.070	0.094 ± 0.067	0.248 ± 0.134	0.181 ± 0.073	0.192 ± 0.071	0.150 ± 0.081
M4	-0.014 ± 0.084	-0.002 ± 0.082	0.121 ± 0.234	0.034 ± 0.095	0.045 ± 0.093	0.073 ± 0.142
M7	0.139 ± 0.070	0.143 ± 0.070	0.325 ± 0.137	0.267 ± 0.074	0.271 ± 0.072	0.196 ± 0.083
M10	0.162 ± 0.071	0.162 ± 0.069	0.368 ± 0.150	0.307 ± 0.076	0.307 ± 0.073	0.223 ± 0.091
M11	0.111 ± 0.082	0.113 ± 0.080	0.319 ± 0.221	0.236 ± 0.091	0.239 ± 0.090	0.193 ± 0.134
M5	-0.061 ± 0.071	-0.055 ± 0.068	0.089 ± 0.149	-0.025 ± 0.075	-0.019 ± 0.073	0.054 ± 0.090
M6	-0.071 ± 0.073	-0.069 ± 0.070	0.090 ± 0.164	-0.036 ± 0.078	-0.033 ± 0.076	0.054 ± 0.099
M12	0.102 ± 0.069	0.103 ± 0.067	0.327 ± 0.135	0.231 ± 0.073	0.232 ± 0.070	0.198 ± 0.082
M13	-0.016 ± 0.069	-0.001 ± 0.067	0.106 ± 0.135	0.026 ± 0.073	0.041 ± 0.070	0.064 ± 0.082
M9	-0.076 ± 0.069	-0.059 ± 0.066	0.022 ± 0.134	-0.067 ± 0.073	-0.051 ± 0.070	0.013 ± 0.081

Notes. All parameters based on absolute magnitudes were calculated using relations from Sandage et al. (2004, 2009) (see Table 5). This is only an estimate, and we discourage using values presented here in scientific research, as many obtained parameters are nonphysical (values under zero).

^a Total reddening obtained using basic method distances.

^b Total reddening obtained using distances calculated assuming different reddening law (different color term coefficient in Wesenheit index as described in Section 4.5).

^c Theoretical total reddening calculated without assuming any distance to each Cepheid. Here we used Schlegel et al. (1998) reddening laws (see Equation (12)).

galaxy. Sandage et al. (2004) based their calculations on the value from Tammann et al. (2003), which is $\mu_{LMC} = 18.54$ mag. In our basic approach we use $\mu_{LMC} = 18.477$ mag (Pietrzyński et al. 2019). For the SMC the difference is not that significant. Sandage et al. (2009) use $\mu_{SMC} = 18.93$ mag (Tammann et al. 2008), while Graczyk et al. (2014) obtain $\mu_{SMC} = 18.965$ mag.

Following the Haschke et al. (2012a, 2012b) approach, in the next step we calculated color excess for each Cepheid $E(V - I) = (m_V - m_I) - (M_V - M_I)$, where $m_{V,I}$ are observed magnitudes and $M_{V,I}$ are absolute magnitudes in the appropriate filter. We noticed a mistake in Haschke et al. (2012a), Equations (6) and (7), that appears when trying to subtract one from another, and $A(V) - A(I)$ does not result in $E(V - I)$. We thus calculated these relations based on original Schlegel et al. (1998) coefficients to obtain total extinction in each passband:

$$A_V = 3.24(E(V - I)/1.278) \quad (12)$$

$$A_I = 1.96(E(V - I)/1.278). \quad (13)$$

Note that there is 1.278 in the denominator instead of 1.4 as in Haschke et al. (2012a). Calculated reddening parameters are shown in Table 6 and discussed in the following section, as here we concentrate on distances. To calculate distance moduli, we used the I -band magnitudes, as these values are usually more accurate than V -band ones. The distance modulus is simply

$$\mu = m_I - M_I - A_I, \quad (14)$$

and distance is

$$d = 10^{(5+\mu)/5}. \quad (15)$$

Results are presented in the last column of Table 4 and in the right panel of Figure 7. The individual dereddening technique resulted in significantly lower distances for every CC in the Bridge sample than previously discussed methods. Moreover, this technique has changed the entire geometry of the LMC and SMC samples, as is clearly visible in Figure 7. Our basic method relying on fitting the PL relations to the observational

data is very robust, which was proven by many different surveys (e.g., Haschke et al. 2012a, 2012b; Moretti et al. 2014; Paper I; Inno et al. 2016; Ripepi et al. 2017). Thus, we do not think that the individual dereddening technique is suitable to properly determine distances to Magellanic System Cepheids and especially to infer any conclusions about structure and geometry.

4.6. Reddening Parameters

Table 5 shows local IDs and absolute magnitudes in I and V bands, as well as color excesses of our Bridge CCs. For each passband we present two values for each parameter calculated using different PL relations (Sandage et al. 2004, 2009; Gieren et al. 2018). As expected, the longer the period, the younger the Cepheid, and thus more luminous. Relations from Sandage et al. (2004, 2009) have significantly different zero-points than those of Gieren et al. (2018), and this results in CCs being less luminous in the latter case. Relations from Gieren et al. (2018) also have larger uncertainties, and this is reflected in Table 5. On the other hand, slopes are very consistent.

Color excesses, $E(V - I)$, in general have quite low values, consistent with the fact that there is low extinction toward the Bridge area (Schlegel et al. 1998; Wagner-Kaiser & Sarajedini 2017, Skowron et al. 2019, in preparation). $E(V - I)$ calculated using relations from Gieren et al. (2018) in many cases have values that are physical only within the error bars; thus, we use absolute magnitudes based on Sandage et al. (2004, 2009) in further analysis. The discrepancy is probably due to a difference in zero-points between these relations. However, we also note that relations from Gieren et al. (2018) were derived for CCs with periods 4 days $< P < 69$ days, and only 3 out of 10 of our CCs fall into this range.

Values obtained for color excesses of each CC are very well consistent with the mean value of this parameter found toward the Bridge by Wagner-Kaiser & Sarajedini (2017), who studied RRab-type stars in that area. Their median is $E(V - I) = 0.101 \pm 0.007$ mag.

Table 6 presents reddening parameters for our Bridge CCs calculated using absolute magnitudes based on PL relations from Sandage et al. (2004, 2009). $A_{I,V}$ are total extinctions

Table 7
Magellanic Bridge Anomalous Cepheids: Basic Parameters

Mode	OCVS ID	Loc. ID ^a	P (day)	$\langle I \rangle$ (mag)	$\langle V \rangle$ (mag)	R.A.	Decl.	d (kpc) ^b
F	OGLE-LMC-ACEP-084	...	2.0506071	17.033	17.859	03 ^h 49 ^m 00 ^s .53	−75°00′49″.1	51.38 ± 1.46
	OGLE-LMC-ACEP-085	...	0.9156319	17.358	17.974	03 ^h 59 ^m 33 ^s .43	−63°16′40″.5	43.01 ± 1.19
	OGLE-SMC-ACEP-100	...	1.6414839	17.405	17.908	02 ^h 05 ^m 36 ^s .66	−72°24′19″.9	46.05 ± 1.28
	OGLE-SMC-ACEP-104	...	0.8780260	17.197	17.654	02 ^h 14 ^m 51 ^s .37	−66°59′30″.4	43.64 ± 1.21
	OGLE-SMC-ACEP-105	...	0.7559469	18.218	18.840	02 ^h 30 ^m 22 ^s .39	−79°08′25″.9	56.81 ± 1.58
	OGLE-SMC-ACEP-106	...	1.5007656	17.425	18.096	02 ^h 37 ^m 03 ^s .85	−77°03′02″.8	57.14 ± 1.60
	OGLE-SMC-ACEP-107	...	0.9317619	17.254	17.755	02 ^h 41 ^m 27 ^s .95	−73°48′45″.1	44.97 ± 1.25
	OGLE-SMC-ACEP-108	...	0.9147562	18.000	18.589	02 ^h 58 ^m 18 ^s .94	−67°05′46″.8	58.90 ± 1.63
	OGLE-SMC-ACEP-109	...	1.1701982	17.749	18.326	03 ^h 04 ^m 44 ^s .43	−66°11′15″.1	61.23 ± 1.70
	OGLE-LMC-ACEP-146 ^{c,d}	M2	1.4300017	17.376	18.112	03 ^h 43 ^m 04 ^s .54	−76°56′02″.6	51.83 ± 1.45
OGLE-GAL-ACEP-028 ^{c,e}	M3	1.1589986	15.892	16.350	04 ^h 01 ^m 38 ^s .02	−69°28′40″.5	28.18 ± 0.79	
1O	OGLE-SMC-ACEP-102	...	0.9396136	17.347	17.904	02 ^h 13 ^m 39 ^s .52	−66°25′17″.0	58.35 ± 1.67
	OGLE-SMC-ACEP-122 ^f	M8	0.8883309	17.302	17.738	02 ^h 21 ^m 28 ^s .45	−65°45′22″.4	60.05 ± 1.72
	OGLE-LMC-ACEP-147	...	0.7777591	16.537	16.961	04 ^h 35 ^m 35 ^s .29	−81°06′21″.0	39.01 ± 1.13

Notes.

^a Local IDs are provided only for ACs reclassified from CCs.

^b The distance uncertainty does not include the mean LMC distance uncertainty from Pietrzyński et al. (2019) $d_{\text{LMC}} = 49.59 \pm 0.09$ (statistical) ± 0.54 (systematic) kpc.

^c These objects were reclassified from fundamental-mode CCs.

^d Former OGLE-SMC-CEP-4957.

^e Former OGLE-LMC-CEP-3376. This Cepheid was reclassified as a Milky Way object owing to its proximity.

^f This object was reclassified from first-overtone CC. Former OGLE-SMC-CEP-4954.

Table 8
PL Relations for ACs in the Magellanic System in the Wesenheit Magnitude

Galaxy	P. Mode	$W_{I,V-I} = a \log P + b$					N_{inc}	N_{rej}
		a	b (mag)	σ (mag)	χ^2/dof			
LMC	F	-2.960 ± 0.044	16.599 ± 0.007	0.165	7.880	97	4	
	1O	-3.297 ± 0.081	16.041 ± 0.017	0.144	6.260	39	1	
SMC	F	-2.725 ± 0.054	16.927 ± 0.009	0.178	9.228	74	1	
	1O	-3.710 ± 0.094	16.539 ± 0.017	0.169	8.592	40	0	

Note. F stands for fundamental mode, while 1O stands for first-overtone pulsators. N_{inc} is the number of objects included in the fit, while N_{rej} is the number of objects rejected during the 3σ -clipping procedure.

obtained using our basic method distances, and $A_{(I,V),W44}$ are calculated using distances obtained with a slightly different reddening law—assuming a different color term coefficient in the Wesenheit index (as described in Section 4.5). Both values are very similar, showing again that the adopted reddening law does not influence our technique much. However, the total extinction is of a quite low value, close to zero, and has a rather low precision (uncertainties are twice the obtained values or even higher). In some cases, the obtained value is even less than zero. We want to emphasize here that these values are still physical, as they are consistent with zero or very low positive values within the error bars.

Similarly to Haschke et al. (2012a, 2012b), we also calculated extinction without using a priori distances but assuming a reddening law as described in Section 4.5 (see Equation (12)). Results are shown in Table 6 as $A_{(I,V),t}$. Values obtained for I passband are significantly larger than resulting from previously described methods, however, surprisingly, they are consistent within the error bars. The V -band extinction matches quite well with values obtained using other techniques. On the other hand, the error bars for $A_{(I,V),t}$ are quite high.

5. Anomalous Cepheids

5.1. Final Sample and Basic Parameters

We used the recently published OGLE Collection of ACs in the Magellanic System (Soszyński et al. 2017) to construct our Bridge sample. Based on three-dimensional locations of these stars in comparison to the entire LMC and SMC samples, we decided to classify 10 ACs as Bridge candidates. Due to the latest updates and corrections applied to the OCVS (see Section 2.1), three Bridge CCs were reclassified as ACs. That enlarged our AC MBR sample to 13. Table 7 shows basic parameters of these objects: OCVS ID, local ID used in Paper I and this work (only for Cepheids reclassified from CCs to ACs), pulsation period P , mean magnitudes from both OGLE passbands (I and V), R.A. and decl. (epoch J2000.0), and distance d .

To calculate individual distances of ACs, we used the same technique as for CCs (Section 3.1). We applied one exception to 3σ clipping. We did not exclude one anomalous Cepheid from our sample that was treated by our algorithm as an outlier, namely, OGLE-LMC-ACEP-147. This star is located in the

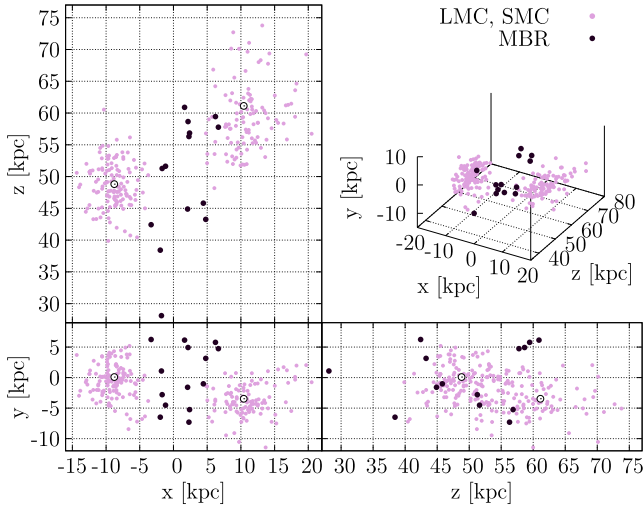


Figure 8. Three-dimensional distribution of anomalous Cepheids in the Magellanic System, with the MBR sample marked with darker circles. The map is represented in Cartesian coordinates with the observer located at (0, 0, 0). White circles mark LMC (van der Marel & Kallivayalil 2014; Pietrzyński et al. 2019) and SMC (Stanimirović et al. 2004; Graczyk et al. 2014) centers.

newly added southern extension of the OGLE fields. The parameters of the fits are presented in Table 8 and are consistent with those of Iwanek et al. (2018). There is a slight discrepancy between our results and those of Groenewegen & Jurkovic (2017) and Ripepi et al. (2014) that is probably caused by the latter being based on less numerous samples.

5.2. Two- and Three-dimensional Analysis

The on-sky locations of all OGLE ACs along with CCs and T2Cs are presented in Figure 1, where the Bridge sample is highlighted with larger circles. Figure 3 shows a close-up of the central Bridge area. The Cepheid locations are compared to young stars (Skowron et al. 2014) and HI distribution (the Galactic All Sky HI Survey, McClure-Griffiths et al. 2009; Kalberla et al. 2010; Kalberla & Haud 2015). Both plots clearly show that ACs are more spread than CCs and do not form as evident substructures as the latter in any area of the Magellanic System, including the Bridge. In contrary to CCs, ACs do not follow any line or bridge-like connection between the Clouds and do not match either the neutral hydrogen or young population distribution. Nevertheless, this is what we could expect for an older stellar population. For a detailed statistical analysis of the three-dimensional distribution of ACs, see Iwanek et al. (2018).

We were still able to distinguish the Bridge candidates located between the Magellanic Clouds in three dimensions. Figure 8 shows the three-dimensional distribution of ACs in the entire Magellanic System, with the Bridge sample distinguished using larger circles. Although not very numerous, the ACs seem to create a rather smooth connection between the Clouds. However, we cannot state that this connection is bridge-like because these ACs may also be LMC and/or SMC outliers that we also see located in different directions around these galaxies.

5.3. Proper Motions

Similarly to CCs, we also used *Gaia* DR2 (Gaia Collaboration et al. 2018) to analyze PMs of our Bridge ACs. Again, we

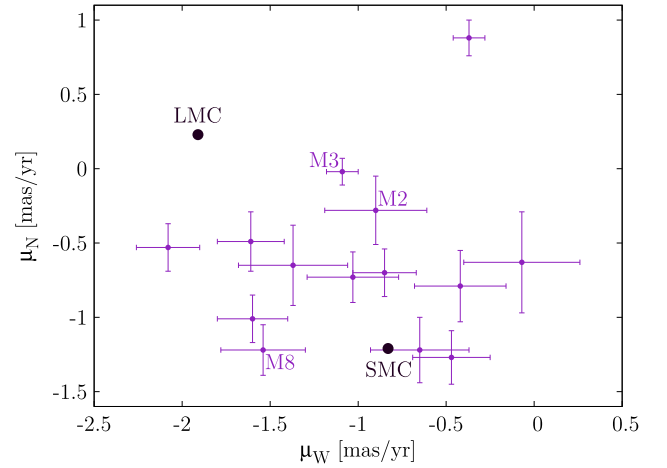


Figure 9. PMs of Bridge ACs as compared to the PM of the LMC (Kallivayalil et al. 2013) and SMC (Zivick et al. 2018). Three reclassified Cepheids are shown with their local IDs.

compare results to the LMC and SMC PMs in Figures 9 and 10. ACs follow the general on-sky movement of the entire Magellanic System. Almost all of them fall into the PM range that we would expect for Bridge objects (see Figure 3 from Zivick et al. 2019).

6. Reclassified Cepheids

The latest reclassification of four CCs is slightly disputable, as all of these objects have parameters located close to the CC/AC (or CC F/1O) boundary. In Table 9 we compare basic parameters of the four stars before and after the reclassification and list the following: local ID, type, and mode, as well as distance and age before and after the reclassification. The estimates for the latter were already presented in the previous sections. The estimates for before the reclassification were calculated simply including these objects in the appropriate CC or AC sample and using the same technique as for the entire samples that we present in this paper.

The bottom row of Figure 2 shows the four reclassified Cepheids on the PL relations for the entire LMC (left panel) and SMC (right panel) CC and AC samples. The Bridge Cepheid sample is overplotted in each panel using large symbols. Additionally, the reclassified Cepheids are also marked with a star and their local ID. We discuss locations of these objects on the PL diagrams according to all of the presented relations, as these Cepheids may be neither LMC nor SMC members. Thus, their parameters need to be analyzed in a broader context. Note that we do not classify objects based only on their location on the PL diagrams, but we mainly use their light curve (shape and Fourier decomposition parameters; Soszyński et al. 2015a).

M7, which was reclassified from first-overtone CC to fundamental-mode CC, is indeed located much closer to the fundamental mode than first-overtone PL relations. This object is also situated close to the LMC fundamental-mode ACs but at the same time is close to the SMC fundamental-mode CCs. M2, recently reclassified from fundamental-mode CC to fundamental-mode AC, is very close to the LMC fundamental-mode AC PL relation. On the other hand, it is located in between the fundamental-mode CC and AC PL relations for the SMC. M3 is another object reclassified in the same way as M2. M3 is

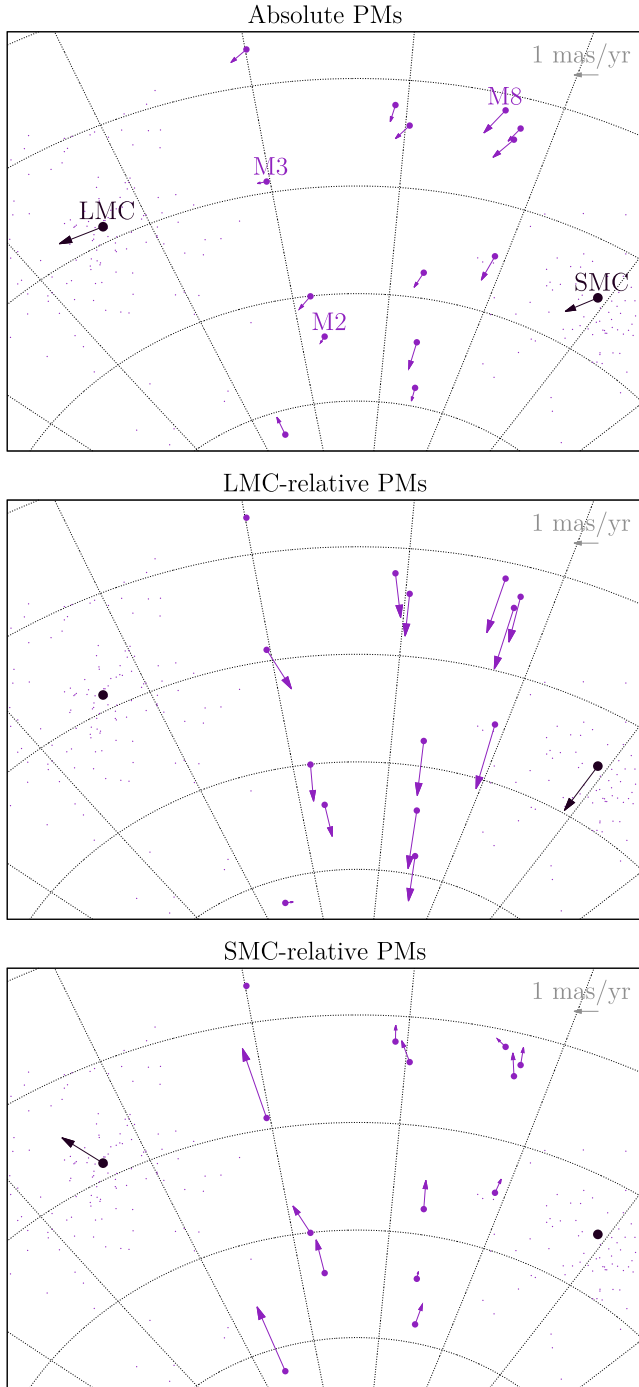


Figure 10. PMs of Bridge ACs, as well as LMC (Kallivayalil et al. 2013) and SMC (Zivick et al. 2018), shown as vectors on the sky. The top panel presents absolute PMs, while the middle and bottom panels present the LMC- and SMC-related frame, respectively. We adopted the LMC center of van der Marel & Kallivayalil (2014) and the SMC center of Stanimirović et al. (2004).

situated almost on the fit that we obtained for the first-overtone CCs in the LMC. In fact, it is located quite far from the LMC fundamental-mode PL relation for the CCs, and for the ACs, it is even farther. Compared to the SMC relations, M3 definitely seems to be an outlier from the fundamental-mode PL relations. In the case of M8, which was reclassified from the first-overtone CC to the first-overtone AC, the closest PL relations in the LMC are relations for both types of ACs. This star is

located between these relations. When compared to the SMC, M8 is situated close to the first-overtone PL relation for ACs but at the same time is quite close to both PL relations for the CCs.

The reclassification has a significantly changed three-dimensional distribution of Cepheids in the Bridge area, as distances of all reclassified objects have decreased by more than 10 kpc in each case. We show this change in Figure 11, where we plotted projections of a three-dimensional Cartesian distribution of all Cepheids analyzed here (both CCs and ACs), with the Bridge sample highlighted using larger circles. The reclassified objects are marked separately, and the arrows show the change of distances that occurred with the reclassification.

A change of close to or more than 20 kpc has occurred for M2, M7, and M8. If these stars were not reclassified, they would be perfect candidates for Counter Bridge members, as we have already stated in Paper I. Moreover, their ages would match very well the scenario in which they would be formed in situ in this structure. M2 and M8 were reclassified as ACs, and after this change these objects are located in between the Magellanic Clouds, matching very well the three-dimensional distribution of ACs (see Figure 8). M7 is a CC, and even after the reclassification this star could be a Counter Bridge member, though it is now located farther from the center of this structure, and thus this scenario is less plausible (we have discussed M7 location in detail in Section 4.5).

In our Bridge CC sample from Paper I M3 was the closest Cepheid—located even closer than any LMC CC. After the reclassification, this object is located even closer at ~ 28 kpc—halfway between the Sun and the Magellanic System. Due to this, M3 was treated as an LMC outlier by our 3σ -clipping algorithm that we applied to the AC sample. Based on its proximity, we decided to classify this object as Milky Way halo AC.

7. *Gaia* DR2 Cepheids in the Bridge

7.1. Comparison with OCVS

The *Gaia* DR2 contains a list of variable stars including Cepheids and RR Lyrae stars (Gaia Collaboration et al. 2018; Holl et al. 2018; Clementini et al. 2019). As following Holl et al. (2018), due to the probabilistic and automated nature of the classification process, the *Gaia* DR2 catalog of classical variables is not as complete and pure as the OCVS is (see Table 2 in Holl et al. 2018; Clementini et al. 2019). In this section we revive the *Gaia* DR2 classical pulsators, listed in the `vari_cepheid` table (Gaia Collaboration et al. 2018; Holl et al. 2018), in the MBR area and compare it to the OCVS.

Figure 12 compares on-sky locations of individual Cepheids of different types and modes in the Bridge area. The top row shows OGLE data, while the middle and bottom rows show *Gaia* DR2. The latter shows the DR2 Cepheid sample after the reclassification made by Ripepi et al. (2019). The first three columns show CCs of the following modes, both single- and multimode—fundamental, first-overtone, and both of these together. Based on only these plots, it may seem that *Gaia* DR2 discovered several new CCs that were not present in the virtually complete OGLE Collection of CCs (Soszyński et al. 2017).

Comparing distributions of anomalous Cepheids, both fundamental-mode and first-overtone pulsators, as well as entire samples, the *Gaia* DR2 seems to classify no objects as

Table 9
Magellanic Bridge Cepheids: Reclassification

Loc. ID	Type and Mode	Before → After		
		d (kpc) ^a	Age (Myr) ^b	
M2	CC F → AC F	$74.07 \pm 2.08 \rightarrow 51.83 \pm 1.45$	$233 \pm 49 \rightarrow$	NA
M3	CC F → AC F	$39.81 \pm 1.11 \rightarrow 28.18 \pm 0.78$	$275 \pm 57 \rightarrow$	NA
M8	CC 1O → AC 1O	$80.95 \pm 2.23 \rightarrow 60.05 \pm 1.72$	$292 \pm 48 \rightarrow$	NA
M7	CC 1O → CC F	$88.83 \pm 2.45 \rightarrow 69.99 \pm 1.97$	$151 \pm 25 \rightarrow$	209 ± 44

Notes.

^a The distance uncertainty does not include the mean LMC distance uncertainty from Pietrzyński et al. (2019) $d_{\text{LMC}} = 49.59 \pm 0.09$ (statistical) ± 0.54 (systematic) kpc.

^b This age determination was estimated using the period–age relation from Bono et al. (2005) and is available for CCs only.

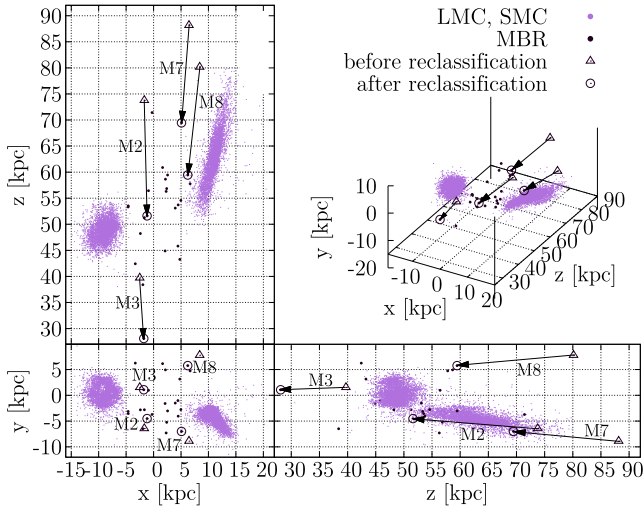


Figure 11. Three-dimensional distribution of CCs and ACs in the Magellanic System, with the MBR sample marked with large circles. Additionally, locations of four reclassified Cepheids are highlighted with different markers. Arrows show the direction of changes in locations. Labels show local IDs of these objects (see Table 9). The map is represented in the Cartesian coordinates with the observer located at (0, 0, 0).

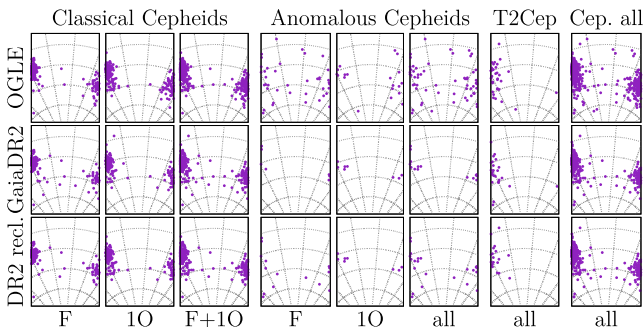


Figure 12. Comparison of OGLE (top row) and *Gaia* DR2 (middle and bottom rows) Cepheids in the Magellanic Bridge area. The bottom row shows the DR2 sample after the reclassification made by Ripepi et al. (2019). It may seem that *Gaia* DR2 discovered more CCs in the Bridge area than contained in the nearly complete OCVS. However, a comparison of different panels leads to a conclusion that many of the ACs were classified in DR2 as CCs. Finally, the OCVS contains several more Cepheids in the Bridge area than DR2.

anomalous Cepheids in the Bridge. At the same time, the OCVS contains many ACs in between the Magellanic Clouds. This leads to a conclusion that many ACs were classified as CCs in DR2. This is probably due to different classification methods used in both cases (i.e., see reclassification of the

Milky Way Cepheids from *Gaia* DR2 in Ripepi et al. 2019). It is very similar for T2Cs, though neither OGLE nor *Gaia* DR2 classifies any objects of this type in the central Bridge area. A comparison of all of the Cepheids between the Magellanic Clouds reveals that the *Gaia* DR2 has incorrectly cataloged a number of objects in the Bridge area.

We compared the OCVS and *Gaia* DR2 Cepheid samples in numbers. For the cross-match we selected a DR2 sample covering the entire OGLE fields in the Magellanic System (see Figure 1). We use the OCVS sample containing the latest updates and corrections as described in Section 2.1. Out of 10,140 Cepheids included in the OGLE Collection in the Magellanic System (9532 CCs, 268 ACs, 340 T2Cs), 7490 objects were found in the *Gaia* DR2 Cepheid sample. Thus, when comparing to the virtually complete OGLE Collection of Cepheids, the *Gaia* DR2 completeness is on a level of 73.9%, which is consistent with Table 2 in Holl et al. (2018). High completeness is not surprising, as the OCVS Cepheid data set from the Magellanic Clouds was a training set for the *Gaia* Cepheid detection algorithms. In other areas of the sky, the *Gaia* DR2 Cepheid sample completeness is significantly lower, i.e., Udalski et al. (2018) showed that in the Milky Way disk and bulge area it is on a level of 9.1%.

We additionally compared the *Gaia* DR2 detections in the region designed as MBR in OGLE-IV fields (Figure 18 in Udalski et al. 2015). A total of 30 *Gaia* DR2 Cepheids are located in the OGLE MBR field footprint; 29 were confirmed in the OGLE Collection as genuine Cepheids, and the one lacking object is likely an eclipsing star. A total of 59 Cepheids in the OGLE Collection (CCs, ACs, and T2Cs) lie in the OGLE MBR fields. Thus, the completeness of the *Gaia* DR2 in this region is $29/59 \simeq 49\%$.

8. Conclusions

In this paper, which is the third in a series of analyzing the three-dimensional structure of the Magellanic System, we present an updated detailed analysis of Cepheids in the MBR. We use data from the OGLE project—released parts of the OCVS (Soszyński et al. 2015b, 2017, 2018, 2019). The collection was recently updated: seven Cepheids were added, and four were reclassified. We present a thorough study of classical and anomalous Cepheid Bridge samples using very precise OGLE photometry. We note that we did not classify any T2C as an MBR member owing to their absence in this area.

Similarly to Paper I, our basic method of calculating distances relies on fitting PL relations using the Wesenheit $W_{I,V-I}$ index to the entire LMC sample. Then, we estimate the

individual distance of each Cepheid relative to the LMC mean distance and the LMC fit. Based on three-dimensional coordinates and on-sky locations of stars in relation to the LMC and SMC entire samples, we selected our Bridge samples.

The updated Bridge CC sample contains 10 objects. As compared to the Paper I sample, we removed three objects (M2, M3, and M8, which were reclassified as ACs) and added four objects (M10, added by Soszyński et al. 2017, and M11–M13). On-sky locations of the CC MBR sample match very well the HI density contours and the young stars' distribution. Only two Cepheids, namely, M7 and M10, are located slightly offset, though still well within the densest regions. The CCs add to the overall distribution of young stars in the Bridge area.

In three dimensions, 8 out of 10 objects from the CC sample form a bridge-like connection between the Magellanic Clouds. Four out of these eight are located close to the LMC (M12 and M13) or SMC (M9 and M11). Two that do not form the bridge-like connection, namely, M1 and M7, are located slightly farther than the main sample; thus, they may constitute a Counter Bridge. However, they may also be genuine MBR members. Further study is needed to test this. We also analyzed different methods of obtaining distances and conclude that the adopted reddening law does not influence results much and the reddening toward the Bridge is low. Moreover, the individual dereddening method used by, e.g., Haschke et al. (2012a, 2012b) seems to be inappropriate in this case.

From 5 up to 8 out of 10 Bridge CCs have ages of less than 300 Myr (as based on the period–age relations from Bono et al. 2005; Anderson et al. 2016). This agrees with a hypothesis that some of the Bridge objects may have been formed in situ after the last encounter of the Magellanic Clouds. The two youngest CCs have ages less than 60 Myr. The two oldest CCs can be LMC or SMC members. Moreover, their periods are shorter than 1 day; thus, their age estimate may not be appropriate, as the models do not predict ages of such short-period pulsators.

Our Bridge AC sample consists of 13 objects. Their on-sky locations do not match HI or young star density contours. AC distribution is very spread out in both two and three dimensions. However, they form a rather smooth connection between the Magellanic Clouds. But we also cannot state that this connection is bridge-like, as these stars may also be LMC/SMC outliers.

We also tested *Gaia* DR2 Cepheids' on-sky distribution in the Bridge area. DR2 contains more CCs in the MBR than the OCVS. However, DR2 does not include virtually any AC in between the Magellanic Clouds. This is explained by a different classification process, where many ACs are classified as CCs in DR2. A comparison of all types of Cepheids shows that the OCVS has more objects in the MBR and thus is definitely more complete.

We present a complementing study of older classical pulsators in the MBR—RR Lyrae stars—in a closely following Paper IV.


A.M.J.-D. is supported by the Polish Ministry of Science and Higher Education under “Diamond Grant” No. DI2013 014843 and by the Deutsche Forschungsgemeinschaft (DFG, German Research Foundation)—Project-ID 138713538—SFB 881 (“The Milky Way System,” subproject A03). The OGLE project has received funding from the National Science Centre, Poland, grant MAESTRO 2014/14/A/ST9/00121 to A.U.

We would like to thank all of those whose remarks and comments inspired us and helped to make this work more valuable, especially the anonymous referee. In particular, we would also like to thank Richard Anderson, Abhijit Saha, Vasily Belokurov, Anthony Brown, Laurent Eyer, Martin Groenewegen, Vincenzo Ripepi, Radosław Smolec, Martino Romaniello, and Krzysztof Stanek.

This research was supported by the Munich Institute for Astro- and Particle Physics (MIAPP) of the DFG cluster of excellence “Origin and Structure of the Universe,” as it benefited from the MIAPP program “The Extragalactic Distance Scale in the *Gaia* Era,” as well as the International Max Planck Research School (IMPRS) Summer School on “*Gaia* Data and Science 2018.”

This work has made use of data from the European Space Agency (ESA) mission *Gaia* (<https://www.cosmos.esa.int/gaia>), processed by the *Gaia* Data Processing and Analysis Consortium (DPAC, <https://www.cosmos.esa.int/web/gaia/dpac/consortium>). Funding for the DPAC has been provided by national institutions, in particular the institutions participating in the *Gaia* Multilateral Agreement.

ORCID iDs

Anna M. Jacyszyn-Dobrzniecka  <https://orcid.org/0000-0002-5649-536X>

Igor Soszyński  <https://orcid.org/0000-0002-7777-0842>


Jan Skowron  <https://orcid.org/0000-0002-2335-1730>

Przemek Mróz  <https://orcid.org/0000-0001-7016-1692>

Patryk Iwanek  <https://orcid.org/0000-0002-6212-7221>

Paweł Pietrukowicz  <https://orcid.org/0000-0002-2339-5899>

Radosław Poleski  <https://orcid.org/0000-0002-9245-6368>

Szymon Kozłowski  <https://orcid.org/0000-0003-4084-880X>

Krzysztof Ulaczyk  <https://orcid.org/0000-0001-6364-408X>





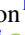
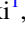
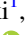






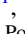

References

- Alcock, C., Allsman, R. A., Axelrod, T. S., et al. 1995, *AJ*, 109, 1653
- Anderson, R. I., Saio, H., Ekström, S., Georgy, C., & Meynet, G. 2016, *A&A*, 591, A8
- Bagheri, G., Cioni, M.-R. L., & Napiwotzki, R. 2013, *A&A*, 551, A78
- Barger, K. A., Haffner, L. M., & Bland-Hawthorn, J. 2013, *ApJ*, 771, 132
- Belokurov, V., Erkal, D., Deason, A. J., et al. 2017, *MNRAS*, 466, 4711
- Besla, G., Kallivayalil, N., Hernquist, L., et al. 2012, *MNRAS*, 421, 2109
- Bhardwaj, A., Ngeow, C.-C., Kanbur, S. M., & Singh, H. P. 2016, *MNRAS*, 458, 3705
- Bica, E. L. D., Santiago, B., Bonatto, C., et al. 2015, *MNRAS*, 453, 3190
- Bica, E. L. D., & Schmitt, H. R. 1995, *ApJS*, 101, 41
- Bono, G., Marconi, M., Cassisi, S., et al. 2005, *ApJ*, 621, 966
- Carrera, R., Conn, B. C., Noël, N. E. D., et al. 2017, *MNRAS*, 471, 4571
- Clementini, G., Ripepi, V., Molinaro, R., et al. 2019, *A&A*, 622, A60
- Deason, A. J., Belokurov, V., Erkal, D., Koposov, S. E., & Mackey, D. 2017, *MNRAS*, 467, 2636
- Deb, S., Ngeow, C.-C., Kanbur, S. M., et al. 2018, *MNRAS*, 478, 2526
- Demers, S., & Battinelli, P. 1998, *AJ*, 115, 154
- Diaz, J. D., & Bekki, K. 2012, *ApJ*, 750, 36
- D’Onghia, E., & Fox, A. J. 2016, *ARA&A*, 54, 363
- Fiorentino, G., & Monelli, M. 2012, *A&A*, 540, A102
- Fouqué, P., Arriagada, P., Storm, J., et al. 2007, *A&A*, 476, 73
- Gaia Collaboration, Brown, A. G. A., et al. 2018, *A&A*, 616, A1
- Gallenne, A., Kervella, P., Mérand, A., et al. 2017, *A&A*, 608, A18
- Gardiner, L. T., & Noguchi, M. 1996, *MNRAS*, 278, 191
- Gardiner, L. T., Sawa, T., & Fujimoto, M. 1994, *MNRAS*, 266, 567
- Gieren, W., Storm, J., Konorski, P., et al. 2018, *A&A*, 620, 99
- Graczyk, D., Pietrzyński, G., Thompson, I. B., et al. 2014, *ApJ*, 780, 59
- Groenewegen, M. A. T., & Jurkovic, M. I. 2017, *A&A*, 604, A29
- Groenewegen, M. A. T., & Oudmaijer, R. D. 2000, *A&A*, 356, 849
- Guglielmo, M., Lewis, G. F., & Bland-Hawthorn, J. 2014, *MNRAS*, 444, 1759

- Harris, J. 2007, *ApJ*, **658**, 345
- Haschke, R., Grebel, E. K., & Duffau, S. 2012a, *AJ*, **144**, 106
- Haschke, R., Grebel, E. K., & Duffau, S. 2012b, *AJ*, **144**, 107
- Hindman, J. V., Kerr, F. J., & McGee, R. X. 1963, *AuJPh*, **16**, 570
- Holl, B., Audard, M., Nienartowicz, K., et al. 2018, *A&A*, **618**, A30
- Indu, G., & Subramaniam, A. 2015, *A&A*, **573**, A136
- Inno, L., Bono, G., Matsunaga, N., et al. 2016, *ApJ*, **832**, 176
- Inno, L., Matsunaga, N., Bono, G., et al. 2013, *ApJ*, **764**, 84
- Irwin, M. J., Kunkel, W. E., & Demers, S. 1985, *Natur*, **318**, 160
- Iwanek, P., Soszyński, I., Skowron, D., et al. 2018, *AcA*, **68**, 213
- Jacyszyn-Dobrzniecka, A. M., Kruszyńska, K., Mróz, P., et al. 2020, *ApJ*, **889**, 26
- Jacyszyn-Dobrzniecka, A. M., Skowron, D. M., Mróz, P., et al. 2016, *AcA*, **66**, 149
- Jacyszyn-Dobrzniecka, A. M., Skowron, D. M., Mróz, P., et al. 2017, *AcA*, **67**, 1
- Kalberla, P. M. W., & Haud, U. 2015, *A&A*, **578**, A78
- Kalberla, P. M. W., McClure-Griffiths, N. M., Pisano, D. J., et al. 2010, *A&A*, **512**, A14
- Kallivayalil, N., van der Marel, R. P., Besla, G., Anderson, J., & Alcock, C. 2013, *ApJ*, **764**, 161
- Kochanek, C. S., Schappee, B. J., Stanek, K. Z., et al. 2017, *PASP*, **129**, 104502
- Koposov, S. E., Walker, M. G., Belokurov, V., et al. 2018, *MNRAS*, **479**, 5343
- Lehner, N., Howk, J. C., Keenan, F. P., & Smoker, J. V. 2008, *ApJ*, **678**, 219
- Lemasle, B., François, B., Genovali, K., et al. 2013, *A&A*, **558**, A31
- Mackey, A. D., Koposov, S. E., Da Costa, G. S., et al. 2017, *MNRAS*, **472**, 2975
- Madore, B. F. 1982, *ApJ*, **253**, 575
- Madore, B. F., Freedman, W. L., & Moak, S. 2017, *ApJ*, **842**, 42
- McClure-Griffiths, N. M., Pisano, D. J., Calabretta, M. R., et al. 2009, *ApJS*, **181**, 398
- Misawa, T., Charlton, J. C., Kobulnicky, H. A., Wakker, B. P., & Bland-Hawthorn, J. 2009, *ApJ*, **695**, 1382
- Moretti, M. I., Clementini, G., Muraveva, T., et al. 2014, *MNRAS*, **437**, 2702
- Ngeow, C.-C. 2012, *ApJ*, **747**, 50
- Ngeow, C.-C., Sarkar, S., Bhardwaj, A., Kanbur, S. M., & Singh, H. P. 2015, *ApJ*, **813**, 57
- Nikolaev, S., Drake, A. J., Keller, S. C., et al. 2004, *ApJ*, **601**, 260
- Noël, N. E. D., Conn, B. C., Carrera, R., et al. 2013, *ApJ*, **768**, 109
- Noël, N. E. D., Conn, B. C., Read, I. J., et al. 2015, *MNRAS*, **452**, 4222
- Oey, M. S., Dorigo Jones, J., Castro, N., et al. 2018, *ApJL*, **867**, L8
- Pietrzyński, G., Graczyk, D., Gallenne, A., et al. 2019, *Natur*, **567**, 200
- Ploeckinger, S., Hensler, G., Recchi, S., Mitchell, N., & Kroupa, P. 2014, *MNRAS*, **437**, 3980
- Ploeckinger, S., Recchi, S., Hensler, G., & Kroupa, P. 2015, *MNRAS*, **447**, 2512
- Ploeckinger, S., Sharma, K., Schaye, J., et al. 2018, *MNRAS*, **474**, 580
- Ripepi, V., Cioni, M.-R., Moretti, M. I., et al. 2017, *MNRAS*, **472**, 808
- Ripepi, V., Marconi, M., Moretti, M. I., et al. 2014, *MNRAS*, **437**, 2307
- Ripepi, V., Molinaro, R., Musella, I., et al. 2019, *A&A*, **625**, A14
- Růžička, A., Theis, C., & Palouš, J. 2010, *ApJ*, **725**, 369
- Sandage, A., Tammann, G. A., & Reindl, B. 2004, *A&A*, **424**, 43
- Sandage, A., Tammann, G. A., & Reindl, B. 2009, *A&A*, **493**, 471
- Schappee, B. J., Prieto, J. L., Grupe, D., et al. 2014, *ApJ*, **788**, 48
- Schlegel, D. J., Finkbeiner, D., & Davis, M. 1998, *ApJ*, **500**, 525
- Scowcroft, V., Freedman, W. L., Madore, B. F., et al. 2016, *ApJ*, **816**, 49
- Shapley, H. 1940, *BHarO*, **914**, 8
- Skowron, D. M., Jacyszyn, A. M., Udalski, A., et al. 2014, *ApJ*, **795**, 108
- Soszyński, I., Poleski, R., Udalski, A., et al. 2008, *AcA*, **58**, 163
- Soszyński, I., Udalski, A., Szymański, M. K., et al. 2015a, *AcA*, **65**, 233
- Soszyński, I., Udalski, A., Szymański, M. K., et al. 2015b, *AcA*, **65**, 297
- Soszyński, I., Udalski, A., Szymański, M. K., et al. 2017, *AcA*, **67**, 103
- Soszyński, I., Udalski, A., Szymański, M. K., et al. 2018, *AcA*, **68**, 89
- Soszyński, I., Udalski, A., Szymański, M. K., et al. 2019, *AcA*, **69**, 87
- Stanimirović, S., Staveley-Smith, L., & Jones, P. A. 2004, *ApJ*, **604**, 176
- Storm, J., Gieren, W., Fouqué, P., et al. 2011, *A&A*, **534**, A95
- Sziládi, K., Vinkó, J., Poretti, E., Szabados, L., & Kun, M. 2007, *A&A*, **473**, 579
- Sziládi, K., Vinkó, J., & Szabados, L. 2018, *AcA*, **68**, 111
- Tammann, G. A., Sandage, A., & Reindl, B. 2003, *A&A*, **404**, 423
- Tammann, G. A., Sandage, A., & Reindl, B. 2008, *ApJ*, **679**, 52
- Udalski, A. 2003, *ApJ*, **590**, 284
- Udalski, A., Soszyński, I., Pietrukowicz, P., et al. 2018, *AcA*, **68**, 315
- Udalski, A., Szymański, M. K., Kubiak, M., et al. 1999, *AcA*, **49**, 201
- Udalski, A., Szymański, M. K., & Szymański, G. 2015, *AcA*, **65**, 1
- van der Marel, R. P., & Kallivayalil, N. 2014, *ApJ*, **781**, 121
- Wagner-Kaiser, R., & Sarajedini, A. 2017, *MNRAS*, **466**, 4138
- Zivick, P., Kallivayalil, N., Besla, G., et al. 2019, *ApJ*, **874**, 78
- Zivick, P., Kallivayalil, N., van der Marel, R. P., et al. 2018, *ApJ*, **864**, 55



OGLE-ing the Magellanic System: RR Lyrae Stars in the Bridge*

Anna M. Jacyszyn-Dobrzeniecka^{1,2} , Przemek Mróz^{1,5} , Katarzyna Kruszyńska¹ , Igor Soszyński¹ , Dorota M. Skowron¹ , Andrzej Udalski¹ , Michał K. Szymański¹ , Patryk Iwanek¹ , Jan Skowron¹ , Paweł Pietrukowicz¹ , Radosław Poleski³ , Szymon Kozłowski¹ , Krzysztof Ulaczyk⁴ , Krzysztof Rybicki¹ , and Marcin Wrona¹ 

¹ Astronomical Observatory, University of Warsaw, Al. Ujazdowskie 4, 00-478 Warszawa, Poland; jacyszyn@uni-heidelberg.de

² Astronomisches Rechen-Institut, Zentrum für Astronomie der Universität Heidelberg, Mönchhofstr. 12-14, D-69120 Heidelberg, Germany

³ Department of Astronomy, Ohio State University, 140 West 18th Avenue, Columbus, OH 43210, USA

⁴ Department of Physics, University of Warwick, Coventry CV4 7AL, UK

⁵ Division of Physics, Mathematics, and Astronomy, California Institute of Technology, Pasadena, CA 91125, USA

Received 2019 April 18; revised 2019 November 10; accepted 2019 November 29; published 2020 January 22

Abstract

We use the extended and updated Optical Gravitational Lensing Experiment (OGLE) Collection of Variable Stars to thoroughly analyze the distribution of RR Lyrae stars in the Magellanic Bridge. We use photometric metallicities to derive the absolute Wesenheit magnitude and individual distance of each RR Lyrae star. We confirm results from our earlier study showing that RR Lyrae stars are present in between the Magellanic Clouds, though their three-dimensional distribution more resembles two extended overlapping structures than a strict bridge-like connection. The contours do connect in the southern parts of the Bridge, albeit on a level too low to state that an evident connection exists. To test the sample numerically, we use multi-Gaussian fitting and conclude that there is no additional population or overdensity located in the Bridge. We also try to reproduce results on the putative RR Lyrae Magellanic Bridge stream by selecting RR Lyrae candidates from *Gaia* Data Release 1. We show that we are not able to obtain the evident connection of the Clouds without many spurious sources in the sample, as the cuts are not able to remove artifacts without eliminating the evident connection at the same time. Moreover, for the first time, we present the *Gaia* Data Release 2 RR Lyrae stars in the Magellanic Bridge area and show that their distribution matches our results.

Key words: galaxies: Magellanic Clouds – stars: variables: RR Lyrae

1. Introduction

Interactions between the Magellanic Clouds, and probably between the pair and the Milky Way, led to the formation of an entire complex of structures, together with the Clouds, referred to as the Magellanic System (e.g., Gardiner et al. 1994; Gardiner & Noguchi 1996; Yoshizawa & Noguchi 2003; Connors et al. 2006; Růžička et al. 2009, 2010; Besla et al. 2010, 2012; Diaz & Bekki 2012a, 2012b; Guglielmo et al. 2014). One piece of evidence of the latest encounter of the Large and Small Magellanic Clouds (LMC and SMC, respectively) is the Magellanic Bridge (MBR; i.e., Harris 2007).

Many studies proved that there are young stars located in between the LMC and SMC (Shapley 1940; Irwin et al. 1985; Demers & Battinelli 1998; Harris 2007; Nöel et al. 2013, 2015), and moreover, that they form a continuous connection matching the neutral hydrogen (HI) contours (Skowron et al. 2014). The young ages of some objects suggest an in situ Bridge formation (e.g., Jacyszyn-Dobrzeniecka et al. 2016, 2020, hereafter Paper I and Paper III, respectively). This implies that the interactions were strong enough to pull out gas from the Magellanic Clouds and trigger star formation outside these galaxies. For a better understanding of the processes leading to these events, it is also important to test the older stellar populations in the MBR. Were the interactions strong enough to pull out not only gas but also stars from either the LMC, the SMC, or both? Hereafter, we focus on the older population of stars. For more information about different characteristics of the Bridge, see the introduction in Paper III.

Candidates for a stellar Bridge counterpart belonging to the older population were found by Bagheri et al. (2013) and Skowron et al. (2014). Wagner-Kaiser & Sarajedini (2017) analyzed RR Lyrae (RRL) stars using the Optical Gravitational Lensing Experiment (OGLE) collection of RRL stars and demonstrated that there exists a continuous flow of these objects between the Magellanic Clouds. The authors pointed out that the metallicities and distances of old population members show a smooth transition between the LMC and SMC. Moreover, the RRL star distribution does not match the HI density distribution. Thus, they suggest that RRL stars better resemble two overlapping structures than a tidally stripped bridge. Recently, Zivick et al. (2019) used *Gaia* data to show that an old stellar population is more broadly distributed and does not follow the HI bridge, in contrast to a young population.

Jacyszyn-Dobrzeniecka et al. (2017, hereafter Paper II) also used the RRL sample from the OGLE Collection of Variable Stars (OCVS; Soszyński et al. 2016) to analyze the three-dimensional distribution of RRL stars in the Magellanic System and the Bridge. Their results are perfectly consistent with those of Wagner-Kaiser & Sarajedini (2017), showing that there is little evidence for a bridge-like structure formed by an old population between the Magellanic Clouds.

On the other hand, Carrera et al. (2017) studied 39 intermediate-age and old stars in two Bridge fields located near the highest HI density contours and close to the SMC (between R.A. 2^h and 3^h) and found that, based on chemistry and kinematics, these objects are tidally stripped from the SMC. Their metallicities are consistent with those of Wagner-Kaiser & Sarajedini (2017). Both results are not necessarily incoherent, as stars analyzed by Carrera et al. (2017) may just

* Draft version prepared on 2019 December 5.

be SMC halo members. Their kinematics are in agreement with recent studies by Oey et al. (2018) and Zivick et al. (2019), who found that both young and old stellar populations are moving away from the SMC toward the LMC.

Another study of the Bridge old population was carried out using *Gaia* Data Release 1 (DR1; Gaia Collaboration et al. 2016). Belokurov et al. (2017, hereafter B17) developed a procedure to select RRL candidates from DR1 and analyzed their distribution in the MBR. They found an evident stellar bridge between the Magellanic Clouds that is shifted from the young star bridge, and thus from the highest HI density contours, by about 5° . They explained this difference with an older bridge trailing rather than following the Magellanic System. Moreover, they also performed a simulation to test whether such a scenario is plausible. Later, at least one stellar substructure partially cospatial with the B17 RRL bridge was found by Mackey et al. (2018), who used a deep panoramic survey conducted with the Dark Energy Camera. Also, Belokurov & Erkal (2018) found such substructures in the red giant distribution using *Gaia* Data Release 2 (DR2).

Similarly to B17, Deason et al. (2017) selected Mira candidates from DR1 and analyzed their distribution in the Magellanic System. They found that there are not as many Miras as RRL stars in the Bridge, and no bridge-like connection could be found. However, Miras form a slightly extended feature stretching out of the SMC toward the RRL bridge discovered by B17.

In this paper, which is the fourth in a series devoted to analysis of three-dimensional structure of the Magellanic System using the OCVS, we examine the RRL star distribution in the Bridge area with extended and updated OGLE data. We also compare our results to those of B17, whose results are not in agreement with Paper II. Moreover, we perform an analysis of the DR1 data using the B17 method and show their distribution of RRL candidates. We also show, for the first time, the distribution of RRL stars from *Gaia* DR2 (Gaia Collaboration et al. 2018; Holl et al. 2018; Clementini et al. 2019) in the Bridge area.

We have organized the paper as follows. Section 2 describes the RRL stars from the OCVS and the updates, corrections, and extensions that were later applied to the collection. Sample selection, as well as the methods used for analysis, are found in Section 3. In Section 4 we describe a study of the three-dimensional distribution of RRL stars from the OCVS. Section 5 presents a reanalysis of the OCVS sample using a different method, which is an attempt to reproduce the B17 results. In Section 6 we present our analysis of DR1 data using the B17 method to select RRL candidates. In Section 7 we compare distributions of different stellar tracers in the Bridge and present the DR2 RRL star distribution. We conclude the paper in Section 8.

2. Observational Data

2.1. OCVS

Since Paper II was published, the OCVS has been updated, and a number of new RRL pulsators were added (Soszyński et al. 2016, 2017, 2019). In this paper, similarly to Paper III, we use the newest data from the OCVS. The largest number of newly included objects was added from the newest fields located east and south of the LMC—almost 1000 RRL stars. The newest fields in the southern parts of the MBR resulted in

an addition of over 100 RRL pulsators. For a current OGLE-IV footprint with the newly added fields and the on-sky distribution of all OCVS RRL stars, see Figure 1. For more technical details about the fourth phase of the OGLE project, see Udalski et al. (2015).

3. Data Analysis

3.1. Sample Selection

In our basic approach, we use a very similar method to Paper II. Hereafter, we only analyze the RRab stars, as these are the most common type, and about 70% of all RRL stars pulsate solely in the fundamental mode (i.e., see number of RRL stars published by Soszyński et al. 2011, 2014, 2016, 2017).

We select a few different samples from the entire OGLE collection of RRL stars in the Magellanic System. The first sample (hereafter the entire sample) contains all of the RRab stars and can only be represented in the on-sky maps, as we are not able to calculate distance for each star in this sample. All of the RRab stars for which we were able to calculate distance constitute the second sample (hereafter the uncleaned sample). These stars must have both I - and V -passband magnitudes and a well-estimated ϕ_{31} coefficient (this is one of the light-curve Fourier decomposition parameters; Simon & Lee 1981). To create the third sample (the cleaned sample), we made an additional cut on the Bailey diagram, the same as we did in Paper II (see Section 2.2 and Figure 1 therein for more details). Then we fit period–luminosity (PL) relations to the second sample using the Wesenheit magnitude and iteratively applied 3σ clipping to the data after each fit (see Section 3.1 in Paper II for more details). The number of RRL stars in each sample is presented in Table 1. Any other additional cuts or selections made to the three described samples are discussed later.

Taking into account the updates made and less complicated cleaning process, this sample should not be identical to our Paper II sample.

3.2. Individual Distances and Coordinates

To calculate individual distances of RRab stars, we use exactly the same method as we did in Paper II and Skowron et al. (2016). We use the Fourier coefficient ϕ_{31} , which we obtained from Fourier decomposition of OGLE light curves, to determine the photometric metallicity (we apply the relation from Nemec et al. 2013). Then we use relations from Braga et al. (2015) to calculate absolute Wesenheit magnitudes. We are aware that their relations are not best suited to our data set, as they were derived for the M4 cluster with different value of R_V . This will cause a systematic shift in our distances and will not influence the geometry of obtained distributions. We continue to use these relations to keep our calculations consistent with Paper II. Having photometric metallicity, as well as absolute and observed magnitudes, we were able to determine the distance to each RRab star. For more details on the relations used and exact transformations, see Section 3.2 in Paper II and Section 5 in Skowron et al. (2016).

Similarly to Jacyszyn-Dobrzniecka et al. (2016, 2017) and Paper III, we use a Hammer equal-area projection for on-sky plots and the Cartesian three-dimensional coordinate system. The exact equations can be found in Section 3.2 of Paper III (Equations (1)–(5)).

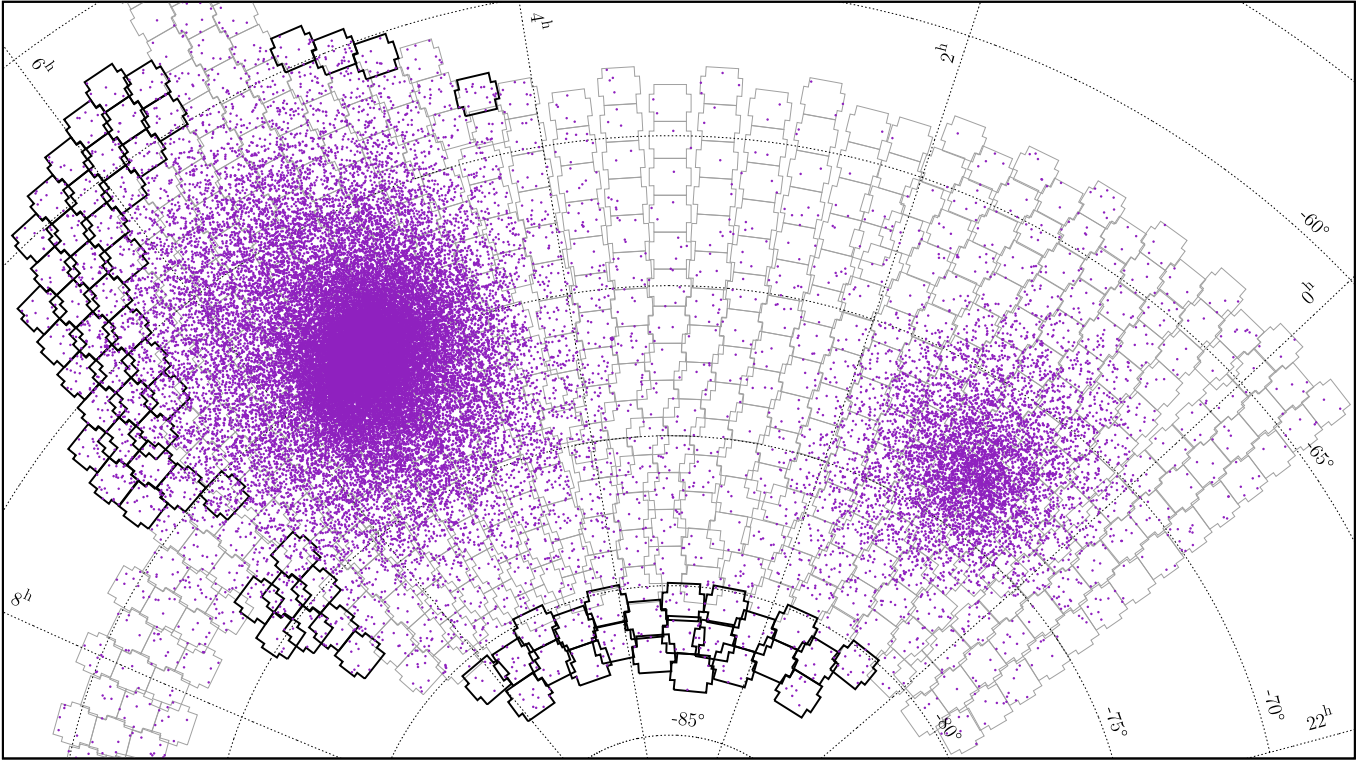


Figure 1. On-sky locations of RRL stars in the Magellanic System. Black contours show the newest additions to the OGLE-IV fields, while gray ones show the main OGLE-IV fields in the Magellanic System that were already observed before 2017 July.

Table 1
Number of RRL Stars in the Samples

Sample	Number
Entire	34,177
Uncleaned	30,675
Cleaned	27,212

4. OGLE RRL Sample

4.1. Three-dimensional Distribution

Figure 2 shows top (upper row) and front (bottom row) view of the three-dimensional distribution of RRab stars in the Magellanic System. The plots were made using two-dimensional Cartesian space projections. The left panels show the uncleaned sample with a clearly visible “blend artifact” in the LMC. This is a nonphysical structure that seems to be emanating from the LMC center and is caused by blending and crowding effects (for a more detailed description, see Section 2.2 and Figure 3 in Paper II). The blend artifact is not protruding and elongated in the next panels, where we show the cleaned sample. The three middle panels show the same sample but with different bin sizes. The contours fitted to the middle panels (medium-sized bins) are shown in the right panels. The lines are on the levels of 1, 5, 20, and 100 RRab stars kpc^{-2} .

All of the panels in Figure 2 show the Bridge area. As in Paper II, we do see some RRab stars located between the Magellanic Clouds. These objects may belong to broad halos, though some evidence was found that the LMC may also have an extended disk (Saha et al. 2010; Balbinot et al. 2015;

Besla et al. 2016; Mackey et al. 2016; Nidever et al. 2019). However, again, we do not see any evident bridge-like connection between the Magellanic Clouds formed by RRL stars in any dimension—neither xz nor xy projection. Note that the xy projection is very similar to the on-sky view. The contours do connect but on a very low level (1 star kpc^{-2} and below). It is too low to state, based on the maps only, that there is an overdensity or evident connection in the Bridge area. Based on three-dimensional maps, we can only state that we do see two extended structures overlapping.

4.2. Numerical Analysis

To analyze our RRab sample quantitatively, we performed a multi-Gaussian fitting to our cleaned sample. We approximate the spatial distribution using a Gaussian mixture model with 32 components. The underlying space density of stars is approximated as a sum of Gaussians. Their relative weights and parameters (means, covariances) are found using an expectation-maximization algorithm (Dempster et al. 1977) implemented in the Python scikit-learn package (Pedregosa et al. 2011). We tested whether the multi-Gaussian fitting properly describes our data by comparing histograms of the real distribution of stars with the simulated ones. We did not specify any parameters—only the number of Gaussians and the three-dimensional locations of stars from our sample. We separately tested models with 32, 64, 128, and 256 Gaussians and did not find any significant difference between the obtained results.

Results of the multi-Gaussian procedure for 32 Gaussians are shown in Figure 3, where we overlapped Gaussian centers on the three-dimensional distribution of RRab stars from our sample. Each resulting Gaussian is represented with an open circle. The circle size marks the number of stars included in

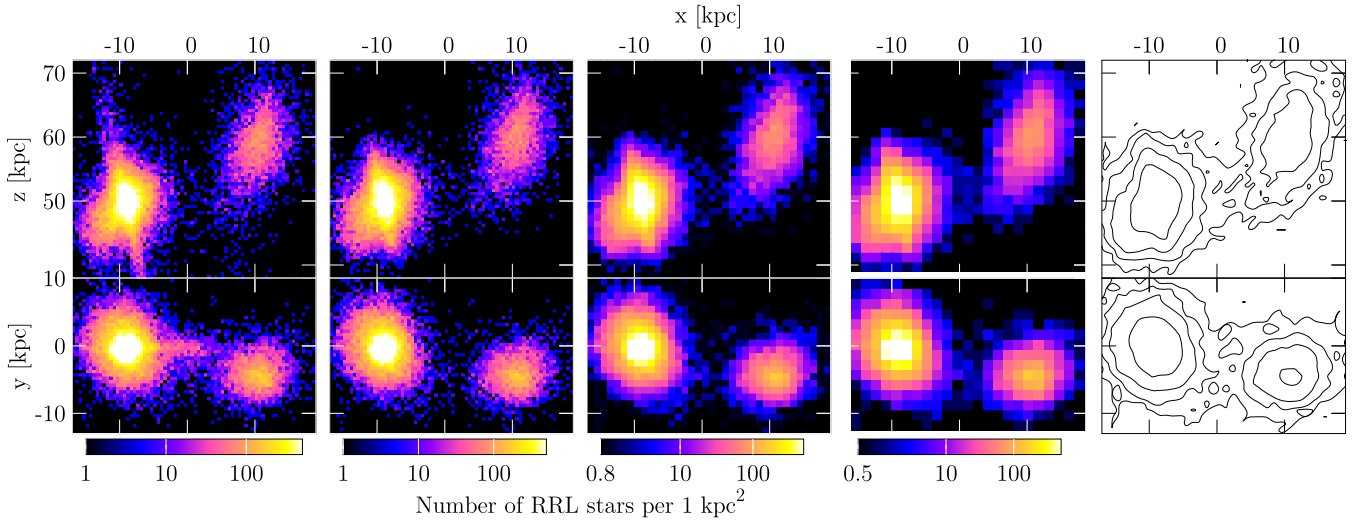


Figure 2. Top (upper row) and front (bottom row) view of the RRL stars in the Magellanic System using Cartesian space projections. The left panels show the uncleaned sample. The blend artifact, a nonphysical structure seemingly emanating from the LMC center, is very clearly visible. Note the characteristic shape the blend artifact represents in the Cartesian xy projection, which is not identical to the on-sky view (and the observer is located at $(0, 0, 0)$). The blend artifact is not protruding and elongated in the other panels, where we show the cleaned sample. The three middle panels present the same sample but with different bin sizes of (left to right) 0.5, 1, and 1.5 kpc. The right panels show the contours fitted to the middle panels (medium-sized bins, 1 kpc). Contours are on the levels of 1, 5, 20, and 100 RRL stars kpc^{-2} . The lines do connect but on a very low level.

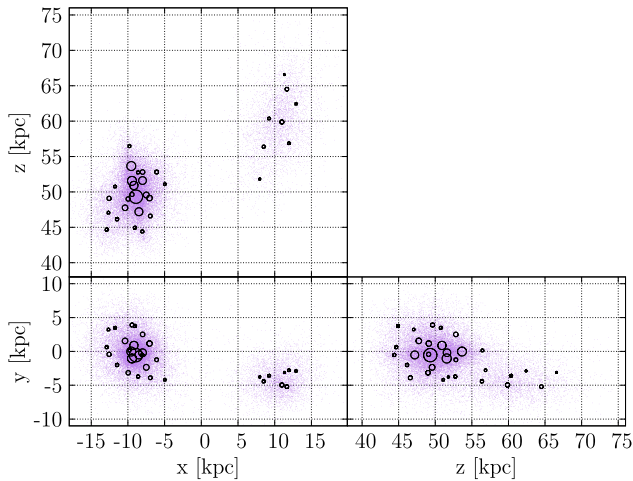


Figure 3. Centers of 32 fitted Gaussians overplotted on the three-dimensional distribution of RRL stars from the cleaned sample to which the fit was performed. Each Gaussian center is represented as an open circle, while the circle size marks the number of stars included in each Gaussian. No Gaussian is centered in the genuine Bridge area, leading to the conclusion that there is no additional population or overdensity located there.

each Gaussian: the smallest circle represents 237 objects, and the largest represents 2362 objects. The circle radius increases linearly with the number of objects.

Figure 3 shows that all of the Gaussians are centered in either the LMC or SMC, and none of them is centered in the genuine Bridge area. This leads to the conclusion that there is no additional population or overdensity located there. Note that this does not mean that there are no stars in the Bridge, as the Gaussians have their own individual spread. The Bridge RRL stars are thus modeled as objects located in the Gaussian wings.

To show how and when the contours connect, we use a multi-Gaussian fit to simulate the distribution of objects in the Magellanic System while adding an offset to each Magellanic Cloud sample. We use the three-dimensional Cartesian coordinates of our cleaned sample and add an offset to the x

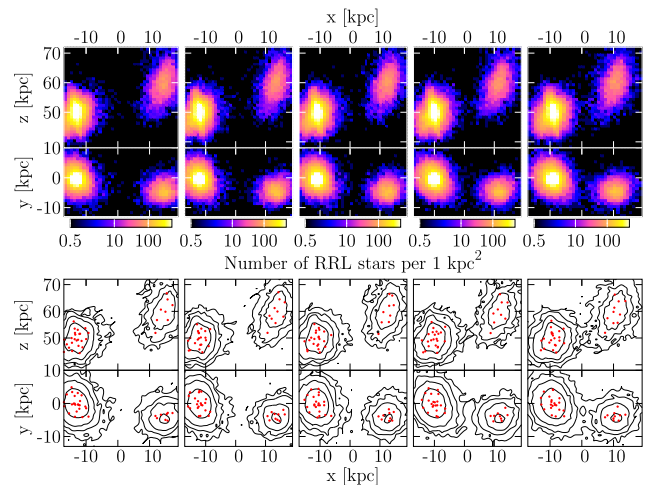


Figure 4. Two-dimensional plots of three-dimensional Cartesian space projections showing points simulated using a multi-Gaussian fit. The top panel shows binned data, while the bottom panel shows fitted contours (black lines) and Gaussian centers (red points). Each column represents a different separation between the LMC and SMC samples, starting with 8 kpc in the left column and decreasing by 2 kpc toward the right. The right column shows points simulated for no additional offset. The bin size is 1 kpc along every axis, and the color scale is the same in each plot in the top panel. The contours are on the same levels as in Figure 2, namely 1, 5, 20, and 100 RRL stars kpc^{-2} .

coordinate of each Magellanic Cloud sample separately for the LMC and SMC. We then fit the Gaussians and simulate the locations of the exact number of points that are included in our cleaned sample, precisely 27,212. We bin the data and fit contours. The results are shown in Figure 4. The top panel shows binned data with color-coded column density, while the bottom panel shows contours (black lines) and Gaussian centers (red points). The bin size and contour levels are the same as in the middle and right columns of Figure 2. The total offset added or subtracted from the x coordinate decreases from left to right. In the left column, the offset is 8 kpc (4 kpc added in the case of SMC, 4 kpc subtracted for the LMC), and it

decreases by 2 kpc in each column. The right column shows the simulated data with no additional offset. Comparing this column to the middle column of Figure 2, it is clearly visible that the multi-Gaussian fit reconstructs the real three-dimensional distribution of our data very well.

In the left column, where the distance between the LMC and SMC is largest, the contours do not connect, and these galaxies are separated. Once we reduce the offset, the lowest contours finally connect at a level of 2 kpc of additional offset. The galaxies' outermost regions seem to merge as the Clouds are at their current natural separation. This occurs in both the xy and xz Cartesian planes shown in Figure 4. This simulation shows that the effect of merging contours is natural for galaxies that are close enough. It does not necessarily imply that there is an additional structure between these objects, i.e., the Bridge, as the model itself has proven that there is no overdensity located in the genuine Bridge area.

However, one can argue that the lowest contours are spread more in the direction toward the MBR than in any other direction (in every plot in Figure 4). In order to verify this, we would need to significantly improve our analysis, and this is beyond the scope of this paper. First, we would need to abandon the σ -clipping and choose another method of rejecting outliers that would take into account the real error distribution, which is not normal in the case of PL relations (Nikolaev et al. 2004; Deb et al. 2018). By using σ -clipping, we probably remove some of the objects that are truly located at lower and higher distances in the outskirts of the LMC and SMC. Thus, the lowest contours perpendicular to the line of sight should not be used in such a detailed analysis. Second, we would need to observe the entire LMC outskirts located in the eastern, northern, and southern directions. Even though OGLE has lately significantly improved its sky coverage in the Magellanic System, it is still not sufficient for such an analysis, where we need to compare the very lowest contours.

Summarizing this subsection, we want to emphasize that comparison of the lowest-level contours is not sufficient to state whether or not there exists a bridge-like connection between the Magellanic Clouds.

5. A Reanalysis

The results that we presented in the previous section agree with our findings from Paper II. We do not see any evident connection in the MBR area but rather only two extended structures in the LMC and SMC outskirts that are overlapping. Recently, B17 also presented a map of the OGLE RRL stars in the Magellanic System (their Figure 18). This map clearly shows a connection between the Magellanic Clouds that was supposed to be consistent with the *Gaia* DR1 RRL candidate distribution presented in their paper. This seems to be in contradiction with any of our results—for comparison, see Figure 16 from Paper II or Figure 2 in this paper. We tried to reconstruct the results from B17. In this subsection, we describe the method that we used to reanalyze the OGLE sample of RRab stars.

5.1. No Evident Connection

In order to thoroughly check whether we actually see the connection in the OGLE data, we have reanalyzed the entire sample of RRab stars. To reproduce the B17 map precisely (their Figure 18), we have once again calculated metallicities and distance moduli using the same technique as they did

(V. Belokurov 2019, private communication). In the next paragraphs, we describe this method, and later, we discuss our results.

We used the Smolec (2005) relation for the OGLE I band to calculate the metallicity of each RRL star. This relation was derived for Fourier sine decomposition, and Soszyński et al. (2016) gave coefficients for the cosine decomposition; thus, we transformed the ϕ_{31} coefficient before applying the Smolec (2005) relations:

$$\phi_{31,\sin} = \phi_{31,\cos} + \pi. \quad (1)$$

The relation is (Equation (2) from Smolec 2005)

$$[\text{Fe}/\text{H}] = -3.142 - 4.902P + 0.824\phi_{31}. \quad (2)$$

Then we transformed $[\text{Fe}/\text{H}]$ to Z using Equations (9) and (10) from Catelan et al. (2004),

$$\log Z = [\text{Fe}/\text{H}] + \log(0.638f + 0.362) - 1.765, \quad (3)$$

where $f = 10^{[\alpha/\text{Fe}]}$. We assumed $[\alpha/\text{Fe}] = 0$ following B17, although Carney (1996) suggested $[\alpha/\text{Fe}] = 0.30$ based on stellar clusters. We have tested both options in our analysis and found that this value does not influence our main conclusions. Then we used theoretical calibrations of the PL relations from Catelan et al. (2004) to calculate the absolute magnitudes of the RRab stars. Their Equation (8) shows a quadratic dependency between metallicity and absolute V -band magnitude,

$$M_V = 2.288 + 0.8824 \log Z + 0.1079(\log Z)^2, \quad (4)$$

and Equation (3) from Catelan et al. (2004) for the I -band absolute magnitude,

$$M_I = 0.4711 - 1.1318 \log P + 0.2053 \log Z, \quad (5)$$

where P is the fundamental mode pulsation period.

Having absolute magnitudes, we were able to calculate color excesses,

$$E(V - I) = m_V - m_I - (M_V - M_I), \quad (6)$$

where $m_{V,I}$ are the observed mean magnitudes. We used the value obtained by Nataf et al. (2013), $dA_I/d(E(V - I)) = 1.215$, and assumed that $A_I = 1.215E(V - I)$. Note that these values were obtained for the Galactic bulge, where the extinction is nonuniform and anomalous (standard extinction is around 1.5; see Udalski 2003). However, we decided to apply values from Nataf et al. (2013) in order to exactly follow the procedure used by B17.

In the last step, we calculated distance moduli using magnitudes in the I passband:

$$\mu_0 = m_I - M_I - A_I. \quad (7)$$

The reproduced map is shown in the bottom panel of Figure 5, and the original map from B17 is shown in the top panel. Both plots show the OGLE RRab sample, though in the case of our map (bottom panel), we used the updated sample. Both plots present samples with the same cuts: distance moduli falling into the range $18.5 < m_I - M_I < 19$ and metallicities $[\text{Fe}/\text{H}] < -1.5$, as well as other parameters including coordinates, sphere projections, method of calculation, bin sizes and ranges, and color-scale range. Under all of these conditions, we were able to reproduce the connection visible in the B17 map. The bridge-like structure is visible only on a very low level of counts. Moreover, due to the large bin size and

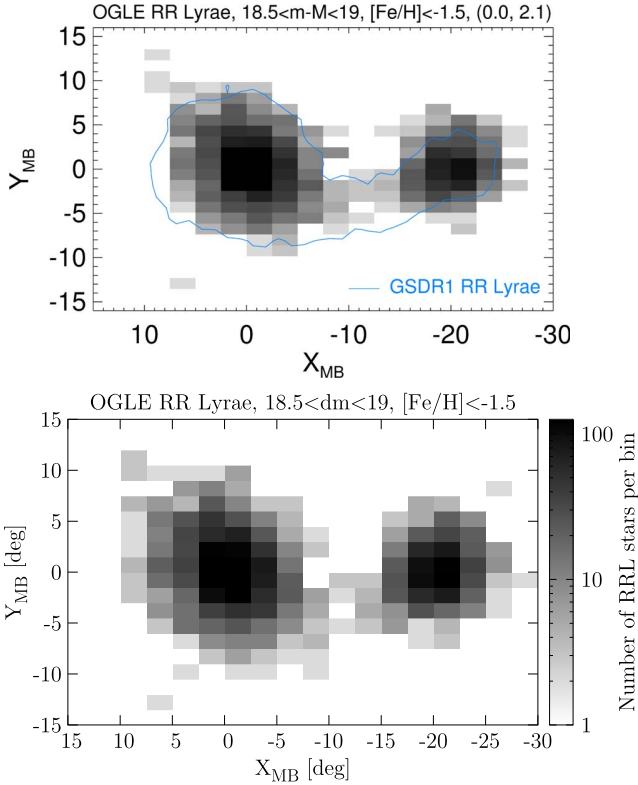


Figure 5. Top: bottom panel of Figure 18 from B17 showing OGLE RRab stars in the Magellanic System. The data are binned into rectangles, and a gray color scale is applied to show the column density. We only show RRab stars with distance moduli falling into the range $18.5 < m_l - M_l < 19$ and metallicities $[\text{Fe}/\text{H}] < -1.5$. The scale is logarithmic and limited to $10^0 - 10^{2.1}$ RRab stars deg^{-2} . The blue contour represents the density of *Gaia* DR1 RRL candidates analyzed by B17. The coordinates used are in the MBR system, and the sky projection is not equal-plane. Bottom: our map showing OGLE RRab stars in the Magellanic System with parameters calculated using the same method as in B17. Note that the bridge-like structure is even more visible due to the elongation of bins along the connection (and equator).

elongation of bins along the x -axis, and thus along the Bridge, the connection is even more pronounced.

To test whether the choice of coordinate system also influences the visibility of the bridge-like connection, we plotted the same sample as in Figure 5 using different transformations. The top panels of Figure 6 show the same rectangular bins with a gray color scale but using an equal-area Hammer projection applied to the MBR (top row) and equatorial (bottom row) coordinate systems.

In the left column of Figure 6, where the color-scale range starts at 1 star deg^{-2} , the connection is not visible in either coordinate system. It only starts to emerge in the second column, where the bottom of the color-scale range is under the level of 1 star deg^{-2} —namely, 0.3. The bridge-like structure is even more pronounced in the third column, where the range is even lower. However, in the latter plot, other extended features are starting to emerge. Moreover, comparing the top and bottom gray rows demonstrates that the connection is more clearly visible in the MBR coordinates. This is due to the fact that in this system, the bridge-like structure is located along the equator. Comparing contours for both coordinate systems, we conclude that the contours do connect in both cases but on a

very low level. Again, the connection is slightly more visible in the MBR coordinate system.

Furthermore, to test whether the binning influences the results, we also plotted the same sample using square bins of different sizes. Results are shown in the bottom panels of Figure 6. Similarly to the gray panels, the top row shows the MBR, and the bottom row shows the equatorial coordinates. Comparison of rectangular and square bins leads to the conclusion that binning does indeed have an impact on the visibility of the bridge-like structure. The square bins make the connection appear significantly less visible than the rectangular bins. This is not a surprise, as the rectangular bins used by B17 were aligned with the bridge.

6. B17 RRL Candidates from *Gaia* DR1

6.1. Selection Process

In this section, we present the results of an analysis of the *Gaia* DR1 data (Gaia Collaboration et al. 2016) performed the same way as in B17. The main goal of B17 was to select RRL candidates from *Gaia* DR1 and analyze the on-sky distribution of these stars in the Magellanic System area, with an emphasis on the Bridge. They found that there is an evident connection between the Magellanic Clouds. Hereafter, we try to reproduce their results and compare with the OGLE and *Gaia* DR2 databases.

In order to reproduce the B17 list of RRL candidates using *Gaia* DR1, we use their procedure with the following steps.

1. From the entire *Gaia* DR1 database, we selected all sources located in an area where $\text{R.A.} \in (0^{\text{h}}, 9^{\text{h}}) \cup (22^{\text{h}}, 24^{\text{h}})$ and $\text{decl.} \in (-85^{\circ}, -45^{\circ})$ with more than 70 CCD crossings and Galactic longitude $b \leq -15^{\circ}$. The latter two requirements are corresponding to *iv* and *vii* cuts from B17 (see their Section 3.3).
2. An appropriate value of extinction $E(B - V)$ was found for all sources using Schlegel et al. (1998) maps. This allowed us to deredden all of the objects from the selected sample using the following relation for the extinction coefficient for the *Gaia* G band (Equation (1) from B17), A_G :

$$A_G = 2.55E(B - V). \quad (8)$$

3. Then we calculated the amplitude value, Amp, using the following relation (Equation (2) from B17):

$$\text{Amp} = \log_{10} \left(\sqrt{N_{\text{obs}}} \frac{\sigma_{\bar{I}_G}}{\bar{I}_G} \right), \quad (9)$$

where N_{obs} is the number of CCD crossings, \bar{I}_G is the mean flux in the *Gaia* G band, and $\sigma_{\bar{I}_G}$ is the error of the mean flux.

4. Finally, the remaining cuts presented in Section 3.3 of B17 were applied. The cuts concern amplitude as defined above, astrometric excess noise (AEN), G -band magnitude, and reddening.

We applied different versions of cuts *ii* and *vi* as presented in B17. We use both strict and weak cuts on the amplitude, $-0.75 < \text{Amp} < -0.3$ and $-0.65 < \text{Amp} < -0.3$, respectively. Similarly for the AEN, $\log_{10}(\text{AEN}) < -0.2$ is a strict cut, and $\log_{10}(\text{AEN}) < -0.2$ is weak. Additionally, we analyzed an even weaker version of the AEN cut, where $\log_{10}(\text{AEN}) < 0.3$. Results are presented in Figure 7.

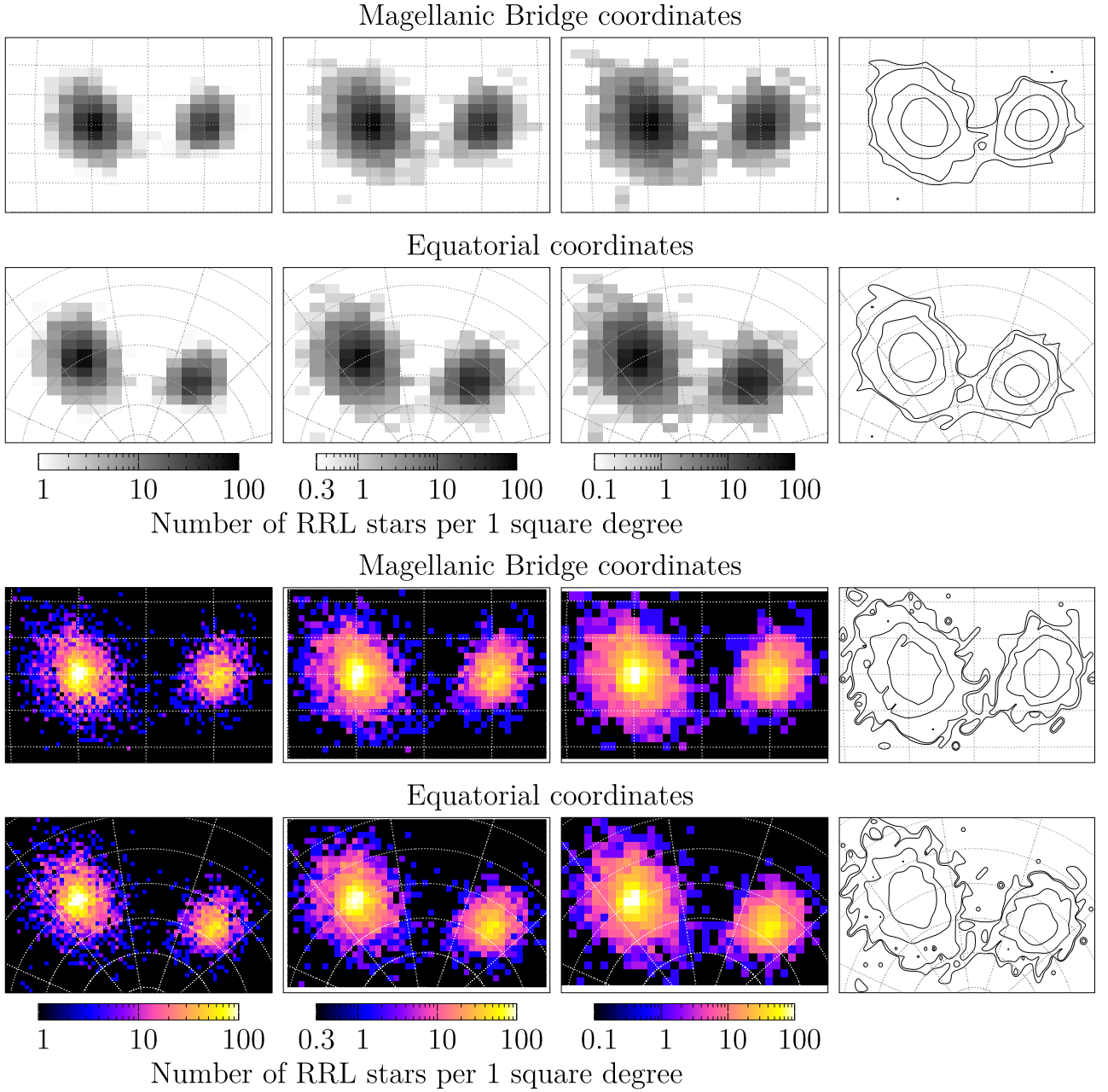


Figure 6. Every plot shows the same sample as in the bottom panel of Figure 5. In the top panels, we used the same binning as in Figure 5 but in Hammer equal-area projection applied to the MBR (top row) and equatorial (bottom row) coordinate system. Each column shows a different bottom range of color scale. The right column shows contours that are on the levels of 0.5, 1, 5, and 15 RRab stars deg^{-2} . In the bottom panels, we used square bins instead of rectangular ones. We also applied a different color scale with a different range to show the subtlest features. The bin size is linearly different between each column. The top row shows the MBR, while the bottom row shows the equatorial coordinate system. Both are represented using Hammer equal-area projection. Additionally, the right column shows contours fitted to the binning shown in the second column. The contours levels are 0.5, 1, 5, and 15 RRab stars deg^{-2} .

6.2. Two-dimensional Analysis

Figure 7 clearly shows that when using the Amp and AEN cuts, both in strict versions, there are not many stars left in between the Magellanic Clouds. To test whether this result reproduces the RRL bridge reported by B17, we binned the data in the same way as their Figure 11. The bins are on too low a level, and no connection is visible; thus, strict cuts do not reproduce their bridge. Moreover, the sample we obtained using strict versions of cuts consisted of ~ 7000 objects, which is three times less numerous than the B17 sample ($\sim 21,500$ objects). In the case of applying at least one cut in the weak

version, we obtained a distribution revealing stripes in the Bridge area.

The right panel of Figure 5 in B17 shows an on-sky distribution of all nominally variable stars selected from DR1. Many nonphysical features are visible, including the artifact east of the LMC. A detailed analysis of the stripes appearing in this plot was performed by B17 (for details, see their Section 3.2 and Figure 6). These stripes are aligned with the *Gaia* scanning pattern and caused by cross-match failures. Thus, most of the sources forming the stripes are not physical. Further, B17 claimed that the stripes disappear due to the cuts

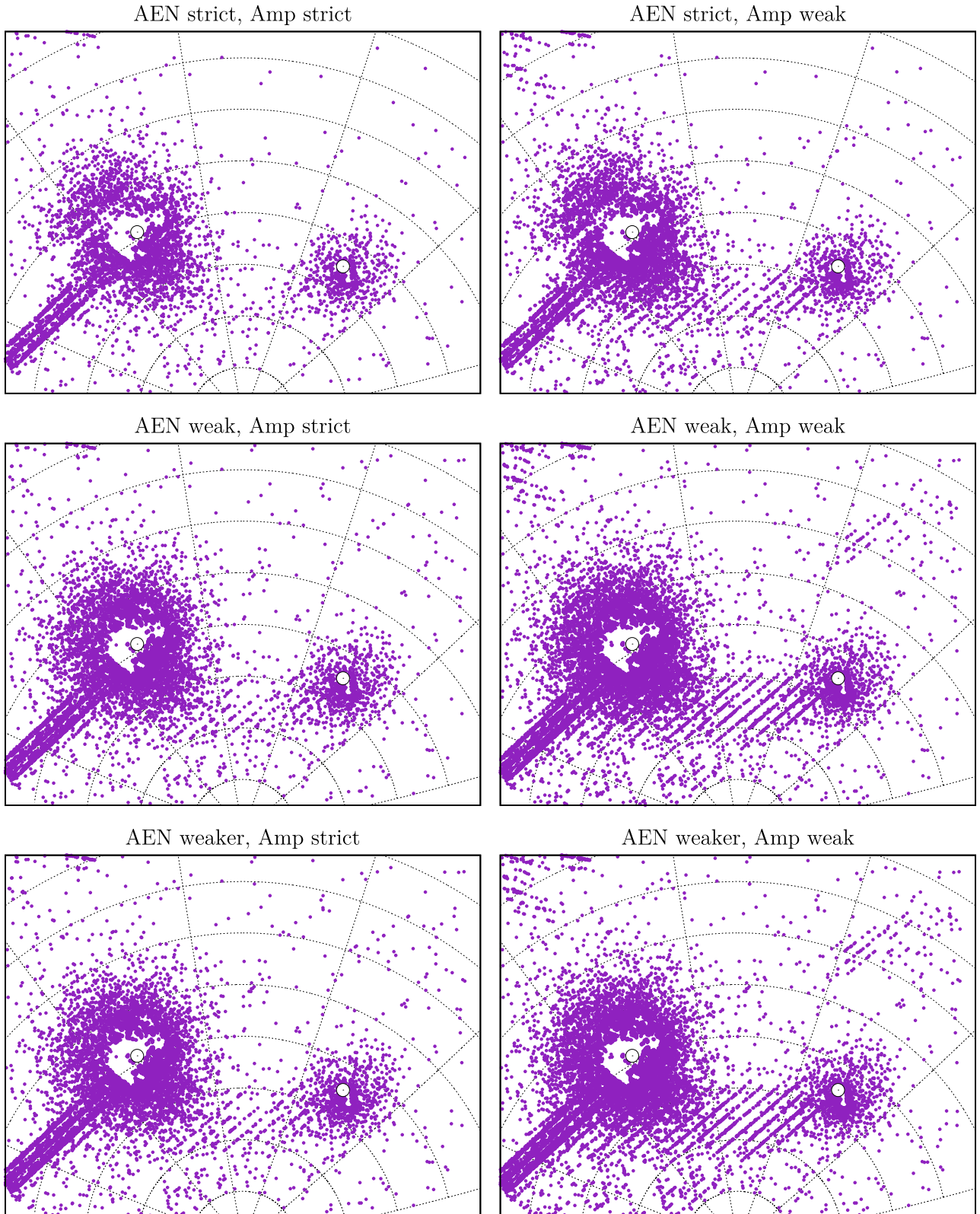


Figure 7. On-sky locations of RRL candidates using different versions of B17 cuts. Clearly visible is the nonphysical artifact east of the LMC that we did not remove. It is created by spurious variables, which are caused by *Gaia* DR1 cross-match failures (B17). Stripes are the matching *Gaia* scanning pattern. Similar stripes visible in the Bridge area suggest that many of the objects located there are nonphysical sources. Additionally, white circles mark the LMC (van der Marel & Kallivayalil 2014) and SMC (Stanimirović et al. 2004) centers.

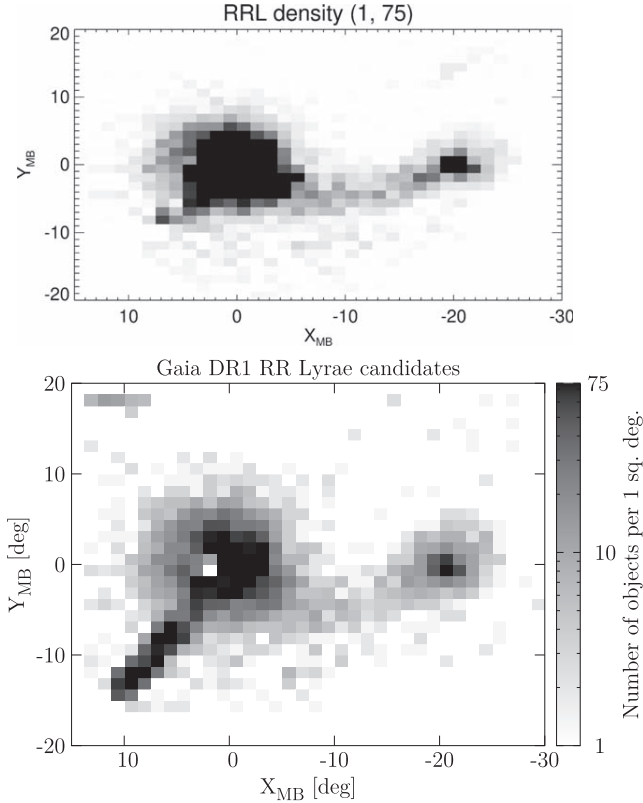


Figure 8. Comparison of the top panel of Figure 11 from B17 (top panel) with the map obtained using the same technique (bottom panel). The bottom panel shows a sample with strict Amp cut and weaker AEN cut.

applied, and only a small number of spurious sources fall into the selected RRL regions. Our study reveals that this is not the case and that the final RRL candidate sample still contains a number of nonphysical sources forming the stripes. Comparing our Figure 7 with Figure 5 from B17, it is clearly visible that the features in the MBR area are not removed by the applied procedure. Thus, the discovery of the bridge-like connection by B17 was likely based on a nonphysical structure.

Moreover, clearly visible in Figure 7 is a nonphysical artifact located east of the LMC that we did not remove. This feature is located in the area most influenced by cross-match failures in *Gaia* DR1 (see masked pixels in the left panel of Figure 5 in B17). The sources in between the Magellanic Clouds are forming stripes that are aligned with the nonphysical artifact east of the LMC. This supports our conclusion from the previous paragraph that the Bridge area is highly influenced by nonphysical sources. Additionally, we obtain a distribution close to the center of the LMC, where the sources are missing, due to the requirement of $N_{\text{obs}} > 70$. However, we managed to recreate the sample in the MBR, which is our main area of interest.

As our final sample of RRL candidates, we selected the one with a strict cut on Amp and weaker cut on AEN, as it perfectly reproduced a sample of 113 central Bridge objects from the B17 analysis (V. Belokurov 2019, private communication). In Figure 8, we show a comparison of a binned map of this sample with Figure 11 from B17. Both maps are plotted using the same coordinate system, sphere projection, bin size, and color-scale range. We managed to reproduce the Bridge features

Table 2
B17 RRL Candidates from *Gaia* DR1: Cross-match

Sample	No. Obj.	Cross-match with			
		OGLE RRL		<i>Gaia</i> DR2 RRL	
Entire	13,327	5516	(41.4%)	4872	(36.6%)
MBR	6041	2971	(47.5%)	2542	(42.1%)
Cen. MBR	113	17	(15.0%)	15	(13.3%)

Note. The MBR sample consists of objects located in the range $-20^\circ < X_{MB} < 0^\circ$. The central MBR sample consists of objects located between the Magellanic Clouds that contribute to B17 overdensity.

very well. One main difference between our map and that of B17 is the nonphysical artifact located east of the LMC. Note that in this binning, the *Gaia* stripes are not visible. The sample we select as our final one contains more than 13,300 stars. This is more than half of the B17 sample, indicating that they have applied even weaker cuts in their final sample.

In Figure 9, we also show our final sample using square bins of different sizes. We represented the data in the MBR coordinates using Hammer equal-area projection. As the bin size increases from left to right, the *Gaia* stripes appear less visible. The contours shown in the right panel match very well contours obtained by B17 (see their Figure 12).

6.3. Comparison with OGLE and *Gaia* DR2

The OGLE collection of RRL stars in the Magellanic Clouds is nearly complete—the level of completeness is higher than 95% (Soszyński et al. 2016, 2017). Therefore, we cross-matched the list of RRL candidates obtained in this section with the OCVS to test how many of these objects are genuine RRL stars. We separately cross-matched the entire sample of B17 DR1 RRL candidates and a subsample created by selecting only objects in the Bridge area located between the LMC and SMC centers. This Bridge subsample consists of sources located within $-20^\circ < X_{MB} < 0^\circ$.

Results are presented in Table 2, which shows that only about 41.4% of the objects in the entire RRL candidate sample are genuine RRL stars. For the Bridge subsample, this ratio is at the level of about 47.5%. Moreover, we separately tested a subsample of 113 objects in the central Bridge area, where the B17 overdensity is located. Only 17 of these objects are RRL stars, which leads to a total ratio of 15.0%. The difference between this ratio for the entire sample and the central Bridge subsample indicates a higher contamination in the latter. This is consistent with the fact that many sources in the Bridge area are nonphysical. The contamination of 85% in the central Bridge sample is not consistent with B17, who gave a value of 30%–40% for their entire sample.

Note that the area that we use for the RRL candidate selection process is larger than the OGLE-IV field coverage (see Figure 1), so our *Gaia* search window is larger than the plotted area. For the entire sample, the difference in purity level is larger than for the Bridge sample, as the former includes the nonphysical artifact in DR1 data that is not entirely covered by the OGLE fields. For the Bridge sample, only a few sources are located north and south of the OGLE footprint. Thus, this effect should not be significant for the selected Bridge subsample. It also explains the significant difference between the cross-matches of RRL candidate samples with the OGLE data.

We would expect that a proper technique of selecting RRL candidates would lead to a result of high completeness. To test

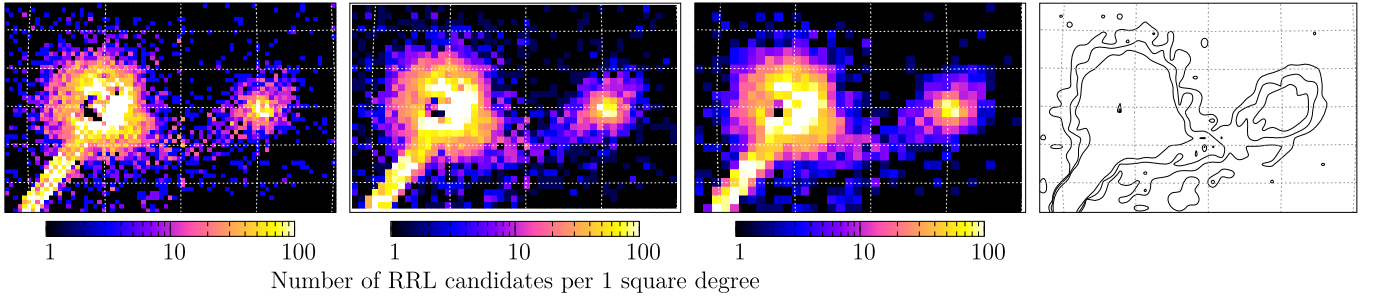


Figure 9. Same sample as in Figure 8 (bottom panel) but binned using square bins.

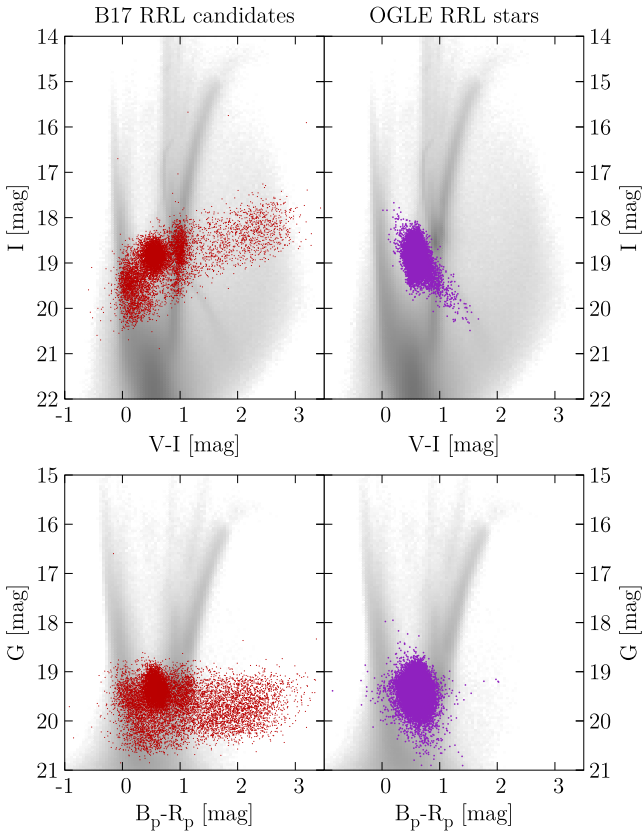


Figure 10. The CMDs of the B17 RRL candidates (left; red) obtained in this section and the cleaned sample of OCVS RRL stars (right; purple) overplotted on the Hess diagrams for the data from selected fields in the Magellanic System. Top: OGLE photometry. Bottom: *Gaia* DR2 photometry.

that, we compared the number of RRL stars from our reconstructed sample using the described technique to the total number of these objects in the OGLE database in the Magellanic System. The entire RRL candidate list has a completeness level of 11.6%, while for the Bridge sample, it is 12.4%, which is consistent with what B17 estimated. This means that almost 90% of RRL stars located in the OGLE-IV fields in the Magellanic System were not discovered in the reconstructed sample of B17.

Moreover, we also cross-matched the obtained RRL candidate lists with the entire OCVS published to date and the entire OGLE database. About 2.3% of objects from the candidate samples are eclipsing binaries. A few are also classified in the OCVS as long-period variables. We show in Figure 10 a comparison of the color–magnitude diagram

(CMD) of the sample obtained in this section with the cleaned sample of RRL stars. Both are overplotted on the OGLE (top panels) and *Gaia* DR2 (bottom panels) data from selected fields in the Magellanic System. The reconstructed B17 sample spans different areas than those usually occupied by the genuine RRL stars. Thus, this sample contains a lot of different types of objects.

We have also performed a cross-match between the RRL candidate sample from *Gaia* DR1 obtained in this section and the *Gaia* DR2 RRL stars listed in the `vari_rrlyrae` table (Gaia Collaboration et al. 2018; Holl et al. 2018; Clementini et al. 2019). Table 2 lists the exact results. Only about 37% of sources from the RRL candidate sample are present in the *Gaia* DR2. For the Bridge sample, this result is slightly higher: 42%. Lower numbers as compared to the cross-match with the OGLE data are probably a result of lower DR2 RRL sample completeness, which we describe in the following section.

7. Comparison of Different Tracer Distribution

In this section, we compare on-sky distributions of different tracers in the MBR area. The main plot that we discuss is shown in Figure 11. The first row contains the HI density contours from the Leiden/Argentine/Bonn HI Survey (Kalberla et al. 2005; same as Figure 8 in Skowron et al. 2014) and the Galactic All Sky HI Survey (McClure-Griffiths et al. 2009; Kalberla et al. 2010; Kalberla & Haud 2015) and the young population, red clump, and top and bottom of the red giant branch (RGB) distributions (Figures 8, 9, 11, and 13 from Skowron et al. 2014). The middle row shows the different types of classical pulsators from the OCVS that we investigated in Paper III and this paper, namely classical Cepheids (CCs), anomalous Cepheids (ACs), both these types plotted together, RRabs of the cleaned sample, RRabs of the entire sample, and RRLs of all types plotted together. Similarly, these types of objects are shown in the bottom row using data from *Gaia* DR2 (with the exception of the cleaned RRab sample that we calculated only for the OCVS). All of these plots show a color-coded column density, while lines represent density contours. For each plot, the color scale and contour levels are different.

Comparing neutral hydrogen with other maps, it is clearly visible that the most matches are distributions of young stars and CCs. Each of these three seems to follow a bridge-like connection between the Magellanic Clouds along a similar decl. range: $\text{decl.} \in (70^\circ, 72^\circ)$. Older tracers are more spread out and do not follow such strict connection. Red clump and RGB bottom stars are more concentrated in the southern parts of the Bridge than RGB top and RRL stars. The RGB top objects are very spread out, and the lowest-density contours show some clumps, with the most populated stripe located along the young

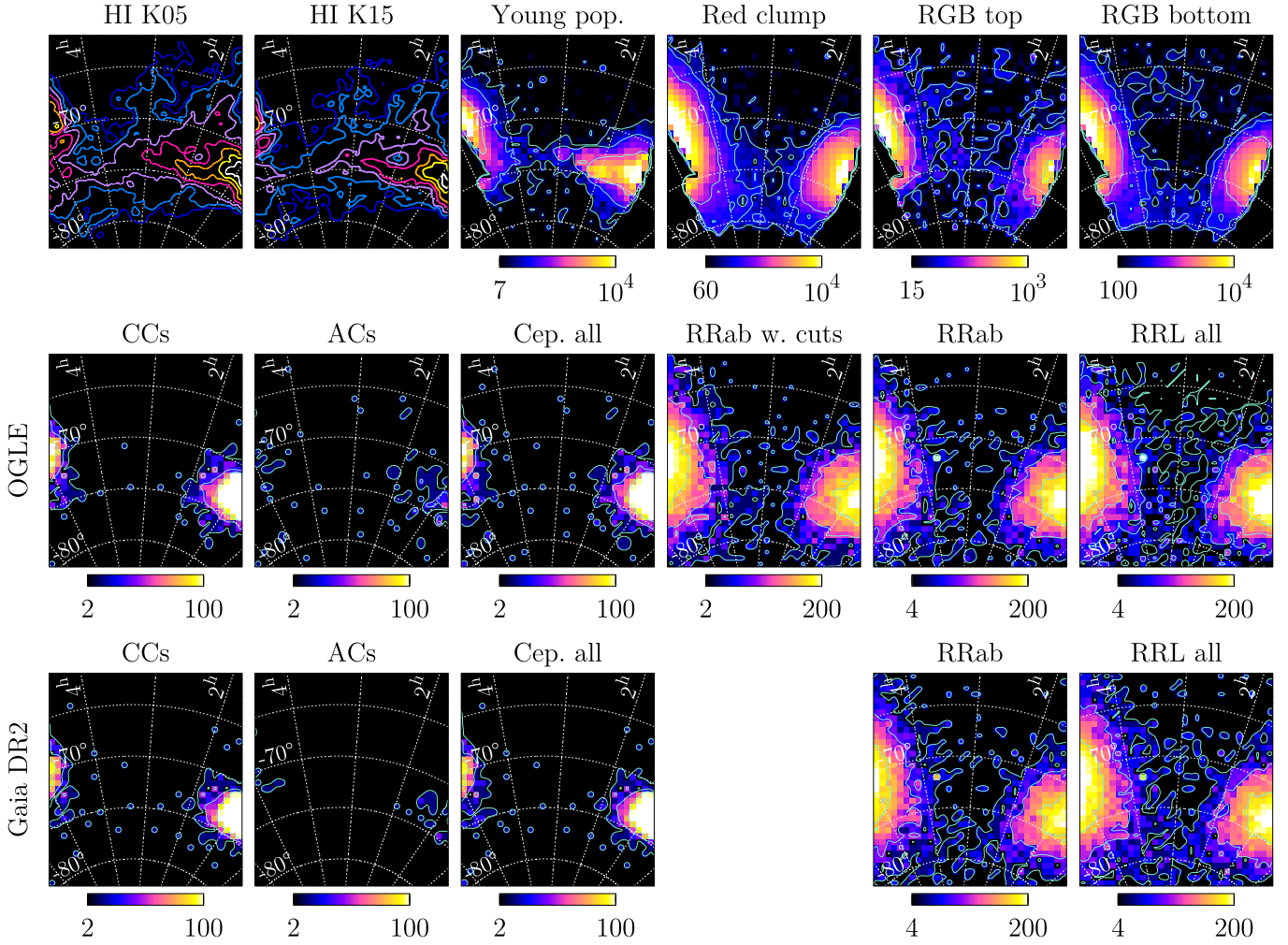


Figure 11. Comparison of on-sky locations of different tracers in a Hammer equal-area projection. Each plot has its own color scale and contour levels. Top row: The first panel shows neutral hydrogen density contours from the Leiden/Argentine/Bonn H I Survey (Kalberla et al. 2005, the same as in Figure 8 in Skowron et al. (2014); see that figure description for details). The second panel shows H I from the Galactic All Sky H I Survey (McClure-Griffiths et al. 2009; Kalberla et al. 2010; Kalberla & Haud 2015). Contours are on the levels $(1, 2, 4, 8, 16, 32, 64) \cdot 10^{20} \text{ cm}^{-2}$. In both panels, the H I is integrated over the velocity range $80 \text{ km s}^{-1} < v < 400 \text{ km s}^{-1}$. The third to fifth panels show column densities of different stellar populations as selected in the CMDs in Skowron et al. (2014). Shown here for comparison are the young population, red clump objects, and the top and bottom of the RGB. Middle row: classical pulsators from the OGLE. Bottom row: classical pulsators from the *Gaia* DR2.

population bridge. However, the connection is on too low a level to enable us to state that we see a connection similar to the young bridge. Summing up, for all intermediate-age and older tracers from Skowron et al. (2014), we can see two extended structures overlapping with no evident bridge-like connection.

The RRL star on-sky distribution shows that these stars are very spread out in many directions—even more than the other tracers that we discussed in the previous paragraph. Among the presented distributions, the distribution of RGB stars is the most similar to the distribution of RRL stars. The difference between the RRab cleaned and entire samples shows that a number of objects are rejected from the Bridge sample. Note, however, that the column density in this area is low, and removing even a small number of objects can result in a significantly different density contour distribution. The entire RRab sample is distributed very similarly to all RRL types, though the lowest-density contours are slightly different. This is caused by the fact that the entire RRL sample is more numerous. Moreover, one can state that the ACs are similarly spread out as the intermediate-age and older tracers. On the

other hand, the ACs sample is significantly less numerous. We do not discuss further differences or similarities between different types of classical pulsators in this paper; for a detailed statistical study of three-dimensional distributions, see Iwanek et al. (2018).

Figure 11 shows that in DR2, many ACs were classified as CCs. This is the main reason for the differences between the OGLE and DR2 CC distributions. For a detailed description, see Section 7 in Paper III. Note also that Ripepi et al. (2019) recently reclassified the DR2 sample of CCs. For a comparison, see Figure 12 in Paper III. The *Gaia* DR2 RRL stars are distributed very similarly to the OGLE RRL stars, both RRab and all types of these pulsators. These objects are very spread out, and while the lowest-density contours do connect, it occurs on a very low level, below 1 star deg^{-2} . Thus, this cannot be the reason for stating that we see an evident bridge-like connection; we actually do not.

Using our updated OGLE sample of RRL stars and the *Gaia* DR2 sample, we performed a cross-match between these two. Similarly to Paper III, we selected a DR2 sample covering the

entire OGLE field in the Magellanic System. In this area, *Gaia* DR2 has a completeness of 69.0% for all RRL stars. This value is consistent with Table 2 in Holl et al. (2018). Again, this is not surprising, as the OGLE collection of RRL stars was a training set for the *Gaia* selection algorithms.

8. Conclusions

In this paper, closely following our analysis of CCs in the MBR area (Paper III), we present a detailed study of RRL stars in between the Magellanic Clouds using an extended OCVS (Soszyński et al. 2016, 2017, 2019). We calculated absolute Wesenheit magnitudes for each RRL star, starting with estimating photometric metallicities (Nemec et al. 2013) and applying Braga et al. (2015) relations. This led to us calculating individual distances for our sample, the same technique as in Paper II and Skowron et al. (2016).

We analyzed a three-dimensional distribution of RRL stars between the Magellanic Clouds in Cartesian coordinates. We show—confirming the results from Paper II, as well as Wagner-Kaiser & Sarajedini (2017)—that we do not see an evident connection between the Magellanic Clouds in RRL stars. Objects located in the Bridge area form a smooth transition between the Clouds, rather than a bridge-like connection. The RRL distribution seems to represent two extended structures overlapping (i.e., halos or extended disks of the LMC and SMC). Additionally, we bin the data and show that the contours do connect, though on a very low level (below 1 star deg^{-2} or kpc^{-2}). It is too low to state that an evident overdensity exists.

To test our sample numerically, we performed a multi-Gaussian fit. We made only two assumptions: the number of Gaussians and the number of points to be simulated. Our results show that there is no Gaussian centered in the Bridge area. Thus, there is no additional population or overdensity therein. We also used the multi-Gaussian procedure to show that when we separate the Magellanic Clouds by 8 kpc along the Cartesian x -axis, and then gradually shift the LMC and SMC back together, the lowest-density contours start to connect at some point. Thus, the fact that the contours connect is not necessarily evidence of the existence of an old bridge, as any contours will connect when the galaxies are close enough.

Moreover, to carefully study the lowest-density contours, one needs to use a very precise technique to classify and analyze RRL stars. Even though the method we use is quite robust, as it is used in many different studies of three-dimensional structure, we do not think that it is precise enough to test the very outskirts of the Magellanic Clouds.

Lately, B17 presented a distribution of OGLE RRL stars in the Bridge that revealed a bridge-like connection (see their Figure 18). This is in contradiction with results from Paper II or even from this paper that were described earlier. We reanalyzed our OGLE sample using a different technique to test consistency. We show that the way the data are plotted influences the final impression. Carefully testing how the sample looks in different coordinate systems and using different bin sizes and types of bins, we show that we are able to reproduce the B17 plot only under specific conditions. Thus, because the connection is not always visible, we are even more convinced that it is on a very low level.

Using the same method as B17, we also reproduced their main results by selecting RRL candidates from *Gaia* DR1 data. We applied a series of cuts to the data, as presented in B17.

When all of the selection methods are used in strict versions, we obtain a very small number of objects in between the Magellanic Clouds. On the other hand, if at least one cut is weaker, the resulting distribution contains many spurious sources in the MBR area. Thus, we conclude that we are not able to reproduce the B17 RRL bridge without nonphysical artifacts, and we do not agree with their statement that the cuts presented remove most of the spurious sources. We also present a map of selected objects showing very evident stripes that, according to B17, match the *Gaia* overlapping fields. This nonphysical overdensity is matching the B17 discovery very well. In the central Bridge area, only 15% of the sample are genuine RRL stars.

We also show, for the first time, the distribution of *Gaia* DR2 RRL stars in the MBR and compare it to the OCVS. On-sky locations of RRL stars from both samples are very consistent. Similarly to the OCVS RRL stars, the DR2 sample reveals a very spread out distribution that more resembles two overlapping structures than a strict bridge-like connection. The lowest-density contours do connect, though on a very low level, again below 1 star deg^{-2} . These contours look slightly different when using only RRab stars instead of the entire RRL sample. This is probably due to the latter being more numerous. Again, we conclude that the existence of a bridge-like structure should not be based on the lowest-density contours.

At the same time, we want to emphasize that we do not state that the RRL bridge does not exist. There are different surveys showing that there are some substructures in between the Magellanic Clouds. This is in agreement with our own study, as we also show that there are RRL stars in the Bridge area, though their distribution is not very bridge-like, and the overdensity is on a very low level.

A.M.J.D. is supported by the Polish Ministry of Science and Higher Education under “Diamond grant” No. DI2013 014843 and the Deutsche Forschungsgemeinschaft (DFG; German Research Foundation)—Project-ID 138713538—SFB 881 (“The Milky Way System,” subproject A03). P.M. acknowledges support from the Foundation for Polish Science (Program START). The OGLE project has received funding from the National Science Centre, Poland, grant MAESTRO 2014/14/A/ST9/00121 to A.U.

We would like to thank all of those whose remarks and comments inspired us and helped to make this work more valuable, especially the anonymous referee. In particular, we would like to thank Richard Anderson, Abhijit Saha, Vasily Belokurov, Anthony Brown, Laurent Eyer, Martin Groenewegen, Vincenzo Ripepi, Radosław Smolec, Martino Romaniello, and Krzysztof Stanek.

This research was supported by the Munich Institute for Astro- and Particle Physics (MIAPP) of the DFG cluster of excellence “Origin and Structure of the Universe,” as it benefited from the MIAPP program “The Extragalactic Distance Scale in the *Gaia* Era,” as well as the International Max Planck Research School (IMPRS) Summer School on “*Gaia* Data and Science 2018.”

This work has made use of data from the European Space Agency (ESA) mission *Gaia* (<https://www.cosmos.esa.int/gaia>), processed by the *Gaia* Data Processing and Analysis Consortium (DPAC; <https://www.cosmos.esa.int/web/gaia/dpac/consortium>). Funding for the DPAC has been provided by national institutions, in particular the institutions participating in the *Gaia* Multilateral Agreement.

ORCID iDs

Anna M. Jacyszyn-Dobrzeniecka  <https://orcid.org/0000-0002-5649-536X>
 Przemek Mróz  <https://orcid.org/0000-0001-7016-1692>
 Igor Soszyński  <https://orcid.org/0000-0002-7777-0842>
 Patryk Iwanek  <https://orcid.org/0000-0002-6212-7221>
 Jan Skowron  <https://orcid.org/0000-0002-2335-1730>
 Paweł Pietrukowicz  <https://orcid.org/0000-0002-2339-5899>
 Radosław Poleski  <https://orcid.org/0000-0002-9245-6368>
 Szymon Kozłowski  <https://orcid.org/0000-0003-4084-880X>
 Krzysztof Ulaczyk  <https://orcid.org/0000-0001-6364-408X>

References

- Bagheri, G., Cioni, M.-R. L., & Napiwotzki, R. 2013, *A&A*, 551, A78
 Balbinot, E., Santiago, B. X., Girardi, L., et al. 2015, *MNRAS*, 449, 1129
 Belokurov, V. A., & Erkal, D. 2018, *MNRAS*, 482, L9
 Belokurov, V. A., Erkal, D., Deason, A. J., et al. 2017, *MNRAS*, 466, 4711
 Besla, G., Kallivayalil, N., Hernquist, L., et al. 2010, *ApJL*, 721, L97
 Besla, G., Kallivayalil, N., Hernquist, L., et al. 2012, *MNRAS*, 421, 2109
 Besla, G., Martínez-Delgado, D., van der Marel, R., et al. 2016, *ApJ*, 825, 20
 Braga, V. F., Dall’Ora, M., Bono, G., et al. 2015, *ApJ*, 799, 165
 Carney, B. W. 1996, *PASP*, 108, 900
 Carrera, R., Conn, B. C., Nöel, N. E. D., et al. 2017, *MNRAS*, 471, 4571
 Catelan, M., Pritzl, B. J., & Smith, H. A. 2004, *ApJS*, 154, 633
 Clementini, G., Ripepi, V., Molinaro, R., et al. 2019, *A&A*, 622, A60
 Connors, T. W., Kawata, D., & Gibson, B. K. 2006, *MNRAS*, 371, 108
 Deason, A. J., Belokurov, V., Erkal, D., Koposov, S. E., & Mackey, D. 2017, *MNRAS*, 467, 2636
 Deb, S., Ngeow, C.-C., Kanbur, S. M., et al. 2018, *MNRAS*, 478, 2526
 Demers, S., & Battinelli, P. 1998, *AJ*, 115, 154
 Dempster, A. P., Laird, N. M., & Rubin, D. B. 1977, *Journal of the Royal Statistical Society*, 39, 1
 Diaz, J. D., & Bekki, K. 2012a, *MNRAS*, 413, 2015
 Diaz, J. D., & Bekki, K. 2012b, *ApJ*, 750, 36
 Gaia Collaboration, Brown, A. G. A., Vallenari, A., et al. 2016, *A&A*, 595, A2
 Gaia Collaboration, Brown, A. G. A., Vallenari, A., et al. 2018, *A&A*, 616, A1
 Gardiner, L. T., & Noguchi, M. 1996, *MNRAS*, 278, 191
 Gardiner, L. T., Sawa, T., & Fujimoto, M. 1994, *MNRAS*, 266, 567
 Guglielmo, M., Lewis, G. F., & Bland-Hawthorn, J. 2014, *MNRAS*, 444, 1759
 Harris, J. 2007, *ApJ*, 658, 345
 Holl, B., Audard, M., Nienartowicz, K., et al. 2018, *A&A*, 618, A30
 Irwin, M. J., Kunkel, W. E., & Demers, S. 1985, *Natur*, 318, 160
 Iwanek, P., Soszyński, I., Skowron, D. M., et al. 2018, *AcA*, 68, 213
 Jacyszyn-Dobrzeniecka, A. M., Skowron, D. M., Mróz, P., et al. 2016, *AcA*, 66, 149
 Jacyszyn-Dobrzeniecka, A. M., Skowron, D. M., Mróz, P., et al. 2017, *AcA*, 67, 1
 Jacyszyn-Dobrzeniecka, A. M., Soszyński, I., Udalski, A., et al. 2020, *ApJ*, 889, 25
 Kalberla, P. M. W., Burton, W. B., Hartmann, D., et al. 2005, *A&A*, 440, 775
 Kalberla, P. M. W., & Haud, U. 2015, *A&A*, 578, A78
 Kalberla, P. M. W., McClure-Griffiths, N. M., Pisano, D. J., et al. 2010, *A&A*, 512, A14
 Mackey, A. D., Koposov, S. E., Da Costa, G. S., et al. 2018, *ApJL*, 858, L21
 Mackey, A. D., Koposov, S. E., Erkal, D., et al. 2016, *MNRAS*, 459, 239
 McClure-Griffiths, N. M., Pisano, D. J., Calabretta, M. R., et al. 2009, *ApJS*, 181, 398
 Nataf, D. M., Gould, A., Fouqué, P., et al. 2013, *ApJ*, 769, 88
 Nemeč, J. M., Cohen, J. G., Ripepi, V., et al. 2013, *ApJ*, 773, 181
 Nidever, D., Olsen, K., Choi, Y., et al. 2019, *ApJ*, 874, 118
 Nikolaev, S., Drake, A. J., Keller, S. C., et al. 2004, *ApJ*, 601, 260
 Nöel, N. E. D., Conn, B. C., Carrera, R., et al. 2013, *ApJ*, 768, 109
 Nöel, N. E. D., Conn, B. C., Read, I. J., et al. 2015, *MNRAS*, 452, 4222
 Oey, M. S., Dorigo Jones, J., Castro, N., et al. 2018, *ApJL*, 867, L8
 Pedregosa, F., Varoquaux, G., Gramfort, A., et al. 2011, *Journal of Machine Learning Research*, 12, 2825, <http://www.jmlr.org/papers/volume12/pedregosa11a/pedregosa11a.pdf>
 Ripepi, V., Molinaro, R., Musella, I., et al. 2019, *A&A*, 625, A14
 Růžička, A., Theis, C., & Palouš, J. 2009, *ApJ*, 691, 1807
 Růžička, A., Theis, C., & Palouš, J. 2010, *ApJ*, 725, 369
 Saha, A., Olszewski, E. W., Brondel, B., et al. 2010, *AJ*, 140, 1719
 Schlegel, D. J., Finkbeiner, D., & Davis, M. 1998, *ApJ*, 500, 525
 Shapley, H. 1940, *BHarO*, 914, 8
 Simon, N. R., & Lee, A. 1981, *ApJ*, 248, 291
 Skowron, D. M., Jacyszyn, A. M., Udalski, A., et al. 2014, *ApJ*, 795, 108
 Skowron, D. M., Soszyński, I., Udalski, A., et al. 2016, *AcA*, 66, 269
 Smolec, R. 2005, *AcA*, 55, 59
 Soszyński, I., Dziembowski, W. A., Udalski, A., et al. 2011, *AcA*, 61, 1
 Soszyński, I., Udalski, A., Szymański, M. K., et al. 2014, *AcA*, 64, 177
 Soszyński, I., Udalski, A., Szymański, M. K., et al. 2016, *AcA*, 66, 131
 Soszyński, I., Udalski, A., Szymański, M. K., et al. 2017, *AcA*, 67, 103
 Soszyński, I., Udalski, A., Szymański, M. K., et al. 2019, *AcA*, 69, 87
 Stanimirović, S., Staveley-Smith, L., & Jones, P. A. 2004, *ApJ*, 604, 176
 Udalski, A. 2003, *ApJ*, 590, 284
 Udalski, A., Szymański, M. K., & Szymański, G. 2015, *AcA*, 65, 1
 van der Marel, R. P., & Kallivayalil, N. 2014, *ApJ*, 781, 121
 Wagner-Kaiser, R., & Sarajedini, A. 2017, *MNRAS*, 466, 4138
 Yoshizawa, A. M., & Noguchi, M. 2003, *MNRAS*, 339, 1135
 Zivick, P., Kallivayalil, N., Besla, G., et al. 2019, *ApJ*, 874, 78